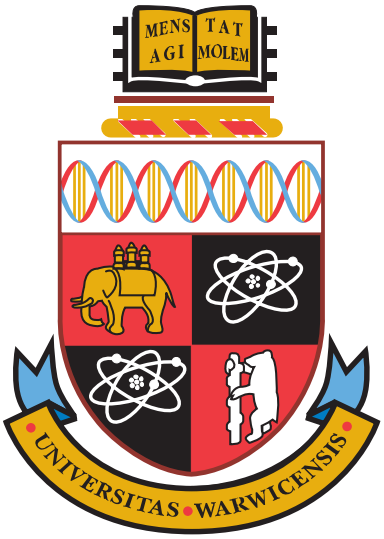

Development of a method to characterise the expression profile of electrogenic transmembrane proteins in excitable cells

by

Jolene Atia

Thesis

Submitted to the University of Warwick

for the degree of

Doctor of Philosophy

Department of Systems Biology

January 2015

THE UNIVERSITY OF WARWICK

Contents

List of Tables

List of Figures

Acknowledgments

To begin, I must thank my Lord and Saviour Jesus Christ. Indeed, Your words have always been my support during this entire study: " I can do all things through Christ who strengthens me".

There are a number of people without whom this thesis might not have been written, and to whom I am greatly indebted. I would like to express my special appreciation and thanks to my supervisors Dr Andrew Blanks and Dr Hugo van den Berg. You have been a tremendous mentors to me. I would like to thank you for encouraging my research. Your advice on my research have been priceless. You have been extremely supportive and inspirational. I would like to thank Dr David Rand for contributing to acquiring the funding of my grant. My thanks goes to everyone in the lab who worked hard to provide me with all the data: Dr Shmygol, Conor McCloskey, and Yi Chan.

A special thanks goes to my family. Words cannot express how grateful I am to my dear husband Moheb Shalaby, my beloved son Joseph Shalaby, and my lovely girls Marie-Anne and Emily Shalaby for their love, care, understanding, and all of the sacrifices that they've made on my behalf. Your prayers for me was what sustained me this far. Finally my parents, Kamal Atia and Lucy Ebaid, my brother George Atia, and my mother in law Aida Salib, have been the driving force behind my success in life and I could never thank them enough for the support. I am particularly grateful to my best friends Maggie Tawfik, Katy Sharobeem, and Abir Farag for their support, encouragement, interest, and prayers.

Declarations

This thesis is submitted to the University of Warwick in support of my application for the degree of Doctor of Philosophy. It has been composed by myself and has not been submitted in any previous application for any degree apart from the experimental part in Chapter 2. The work presented (including data generated and data analysis) was carried out by myself except where otherwise stated.

Abstract

Computational and mathematical models have become increasingly important and have contributed to significant advances in our understanding of complex biological systems. We developed a mathematical model to characterise the expression profile of transmembrane electrogenic proteins of excitable cells.

The cell of interest is the myometrium smooth muscle cell, which is the principal unit of electrical activity in the uterus. These cells remain quiescent throughout most of gestation, whereas just prior to and during labour they are able to generate spontaneous action potentials. A more detailed and comprehensive characterisation of these cells, in comparison to previous models, would furnish an appropriate tool for the development of therapeutics to manage preterm birth and other perinatal problems associated with uterine contractility, such as postpartum haemorrhage.

The "conductome" can be defined as the totality of ion channels and ion transporters expressed by an electrically active cell, i.e., a list specifying the cell surface density and oligomeric composition of each of these species. Gene expression techniques can accurately survey the complete set of all mRNA species encoding electrogenic proteins (e.g., subunits of channels). The conductome is constrained by this transcriptome, but the link between the two is complicated by the facts that (i) presence of an mRNA species does not necessarily imply the presence at the transmembrane proteomics level; and (ii) subunits can combine in various ways to give rise to conducting channels with different properties.

Every individual potential oligomeric channel complex was represented as a mathematical model on the basis of biophysical data taken from the literature; these data were obtained mainly using heterologous expression systems. We investigate the possibility of combining the behavioural information of the action potential with the detailed molecular data of the transcriptome. The general problem is that electrical behaviour does not necessarily lead to a unique solution. The question addressed here is to what extent the additional information provided by transcriptomics helps to constrain the solution space.

We develop and apply a method to characterise the functional redundancy of electrically active cells. We use mRNA sequencing to determine which electrogenic species the cell is capable of expressing, combined with a least-squares parameter estimation procedure to determine the conductome from electrophysiological data. Moreover, we estimate the parameters associated with the gating kinetics from published data, so that the *only* remaining free parameters are the surface densities of the species on the list defined by the transcriptomics analysis.

Abbreviations

AP	action potential
ATP	adenosine triphosphate
$[ATP]_o$	extracellular ATP concentration
Ca^{2+}	calcium ion
$[Ca^{2+}]_i$	intracellular calcium concentration
$[Ca^{2+}]_o$	extracellular calcium concentration
CICR	calcium-induced calcium release
Cl^-	chloride ions
$[Cl^-]_i$	intracellular chloride concentration
$[Cl^-]_o$	extracellular chloride concentration
D15	gestation day 15
D18	gestation day 18
DAG	diacylglycerol
EMG	electromyography
ER	endoplasmic reticulum
GHK	Goldman-Hodgkin-Katz

GPCR	G-protein-couple receptor
IP_3	inositol-triphosphate
K^+	potassium ion
$[K^+]_i$	intracellular potassium concentration
$[K^+]_o$	extracellular potassium concentration
LSE	least-squares estimator
MLCK	myosin light chain kinase
MLCP	myosin light chain phosphatase
MMG	magnetomyography
MSMC	myometrium smooth muscle cell
Na^+	sodium ion
$[Na^+]_i$	intracellular sodium concentration
$[Na^+]_o$	extracellular sodium concentration
NCX	Na^+-Ca^{2+} exchanger
ODE	ordinary differential equation
PIP_2	phosphatidyl inositol bisphosphate
PKC	protein kinase C
PLC	phospholipase C
PMCA	plasma membrane calcium ATPase
RMP	resting membrane potential
RhoK	Rho kinase

RyR	Ryanodine receptors
ScTx	Stromatoxin
SERCA	SR calcium ATPase
SR	sarcoplasmic reticulum
SVD	singular value decomposition
SARA	SQUID array for reproductive assessment
SQUID	superconducting quantum interference devices

Chapter 1

Introduction

The main aim of this thesis is to investigate the role of various ionic conductances in mediating the action potential of the uterine smooth muscle cell. In particular, a method is presented that combines transcriptomics with biophysical recordings to estimate the conductome of the smooth muscle cell to within the null kernel of a certain operator. The analysis offers an insight into the inherent redundancy structure of the conductome, relative to a given set of biophysical behaviours. Whereas subsequent chapters will detail the method as well as its potential applications, the present chapter surveys aspects of the biological, biophysical, and mathematical background that have motivated the research.

1.1 Anatomy of the human female reproductive system

The female reproductive system comprises the ovaries, the uterine tubes (Fallopian tubes), the womb (uterus), the vagina, and the pudenda (Figure 1.1). Baggish [27] and Chard [28] are standard textbooks which serve as references for the uterine anatomy. The ovaries are the female sexual glands. These are ovoid organs 5 cm long, 2 cm wide, and 8 mm thick, found in pairs; they lie against the lateral walls of the pelvic cavity in a depression called the ovarian fossa. They also release the ova (unfertilised eggs) into the uterine tubes. Ovaries take turn in releasing ova at various intervals. The ovaries are attached to the Fallopian tubes to the outer layer uterus via the ovarian ligaments. The Fallopian tubes are fine tubes, that conduct the ova to the uterus, which lies within the pelvis. The uterus connects with the vagina through the cervical canal.

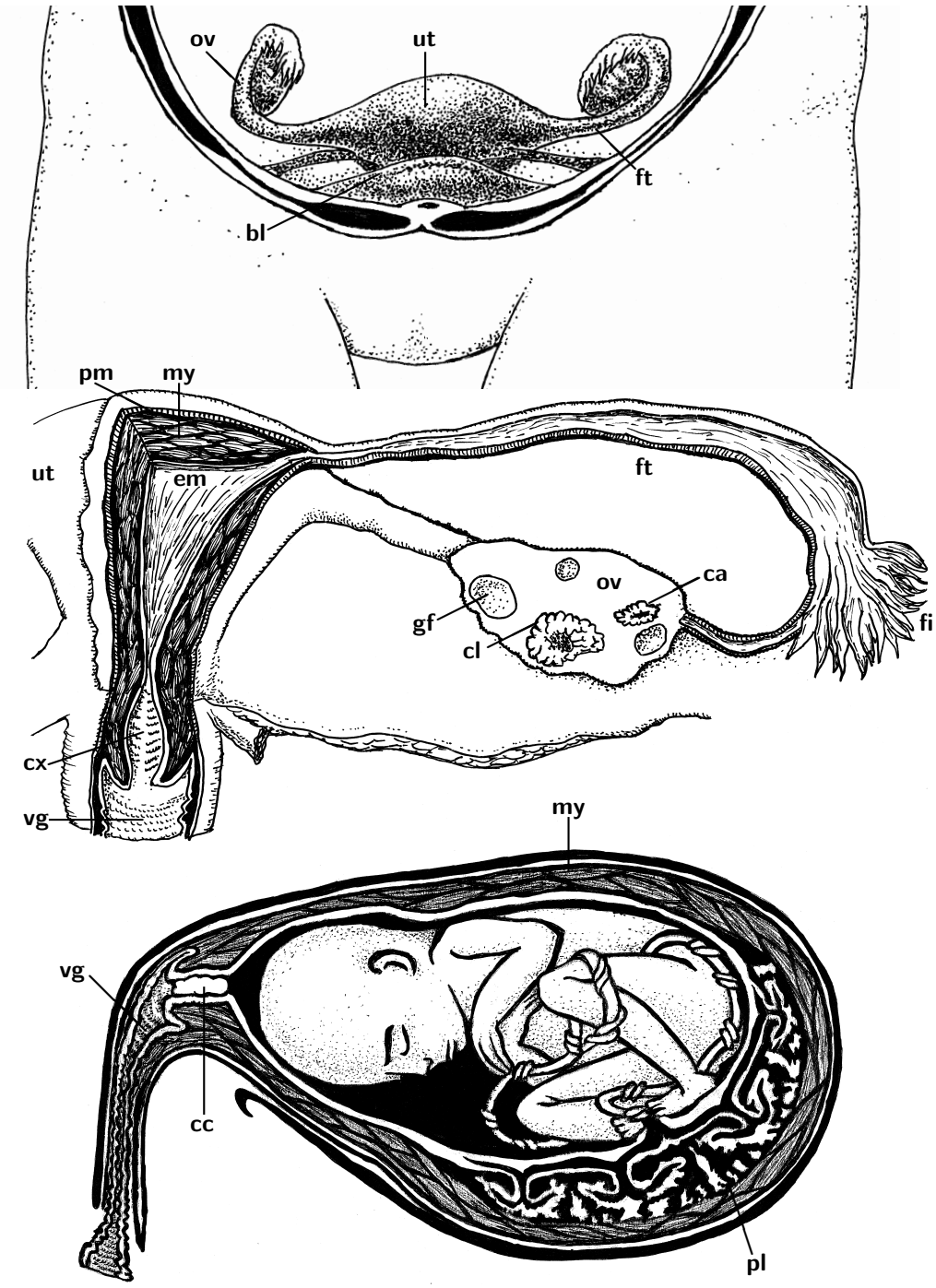

Figure 1.1: Anatomy of the human female reproductive system. Top: location in the lower abdomen; middle: partially dissected uterus showing the layers of the uterine wall and the Fallopian tube; bottom: the gravid uterus at term. The following structures are indicated: **ut**: uterus; **ov**: ovary; **ft**: Fallopian tube; **fi**: fimbria; **bl**: bladder; **pm**: perimetrium; **my**: myometrium; **em**: endometrium; **gf**: Graafian follicle; **cl**: corpus luteum; **ca**: corpus albicans; **cx**: cervix; **cc**: cervical canal with mucus plug; **vg**: vagina; **pl**: placenta. (Figure by Dr Hugo van den Berg)

1.1.1 The uterus

The uterus is involved in many reproductive functions including menses, implantation, gestation, labor, and delivery. It responds to the hormonal environment within the body. This allows the uterus to adapt to the different stages of a woman's reproductive life. The uterus, in particular the endometrium, adjusts to reflect changes in ovarian steroid production during the menstrual cycle and displays rapid growth and specialised contractile activity during pregnancy and childbirth. During the prepubertal and post-menopausal years, the uterus remains in a relatively quiescent state. The uterus is shaped like an upside-down pear. It is a hollow, muscular organ with thick walls situated deep in the pelvic cavity between the bladder and rectum. In the adult, the uterus is 7.5 cm long, 5 cm in width, and 2.5 cm thick and weighs up to 40 g. In pregnancy, the uterus becomes up to five times larger. Into the upper part, the uterus is connected to the Fallopian tubes, one on either side, while its lower part narrows into the cervix. The wall of latter is composed of fibrous connective tissue which is of a firmer texture than the wall of the uterus.

When the ova are released from the ovaries, they are carried to the uterine cavity through the Fallopian tubes. If an ovum is fertilised as it travels down the Fallopian tube, it may subsequently embed in the uterine wall, where it grows into the embryonic structures which include the placenta and the membranes that enclose the developing fetus. Changes in both the size and the structure of the uterus occur to accommodate the needs of the growing fetus.

The uterine wall consists of three layers: the endometrium, the myometrium, and the perimetrium. The endometrium is a glandular layer that lines the uterus. It prevents adhesions between the opposed walls of the myometrium. This layer is sensitive to cyclic changes in the levels of the ovarian hormones. During the menstrual cycle, the steroid hormone estrogen causes the endometrium to grow to a thick, blood vessel-rich, glandular tissue layer. This environment is suitable for the implantation of the fertilised egg (zygote) upon its arrival in the uterus from the Fallopian tube (where the egg is fertilised). If the ovum is not fertilised, conception does not occur and estrogen is produced in reduced amounts and the production of the steroid hormone progesterone is decreased. As a result, the endometrial lining begins to breakdown and sheds through menstruation. The myometrium, the middle layer, is the main structure element of the uterus and makes up most of its volume. This layer is a muscular layer composed mainly of smooth muscle cells known as the myometrial smooth muscle cells (MSMCs), also called uterine myocytes or myometriocytes. The outer layer of the uterus, the perimetrium, is a thin layer of tissue made of epithelial cells that envelop the uterus.

1.1.2 The myometrium

The myometrial smooth muscle coat undergoes dramatic remodelling during pregnancy in order to accommodate the growing fetus [29]. Uterine contractions consist of the concerted activation of large groups of MSMCs. During pregnancy, the myometrium expands to accommodate the growing fetus. This layer contains arteries that support the placenta, which furnishes the fetus with nutrients and oxygen and carries away its waste products and carbon dioxide. Once the baby has been delivered, the muscles of the myometrium continue to contract to push out the placenta. This continued contraction also compresses the blood vessels, which minimises the loss of blood after delivery.

1.2 Cellular excitability

All cells are characterised by a difference in electric charge across the cell membrane, which is called the resting membrane potential (RMP). In certain cells, such as nerve cells, muscle cells, and sensory receptor cells in animals, as well as specialised cells in certain plants, this potential difference can undergo rapid and dramatic changes such as a reversal of its polarity and those cells are capable of generation and transmission of electrochemical impulses along the membrane. Such cells are said to be electrically excitable; the changes in membrane potential can be transmitted to neighbouring cells and can serve as a rapidly travelling signal that coordinates activity at the whole-organ or whole-body level. Excitation and electrical signalling in cells involve the ionic distribution across the membrane, the permeability of the membrane to those ions, and the movement of those ions through electrogenic proteins such as ion channels and ion pumps. The major ions are potassium ions (K^+), sodium ions (Na^+), calcium ions (Ca^{2+}), and chloride ions (Cl^-). At rest, the electric potential of the cell cytosol is negative relative to the medium surrounding the cell (excitable cells have a more negative RMP than non-excitable cells). Numerous physiochemical variables affect the RMP, such as temperature, pH, and the intra- and extra-cellular concentrations of electrolytes; Keener and Sneyd [30] give typical values for intracellular and extracellular ionic concentrations in different cell types. Concentration differences of various ions are set up and maintained by active mechanisms that expend energy to pump ions against their concentration gradient. The RMP arises mainly from many simultaneous processes. The sodium/potassium ATPase, is a pump that uses energy stored in ATP molecules to force two potassium ions (K^+) into the cell for every three sodium ions (Na^+) removed from the cell against their concentration gradient. The Na/K ATPase produces a concentration

of Na^+ outside the cell that is about 10 times greater than that inside the cell. At the same time, it produces a concentration of K^+ inside the cell that is about 20 times greater than that outside the cell [30, 31]. Concomitantly, a number of potassium leakage channels (always open) in the plasma membrane allow a slow diffusion of K^+ out of the cell. A very small leakage of Na^+ into the cell occurs due to a small number of sodium leakage channels in the plasma membrane. The membrane at rest is far more permeable to potassium than it is to sodium. The concentrations of chloride ions (Cl^-) and calcium ions (Ca^{2+}) are also maintained at higher levels outside the cell, while negatively charged proteins are present at high concentrations inside the cell. A typical RMP is around -55 mV to -90 mV, the magnitude is a measure of the charge separation across the membrane. The negative sign is attributed to the widely used convention that defines the extracellular potential to be zero.

1.2.1 Action potential

When an electric current is passed through the cellular membrane of an excitable cell, the charge separation and hence the membrane potential is perturbed. When the perturbation is small, the perturbed membrane potential is called a graded potential; it returns to the RMP via passive electro-diffusive processes. However, the electrogenic proteins spanning the membrane are sensitive to the membrane potential and change their conductivity in response to this perturbation. This is called voltage-gating; it can lead to a further depolarisation, far exceeding the initial perturbation, which is called an action potential (AP; Figure 1.2). Electrically excitable cells can generate both APs and graded potentials, while electrically inexcitable cells produce graded potentials only.

The production of APs results from the presence of a sufficient number of voltage-gated ion channels in the membranes of electrically excitable cells. If some fraction of the voltage-gated ion channels are blocked by specific pharmacological agents, the cells cannot produce APs. When these voltage-gated channels open, allowing passage of sodium or calcium ions, the membrane potential becomes less negative (more depolarised) and in some cases may even become positive. The AP ends in a return to the RMP mediated by several process, such as (i) the activation of specific potassium channels, which allows potassium ions efflux; (ii) the inactivation of sodium and calcium channels, preventing further sodium and calcium ions from crossing the membrane; (iii) the action of pumps restores the original cytosolic sodium and calcium ionic concentrations. The final phase may include a period during which the cell is hyperpolarised, that is, the membrane potential is more

negative than the RMP.

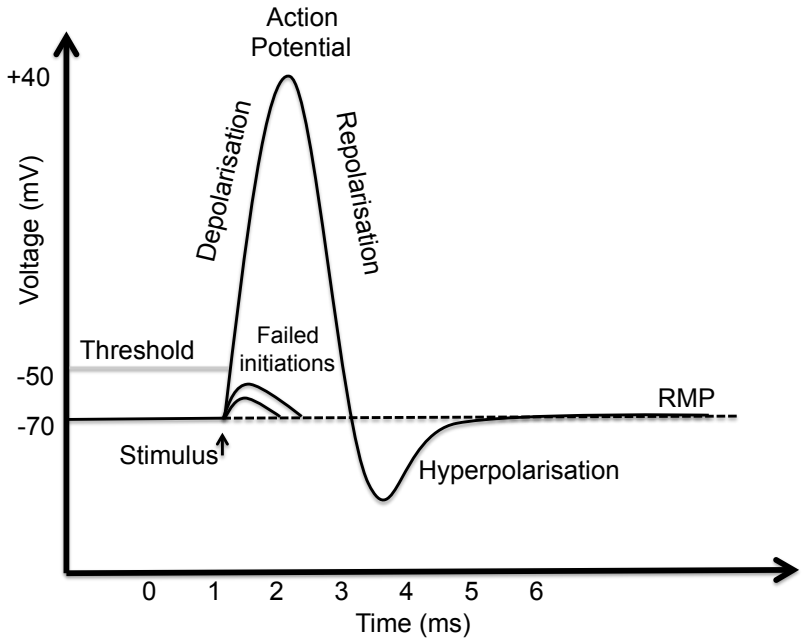

Figure 1.2: A schematic view of an idealised AP. The diagram illustrates the various phases as the AP passes a point on a cell membrane.

Waveforms of APs

The amplitude of the AP tends to be in the range of 10 to 100 mV. This range is determined by the Nernst equilibrium potentials of the various permeant ionic species. Whereas there is relatively little variation in AP amplitude across various cell types, the time course does vary greatly, ranging from 1 ms in certain neurones, to 10 ms in skeletal muscle fibres, to the order of 0.5 s in cardiac muscle fibres, and many seconds in certain electrically excitable plant cells and in MSMCs [5]. Furthermore, APs can have many different shapes, as shown in Figure 1.3, which plots various membrane potentials as function of time at one particular point on the membrane.

Properties of action potentials

The threshold potential is a level to which the membrane potential must be depolarised in order to initiate an AP (Figure 1.2). In other words, it is the value of the membrane voltage that needs to be attained in order that an AP can be generated. Physiologically, it is the membrane voltage at which the inward (sodium or calcium)

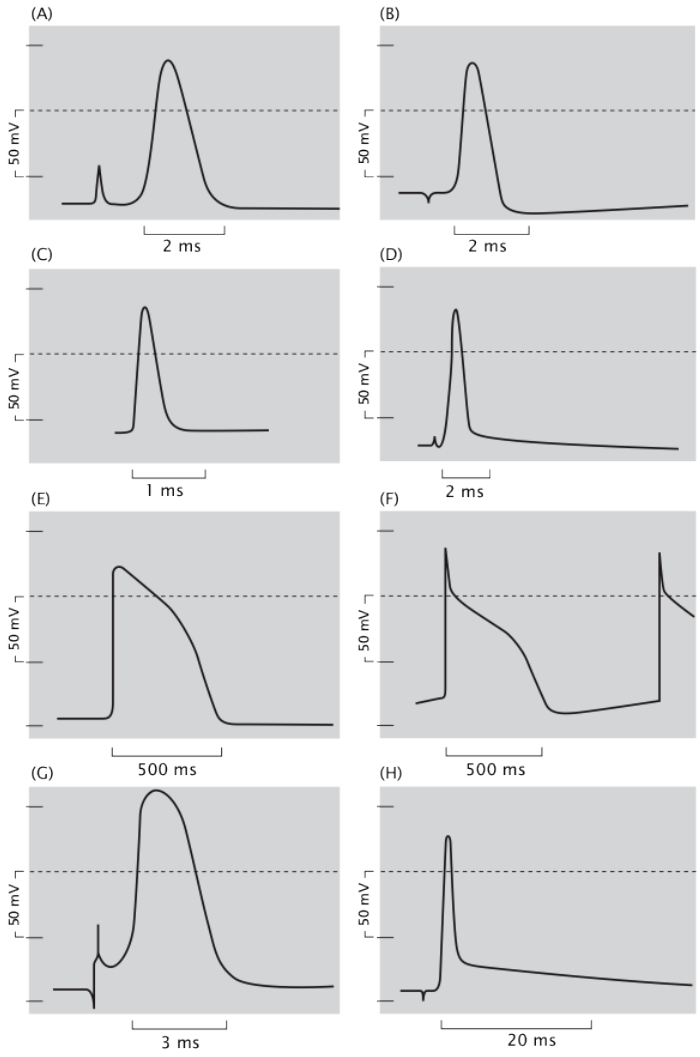

Figure 1.3: Many shapes of APs recorded from different cell types in different animals. The horizontal dashed white line is zero potential. The top row compares the APs in the squid giant axon as recorded (A) in the animal and (B) after isolation by dissection. (C) AP measured in the axon of a cell from a cats peripheral nervous system. (D) AP recorded from the cell body of a neuron from a cats spinal cord. (E) AP recorded from a muscle fibre in the heart of a frog. (F) AP recorded from a regulatory neuron in a sheeps heart. (G) Potential generated in the specialised muscle tissue that forms the electric organ of a fish that can shock its prey. (H) AP recorded from a more typical muscle from a frogs thigh. (from R.D.Keynes and D.J. Aidley [1])

current exceeds the outward (potassium) current, triggering a positive feedback cycle that defines the early part (rising phase) of the AP. If the threshold point is not reached, no AP will fire, but if the stimulus is above the threshold, an AP of maximum magnitude is triggered. For this reason, the AP is said to be all-or-none potential.

Immediately following an AP, a subsequent AP is less readily evoked; the cell is said to be refractory. For a brief interval (on the order of few milliseconds), called the absolute refractory period, a second AP cannot be elicited regardless of the intensity of the stimulus. Then for an interval greater than the absolute refractory period, there is a relative refractory period in which a second AP can be elicited, but with higher threshold. The refractory period is caused by the inactivation of sodium and calcium channels. These refractory periods indicate that the mechanism that generates the AP requires some time to recover.

Intercellular transmission of electric potential

After the triggering of an AP in a part of the membrane, the positive charges inside the cell will move to the adjacent region of the membrane causing the adjacent region to depolarise too and thus the AP spreads. Membrane potential changes in one cell can result in membrane potential changes in adjacent cells. In certain tissues, including smooth and cardiac muscle, there exist specialised membrane junctions at which the membranes of adjacent cells are in close proximity. These communicating junctions or gap junctions are composed of six connexin proteins that combine to form a cylinder with a pore in the centre region (Figure 1.4). The cytoplasms of adjacent cells are connected through this low resistance pathways. These pathways allow direct passage for electrical, chemical, and metabolic signalling between cells [32–35]. Hence, if a current is injected into a cell in a tissue, a fraction of this current is coupled via gap junctions to the adjacent cells. Gap junctions are found in tissues where synchronisation of electrical activity of many cells occurs [5].

1.2.2 Myometrial contractions and AP waveforms in human MSMC

During most of gestation, the myometrium remains quiescent even while it undergoes weak and unsynchronised contractions. These contractions then progressively increase in frequency and amplitude towards the end of pregnancy, finally culminating in brief periods of powerful contractions during labour. To understand the myometrial function in pregnancy and labour, it is vital to investigate the mechanisms underlying the generation and propagation of APs and its coupling to contraction

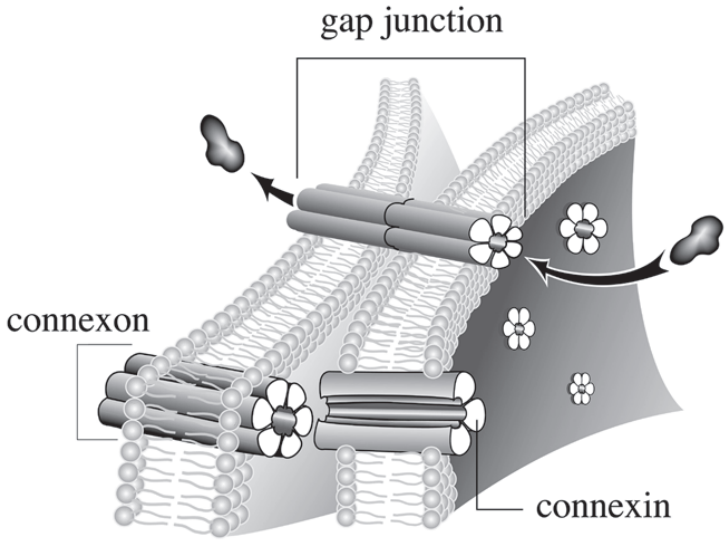

Figure 1.4: Schematic of gap junctions with terminology [2].

via the increase in cytosolic calcium concentration ($[Ca^{2+}]_i$) [36].

The myometrium contains MSMCs that are able to generate spontaneous APs in the absence of neuronal or hormonal stimuli [29]. Nakao et al [3] performed a detailed study on human myometrial sample taken at the end of pregnancy. Two types of spontaneous APs were observed: a spike-like variant and a long-plateau variant [37–39]. The long-plateau type is observed in more than 50% of preparations [36]. It comprises a fast upstroke followed by a sustained plateau of depolarisation between -30 and -20 mV lasting approximately 1 min. The spike-like type is made of individual spikes grouped into bursts superimposed on elevated level of interspike potential. Recordings of APs from human myometrium by Nakao et al [3] are shown in Figure 1.5. Both types of AP are associated with $[Ca^{2+}]_i$ transients and trigger contractions that last for the duration of the AP. However, the shape of the $[Ca^{2+}]_i$ transients and the contractions caused by each AP differ. The contractions triggered by the plateau-type AP reach their peak after the fast upstroke of the AP, then slowly decay during the plateau phase. Upon repolarisation, the rate of decay increases, causing the muscle to relax to its baseline tone. By contrast, the contractions elicited by the spike-type AP are ragged, continue to rise for the whole duration of the AP burst, and relax upon the termination of spikes. The $[Ca^{2+}]_i$ transients precede and assume the same shape as the associated contractions [36].

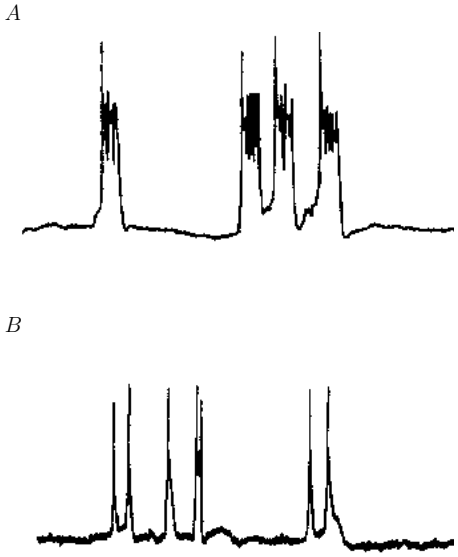

Figure 1.5: AP recorded from pregnant human myometrium (A) Plateau-like, (B) Spike-like (from Nakao et al [3]).

1.2.3 Excitation-contraction signal pathways in MSMC

Excitation-contraction coupling is the sequence of events that intervene between AP generation and contraction initiation [40]. The sequence of events is shown in Figure 1.6. These events are as follows:

(i) During the depolarising phase of the AP, Ca^{2+} enter the cell through the voltage-gated calcium channels located in the plasma membrane. The primary channel responsible for the calcium entry observed during AP in the MSMC is the L-type calcium channel [36]. The incoming Ca^{2+} contribute to the rising phase of the AP as well as being responsible for uterine myocyte contraction [41, 42].

(ii) Another independently controlled release of Ca^{2+} occurs; certain first messengers such as oxytocin bind to and activate specific G-protein-couple receptors (GPCRs) that span the cell membrane. This stimulation of GPCR results in the liberation of inositol-triphosphate (IP_3) and diacylglycerol (DAG) from the plasma membrane. The transmission of a signal between oxytocin receptor, GPCR, and the liberation of IP_3 is mediated by phopholipase C (PLC), which hydrolyses phosphatidyl inositol bisphophate (PIP_2) producing IP_3 and DAG. This is shown in Figure 1.6.

(iii) The IP_3 molecules diffuse into the cytosol and bind specific receptors on the sarcoplasmic reticulum (SR), resulting in the release of Ca^{2+} from the SR. The transient increase in Ca^{2+} activates the calcium-activated non-specific cationic conductance in the plasma membrane, leading to a transient depolarisation that

leads to the opening of the voltage-gated L-type calcium channels. As a result, a sizable calcium influx occurs and the cell contracts [43]. Even under agonist (oxytocin) stimulation and IP_3 production, no force is produced (via Ca^{2+} entry) in the uterus if plasma membrane voltage-gated calcium channels are inhibited, because Ca^{2+} entry from the SR is transient and rapidly depletes [43].

(iv) Following the elevation of $[Ca^{2+}]_i$, calmodulin molecules bind Ca^{2+} (four ions to each molecule), which allows them to activate myosin light chain kinase (MLCK). MLCK phosphorylates the light chains of myosin at the serine at position 19. The phosphorylated myosin can then interact with actin microfilaments to generate force (causing MSMC contraction) [44]. The conformational change in actin and myosin requires ATP hydrolysis.

(v) DAG and Ca^{2+}/calmodulin complex potentiate protein kinase C (PKC). This facilitates the translocation of PKC from the cytosol to the plasma membrane. The PKC increases the sensitivity of the contractile machinery to Ca^{2+} by inhibiting myosin light chain phosphatase (MLCP).

(vi) At the same time as the activation of PLC, another calcium-sensitising mechanism is activated. A small guanine triphosphate (GTP)-binding protein RhoA is activated, which increases Rho kinase (RhoK) activity, resulting in inhibition of MLCP. This prevents the light chain of myosin from being dephosphorylated by MLCP; a delicate balance of contraction and relaxation is mediated by the activity ratio of MLCK to MLCP.

(vii) To return to the resting state, MSMC requires the decrease of $[Ca^{2+}]_i$ and the dephosphorylation of myosin light chains by MLCP, which removes the phosphate group from the light chain of myosin to promote muscle relaxation. Calcium is removed from the cell either to the external environment through the plasma membrane calcium ATPase (PMCA) or the sodium-calcium exchanger (NCX), or back to SR through SR calcium ATPase (SERCA).

1.2.4 Measurement of uterine electrical activity

Prediction of delivery (both at term and preterm) might be improved by monitoring the changes in the electrical signalling characteristics that occur during the transition between quiescent to fully contractile uterus. Two methods are being developed to record electrophysiological activity associated with uterine contractions; electromyography (EMG) and magnetomyography (MMG). The former detects contractions using two electrodes attached directly to the uterus or non-invasively to the maternal abdominal surface [45–48] (Figure 1.7A). Several EMG parameters reflect the changes in cell excitability and cell-to-cell coupling that are required for

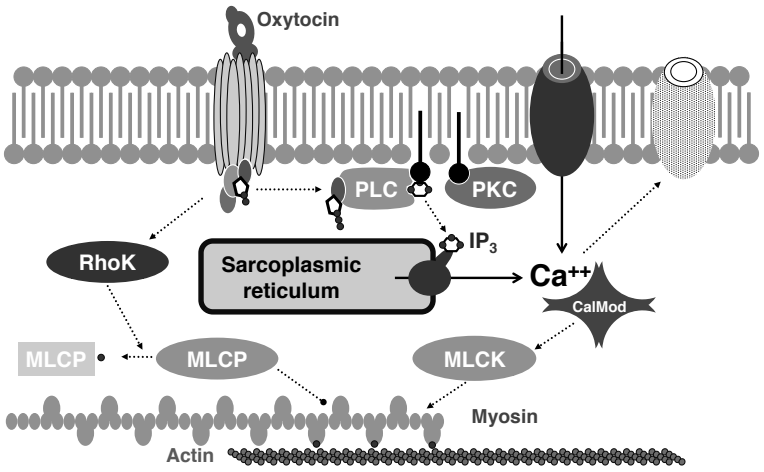

Figure 1.6: Schematic diagram showing the major components that control $[Ca^{2+}]_i$ in myometrium. The following components are indicated: **MLCP**: myosin light chain phosphatase; **MLCK**: myosin light chain kinase; **PKC**: protein kinase C; **PLC**: phospholipase C; **CalMod**: calmodulin; **RhoK**: Rho kinase; **IP_3**: inositol triphosphate. (Figure by Dr Hugo van den Berg)

effective contractions leading to delivery. These parameters include burst amplitude, duration, and power, as well as peak frequency, total energy, and propagation velocity. Uterine EMG predicts delivery within 24 hours at term and within 4 days preterm [49]. On the other hand, MMG relies on non-invasive recordings of the magnetic fields corresponding to the electrical fields from the abdominal surface [50,51]. The magnetic field, associated with the APs that are responsible for the contractility of the uterus, can be measured using magnetic sensors that detect signals outside the boundary of the skin, without making electrical contact with the body. The magnetic field sensors are called superconducting quantum interference devices (SQUID). Using a 151-channel SQUID array for reproductive assessment (SARA), non-invasive magnetic field recordings can be obtained (Figure 1.7 B and C). SARA has the advantage of measuring the activity with a high spatial-temporal resolution, which will help determine the regions of localised activation (i.e., localising the pacemaker cells), the propagation velocity, as well as the direction and spread of the uterine activity as a function of distance [50]. The use of both EMG and MMG can help to identify patients with contractions in true term and preterm labour.

1.3 Cell-level models

Mathematical models of the dynamics of the membrane potential, in terms of the behaviour of the individual species of the electrogenic proteins, constitute a key

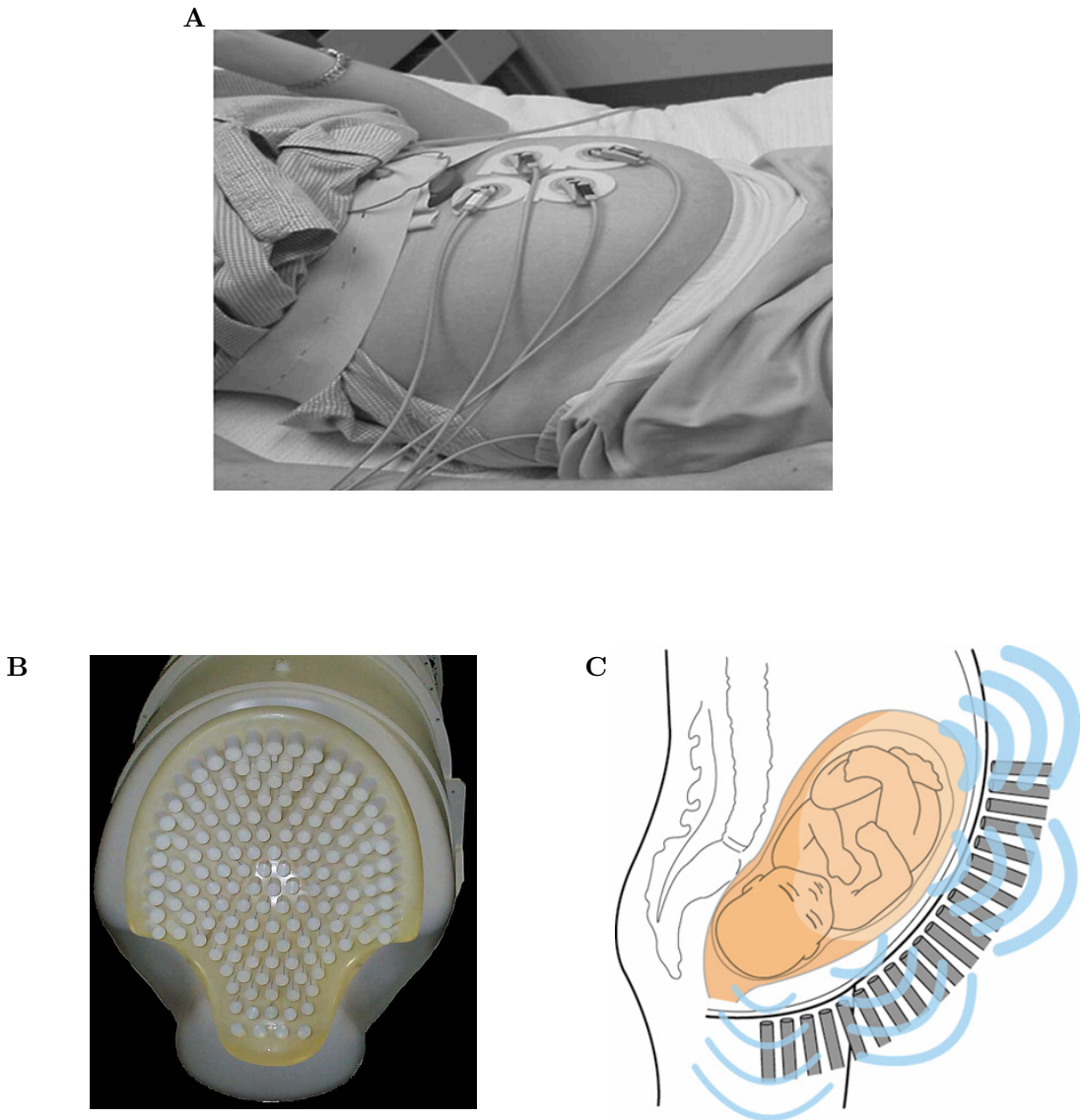

Figure 1.7: Methods of measurement of the uterine electrical activity. (A) Typical uterine EMG setup [4]. (B) The 151-channel sensor SARA array (from http://www.ese.wustl.edu/ nehorai/research/ra/back.html). (C) A simplified illustration of the uterine MMG field (from www.uams.edu).

component of the work presented in subsequent chapters. The paradigm of such models is the classic Hodgkin-Huxley model, which will be reviewed first, followed by more recent developments.

1.3.1 The membrane potential

The relationship between electrolyte concentrations and membrane potential is a cornerstone of any theory of electrical activity in biological cells. These relationships are given by the Nernst and Goldman-Hodgkin-Katz (GHK) equations.

The Nernst potential

The permeability of the cell membrane for specific ions is determined by the number of ion channels of various species that are open at the prevailing membrane potential. Ion channels can exhibit various degrees of ion selectivity: some are permeable to only a single species of ion, others can be permeable to a wide range. In a case where the plasma membrane is permeable to a single ion, two forces are exerted on this specific ion: the first is diffusion of ions down their concentration gradient (from high to low concentrations); the second is an electrical driving force resulting from a charge separation between the inside and the outside of the cell, caused by the active displacement of ions from one side of the membrane to the other, which is mediated by ion pumps such as Na/K ATPase. The electrical driving force depends on the prevailing potential difference across the channel. Thus there will be a value of the membrane potential such that the drift due to diffusion and due to the electromotive force exactly cancel. This value is called the *equilibrium potential* for that ion.

Glial cells provide an instructive elementary example, since in these cells, the membrane is permeable to almost solely potassium ions at the RMP. The cell has a higher concentration of potassium inside than outside. Net diffusion of potassium ions takes place from inside to outside the cell. As a result, excess potassium ions accumulate on the outside of the membrane (and negative charge on the inside of the membrane because of the deficit of potassium ions and the excess of anions inside the cell). A separation of charge resulting from the diffusion of potassium gives rise to a potential difference. The latter opposes further diffusion of potassium to the outside of the cell. When both forces exactly balance each other, the potential difference across the membrane is called the potassium equilibrium potential, E_{K}. In this cell, which is permeable to potassium only, E_{K} determines the RMP.

The equilibrium condition depends only on the electric energy per particle of a given species on either side of the membrane. Hence the potential difference is

directly related to the concentration difference by the Boltzmann equation. Solving the latter for the potential difference, the *Nernst equation* is obtained:

$$E_i = \frac{RT}{zF} \ln \frac{[\text{ion}^+]_o}{[\text{ion}^+]_i} \,, \tag{1.1}$$

where R is the universal gas constant, F is the Faraday constant, T is the absolute temperature, z is the valency of the the ion, $[\text{ion}^+]_o$ and $[\text{ion}^+]_i$ are the extracellular and the intracellular ion concentrations for that particular cell. Values of these constants, and their units are given in Table 4.33.

The Goldman-Hodgkin-Katz potential

The Goldman-Hodgkin-Katz (GHK) equation describes the steady-state membrane potential for a cell with a membrane permeable to various ionic species. This RMP is determined not only by the intracellular and extracellular ion concentrations but also by how readily the ions cross the membrane. A constant steady-state membrane potential occurs when the sum of fluxes add up to zero (zero net current) as follows:

$$I_{\text{total}} = I_{\text{K}} + I_{\text{Na}} + I_{\text{Cl}} = 0 \,. \tag{1.2}$$

When the net flux of permeable ions is not equal to zero, there will be fluxes of all the ions involved driven by their concentration gradients. To obtain a constant steady-state membrane potential in a membrane permeable to K^+, Na^+, and Cl^- ($dV/dt = 0$, where $V = V_{\text{in}} - V_{\text{out}}$), there must be zero net current.

The RMP lies between the individual equilibrium potentials of the different ions that are crossing the membrane. The assumption for the GHK model is that the potential drops linearly over the membrane; this means that the electric field ($E = \Delta V$) is constant and proportional to the membrane potential V as illustrated in Figure 1.8. The GHK constant-field equation is as follows:

$$E_{\text{m}} = \frac{RT}{2F} \ln \frac{P_{\text{K}}[\text{K}^+]_o + P_{\text{Na}}[\text{Na}^+]_o + P_{\text{Cl}}[\text{Cl}^-]_i}{P_{\text{K}}[\text{K}^+]_i + P_{\text{Na}}[\text{Na}^+]_i + P_{\text{Cl}}[\text{Cl}^-]_o} \,, \tag{1.3}$$

where $[\text{K}^+]_o$, $[\text{Na}^+]_o$, and $[\text{Cl}^-]_o$ are the extracellular ion concentrations and $[\text{K}^+]_i$, $[\text{Na}^+]_i$, and $[\text{Cl}^-]_i$ are intracellular ion concentrations for that particular cell. The permeabilities of the membrane to K^+, Na^+, and Cl^- are denoted by P_{K}, P_{Na}, and P_{Cl} respectively. Goldman et al [52] give a derivation of the GHK equation. This equation is valid only for permeant ions that have the same valence. When the ions differ in valence the equation is more complicated. Several expressions were derived

for combinations of different valences [53–56]. For instance, Fatt et al [53] derived a modified equation that includes currents carried by divalent ions, such as Ca^{2+}, as well as monovalent ions. The equation by Fatt et al [53] of extracellular Ca^{2+} versus intracellular K^+ is as follows:

$$E_{\rm m} = \frac{RT}{F} \ln \sqrt{\frac{4P_{\rm Ca}[{\rm Ca}^{2+}]_o}{P_{\rm K}[{\rm K}^+]_i} + \frac{1}{4}} - \frac{1}{2} \, . \tag{1.4}$$

When the relative permeability of the membrane for a specific ion is significantly higher than it is for the remaining ions, the GHK equation reduces to the Nernst equation for that particular ion.

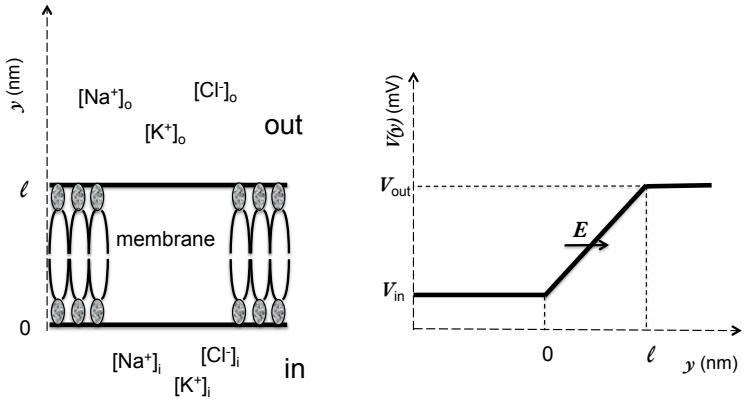

Figure 1.8: A section of a membrane. The following symbols are indicated: E: electric field; ℓ: membrane thickness; $V_{\rm out}$: extracellular potential; $V_{\rm in}$: intracellular potential; $[{\rm ion}^{+/-}]_o$: extracellular ions concentration; $[{\rm ion}^{+/-}]_i$: intracellular ions concentration.

Voltage clamp

The dynamics of the conductances of various ions can be both explicitly time-dependent and time-dependent through the dependence on the membrane potential [57]. It was realised that the former of these two dependencies could be made more manageable to study if the latter could be eliminated by keeping the membrane potential constant. This is accomplished using the voltage clamp technique. The voltage across the membrane is clamped, by means of an electronic servo circuit, to a constant desired value, as shown in Figure 1.9. The explicit time-dependence of the conductances can then be studied at various constant 'set' values of the voltage, or, in more modern variations of the technique, under imposed voltage time series. A specialised version of voltage clamp was introduced later. This was the patch clamp, which measures the current across a specific patch allowing us to measure the current across single or multiple channels. In the pioneering studies, a giant axon

from a squid was used in view of the technical difficulties involved in introducing an electrode into the cell. Using specific blocking agents that block either sodium or potassium channels, the two corresponding currents could be further isolated. Thus, the combined application of voltage clamp and pharmacology essentially dissected out the dynamic behaviour of isolated ionic currents.

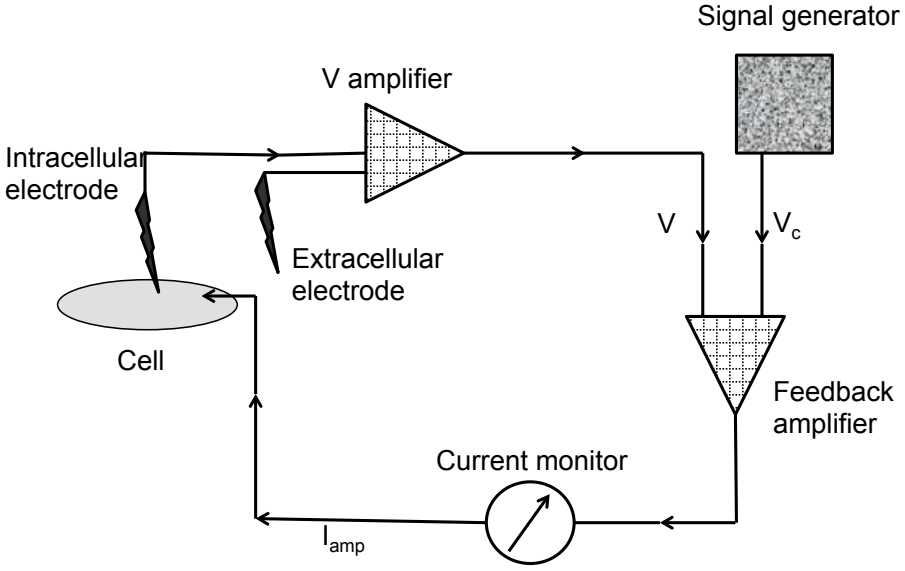

Figure 1.9: Two-electrodes voltage clamp circuit.

Let V_c denote the command voltage or the desired membrane voltage. As soon as the membrane potential V deviates ever so slightly from V_c, a difference signal is generated instructing the amplifier to produce current I_{app} that is injected into the cell forcing V to be equal to V_c. This current needed to keep $V = V_c$ is the recorded current which gives an insight into the opening and closing response of the ion channels (whose very existence was still at issue in 1952, Hodgkin and Huxley developed the theory).

When a depolarising step is applied, the sodium channels activate rapidly, leading to high Na^+ permeability and an inward Na^+ current is produced. Then the channel inactivates spontaneously because Na^+ permeability decreases, the K^+ permeability rises slowly causing an outward current. In the actual squid axon cell, both these currents shape the AP as a response to stimulus.

1.3.2 Hodgkin-Huxley model

The relation between current stimulation and the occurrence of APs could be studied in more detail with the advent of intracellular recording techniques, which allowed

the electrical properties of membranes to be investigated directly. These attempts lead up to the Hodgkin-Huxley model [58–61] for the generation of the nerve AP. Hodgkin-Huxley were able to relate the properties of the electrically excitable squid giant axon in terms of the measured relations of the membrane potential and the membrane current, in terms of the dynamic behaviour of (at the time) hypothetical transmembrane ionic channels.

The points of departure for Hodgkin and Huxley were as follows: (i) The RMP had been explained on the basis of a semipermeable membrane whose permeability to potassium exceeds that to other ions. The conductance g_i, of an ion type i, represents the ease with which ions pass through the membrane. At rest, the potassium conductance, g_{K}, is considerably larger than the sodium conductance, g_{Na}. Hence, the RMP is near the potassium Nernst potential E_{K}. The driving force for the ion i is the electrochemical potential difference, $V - E_i$. (ii) During an AP, the membrane capacitance is constant, but the membrane conductance changes transiently [62]. (iii) The first intracellular measurements of AP [63, 64] indicated that the peak of the AP of the squid axon exceeds a potential of zero. Then it was shown that the AP is sensitive to the extracellular concentration of Na^+ [65] and that membrane transiently reverses its selective permeability from being more permeable to potassium than to sodium at rest to being transiently more permeable to sodium to potassium at the peak of the AP. Thus, the membrane potential approaches the sodium Nernst potential E_{Na}.

Mathematical aspects of the Hodgkin-Huxley model

Hodgkin and Huxley suggested that the electrical behaviour of the membrane may be represented by the network shown in Figure 1.10. The network relates the membrane current density, J_{m}, to the membrane potential, V. The membrane can be viewed as a capacitor, since it separates charge. In the diagram in Figure 1.10, Js represent the current densities ($\mathrm{A/cm^2}$), the Es are the potentials (V), C_{m} is the specific capacitance of the membrane ($\mathrm{F/cm^2}$), and the gs are the specific ionic conductances ($\mathrm{S/cm^2}$). In the equivalent circuit, current flow across the membrane has two major components, one associated with charging the membrane capacitance and one associated with the movement of specific types of ions across the membrane, as follows:

$$J_{\mathrm{m}} = J_{\mathrm{C}} + J_{\mathrm{ion}}. \tag{1.5}$$

The ionic current density is further subdivided into three components, a sodium current (J_{Na}), a potassium current (J_{K}), and a small leakage current (J_{L}) repre-

senting the sum of membrane currents other than those flowing through the sodium and potassium branches. Hence,

$$J_{\mathrm{m}} = J_{\mathrm{C}} + J_{\mathrm{K}} + J_{\mathrm{Na}} + J_{\mathrm{L}}. \tag{1.6}$$

Ohm's law for each of the conductance and the constitutive law for the membrane capacitance were used. To express the various ionic currents, it is customary to make the ohmic assumption, which overlooks the fact that the conductances are non-linear [30]. Equation (1.6) yields

$$\begin{aligned} J_{\mathrm{m}} &= C_{\mathrm{m}}\frac{dV}{dt} + g_{\mathrm{K}}(V,t)\ (V - E_{\mathrm{K}}) \\ &\quad + g_{\mathrm{Na}}(V,t)\ (V - E_{\mathrm{Na}}) + g_L(V,t)\ (V - E_{\mathrm{L}})\ , \end{aligned} \tag{1.7}$$

where E_{K} and E_{Na} are the Nernst equilibrium potential as in equation (1.1).

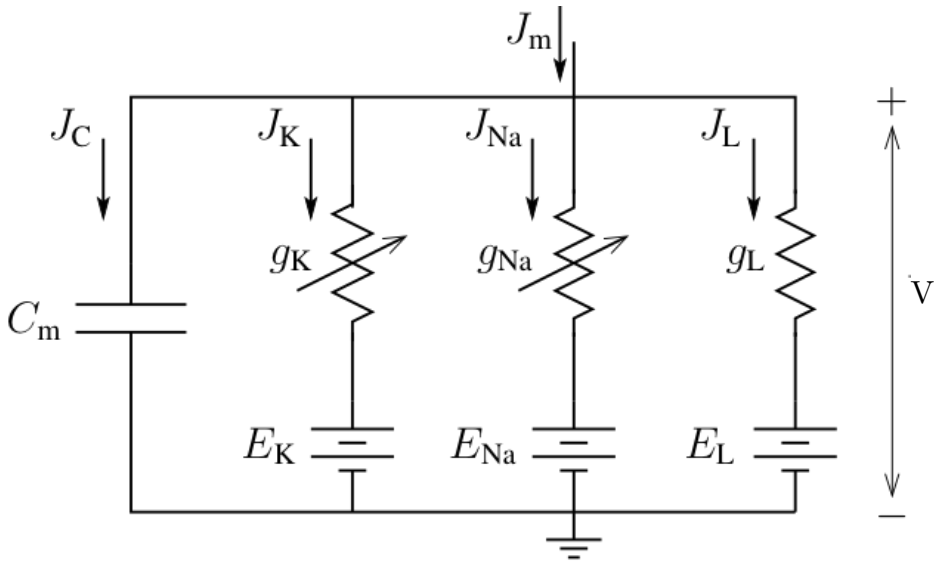

Figure 1.10: Electrical equivalent circuit proposed by Hodgkin-Huxley for a patch of the membrane of the squid giant axon [5].

In order to explain their experimental data, Hodgkin and Huxley postulated that g_{K} and g_{Na} changed dynamically as a function of membrane voltage. The potassium and sodium conductances can be obtained from the ionic currents measured under voltage clamp,

$$g_{\mathrm{K}}(V,t) = \frac{J_{\mathrm{K}}(V,t)}{(V - E_{\mathrm{K}})} \tag{1.8}$$

and

$$g_{\mathrm{Na}}(V,t) = \frac{J_{\mathrm{Na}}(V,t)}{(V - E_{\mathrm{Na}})} \, . \tag{1.9}$$

For several values of V, the ionic conductances can be calculated as a function of time from measurements of the sodium and potassium currents. In response to step of depolarisation, the sodium conductance rises rapidly along a sigmoid curve to a maximum, then decays exponentially to zero with a slower time course, whereas the potassium conductance rises along a sigmoid curve to a persistent steady state value. Both the time course and amplitude of the potassium and sodium conductances are functions of the membrane potential. The ionic conductances were fitted with powers of variables satisfying first-order relaxation dynamics, as follows:

$$g_{\mathrm{K}}(V,t) = G_{\mathrm{K}} \; n(V,t)^4, \tag{1.10}$$

and

$$g_{\mathrm{Na}}(V,t) = G_{\mathrm{Na}} \; m(V,t)^3 \; h(V,t), \tag{1.11}$$

where G_{K} and G_{Na} are the unitary conductances (also called the single-channel conductance, which is the conductance of one channel and is a constant value), n, m, and h are solutions of first-order ordinary differential equations whose coefficients are functions of the membrane potential, V (Figure 1.11). Let x be a generalised notation for activation/inactivation factor that represents any of the variables n, m, or h and satisfies a first-order kinetic equation. The latter can be written in two forms. The first is expressed in terms of rate constants,

$$\frac{dx}{dt} = \alpha_x(1 - x) - \beta_x x. \tag{1.12}$$

The second form is in terms of a time constant and the steady state value,

$$\frac{dx}{dt} = \frac{x_\infty - x}{\tau_x}, \tag{1.13}$$

where α_x, β_x, τ_x, x_∞, are all functions of the membrane potential and depend on time t through their dependence on $V(t)$. The relations between the steady state of x, x_∞, and its time constant, τ_x, and the rate constants, α_x and β_x, are $x_\infty = \alpha_x/(\alpha_x + \beta_x)$ and $\tau_x = 1/(\alpha_x + \beta_x)$. Hodgkin and Huxley measured the voltage dependence of all the rate constants and fitted the rate constants with mathematical expressions. An in-depth treatment of the model and full list of equations and expressions can be found in Keener and Sneyd [30] or Weiss [5].

Membrane channels were yet to be characterised at the molecular level when

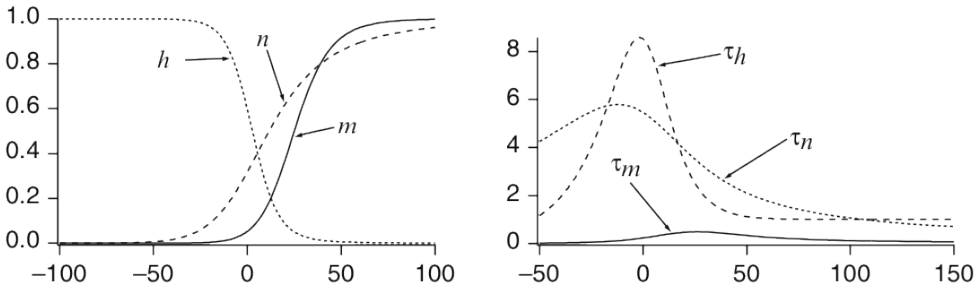

Figure 1.11: Various functions in the Hodgkin-Huxley equations as a function of membrane potential [6].

Hodgkin and Huxley developed the theory. These channels are now known to be membrane-spanning proteins with a pore running through the centre that forms the conduit for the ions [31]. The biophysical properties of these electrogenic proteins, such as voltage-dependence and ion selectivity, can be related to the behaviour of the peptide chains at the atomistic level.

In accordance with this modern molecular perspective, the gating variables can be interpreted probabilistically. The macroscopic conductances g_{K} of the Hodgkin-Huxley model can be considered as the combined effects of a large number of microscopic ion channels embedded in the membrane. Each individual ion channel contains a series of small number of physical gates that controls the flow of ions though the channel. An individual gate can be in one of two states, permissive or non-permissive. The channel is open when all the gates for that particular channel are in the permissive state and ions can pass through the channel. On the other hand, the channel is closed if any of the gates are in the non-permissive state and ions cannot flow.

The membrane voltage has two effects on the current carried by an ion i. The first effect arises from the membrane potential acting as a driving force on different ions. That is, a change in potential causes a change in the ionic current directly by changing the electrochemical potential difference $(V - E_i)$, which drives the ions across the membrane. The second effect is from the voltage-dependence of the gating of the channels. That is, variations in potential change the ionic conductance of the membrane, $g_i(V, t)$, which affects the ionic current.

1.3.3 Continuous time, discrete state Markov chain model

A commonly used class of models to describe single-channel gating kinetics is based on continuous-time, discrete-state Markov chains. This approach presupposes that the conducting channel can exist in a number of distinct conformational states; these

are represented as the states of a Markov chain. The conformational configurations differ with respect to the conductivity of the channel, i.e., the ease with which ions can pass through the central pore. The discrete states correspond to the local energy minima of the system, separated by energy barriers, that need to be crossed in order to transition between the various states. Thermal fluctuations cause the channel to transition between these conducting and non-conducting states. Accordingly, the heights of these barriers determine the probabilistic rates of passage from one minimum to another. These rates are represented by the transition rates of the Markov chain. Factors such as transmembrane voltage, covalent modifications, and ligand binding all affect the "energy landscape" of the ion channel and hence the depths of the minima and the heights of the barriers between them. In general, the Markov chain can have any number of states and complex topological arrangements to account for voltage- or ligand-gated activation, deactivation, inactivation and de-inactivation.

A simple Markov chain model with only two states is shown in Figure 1.12. The states correspond to the 'closed' (non-conducting) and 'open' (conducting) conformations of the ion channel. The forward and backward transitions between the two states are denoted by k_{co} and k_{oc}. The ion channel remains in one of the states for an amount of time after which it moves to the other state. In chains with more than two states, the state that is visited next is probabilistic as well and is governed by relationships between the transition rates.

A common expression of the transition rates is shown in equation (1.14); this formula is used when the transition rates are voltage-dependent:

$$k_{ij} = k_{ij}^{0} \exp\left[-\frac{\Delta E_{ij}}{k_B T}\right] = k_{ij}^{0} \exp\left[-\frac{z_{ij} V_{\mathrm{m}} F}{RT}\right] , \tag{1.14}$$

where k_{ij} is the transition rate between states i and j, k_{ij}^{0} is a rate related to the frequency factor, ΔE_{ij} is the energy barrier between the two states, z_{ij} denotes the amount of charge moving in the corresponding transitions, and the remaining constants are listed in Table 4.33.

The dynamics of the state probabilities is described by a system of ordinary differential equations (ODEs) based on these transition rates. When the channel is in the conducting state, and based on the ohmic assumption, the current flowing is given by the following formula:

$$I_{\mathrm{ion}} = \kappa_{\mathrm{ion}}\ G_{\mathrm{ion}} P_{\mathrm{open}} (V - E_i) ,$$

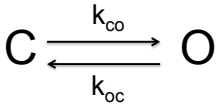

Figure 1.12: Two-states continuous-state time-discrete state Markov model.

where κ_{ion} is the channel density, G_{ion} is the unitary conductance and P_{open} is the channel-open probability which is furnished by the ODEs.

The transition rates are determined from experimental data; in particular, the rates are related to statistics that can be gleaned from the empirical distribution of persistence times of the various conducting states. In some cases it may prove to be challenging to obtain estimates from the available data when the Markov chain model allows for a large number of states, and the transition rates may not be fully determined by the data. In such cases it may be necessary to make simplifying assumptions, such as equality of the rates at which one or more transitions take place, to arrive at an identifiable model. Basic definitions, properties, and theorems of continuous-time Markov Chains are presented in Stewart [66].

1.4 Dynamics of intracellular calcium

Intracellular calcium governs the driving potential that determines the depolarisation phase of the MSMC AP [36,40,67]; numerous conductances are gated by intracellular calcium, and calcium is essential in excitation-contraction coupling [68,69]. At rest, cytosolic calcium is kept at around 100 nM, while extracellular calcium is about 1 mM, which creates a steep concentration gradient from outside the cell to inside the cell [30]. Due to this concentration gradient, intracellular calcium can be raised quickly by opening plasma membrane calcium channels [36]. On the other hand, energy must be expended to keep the cytosolic calcium sufficiently low (in fact, prolonged elevation of intracellular calcium is toxic [70, 71]). Finally, tightly controlled mechanisms are required to control the influx and the removal of calcium. Cytosolic calcium increases via several pathways, which are depicted schematically in Figure 1.13 and include: calcium channels in the plasma membrane (voltage-gated calcium channels, as well as receptor-, second-messenger, and mechanically-operated channels); calcium release from internal stores such as the endoplasmic reticulum (ER), and mitochondria. This release is mediated by calcium channels or receptors: the ryanodine receptor (RyR), also called the calcium-induced calcium-release channel (CICR), and the inositol (1,4,5)-triphosphate (IP_3) receptor which responds to IP_3 concentrations and release calcium from internal stores [30]. Calcium is removed

from the cell mainly through calcium ATPase pumps (PMCA: this is a plasma membrane calcium pump, which used the energy in the form of ATP to displace calcium against its concentration gradient) and via sodium-calcium exchange (NCX) which exploits the energy stored in the Na^+ gradient to remove calcium out of the cell at the expense of Na^+ entry [30]. Moreover, calcium can be sequestered in internal stores (ER, mitochondria) through ATPase pumps such as SERCA, a calcium pump located in the membrane of the ER whose function is to accumulate calcium in the internal stores using energy of ATP. Finally, cytosolic calcium is buffered by large cytosolic proteins. In fact, approximately 99% of total intracellular calcium is bound to buffers. An in-depth treatment is provided by Keener and Sneyd [30].

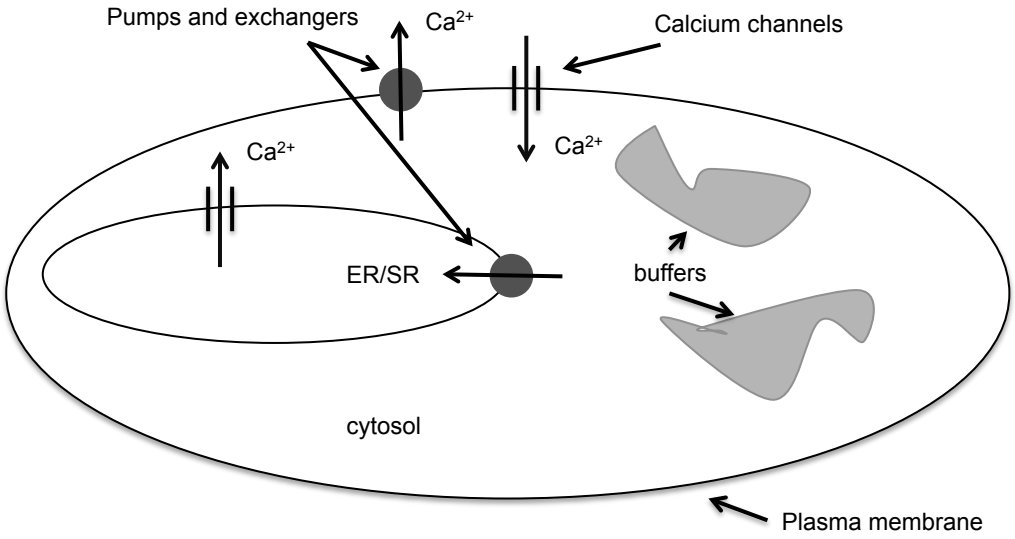

Figure 1.13: General scheme of the main processes involved in changes in cytosolic calcium.

Mathematical models in the literature can be based on a description of the influxes and effluxes of calcium through the plasma membrane and internal stores. Depending on the level of biological detail, the resulting model can range from simple two-variables models to complex models with thousands of variables [30]. A simplification that is often made is that the concentration of calcium is the same throughout the cell. This eliminates spatial-dependent variables and leaves only dependence on time. There are, however, important spatial patterns that are not accounted for in such models, such as calcium waves spreading through the MSMC (detailed discussion in Chapter 6).

1.4.1 The two-pool model

The two-pool model, proposed by Goldbeter et al [72], distinguishes two separate pools: one being IP_3-sensitive and the other being Ca^{2+}-sensitive. Agonists stimulation results in a rise of IP_3. The rise allows the release of a certain amount of Ca^{2+} from an IP_3-sensitive store. The release of Ca^{2+} then triggers further release of Ca^{2+} from a second store, sensitive to Ca^{2+} and insensitive to IP_3, through other receptors (CICR; calcium-induced, calcium release). The state variables are the calcium concentrations in the cytosol and in the Ca^{2+}-sensitive pool. In the model, a steady Ca^{2+} flux into the cytosol is caused by IP_3; this flux is constant for constant intracellular IP_3 concentration and is treated as a control parameter. Thus, by varying this flux, the behaviour of the model can be studied at different constant IP_3 concentrations [30]. The concentration of Ca^{2+} in the IP_3-sensitive store is assumed to be constant as the store refills quickly from the extracellular medium. A diagram of the model is shown in Figure 1.14. The model describes IP_3-induced oscillations, but experimental evidence indicates that the role of Ca^{2+} is more complicated than is assumed in this model. Moreover, the model does not encompass all of the signalling pathways. Other models extend the two-pool to describe additional pathways in Ca^{2+} signalling by adding a third pool to model the role of mitochondria.

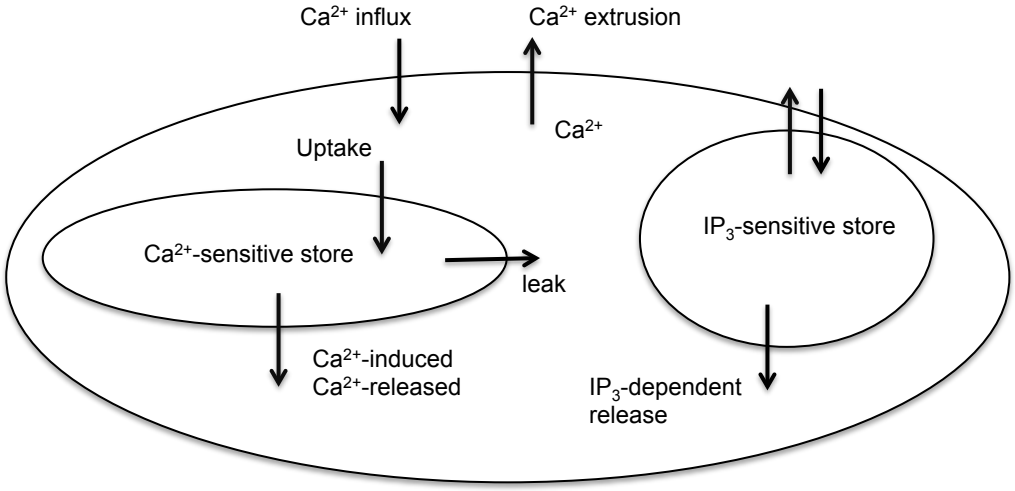

Figure 1.14: Schematic diagram of the two-pool model.

1.4.2 The De Young Keizer model

Higher-dimensional models were subsequently developed. The De Young Keizer approach [73] incorporates a detailed model of the IP_3 receptors. De Young et

al [73] assumed that the IP_3 receptor is composed of three independent and identical subunits [73]. Each subunit has three binding sites: an IP_3-activation binding site; a Ca^{2+}-activation binding site; and a Ca^{2+}-inactivation binding site. Each of these binding sites can be either occupied or unoccupied. Hence, the subunits have eight different states. Ca^{2+} flux is induced by the IP_3 receptor only if IP_3 and Ca^{2+} are both bound. Even though this model is based on more realistic assumptions, it does not agree as well with experimental data as does the two-pool model [30].

1.4.3 The Atri model

Atri et al [74] suggested another approach to modelling calcium release, based on the assumption that Ca^{2+} inactivates the IP_3 receptors in a cooperative manner. Their model assumes that the IP_3 receptor consists of three binding domains: domain 1 for IP_3 activation; domain 2 for Ca^{2+} activation; and domain 3 for Ca^{2+} inactivation. Accordingly, for the receptor to conduct Ca^{2+} current, IP_3 needs to be bound to domain 1, Ca^{2+} bound to domain 2, and Ca^{2+} not bound to domain 3. Consequently, Ca^{2+} activates the IP_3 receptor if bound to domain 2 and inactivates it if bound to domain 3. The model assumes that the Ca^{2+} concentration in the ER is high and so well buffered, that depletion of the ER has a negligible effect on intracellular Ca^{2+} dynamics [30].

1.4.4 The calcium-induced calcium-release model

Another way to model the calcium release from intracellular stores is through the RyR, which are similar to the IP_3 receptors in that Ca^{2+} can activate and inactivate them, which trigger CICR from the SR/ER. Friel et al [75] developed a simple CICR model that provides a description of the behaviour of the Ca^{2+} dynamics. A diagram of the model is shown in Figure 1.15. CICR is of particular importance in cardiac cells [30], where membrane depolarisation causes a small influx of Ca^{2+} through a plasma membrane voltage-dependent calcium channel, which, in turn, triggers the release of Ca^{2+} through the RyR on the membrane of the intracellular store. Subsequently, higher-dimensional models of CICR [17, 76] and considerably more complex ones [77] have been constructed. In the CICR models, it is not yet clear how Ca^{2+} inactivates the RyR and whether this inactivation plays a significant role [30].

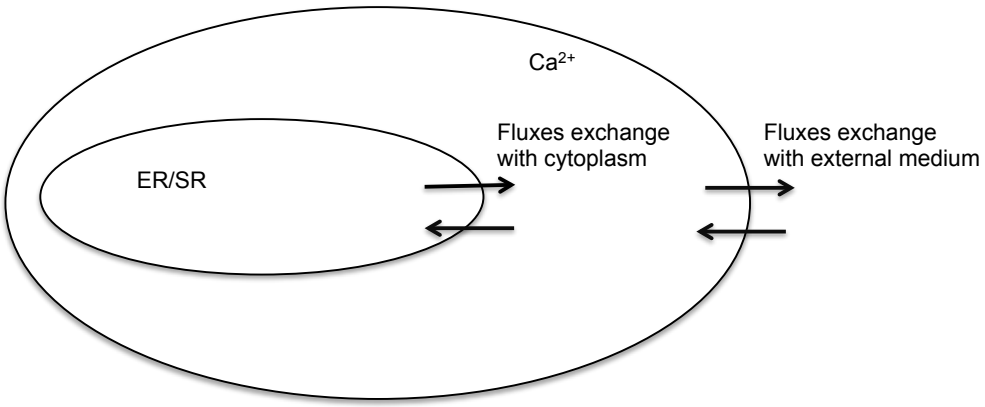

Figure 1.15: Schematic diagram of the CICR model.

1.4.5 A minimal model for the myometriocyte

In cardiac myocytes, calcium enters via voltage-gated calcium channels in the plasma membrane. This calcium entry activates SR calcium release via the RyR. Furthermore, calcium is released via IP_3-dependent calcium release. On the other hand, in the myometrium cells of all species, the increase in cytosolic calcium triggered by the action potential arises mostly from the opening of L-type and T-type voltage-gated calcium channels in the plasma membrane. Although this rise can be augmented by release from the internal stores, calcium entry from the extracellular space is the major source of calcium-triggered contractions [29]. We developed a minimal model for MSMC calcium dynamics. The model only considers the increase of $[Ca^{2+}]_i$ due to the plasma membrane calcium channels, while ignoring the Ca^{2+} release from the stores. Details of the minimal model will be shown in Chapter 4.

1.5 Existing models of myometriocyte activity

Uterine electrical activity has been previously investigated in order to predict the risk of preterm labour and subsequent preterm birth [41, 78, 79]. Modelling the uterine electrical activity generated at a cellular level is an important tool for understanding the propagation mechanisms of this electrical activity, which in turn is crucial for understanding the excitability at the organ or tissue level. Previous models of the myometrium have been developed at the tissue and the organ level [80–82].

1.5.1 The Bursztyn model

Bursztyn et al [41] presented an excitation-contraction model of the uterine muscle cells. The model comprises voltage-gated calcium channels, calcium pumps, and Na^+/Ca^{2+} exchangers. This mathematical model represents the cellular mechanisms of calcium control. However, the Bursztyn model neglects the inactivation process of calcium current, the time dependency of kinetic dynamics, and other ionic currents involving potassium, sodium, and chloride. The model accounted for the processes of MLC phosphorylation and stress production using the cross-bridge model of Hai and Murphy [83].

1.5.2 The Rihana model

Rihana et al [78] presented a model for the ionic channels found in the uterine cells based on voltage clamp experiments from the literature. This model was based on the Hodgkin and Huxley formulation and included macroscopic currents from various ionic channels: a sodium channel, a calcium channel, a voltage-gated potassium channel, a calcium-gated potassium channel, and a background leak channel (mainly chloride ions). The Rihana model has a 10-dimensional state space and can reproduce a single AP or a train of peaks of AP with a RMP of -35 to -40 mV and a duration of about 133-200 ms. In the mouse, RMP is about -55 mV in the first half of gestation to -46 mV at term [84], while in human myometrium the RMP is between -45 and -50 mV [39, 85]. Values of some parameters were extracted from myocytes in different species (rat, human) and from various experimental conditions. A stimulating current was used to trigger the AP of a single cell, even though myometrial cells are known to be myogenic, i.e., are able to contract spontaneously without any stimulus.

1.5.3 The Tong model

Tong et al [79] formulated a mathematical model of rat MSMC electrical activity. The model predicts the changes of ionic concentrations in the intracellular and extracellular media during contraction, in order to reconstruct the transmembrane potential of a myocyte as a function of time. It was claimed that all known individual ionic currents of MSMC close to labour were incorporated in the model and combined into a mathematical model of myometrial AP generation. In addition, the model contains membrane stabilising currents, which hold the potential near the resting potential. Those currents tend to counteract the pacemaker currents that initiate electrical activity. Finally, intracellular calcium transients and their relationship

with the AP have to be accounted for. Although the model contains many channels and is shown to successfully mimic several recordings of spontaneous AP and force in MSMC, several limitations must be considered.

Despite the inclusion of fourteen ionic currents, the number of functional channels that exists in the MSMC is underestimated. Some channels that have been proven to be regulators of myometrial contractility during gestation and labour were left out of the Tong model. According to Bond et al [86], Modzelewska et al [87,88], and Brown et al [89], small conductance Ca^{2+}-sensitive potassium channels (SK3) are critical regulators of myometrial contractility. Myometrial expression of SK3 depresses phasic uterine contraction. There are indications that SK3 channels could be therapeutic targets for regulating uterine contractions during labour [86]. Moreover, a genome-wide screen of MSMC mRNA expression revealed a novel channel (Kir7.1, KCNJ13) that displays biophysical properties that could be responsible for mediating uterine quiescence during pregnancy [90]. Computer simulations [90] predict a two-fold function: maintaining the membrane potential below threshold and mediating AP spiking frequency and hence force during a contraction. Accordingly, the underlying model is inadequate, primarily because the model was constructed before data on inward rectifying potassium channels were available.

The calcium Nernst potential of a cell can be calculated from the following Nernst equation as in equation (1.1):

$$E_{\mathrm{Ca}} = \frac{RT}{2F} \ln \frac{[\mathrm{Ca}^{2+}]_o}{[\mathrm{Ca}^{2+}]_i} \,, \tag{1.15}$$

where R is the universal gas constant, F is the Faraday constant, T is the absolute temperature and $[\mathrm{Ca}^{2+}]_o$ and $[\mathrm{Ca}^{2+}]_i$ are the extracellular and intracellular calcium concentrations for that particular cell. In the Tong model, two *distinct* values of the calcium reversal potential were assumed for the T-type and L-type voltage-dependent calcium channels, respectively. For L-type, $\mathrm{E_{CaL}}$ is fixed at 45 mV, while for the T-type $\mathrm{E_{CaT}} = 42$ mV, which would require the two types of channels to be exposed to different calcium concentrations. Calcium spacial heterogeneity in MSMC could account for this difference in concentrations, but the authors gave no indication that this is what they were trying to convey.

During the model validation, another problem emerged. The model produced a RMP that is too depolarised (-19 mV) and a basal $[\mathrm{Ca}^{2+}]_i$ that was too high (610 nM). The RMP of uterine myocytes is between -35 and -80 mV [91,92], while the initial $[\mathrm{Ca}^{2+}]_i$ =0.15 μM [91]. The major factors in establishing the RMP are the various K^+ channels with different kinetic properties. Those channels conduct a K^+

outward current at rest pulling the RMP towards the potassium reversal potential. Such a depolarised RMP (in the Tong model) could be due to the absence of some of those channels that are open at rest. To counter these problems, it was decided to remove the sodium channel because it renders the model more excitable. After the elimination of the sodium channel, the RMP was -54 mV and the resting $[Ca^{2+}]_i$ dropped to 116 μM.

Tong et al [79] used voltage-clamp and current-clamp experimental data to test the effect of using estradiol, which has been reported to reduce the peak of L-type current and reduce the whole cell potassium current and hence change the MSMC AP configuration from bursting type AP to plateau type AP [93, 94]. The model could not reproduce these changes in the AP. The authors adjusted a number of parameter values, left shifted the half inactivation voltage of the L-type current from -38 to -45 mV, altered the inactivation slope factor to 10 mV, and reduced the total potassium conductance by 40%. The evidence that would justify these alterations appear to be absent from the work on hand.

Much of our understanding of uterine contraction originates from studies of rat myometrium, inasmuch as animal myometrium can be easily acquired at different gestations from pregnant animals, and changes in uterine activity directly measured *in vivo*, so that the transition from quiescence to pre-labour and labour stages can be resolved [95]. On the other hand, it is much harder to acquire human myometrial tissue, in particular the 'non-labour' tissue; with tissue samples originating from women undergoing Caesarean section at term, it is not possible to know whether the uterus smooth muscle is already undergoing molecular changes in preparation for labour. In interpreting results from studies on animal material, we should not lose sight of the differences between animal and human myometrium. While the basic biophysics of ion channels expressed in the myometria of different species may be similar, there is a substantial species-dependent variation in the repertoire of ion channels expressed [96]. The data obtained from animal models are not always applicable to humans. More research is necessary on samples of human myometrium obtained during surgical procedures may provide invaluable evidence in future studies. Moreover, modelling the human MSMC *in silico* is one way to approach this biological problem.

Chapter 2

Experimental methods

This chapter explains all the experiments conducted to support this work. The experiments have been performed by Dr McCloskey.

2.1 Ethical approval

All procedures were conducted within the guidelines of *The Declaration of Helsinki* and were subject to local ethical approval (REC-05/Q2802/107). Prior to surgery, informed written consent for sample collection was obtained.

2.2 Subject criteria and selection

Subjects were recruited into a group defined as >37 and <40 completed weeks gestation not in labour.

2.3 Sample collection

At caesarean section, samples were collected before syntocin administration by knife biopsy from the lower uterine segment incision. Samples for cell isolation were placed in ice cold modified Krebs-Henseleit solution (see below) and utilised the same day.

2.4 Ca^{2+} imaging and current clamp

Smooth muscle cells were impaled with glass microelectrodes filled with 2M KCl of resistance 80–120 MΩ. Transmembrane potentials were recorded at an acquisition

rate of 1 KHz with an amplifier (Axopatch 700b; Axon Instruments) and a Digidata 1440a computer interface running pCLAMP 9.0 software (Molecular Devices, Sunnyvale, CA, USA).

Single myometrial smooth muscle cells were plated onto glass-bottomed, collagen-coated dishes (Matek, Massachusetts, USA) and left to adhere for 10 min on an Olympus IX51 microscope stage. Cells were incubated in the dark for 60 min at room temperature with the Ca^{2+}-sensitive fluorescent dye Fluo4-AM (5 μM, Invitrogen, Paisley, UK), Pluronic F127 (0.025%, w/v) was included to aid dye loading. Cells were washed then maintained at 37°C in m-KHS, an X-cite 120 UV lamp (EXFO, Eastleigh, UK) was used to excite the Fluo-4 and emitted light at 520 nM was captured with a Luca^{EM} EMCCD camera controlled by the IQ software package (Andor Technology, Belfast, UK). Images were acquired at 30 frames s^{-1}.

The mean camera background was subtracted; images were normalised to obtain f/f_0 by dividing the entire image by the mean intensity of the cell during a quiescent period (i.e. the minimum fluorescence obtained between periods of excitation). The value is then multiplied by 10^3. Figure 2.1 shows the single recording used of the simultaneous membrane potential and calcium times series.

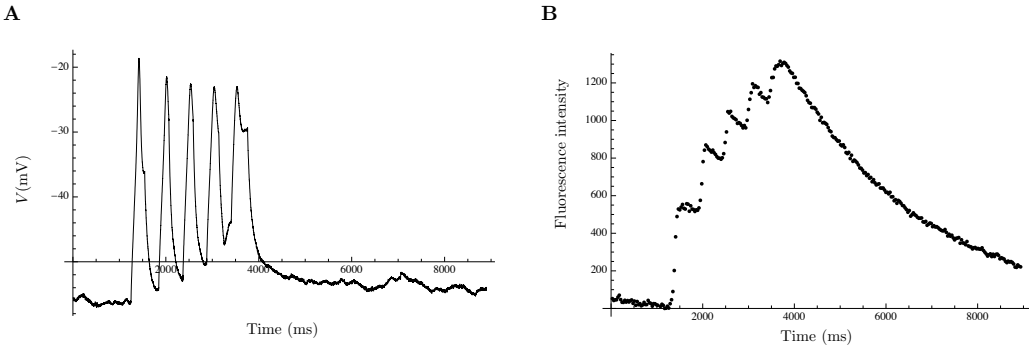

Figure 2.1: Simultaneous voltage and calcium time series.
(A) Observed membrane potential time series acquired using current clamp. (B) Calcium fluorescence signal acquired using calcium imaging using Fluo-4.

2.5 Solutions

Fresh samples were stored in ice cold modified Krebs-Henseleit (m-KHS) solution containing ($mmoll^{-1}$): NaCl, 133; KCl, 4.7; Tes, 10; glucose, 11.1; $MgSO_4$, 1.2; KH_2 PO_4 , 1.2; $CaCl_2$, 2.5; adjusted to pH 7.4 at 25°C with 5 m NaOH. Hanks Balanced Salt Solution (HBSS) containing no calcium or magnesium was purchased

from Invitrogen (Paisley, UK). The electrode (internal) solution for voltage clamp studies contained (mmoll-1): KCL 140; EGTA 1.1; $CaCl_2$ 0.06; Hepes 10; $MgCl_2$ 2; adjusted to pH 7.2 at 25C with 5 m NaOH. 5-BDBD, XE-991 and Paxilline stocks were prepared in DMSO (Tocris Bioscience, Bristol, UK). Apamin stock solution was in water (Tocris Bioscience, Bristol, UK). Stromatoxin (ScTx) stock was prepared in HBSS (alomone Labs, Jerusalem, Israel). Margatoxin stock of 10 μmol^{-1} was prepared in water (Sigma Aldrich, Poole, UK).

2.6 Murine Myometrial Electrophysiology

2.6.1 Cell isolation

Pregnant mice (B6 CB F1) gestation day 15 (D15) and 18 (D18), were humanely killed by CO_2 asphyxiation, the uterine horn was dissected to remove the pups and the myometrium stored in ice cold m-KHS. Strips of myometrium from the longitudinal layer (2×2×20 mm) of time-mated C57BL/6J mice were isolated and washed in Ca^{2+} and Mg^{2+} free Hank's balanced salt solution (HBSS) at 37°C for 10, 20 and 30 minutes respectively, followed by 45 min incubations in digestion solution containing Liberase TM, (Roche, Welwyn Garden City, UK) dissolved in HBSS to a final concentration of 0.13 WU/ml at 37°C. Digestion was terminated by several dilutions with fresh HBSS. Cells were dispersed by slow trituration through a wide bore fire polished glass pipette in HBSS Solution. Singe myometrial cells were filtered through a 200 μM gauze and stored in HBSS for use within 6 hours.

2.6.2 Voltage Clamp

A drop of myometrial cell suspension was placed in a glass-bottomed petri dish and mounted on the stage of an inverted microscope (IX51, Olympus). After settling (approx. 10 min) cells were perfused with bath solution at a rate of 1–2 ml min^{-1} at 37°C. Patch pipettes were fabricated (Model P-87; Sutter Instruments, Novato, CA, USA) from 1.5 mm glass capillaries with a resistance of 2.0–4.0 MΩ when filled with pipette solution. Liquid junction potential was zeroed prior to seal formation. Transmembrane currents were recorded with an amplifier (Axopatch 700b; Axon Instruments) using the perforated patch configuration of the whole cell patch-clamp technique(38). The cell membrane was perforated using the antibiotic amphotericin B (720 μg/ml). Series resistance was compensated after membrane perforation. Currents were elicited by stepping to a range of potentials between −150 and +80 mV from a holding potential of −60 mV. To isolate currents that were sensitive to inhibi-

tion by drug application, difference currents were obtained by electronic subtraction of traces. Currents were filtered at 10 kHz and sampled at 5 kHz. Voltage protocols were delivered via a Digidata 1440a computer interface using pCLAMP 9.0 software (Molecular Devices, Sunnyvale, CA, USA).

2.6.3 Current Clamp

Strips (5×10 mm) of murine myometrium from the longitudinal layer were pinned out on a sylguard base and perfused with m-KHS solution at 37°C on an upright microscope (MVX10, Olympus). Tissue was incubated with 5 μM wortmannin (Sigma) to prevent spontaneous contractions from dislodging impalements. Smooth muscle cells were impaled with glass microelectrodes filled with 2M KCl of resistance 80–120 MΩ. Transmembrane potentials were recorded with an amplifier (Axopatch 700b; Axon Instruments) and a Digidata 1440a computer interface running pCLAMP 9.0 software (Molecular Devices, Sunnyvale, CA, USA).

2.6.4 Murine Myometrial Isometric Tension Recordings

Four strips of myometrium measuring approximately 2×2×10 mm were cut from D15 and D18 mice. Each strip was mounted horizontally on a muscle strip myograph system (800MS, Danish MyoTechnology, Denmark) placed under 2mN tension. Strips were bathed in 4 ml of m-KHS at 37° which was replaced every 30 minutes. After an initial equilibration period, isometric force was recorded using LABCHART software (ADI Instruments, Oxford, UK).

2.7 Human Myometrial Isometric Tension Recordings

Subjects were recruited at time of elective caesarean section at between 38 and 40 weeks gestation. Myometrium muscle strips approximately 10×2×2 mm were mounted vertically in 10ml organ bath chamber perfused in m-KHS at 37°C. Force was measured with FT03C transducers (Grass Instrument Co, Quincy, Mas) and recorded digitally with MacLab Chart software (ADInstruments Ltd, Oxfordshire, UK). Strips were held under 20 mN tension and allowed to equilibrate for 90–120 min, wherein spontaneous contractions were observed. Strips that failed to contract spontaneously were excluded. 5-BDBD and A438079 were added directly to the organ bath chamber.

Chapter 3

Mathematical methods

3.1 Estimation of the biophysical parameters for the conductances in the MSMC

3.1.1 Least squares estimation

Least-squares estimation is a parameter estimation method based on the observed deviations between a given set of data points and a theoretical curve (surface, etc) corresponding to a choice of parameter values. The deviations are called the residuals. The least-squares estimator (LSE) of the parameter vector is the one that globally minimises the sum of squares of the residuals. The resulting curve (surface, etc.) is then referred to as the "the best fit" (by the LS criterion strictly speaking since other criteria are often plausible too). The procedure presupposes a theoretical model that describes the relationship between an independent variable X and a dependent variable Y. The equation relating the two variables can be written as follows:

$$Y_i = f(X_i; \boldsymbol{v}) + \Sigma_i \ , \tag{3.1}$$

where Y_i denotes the value of the dependent variable for the i^{th} observation, X_i is the value of the independent variable, $\boldsymbol{v}$ is the parameter vector containing the model's parameters $v_1, v_2 \ \cdots \ v_i$, $f(X_i; \boldsymbol{v})$ is the function provided by the theoretical model, relating the dependent and independent variables through the unknown parameters, that is, for the model describing the variable Y as a function of the variable X and the parameters, and Σ_i is the error term (the residual). The error term is presumed to account for all the factors that lead to the difference between the i^{th} observed value and the value predicted by the function $f(X_i; \boldsymbol{v})$. The LSE of the parameters is such that the sum of squared deviation between the predicted value and the

measured data, also called the sum of squared errors, S is minimised:

$$S = \sum_{i=1}^{n} (Y_i - f(X_i; \boldsymbol{v}))^2 \, . \tag{3.2}$$

To find the minimum value of the function S, we put the derivatives of the function with respect to the parameters in $\boldsymbol{v}$, $\partial S/\partial v_1, \partial S/\partial v_2, \partial S/\partial v_3 \; \cdots \; = 0$ and solve for the parameters in $\boldsymbol{v}$.

3.1.2 LSE as maximum likelihood estimator

The method of minimising the sum of squared errors can be derived from the maximum likelihood principle on the assumption that the error term is normally distributed around the predicted value of the model, independent, unbiased, i.e. with mean zero, and with the same standard deviation σ for all points. This can be proved as follows. Given the data points, suppose that each data point Y_i has a measured error that is independent, unbiased, and that the standard deviation σ is the same for all the points. Then the likelihood of the parameter values is expressed as the joint probability of the data set. This probability is the product of the probabilities of each point, as follows:

$$p = \prod_{i=1}^{n} (\sigma\sqrt{2\pi})^{-1} \exp\left\{ -\frac{1}{2} \left[\frac{(Y_i - f(X_i; \boldsymbol{v}))}{\sigma} \right]^2 \right\} \, . \tag{3.3}$$

Maximising p is equivalent to maximising its logarithm or minimising the negative of its logarithm. Taking the logarithm of p we find the log-likelihood function:

$$L = n \log \frac{1}{\sigma\sqrt{2\pi}} + \sum_{i=1}^{n} \left(-\frac{1}{2} \left[\frac{(Y_i - f(X_i; \boldsymbol{v}))}{\sigma} \right]^2 \right) \, . \tag{3.4}$$

Omitting prefactors that are not parameter-dependent we obtain:

$$L = -\sum_{i=1}^{n} (Y_i - f(X_i; \boldsymbol{v}))^2 \, . \tag{3.5}$$

Maximising the likelihood in equation (3.5) is therefore equivalent to minimising the sum of squares in equation (3.2), if the measured errors are independent and normally distributed with constant standard deviation. The deleted prefactors cancel when the partial derivatives are set to zero, which is why they can be omitted with impunity. When the assumptions are not valid, e.g. the variance increases with the

mean, or a different error distribution applies, e.g. Poisson, a maximum likelihood estimate can still be obtained but it will not be identical to the LSE.

3.1.3 Example of using the LSF in estimating the time constant of the Type I gap junction

Data acquisition

Data are extracted from the curves using *GraphClick*, a graph digitiser software which allows to retrieve the (x, y)-data from the graph. Figure 3.1 shows a screenshot of the graphical user interface for *GraphClick* software. The plot is from the paper by Miyoshi et al [7], showing gap junction currents recorded from day 22 paired cells from circular muscle using 5 s step pulses between ±90 mV in 20 mV increments and a holding potentials of 0 mV. Data points were chosen on the graph and (x, y)-data can be retrieved and exported to a `txt` file.

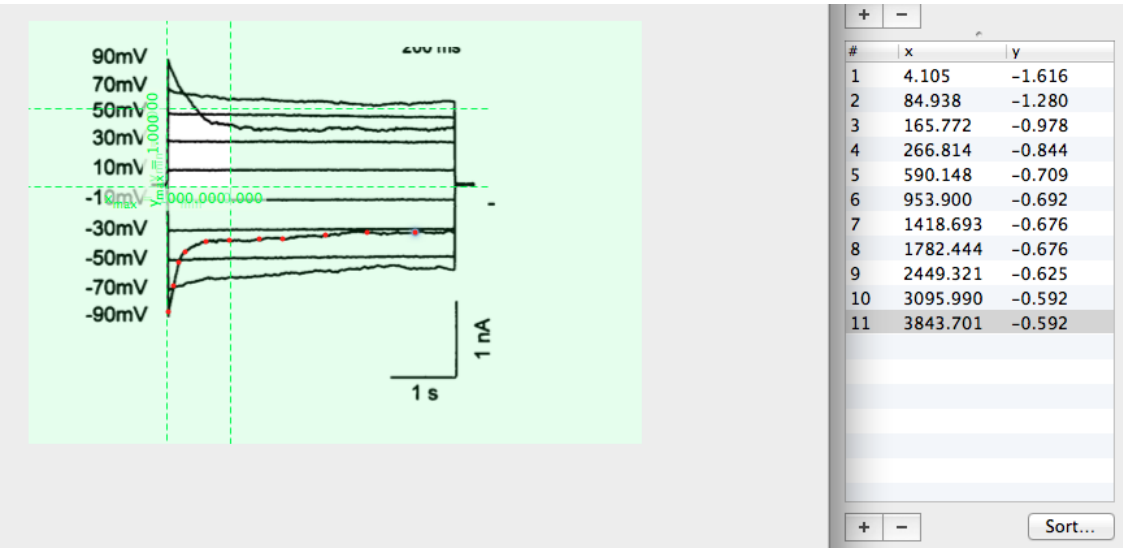

Figure 3.1: Data acquisition. A screenshot displaying the graphical user interface for *GraphClick* (version 3) software used on the current trace data of the gap junction Type I family from Miyoshi et al [7]. The gap junction currents were in response to 5 s step pulses in the voltage range of ±90 mV. The points (in red), extracted from the current that resulted from step pulse to −90mV, were selected and their individual (x, y) values are shown on the right-hand side.

Parameter estimation:

The function `FindFit` of *Mathematica* (Wolfram Research, Champaign, IL) produces LSE for the parameters. The dependent variable in our case is the current

in nA, the independent variable is the time in ms and the four parameters to be estimated are A, A_∞, t_0, and τ. The decaying phase of the gap junction current can be fitted to the function

$$I(t) = A_\infty + A \exp\left[\frac{-(t - t_0)}{\tau}\right] . \tag{3.6}$$

The `Findfit` function obtained the best fitting values for the parameters as follows:

$$I(t) = -0.66 + 0.99 \exp\left[\frac{-t}{162.5}\right] . \tag{3.7}$$

The function described by the equation (3.7) is shown in Figure 3.2. The best-fitting parameter τ was then obtained for each current recording by fitting equation (3.6) using the least square best-fit routine of the *Mathematica* software.

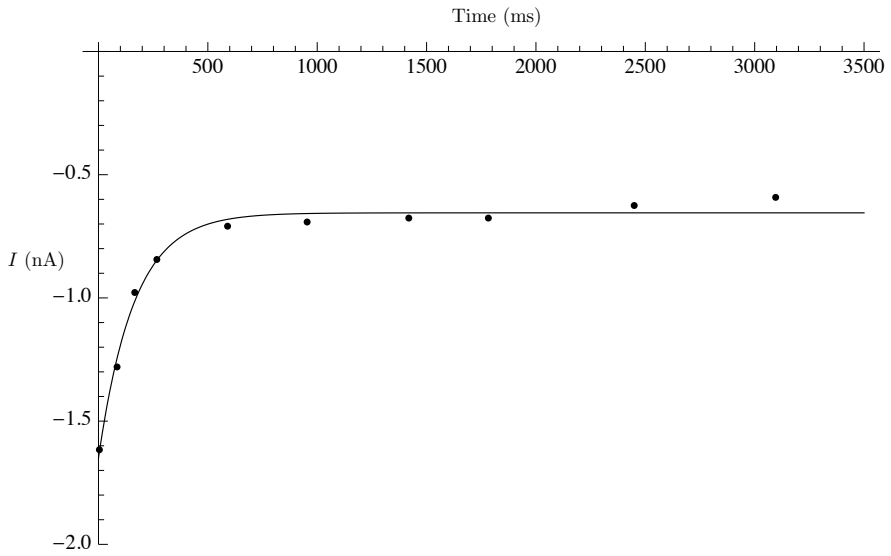

Figure 3.2: Parameter estimation. Least squares best fit curve to the data acquired from the gap junction current resulting from step pulse to −90 mV from a holding potential of 0 mV.

A plot of the residuals gives an indication of how good the least squares best fit is. Each residual is calculated as the difference between the data value and the predicted I value. If a data point is below the prediction line, its residual is negative, and if a point is above the line, its residual is positive as shown in Figure 3.3. Systematic variations in the signs and/or the magnitudes of the residuals is an indication that one or more of the statistical assumptions underlying the maximum likelihood rationale is unwarranted. In this case inspection by eye suggests that

there is no such systematic trend.

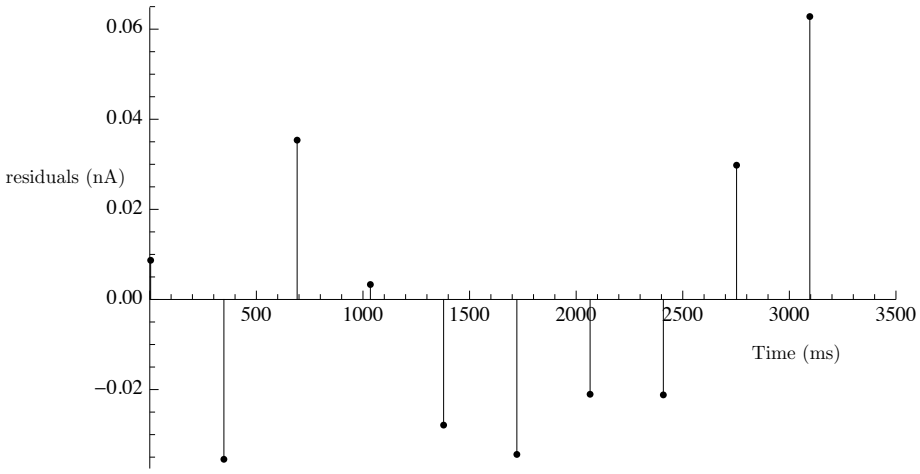

Figure 3.3: The residuals. Plot of the residuals for the fit in Figure 3.2.

Thereafter, an appropriate function describing the voltage-dependence of τ is chosen. The function accounts for the inactivation time constant of the gap junction current:

$$\tau = 9 + \frac{40 \times 10^3}{1 + 0.003\ V^2}\ . \tag{3.8}$$

Figure 3.4 shows the derived inactivation time constant as function of voltage.

Finally, simulated current traces elicited in response to step pulses in the voltage range of ±90 mV from holding potential of 0 mV using the estimated function can be generated and is shown in Figure 3.5.

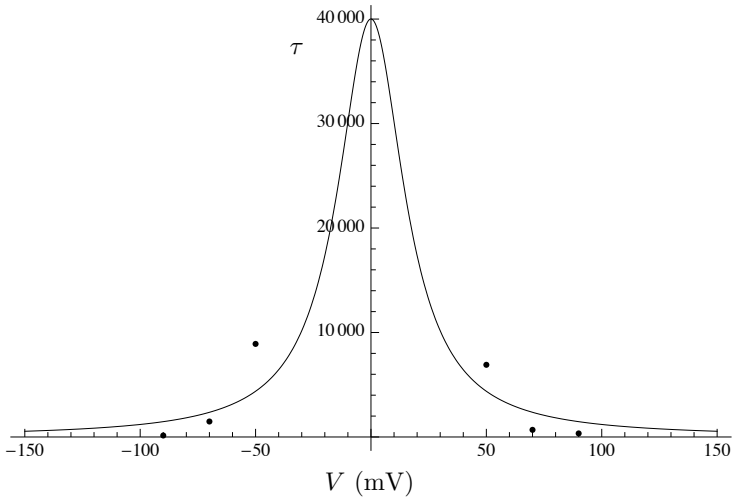

Figure 3.4: The resulting fit. The time constant as function of voltage for Type I gap junction. The fitted function is shown (solid line) together with the parameter τ values (filled circles) extracted from current trace curves elicited in response to 5 sec step pulses in the voltage range of ±90 mV from holding potential 0 mV (Miyoshi et al [7]).

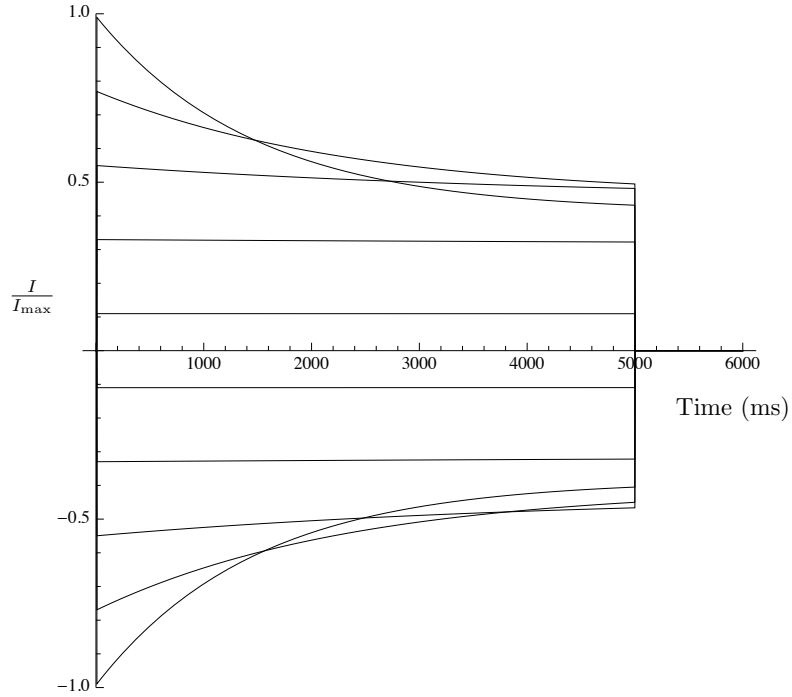

Figure 3.5: Simulated kinetics. Simulated current trace Type I gap junction resulting from voltage step in the voltage range of ±90mV from holding potential 0 mV.

3.2 Parameter estimation of channel density, SVD the general principle

Estimation of ion channel densities

A key objective in the present study is to characterise all possible combinations of plasma membrane densities of the electrogenic protein species that are consistent with observed voltage time series. In general, there is no single unique set of such densities. Instead, it shall become apparent that the solution must generally be stated in terms of the kernel of a linear operator.

Dynamics

The dynamics of the cell membrane potential V_m is given by the current summation law:

$$C\frac{d}{dt}V = I(t) - \sum_{i=1}^{n} \varkappa_i \psi_i(t) \ , \tag{3.9}$$

where C is the membrane capacitance per unit membrane area, I is the injected current, $\varkappa_i$ is the density of the conductance entity (i.e., ion channel, transporter, or exchanger) of type i relative to the same unit area, and ψ_i is the current carried by a single molecule of type i. For most types of conductance entities, the unit currents depend on the resistance and the driving force. The standard model for the current, as explained in Section 1.3.2, is as follows:

$$\psi_i = g_i(\boldsymbol{x})\,(V - E_i) \ , \tag{3.10}$$

where g_i is unit conductance, dependent on gating variables collected in a vector $\boldsymbol{x}$, and E_i is the reversal potential of the ith conductance. The dynamics of the gating variables has the following general form:

$$\frac{d}{dt}\boldsymbol{x} = \boldsymbol{f}(\boldsymbol{x}, V(t), \boldsymbol{u}(t)) \tag{3.11}$$

where $\boldsymbol{u}(t)$ denotes additional input variables such as $[\mathrm{Ca}^{2+}]_i$ and the extracellular ATP concentration ($[\mathrm{ATP}]_o$). The vector $\boldsymbol{x}$ collects the gating variables for all the conductances, transporters, and exchangers in the model, and the map $\boldsymbol{f}$ represents the dynamics of all these variables. Explicit stipulation of this map requires a detailed treatment of each of these electrogenic entities, which follows in Chapter 4.

Inferred currents and cumulative charges

The gating dynamics, equation (3.11), can be numerically integrated using the experimentally observed time series for the membrane potential $V(t)$ (Chapter 2, Figure 2.1A) together with the calcium time series as reconstructed in Chapter 4, Section 4.8 (input variable $u(t)$). Let $\boldsymbol{\xi}(t)$ denote the gating state time series that is obtained in this manner. The currents carried by each of the species can then be reconstructed by substituting $\boldsymbol{\xi}(t)$ for $\boldsymbol{x}(t)$ in equation (3.10). Numerical integration of these currents yields the inferred cumulative charges per entity, which are defined as follows:

$$q_i(t) = \int_0^t g_i(\boldsymbol{\xi}(\tau))\,(V(\tau) - E_i)\,d\tau\ . \tag{3.12}$$

Here $V(\tau)$ is the observed membrane potential at time τ. Substituting by the standard model, equation (3.10), in equation (3.12); the cumulative charges are defined as follows:

$$q_i(t) = \int_0^t \psi_i(\boldsymbol{\xi}(\tau), V(\tau), \boldsymbol{u}(\tau))d\tau\ . \tag{3.13}$$

Integration of equation (3.9) gives an expression for the membrane potential at time t in terms of these cumulative charges:

$$V(t) = V(0) + V_0(t) - \sum_{i=1}^{n} \frac{\varkappa_i}{C} q_i(t) \tag{3.14}$$

where the voltage term due to injected current is given by

$$V_0(t) = \frac{1}{C}\int_0^t I(\tau)d\tau\ . \tag{3.15}$$

The injected current $I(t)$ may be composed of several terms arising from distinct sources, e.g., post-synaptic input and experimental electrodes.

Scaling

To ensure that the problem is well-conditioned, the channel densities have to be scaled in an appropriate manner. For each species i let G_i be a positive number that satisfies

$$G_i > \left|\frac{\psi_i(t)}{E_i(t) - V(t)}\right| \quad \text{for all } t \tag{3.16}$$

and which is reasonably close to the least number satisfying this condition (G_i can be defined regardless of whether the conductance is represented by the standard

model, equation (3.10)). Furthermore, let T be a time scale, such as the duration of the experiment. The product G_iT has the dimensions of electric charge and is used to scale q_i. In the present study, G_i equals the unitary conductance of each entity (values stated in Chapter 4).

Singular-value decomposition

Suppose that the membrane potential has been observed at times t_1, t_2, ..., t_m, where m is an integer larger than n. Let $\boldsymbol{W}$ be an $m \times n$ matrix whose (h,i)th element is defined by

$$W_{hi} = q_i(t_h)(G_iT)^{-1} \,. \tag{3.17}$$

In addition, let $\boldsymbol{Y}$ be an m-vector whose hth element is $V(t_h) - V(0) - V_0(t)$, and let $\boldsymbol{\kappa}$ be an n-vector where $\kappa_i = \varkappa_i G_i T/C$ is a dimensionless coefficient which is proportional to the density of conductance species i, as follows:

$$\boldsymbol{Y} = \begin{bmatrix} V(t_1) - V_0 \\ V(t_2) - V_0 \\ \cdots \\ \vdots \\ \vdots \\ V[t_m] - V_0 \end{bmatrix} , \boldsymbol{W} = \begin{bmatrix} q_{1,1} & q_{1,2} & \cdots & q_{1,n} \\ q_{2,1} & \ddots & & \\ \cdots & \ddots & & \\ \vdots & & & \vdots \\ \vdots & & & \vdots \\ q_{m,1} & \cdots & & q_{m,n} \end{bmatrix} , \boldsymbol{\kappa} = \begin{bmatrix} \kappa_1 \\ \kappa_2 \\ \cdots \\ \vdots \\ \kappa_n \end{bmatrix} \tag{3.18}$$

The scaled densities (collected in $\boldsymbol{\kappa}$) are constrained by the matrix equation

$$\boldsymbol{Y} = \boldsymbol{W} \cdot \boldsymbol{\kappa} \tag{3.19}$$

which can be solved in the least-squares sense. However, uniqueness is not ensured when the rank r of $\boldsymbol{W}$ is smaller than n, as is generally the case.

The kernel of $\boldsymbol{W}$ can be used to obtain all combinations of channel densities that are equally compatible with the observational data (that minimise the discrepancy between the membrane potential calculated according to equation (3.19) and the observed time series in Chapter 2). This kernel can be derived from the singular-value decomposition (SVD) of $\boldsymbol{W}$:

$$\boldsymbol{W} = \boldsymbol{U} \cdot \Sigma \cdot \boldsymbol{V}^{\mathrm{T}} \tag{3.20}$$

where T indicates transposition. The final $n - r$ columns of $\boldsymbol{V}$ constitute an orthonormal basis for the kernel of $\boldsymbol{W}$.

General solution for the channel densities

All combinations of channel densities compatible with the observational data can be expressed as a least-squares solution to equation (3.19) plus a linear combination of this nullspace basis. To obtain such a solution, let $\boldsymbol{V}_r$ denote the matrix containing the first r columns of the $n \times n$ matrix $\boldsymbol{V}$, let $\boldsymbol{D}$ denote an $r \times r$ diagonal matrix containing the non-zero singular values, and let $\boldsymbol{U}_r$ denote the matrix containing the first r columns of the $m \times m$ matrix $\boldsymbol{U}$. The pseudo-inverse of $\boldsymbol{W}$ is given by $\boldsymbol{V}_r \cdot \boldsymbol{D}^{-1} \cdot \boldsymbol{U}_r^T$ and the smallest-length least-squares solution is given by:

$$\boldsymbol{\kappa}^+ = \boldsymbol{V}_r \cdot \boldsymbol{D}^{-1} \cdot \boldsymbol{U}_r^T \cdot \boldsymbol{Y} \ . \tag{3.21}$$

Every vector of channel densities equally compatible with the observational data for the scaled densities can be represented as follows:

$$\widehat{\boldsymbol{\kappa}} = \boldsymbol{\kappa}^+ + \sum_{j=1}^{n-r} \gamma_j \boldsymbol{v}_j^0 \tag{3.22}$$

where $\boldsymbol{v}_1^0$, $\boldsymbol{v}_2^0$, $\ldots$ $\boldsymbol{v}_{n-r}^0$ denote the final $n - r$ columns of $\boldsymbol{V}$. The coefficients γ_1, γ_2, $\ldots$, γ_{n-r} are not determined by the observational data, since each of the vectors $\widehat{\boldsymbol{\kappa}}$ given by equation (3.22) results in exactly the same membrane potential waveform. Each such vector can be interpreted as one particular way for a cell to realise the observed behaviour. In this sense, the vectors $\boldsymbol{v}_1^0$, $\boldsymbol{v}_2^0$, $\ldots$ $\boldsymbol{v}_{n-r}^0$ express the redundancy inherent in the system. Hence a heat map of these vectors provides a visualisation of this functional redundancy.

Feasible solutions

The primary objective of the present analysis is to characterise the set of channel density vectors consistent with the observational data. To select one vector within this space, further constraints must be imposed. A natural first requirement is that the elements of $\widehat{\boldsymbol{\kappa}}$ be non-negative; the pseudo-inverse $\boldsymbol{\kappa}^+$ does not generally satisfy this requirement.

Further possible conditions to constrain the solution set include the following (in addition to the non-negativity requirement): (a) the vector $\widehat{\boldsymbol{\kappa}}$ with the greatest number of zero elements; (b) the vector $\widehat{\boldsymbol{\kappa}}$ that is in the best agreement with (partial) proteomics data; (c) molecular parsomony. The latter criterion can be understood as follows: the solution is set to satisfy the parsimony relative to total channel density. The coefficients $\gamma_1, \ldots, \gamma_{n-r}$ that minimise the sum of the elements of $\widehat{\boldsymbol{\kappa}}$ (such that

$\widehat{\boldsymbol{\kappa}} \in \mathbb{R}_+^n$) can then be determined by means of linear programming. The resulting $\widehat{\boldsymbol{\kappa}}$ represents the expression profile that achieves the observed behaviour with the least amount of molecular building blocks expended.

In practice, it is often the case that the affine space generated by equation (3.22) does not intersect with the positive cone. Accordingly, a vector $\boldsymbol{\kappa}_p$ was found using constrained least-squares fitting that satisfies the non-negativity requirement, and this value was used instead of $\boldsymbol{\kappa}^+$ in equation (3.22) to generate the most-parsimonious solution by means of linear programming. This modification does not affect the analysis of functional redundancy, since the basis of the kernel remains unaltered.

If we are able to obtain time series from various experiments, it may be possible to reduce the dimentionality of the null space of $\boldsymbol{W}$. These time series can be concatenated, if care is taken to reset the state of the system to the appropriate initial condition in between "runs". Thus the matrix $\boldsymbol{W}$ will schematically be organised as follows:

$$\boldsymbol{W} = \begin{bmatrix} \boldsymbol{W}_1 \\ \cdots \\ \boldsymbol{W}_2 \\ \cdots \\ \vdots \end{bmatrix} \tag{3.23}$$

where $\boldsymbol{W}_1$, $\boldsymbol{W}_2$, ... are the matrices for the individual experiments.

3.3 Data analysis and numerical techniques

Least-squares estimation was used to estimate parameter values. The equilibrium point of the dynamics without input current was used as initial condition. All analyses were carried out in *Mathematica* (Wolfram Research, Champaign, IL), using the built-in facilities for the numerical evaluation of differential equations, least-squares estimation, and singular-value decomposition. Briefly, the *Mathematica* function `NDSolve` was used to solve our system of 123 ordinary differential equations, using an adaptive method. The default method, `Automatic`, automatically switches between BDF (Backward differentiation formulas) and Adams multistep methods, depending on the stiffness. The *Mathematica* function `FindFit` was used to perform least-squares fitting for activation, inactivation, and deactivation kinetics. The *Mathematica* function `SingularValueDecomposition` was used to obtain singular value decomposition for numerical matrices (in this case the matrix $\boldsymbol{W}$ defined above). For numerical linear optimisation, the function `LinearProgramming` was

used to find a vector which minimises a linear function subject to certain linear and non-negative constraints.

3.4 Upper bounds on channel density values

There are natural physiological limitations to how high channel densities can become in functional cells. To obtain a conservative estimate of these upper bounds, we attempted to calculate a reasonable estimate for the maximum possible channel density for each of the conductance species in the model, proceeding as follows. From equations (3.9) and (3.10) we obtain the current carried by a species i:

$$I_i = \varkappa_i \; g_i(\boldsymbol{x}) \, (V - E_i) \; . \tag{3.24}$$

Using a set of whole-cell voltage-clamp I-V curves for MSMCs, obtained by Dr. McCloskey (a selection of which is shown in Figure 3.6), we obtain the steady-state current density $\overline{I}(V)$ for a given MSMC. Substituting in equation (3.24), we find:

$$\overline{I}(V) = \varkappa_i \; g_i(\overline{\boldsymbol{x}}(V))(V - E_i) \; , \tag{3.25}$$

where $\overline{\boldsymbol{x}}(V)$ is the steady state of $\boldsymbol{x}$, which can be treated as function of V under voltage-clamp conditions. Hence we have

$$\varkappa_i = \frac{\overline{I}(V)}{g_i(\overline{\boldsymbol{x}}(V))(V - E_i)} \; , \tag{3.26}$$

which can be interpreted as the density that species i would have in order to be the sole carrier of the observed current, which gives a conservative upper bound (since in reality the current may be born by several species). Since we are looking for an upper bound, we maximise this expression, described by equation (3.26), with respect to physiologically achievable V,

$$\widehat{\varkappa}_i = \max_V \left[\frac{\overline{I}(V)}{g_i(\overline{\boldsymbol{x}}(V))(V - E_i)} \right] \; . \tag{3.27}$$

For the calcium-dependent gating variables, we assumed a baseline level of intracellular calcium concentration (100 nM). The lower bounds or minimum possible channel density values are set to zero as no channel density can take a negative value.

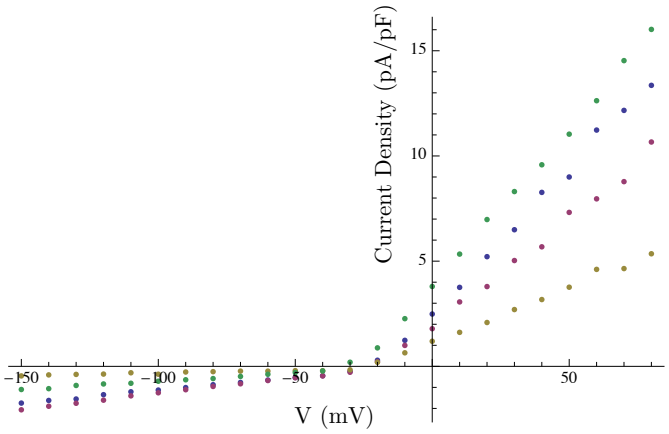

Figure 3.6: Experimentally measured I-V curves in pA/pF.
I-V curves measured for the average whole cell current density in pA/pF from voltage clamp experiments between 450 ms–500 ms from holding potential of −60 mV; the voltage was stepped to test potential from −150 to +80 mV in 10 mV increments.

Table 3.1: Channel density upper bound

Potential conductance species	maximum number of channels/pF
Kv2.1	17
Kv9.3	11.2
Kv6.1	37
BK	1500
BKβ1	700
BKβ3	4
BKβ4	2
SK_2	366
SK_3	1590
SK_4	14
hERG	69.2
Kv4.1	14
Kv4.3	19
Kv4.3+KCNE3	191
Kv4.3+KChIP2b	15
Kv4.3+KChIP2d	10
Kv4.3+KChIP2b+KCNE3	26
Kv3.4	42
Kv7.1	101
Kv7.4	16
Kir7.1	1031
bgK, bgCl	1, 2

Chapter 4

Modelling the conductances involved in myometriocyte excitability and estimating the associated biophysical parameters

This chapter details the various entities included in our model. A complete description of how we acquired the data and modelled the kinetics of each entity is also given. Most of the equations in this chapter have been published in McCloskey et al [90], while the detailed descriptions will be published in a forthcoming paper.

The "conductome" can be defined as the totality of ion channels and ion transporters expressed by an electrically active cell, i.e., a list specifying the cell surface density and oilgomeric composition of each of these species. Defining this list for a given cell poses a considerable challenge, since the human genome contains a large number of distinct ion channels, each of which may be assembled into multiple multimeric complexes that modulate the electrical activity of the cell in a subtly different way [31]. Assaying of the total ion channel repertoire of a given cell may not be feasible using only conventional biophysical techniques such as electrophysiology. By contrast, transcriptomic analysis accurately surveys the complete set of all mRNA coding of all potential conductances. In this chapter, we propose a mathematical model based on individual currents carried by the electrogenic transmembrane proteins in MSMC. First, we characterise the potential repertoire of electrogenic proteins by means of expression studies. McCloskey et al [90] show

the mRNA expression list with the genes that were found at mRNA level in the MSMC, using qRT-PCR in conjunction with laser capture microdisection (LCM), together with the associated ΔCT values normalised to r18s mRNA, in samples taken from pregnant and non-pregnant patients. Also, Chan et al [8] described the detailed transcriptome of human MSMC samples using high throughput RNA sequencing (RNA-seq). The isolated RNA was from myometrium of uterine biopsies from patients at term who were not in labour and at term in spontaneous labour. Second, we construct a complete repertoire of every individual oligomeric channel complex that has been previously attested in the literature and that is consistent with the subunits in the mRNA expression list; the mathematical model, shown in Figure 4.1A, incorporates 31 time-dependent ionic currents. These currents include outward currents such as the voltage-gated potassium current, the voltage- and calcium-gated potassium current, as well as the calcium-gated potassium current. In addition, the model comprises two inward, depolarising currents attributed to the two voltage-gated calcium channels (L-type and T-type). The chloride current is represented as an influx of calcium-activated chloride current, as well as a background chloride current. A background potassium current is incorporated to include the leak potassium current and the leak current arising from the two-pore domain potassium channels. Finally, the model comprises pumps and exchangers: the NCX, the PMCA, and the Na^+-K^+ pump. The individual mathematical model for each oligomeric channel is either based on models that have already been proposed in the literature, or formulated on the basis of the available data. The biophysical and kinetic parameters of several of these entities are furnished directly in the literature, or else have been obtained by means of least-squares fitting to the experimental data on heterologous expression systems as provided by the literature and described in Chapter 3. A summary of the potential conductance species included in our model is shown in Table 4.1.

4.1 Potassium channels

Potassium channels are found in all cell types. These membrane proteins are selectively permeable to potassium ions. They are involved in many functions within the cell: setting up the RMP; controlling the shape and frequency of the AP; taking part in muscle contraction; pacemaking; hormone secretion. They exhibit an important role in cell volume regulation and a wide range of cellular functions [31]. Multiple genes, expressing potassium channels, have been identified; they are the most diverse type of channels due to: (i) alternative splicing of transcripts from a single

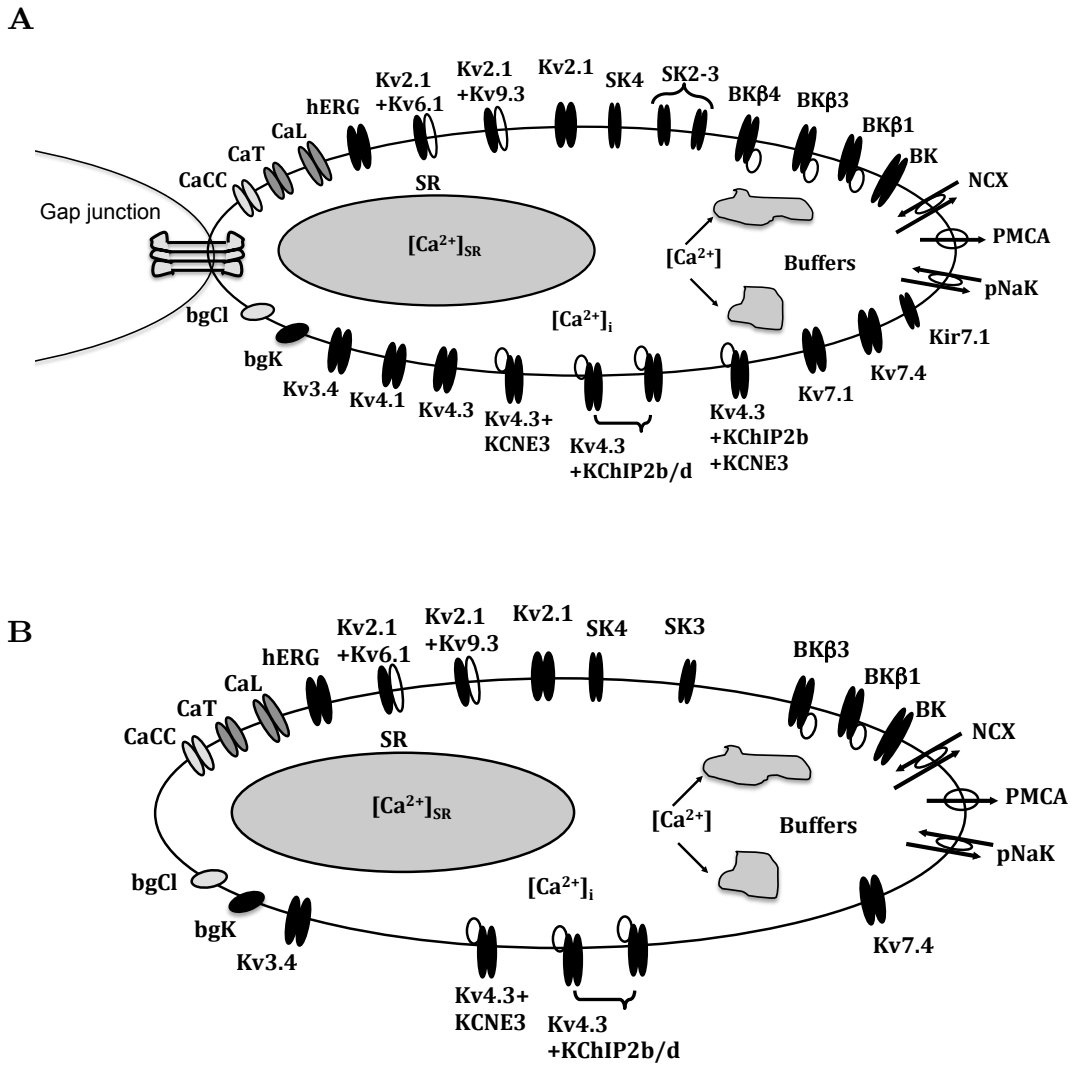

Figure 4.1: Model diagram.
(A) A diagrammatic representation of all potential entities considered in the model repertoire according to mRNA expression data [8]. (B) A diagrammatic representation of the potential entities based on the most parsimonious solution (ℓ_1-norm).

gene; (ii) the expression of the various proteins with different β-subunits or other α-subunits to form distinct homomeric or heteromeric species. The abundance of the potassium channels in the MSMC is evident from the mRNA expression data [8,90].

4.1.1 Voltage-gated potassium channels (Kv)

Voltage-gated potassium channels are membrane proteins that allow potassium ions through their pores following voltage variations. They are usually closed at RMP then activate at different rates upon depolarisation. They carry sustained non-inactivating or inactivating current (e.g. the transient outward current) with variable time- and voltage-dependence depending on the gene involved.

Two types of inactivation of the voltage-gated potassium channels have been identified. The first is the N-type, rapid inactivation; the N-terminus of the protein forms a ball that is coupled to the rest of the protein through a loop [111, 112]. The channel inactivates when the ball transiently blocks the inner pore preventing ion movement through the channel; the channel is said to exhibit "fast ball and chain" inactivation. The channels displaying this rapid inactivation operate in the subthreshold range of AP and are also called A-type channels. The A-type potassium current, also known as the transient outward potassium current, is a current that activates almost instantaneously at potentials positive of the RMP, then undergoes fast inactivation. Many genes that are known to encode channels that contribute to the A-type current are in the mRNA expression [8]. For instance, the genes *KCND1*, and *KCND3* encode the Kv4.1 and Kv4.3 proteins, respectively. Each of the previous channels is represented separately in the model. Other entities arise from the Kv4 channels associating with the auxiliary proteins of the KChIP family.

The second is the C-type, slow inactivation, which involves the C-terminus; the channel, in this case, undergoes slow and incomplete inactivation. The C-type inactivation is not so well defined, but involves intracellular and extracellular conformational changes of the channel [113]. The C-type potassium channels give rise to an outward current known as the delayed rectifier current. The latter is a slowly inactivating or non-inactivating current. Examples of delayed rectifiers in the MSMC are Kv1.3, Kv2.1, Kv7.1, Kv7.4, and Kv11.1 (the corresponding genes are *KCNA1*, *KCNB1*, *KCNQ1*, *KCNQ4*, and *KCNH2*, respectively). Silencers such as Kv6.1 and Kv9.3 have to coexist with Kv2.1 to be functional.

Voltage-gated potassium channels contain four α-subunits and in some cases four β-subunits associated with them on the cytoplasmic side of the membrane. Each α-subunit comprises six segments (S_1-S_6) with the S_4 segment being the voltage sensor. There exist many combinations of both α- and β-subunits, which exhibit different kinetics and properties. The role of voltage-dependent potassium channels is currently well known; it includes maintaining RMP, repolarisation, and controlling the AP duration (APD) [54].

Table 4.1: Potential conductance species included in the model

Name given	Gene combination	State variables	References
Kv2.1	KCNB1	$C_0^{[\mathrm{Kv2.1}]} - C_4^{[\mathrm{Kv2.1}]}$,$O^{[\mathrm{Kv2.1}]}$,$I_0^{[\mathrm{Kv2.1}]} - I_5^{[\mathrm{Kv2.1}]}$	[97]
Kv9.3	KCNB1+KCNS3	$g_1, g_{2_{\mathrm{fast}}}, g_{2_{\mathrm{slow}}}$	[10]
Kv6.1	KCNB1+KCNG1	l_1, l_2	[10, 11]
BK	KCNMA1	$P_{o\mathrm{BK}_\alpha}$	[98]
BKβ1	KCNMA1+KCNMB1	$P_{o\mathrm{BK}_{\alpha+\beta1}}$	[98]
BKβ3	KCNMA1+KCNMB3	$C_0^{[\alpha+\beta3]}$–$C_4^{[\alpha+\beta3]}$,$O_0^{[\alpha+\beta3]}$–$O_4^{[\alpha+\beta3]}$,	[99]
BKβ4	KCNMA1+KCNMB3	$P_{\mathrm{BK}_{\alpha+\beta4}}$	[100, 101]
SK_2	KCNN1	P_{SK2}	[20, 21]
SK_3	KCNN3	P_{SK3}	[22]
SK_4	KCNN4	P_{SK4}	[102]
hERG	KCNH2	$C_0^{[\mathrm{hERG}]} - C_2^{[\mathrm{hERG}]}$,$O_1^{[\mathrm{hERG}]} - I_0^{[\mathrm{hERG}]}$	[103]
CaL (L-type)	CACNA1C	d, f	[104]
CaT (T-type)	CACNA1G	a, c	[105]
CaCC	ANNO1	cc	[106]
Kv3.4	KCNC4	a_1, a_2	[12]
Kv4.1	KCND1	$b_1, b_{2_{\mathrm{fast}}}, b_{2_{\mathrm{inter}}}, b_{2_{\mathrm{slow}}}$	[13, 14]
Kv4.3	KCND3	$C_0^{[\mathrm{Kv4.3}]} - C_4^{[\mathrm{Kv4.3}]}$,$O^{[\mathrm{Kv4.3}]}$, $I_0^{[\mathrm{Kv4.3}]} - I_6^{[\mathrm{Kv4.3}]}$	[107]
Kv4.3+KCNE3	KCND3+KCNE3		
Kv4.3+KChIP2b	KCND3+KChIP2b	$k_1, k_{2_{\mathrm{fast}}}, k_{2_{\mathrm{slow}}}$	[108]
Kv4.3+KChIP2d	KCND3+KChIP2d	$k_1, k_{2_{\mathrm{fast}}}, k_{2_{\mathrm{slow}}}$	[108]
Kv4.3+KChIP2b+KCNE3			
Kv7.1	KCNQ1	$C_1^{[\mathrm{Kv7.1}]}$, $C_2^{[\mathrm{Kv7.1}]}$,$O_1^{[\mathrm{Kv7.1}]}$, $O_2^{[\mathrm{Kv7.1}]}$,$I^{[\mathrm{Kv7.1}]}$	[109]
Kv7.4	KCNQ4	d_1, d_2	[19]
Kir7.1	KCNJ13	$P_{\mathrm{Kir7.1}}$	[23]
bgK, bgCl			
Gap1, Gap2		$P_{\mathrm{GJ}_I}, P_{\mathrm{GJ}_{II}}$	[7]
NCX, PMCA, NaK			[104, 110]
P2X4	P2X4R	$P_{\mathrm{act}}, P_{\mathrm{des}}$	[25]

Delayed rectifier, voltage-gated potassium channel Kv2.1

The $I_{\text{Kv2.1}}$ current is carried by the channel encoded by the *KCNB1* gene. This channel is a voltage-dependent potassium channel related to the shab channel of *Drosophila* [9]. Various lines of evidence indicate that this ion channel plays an important role in uterine contractility. First, it is highly expressed both in the pregnant and non-pregnant human uterus at the mRNA level [8, 90] with the ΔCT of 16.14±0.05 (normalised to r18s mRNA) in samples taken from non-pregnant patients and 16.14±0.14 in samples taken from pregnant patients [90]. This was the second highly expressed channel after BK. Secondly, Knock et al [114] identified three types of voltage-gated potassium currents in pregnant human myometrium. The first current, IK1, was a 4-aminopyridine-insensitive (4-AP) with a negative half-inactivation ($V_{\text{half}} = -61$ mV) and negative activation characteristics (threshold between $-$ 60 and $-$ 40 mV) and slow kinetics. The current was inhibited by tetraethylammonium (TEA) (half-maximal block at 3 mM) but insensitive to higher doses. Kv2.1 is the only cloned channel that has similar electrophysiological and pharmacological properties (slow inactivation, moderate TEA sensitivity and resistance to block by 4-AP [10]). This suggests that Kv2.1 is one of the most important delayed rectifier channels that has a pivotal role in returning the depolarised cell to a resting state.

When expressed in heterologous expression systems, this channel's biophysical characteristics closely match those of delayed rectifier currents. It activates as a result of a brief depolarisation, showing a sigmoidal time course [115] with $V_{\text{half}} = 20$ mV and slope $k = 19.6$ mV [10], then it slowly inactivates during sustained depolarisation with $V_{\text{half}} = -29.8$ mV, and $k = -11.1$ mV [10]. This slow inactivation is possibly physiologically irrelevant for a brief AP, but a train of depolarizations may result in a cumulative inactivation. To account for this cumulative effect, we use a Markov model which incorporates the slow inactivation-related gating states [116]. Our model of the Kv2.1 channel is based on the one proposed by Klemic et al [97], shown in Figure 4.3. The resulting voltage-dependent inactivation is cumulative (i.e., only apparent during repetitive spiking) and U-shaped, with the inactivation being lowest at strong depolarizations. Current (expressed in pA/pF) through this channel is described by the following equation:

$$I_{\text{Kv2.1}} = \kappa_{\text{Kv2.1}} G_{\text{Kv2.1}} O^{[\text{Kv2.1}]} (V - E_{\text{K}}) \,, \tag{4.1}$$

where $G_{\text{Kv2.1}}$ is the single channel conductance (pS) and $O^{[\text{Kv2.1}]}$ is the probability of the Kv2.1 channel being in the open state. $\kappa_{\text{Kv2.1}}$ expresses the channel density

in number of channels/fF. The channel densities of the various entities are to be estimated using the method described in Chapters 3 and 5

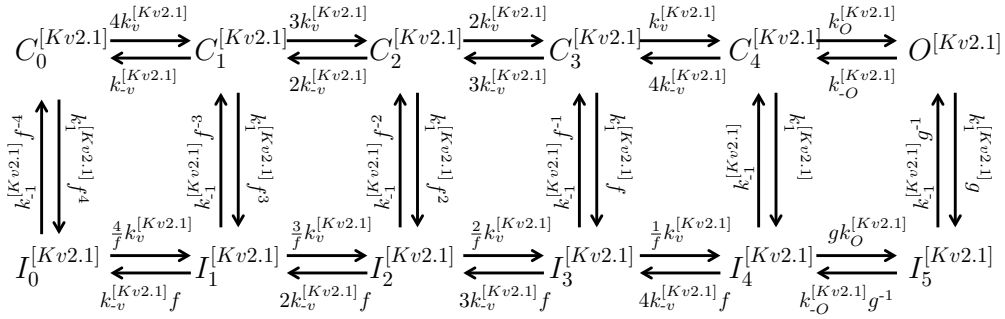

Figure 4.2: State transition diagram of the Markov model for the Kv2.1 channel. $C_0^{[\mathrm{Kv2.1}]}$ – $C_4^{[\mathrm{Kv2.1}]}$ are the closed states; $O^{[\mathrm{Kv2.1}]}$ is the open state, and $I_0^{[\mathrm{Kv2.1}]}$ – $I_5^{[\mathrm{Kv2.1}]}$ are the inactivation states. $K_v^{[\mathrm{Kv2.1}]}$, $K_{-v}^{[\mathrm{Kv2.1}]}$, $k_1^{[\mathrm{Kv2.1}]}$, $k_{\text{-}1}^{[\mathrm{Kv2.1}]}$, $k_0^{[\mathrm{Kv2.1}]}$, and $k_{\text{-}0}^{[\mathrm{Kv2.1}]}$ are the transition rates between the states.

Figure 4.3 shows the simulated I-V curve together with the experimental data from the expression of the potassium channel gene drk1 (≡ Kv2.1) cloned in *Xenopus* oocytes by Frech et al [9]. According to Frech et al, the channel does not inactivate within 500 ms, in keeping with Klemic et al [97] who found a slow, weakly voltage-dependent inactivation ($\tau = 4$ s at 0 mV; $\tau = 7$ s at +80 mV).

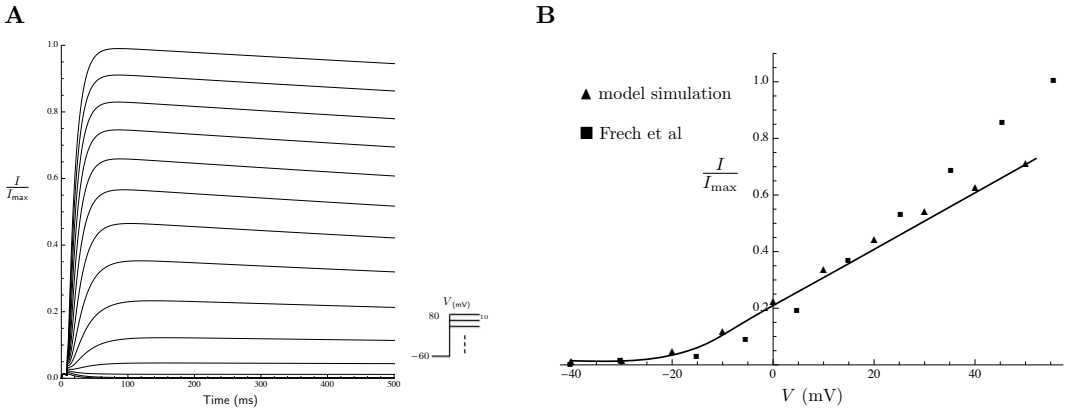

Figure 4.3: Properties of the $I_{\mathrm{Kv2.1}}$. (A) Normalised $I_{\mathrm{Kv2.1}}$ current trace generated by the model during simulated voltage-clamp experiments. Currents are recorded during 1 s voltage steps to potentials ranging from −50 to 80 mV from a holding potential of −60 mV. (B) Simulated (solid triangles) and experimental data from Frech et al [9] (solid squares) peak I-V curve obtained from the series of experiments shown in (A). Values are normalised to the peak current value.

The equations describing the voltage-dependent rates (s^{-1}) shown in Figure 4.2 are:

$$\begin{aligned} k_{v}^{[\mathrm{Kv2.1}]} &= 12\ \exp\left[0.77\frac{VF}{RT}\right] , \\ k_{-v}^{[\mathrm{Kv2.1}]} &= 42\ \exp\left[-0.54\frac{VF}{RT}\right] , \\ k_{-o}^{[\mathrm{Kv2.1}]} &= 31\ \exp\left[-0.5\frac{VF}{RT}\right] , \end{aligned} \tag{4.2}$$

We deduce the following system of 12 ordinary differential equations (ODEs) that corresponds to the Markov state model of 12 states [97] shown in Figure 4.2:

$$\begin{aligned} \frac{dC_0^{[\mathrm{Kv2.1}]}}{dt} &= 1-(O^{[\mathrm{Kv2.1}]}+\sum_{i=1}^{4}C_i^{[\mathrm{Kv2.1}]}+\sum_{i=0}^{5}I_i^{[\mathrm{Kv2.1}]}) , \\ \frac{dC_1^{[\mathrm{Kv2.1}]}}{dt} &= 4k_{v}^{[\mathrm{Kv2.1}]}C_0^{[\mathrm{Kv2.1}]}-(k_{-v}^{[\mathrm{Kv2.1}]}+3k_{v}^{[\mathrm{Kv2.1}]}+k_1^{[\mathrm{Kv2.1}]}f^3)C_1^{[\mathrm{Kv2.1}]} \\ &\quad +2k_{-v}^{[\mathrm{Kv2.1}]}C_2^{[\mathrm{Kv2.1}]}+\frac{k_{-1}^{[\mathrm{Kv2.1}]}}{f^3}I_1^{[\mathrm{Kv2.1}]} , \\ \frac{dC_2^{[\mathrm{Kv2.1}]}}{dt} &= 3k_{v}^{[\mathrm{Kv2.1}]}C_1^{[\mathrm{Kv2.1}]}-(2k_{-v}^{[\mathrm{Kv2.1}]}+2k_{v}^{[\mathrm{Kv2.1}]}+k_1^{[\mathrm{Kv2.1}]}f^2)C_2^{[\mathrm{Kv2.1}]} \\ &\quad +3k_{-v}^{[\mathrm{Kv2.1}]}C_3^{[\mathrm{Kv2.1}]}+\frac{k_{-1}^{[\mathrm{Kv2.1}]}}{f^2}I_2^{[\mathrm{Kv2.1}]} , \\ \frac{dC_3^{[\mathrm{Kv2.1}]}}{dt} &= 2k_{v}^{[\mathrm{Kv2.1}]}C_2^{[\mathrm{Kv2.1}]}-(3k_{-v}^{[\mathrm{Kv2.1}]}+k_{v}^{[\mathrm{Kv2.1}]}+k_1^{[\mathrm{Kv2.1}]}f)C_3^{[\mathrm{Kv2.1}]} \\ &\quad +4k_{-v}^{[\mathrm{Kv2.1}]}C_4^{[\mathrm{Kv2.1}]}+\frac{k_{-1}^{[\mathrm{Kv2.1}]}}{f}I_3^{[\mathrm{Kv2.1}]} , \\ \frac{dC_4^{[\mathrm{Kv2.1}]}}{dt} &= k_{v}^{[\mathrm{Kv2.1}]}C_3^{[\mathrm{Kv2.1}]}-(4k_{-v}^{[\mathrm{Kv2.1}]}+k_{o}^{[\mathrm{Kv2.1}]}+k_1^{[Kv21]})C_4^{[\mathrm{Kv2.1}]} \\ &\quad +k_{-o}^{[\mathrm{Kv2.1}]}O_4^{[\mathrm{Kv2.1}]}+k_{-1}^{[Kv21]}I_4^{[Kv21]} , \end{aligned}$$

$$
\begin{aligned}
\frac{dI_0^{[\mathrm{Kv2.1}]}}{dt} &= k_1^{[\mathrm{Kv2.1}]} f^4 C_0^{[\mathrm{Kv2.1}]} - (\frac{k_{-1}^{[\mathrm{Kv2.1}]}}{f^4} + 4\frac{k_v^{[Kv21]}}{f}) I_0^{[\mathrm{Kv2.1}]} \\
&\quad + k_{-v}^{[\mathrm{Kv2.1}]} f I_1^{[\mathrm{Kv2.1}]} \,, \\
\frac{dI_1^{[\mathrm{Kv2.1}]}}{dt} &= 4\frac{k_v^{[\mathrm{Kv2.1}]}}{f} I_0^{[\mathrm{Kv2.1}]} + k_1^{[\mathrm{Kv2.1}]} f^3 C_1^{[\mathrm{Kv2.1}]} - (f k_{-v}^{[\mathrm{Kv2.1}]} + \frac{k_{-1}^{[\mathrm{Kv2.1}]}}{f^3} \\
&\quad + 3\frac{k_v^{[\mathrm{Kv2.1}]}}{f}) I_1^{[\mathrm{Kv2.1}]} + 2k_{-v}^{[\mathrm{Kv2.1}]} f I_2^{[Kv21]} \,, \\
\frac{dI_2^{[\mathrm{Kv2.1}]}}{dt} &= 3\frac{k_v^{[\mathrm{Kv2.1}]}}{f} I_1^{[\mathrm{Kv2.1}]} + k_1^{[\mathrm{Kv2.1}]} f^2 C_2^{[\mathrm{Kv2.1}]} - (2f k_{-v}^{[\mathrm{Kv2.1}]} + \frac{k_{-1}^{[\mathrm{Kv2.1}]}}{f^2} \\
&\quad + 2\frac{k_v^{[\mathrm{Kv2.1}]}}{f}) I_2^{[\mathrm{Kv2.1}]} + 3k_{-v}^{[\mathrm{Kv2.1}]} f I_3^{[Kv21]} \,, \\
\frac{dI_3^{[\mathrm{Kv2.1}]}}{dt} &= 2\frac{k_v^{[\mathrm{Kv2.1}]}}{f} I_2^{[\mathrm{Kv2.1}]} + k_1^{[\mathrm{Kv2.1}]} f C_3^{[\mathrm{Kv2.1}]} - (3f k_{-v}^{[\mathrm{Kv2.1}]} + \frac{k_{-1}^{[\mathrm{Kv2.1}]}}{f} \\
&\quad + \frac{k_v^{[\mathrm{Kv2.1}]}}{f}) I_3^{[\mathrm{Kv2.1}]} + 4k_{-v}^{[\mathrm{Kv2.1}]} f I_4^{[Kv21]} \,, \\
\frac{dI_4^{[\mathrm{Kv2.1}]}}{dt} &= \frac{k_v^{[\mathrm{Kv2.1}]}}{f} I_3^{[\mathrm{Kv2.1}]} + k_1^{[\mathrm{Kv2.1}]} C_4^{[\mathrm{Kv2.1}]} - (4f k_{-v}^{[\mathrm{Kv2.1}]} + k_{-1}^{[\mathrm{Kv2.1}]} + \\
&\quad k_o^{[\mathrm{Kv2.1}]} g) I_4^{[\mathrm{Kv2.1}]} + \frac{k_{-o}^{[\mathrm{Kv2.1}]}}{g} I_5^{[\mathrm{Kv2.1}]} \,, \\
\frac{dI_5^{[\mathrm{Kv2.1}]}}{dt} &= k_o^{[\mathrm{Kv2.1}]} g I_4^{[\mathrm{Kv2.1}]} - (\frac{(k_{-o}^{[\mathrm{Kv2.1}]} + k_{-1}^{[\mathrm{Kv2.1}]})}{g}) I_5^{[\mathrm{Kv2.1}]} + k_1^{[\mathrm{Kv2.1}]} g O^{[\mathrm{Kv2.1}]} \,, \\
\frac{dO^{[\mathrm{Kv2.1}]}}{dt} &= k_o^{[\mathrm{Kv2.1}]} C_4^{[\mathrm{Kv2.1}]} - (k_{-o}^{[\mathrm{Kv2.1}]} + k_1^{[\mathrm{Kv2.1}]} g) O^{[\mathrm{Kv2.1}]} + \frac{k_{-1}^{[\mathrm{Kv2.1}]}}{g} I_5^{[\mathrm{Kv2.1}]} \,.
\end{aligned}
\tag{4.3}
$$

The parameters of the Markov model of Kv2.1 are stated in Table 4.2.

Because the kinetics of the Kv2.1 is slow, it is unlikely that this channel contributes to a brief AP. However, a potential role of the Kv2.1 channel in the myometrial contractility is the slow wave generation and the contribution to the repolarising phase of the AP. In rabbit urethra smooth muscle cells, the role of Kv2.1 has been investigated [117]; the result of blocking Kv2.1 was a prolonged AP (only when the transient BK current was inhibited). A similar role could be suggested for the Kv2.1 channel in the MSMC, for instance, blocking Kv2.1 could enhance the contractile activity of the myometrium by increasing the amplitude of spontaneous contractions as reported by Kyle et al [117].

Kv2.1 forms heteromers with two of the genes in the mRNA list (*KCNS3* and *KCNG1*) [8]. These genes form the electrically silent delayed rectifier-like potassium

Table 4.2: Notation for the Kv2.1 potassium channel

Notation	Definition	Value
$G_{\text{Kv2.1}}$	Kv2.1unitary conductance	8.5 pS
$\kappa_{\text{Kv2.1}}$	Kv2.1 channel density	–
$k_1^{[\text{Kv2.1}]}$	Rate constant for inactivation with all voltage sensors activated	1.2 s^{-1}
$k_{-1}^{[\text{Kv2.1}]}$	Rate constant for recovery from inactivation	0.005 s^{-1}
$k_v^{[\text{Kv2.1}]}$	Rate constant	
$k_{-v}^{[\text{Kv2.1}]}$	Rate constant	
$k_0^{[\text{Kv2.1}]}$	Rate constant for channel opening at 0 mV	80 s^{-1}
$k_{-0}^{[\text{Kv2.1}]}$	Rate constant for channel closing at 0 mV	
f	Allosteric factor	0.17
g	Allosteric factor	0.02
z_{k_v}	Apparent charge associated for k_v	0.77 e
$z_{k_{-v}}$	Apparent charge associated for k_{-v}	−0.54 e
State Variables		
$C_0^{[\text{Kv2.1}]}$ – $C_4^{[\text{Kv2.1}]}$	Closed states	
$O^{[\text{Kv2.1}]}$	Open state	
$I_0^{[\text{Kv2.1}]}$ – $I_5^{[\text{Kv2.1}]}$	Inactivation states	

channels Kv9.3 and Kv6.1. When coexisting with the Kv2.1, both silencers modify its pharmacological and single channel properties as well as its kinetics. Separate entities comprising the Kv2.1/Kv6.1 and Kv2.1/Kv9.3 channel complexes were incorporated in the model. Their model, kinetics and properties are discussed below.

Delayed rectifier, voltage-gated, heteromeric potassium channel Kv2.1/Kv9.3

The current $I_{Kv9.3}$ is carried by the heteromeric Kv2.1/Kv9.3 channel, which is formed by the coexpression of the Kv2.1 channel with the electrically silent delayed rectifier-like potassium channel Kv9.3. The gene encoding the Kv9.3 channel, *KCNS3*, was present in the mRNA expression data [8]. When Kv9.3 was expressed together with Kv2.1 in *Xenopus* oocytes by Patel et al [10], several alterations were observed in the pharmacological properties, single-channel properties, and kinetics of Kv2.1: the single channel conductance increased, the activation threshold was shifted towards more negative values and the amplitude of the current was enhanced. Both activation and inactivation curves of Kv2.1 were displaced towards more negative values by about 20 mV, which leads to faster activation and inactivation [10]. Kv2.1 inactivates slowly from both the open and intermediate closed state while Kv2.1/Kv9.3 does not inactivate from the open state but in a fast and complete manner from the intermediate closed state. The result is a U-shaped steady-state inactivation-voltage curve [118]. To describe the steady state gating variables, we adopte the Boltzmann function proposed by Patel et al [10] as this resulted in a better fit to the data (equations (4.5) and (4.6)). For activation, $V_{\text{half}} = 3.2$ mV and $k = 21.8$ mV, while for inactivation $V_{\text{half}} = -44.9$ mV, and $k = -10.4$ mV [10]. The time constant τ_{g1} for activation, shown in equation (4.7), is derived by least-squares fitting to kinetic data from Patel et al [10]. Inactivation of Kv2.1/Kv9.3 was faster than Kv2.1 but still relatively slow. The inactivating current is fitted to experimental data from Kerschensteiner et al [118] using a double-exponential model state equations with time constants $\tau_{g_{2_{\text{fast}}}}$ =0.63 s and $\tau_{g_{2_{\text{slow}}}}$ =3.1 s. Figure 4.4 shows the simulated I-V curve for $I_{[\text{Kv9.3}]}$, as well as the channel kinetics and the current traces from simulated voltage-clamp experiments. Current carried by Kv2.1/Kv9.3 is described by the following equation:

$$I_{\text{Kv9.3}} = \kappa_{\text{Kv9.3}}\, G_{\text{Kv9.3}}\, g_1\, (0.7 g_{2_{\text{fast}}} + 0.3 g_{2_{\text{slow}}})\, (V - E_{\text{K}})\,, \tag{4.4}$$

where $G_{\text{Kv9.3}}$ is the unitary conductance of the Kv2.1/Kv9.3 channel, and g_1 and g_2 represent the activation and inactivation gating variables, respectively. The corresponding steady-state activation and inactivation multipliers are $g_{1\infty}$ and $g_{2\infty}$. The equations describing the gating kinetics of this channel are given below and the parameters are stated in Table 4.3.

$$g_{1_\infty} = \frac{1}{1 + \exp\left[\frac{3.2 - V}{21.8}\right]}\,, \tag{4.5}$$

$$g_{2_\infty} = \frac{1}{1 + \exp\left[\frac{44.9+V}{10.4}\right]} , \tag{4.6}$$

$$\tau_{g_1} = \frac{1}{\exp\left[\frac{-80.3-V}{10}\right] + \exp\left[\frac{-137.5+V}{55}\right]} . \tag{4.7}$$

Table 4.3: Notation for the Kv2.1/Kv9.3 potassium channel

Notation	Definition	Value
$G_{\text{Kv9.3}}$	Kv2.1/Kv9.3 conductance	14.5 pS
$\kappa_{\text{Kv9.3}}$	Kv2.1/Kv9.3 channel density	estimated
g_{1_∞}	steady state activation variable	
g_{2_∞}	steady state inactivation variable	
τ_{g_1}	activation time constant in ms	
$\tau_{g_{2_{\text{fast}}}}$	fast inactivation time constant	630 ms
$\tau_{g_{2_{\text{slow}}}}$	slow inactivation time constant	3100 ms
State variables		
g_1	activation gating variable	
$g_{2_{\text{fast}}}$,$g_{2_{\text{slow}}}$	inactivation gating variables	

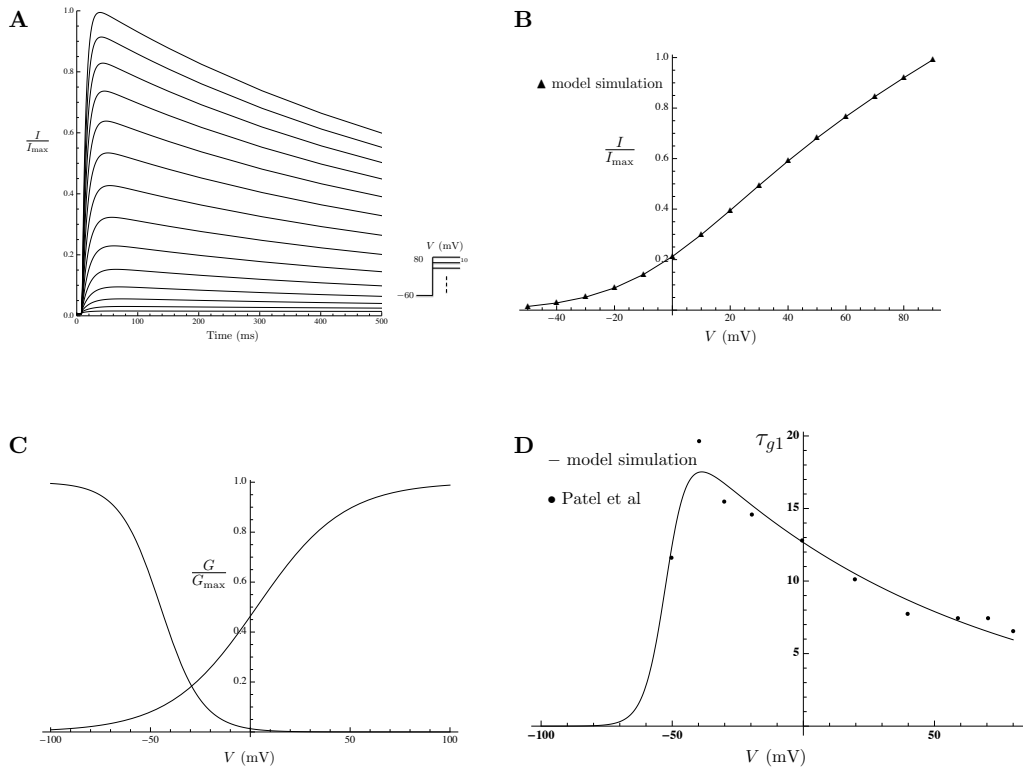

Figure 4.4: Properties of $I_{\mathbf{Kv9.3}}$. (A) Normalised $I_{\mathrm{Kv9.3}}$ current trace generated by the model during simulated voltage-clamp experiments. Currents are recorded during 1 s voltage steps to potentials ranging from −50 to 80 mV from a holding potential of −60 mV. (B) Simulated (solid triangles) peak I-V curve obtained from the series of experiments shown in (A). Values are normalised to the peak current value. (C) Steady state activation and inactivation curves from Patel et al [10]. (D) Simulated activation time constant derived from experimental data (filled circles) from Patel et al [10].

Delayed rectifier, voltage-gated, heteromeric potassium channel Kv2.1/Kv6.1

The channel Kv2.1 can form another heteromeric complex with the electrically silent delayed rectifier Kv6.1 [119]. This complex carries the current $I_{\text{Kv6.1}}$. The gene encoding the Kv6.1 channel, *KCNG1*, was present at the level of mRNA expression in MSMC [8]. Kramer et al [11] co-expressed Kv2.1 with Kv6.1 in *Xenopus* oocytes. Kv6.1 failed to accelerate the inactivation of Kv2.1 at intermediate potentials, had a slowing effect on inactivation at strong depolarisations, and had no effect on cumulative inactivation. Furthermore, Kv6.1 had a strong effect on activation of Kv2.1, shifting the steady-state activation curve towards more negative potentials. The single-channel conductance is not known but we assume it to be similar to the heteromeric channel Kv2.1/Kv5.1 which is about 12.5 pS [11]. The parameter V_{half} for activation is -9.4 mV and the slope is 11.8 mV, while for inactivation, $V_{\text{half}} = -65.9$ mV and $k = -6.4$ mV [11]. Activation and inactivation steady state gating variables are shown in equations (4.9) and (4.10), respectively. Because the presence of Kv6.1 had no significant effect on the activation time constant [11], we assume τ_{l_1} for activation to be the same as the Kv2.1 activation time constant given by Patel et al [10] (equation (4.11)). Figure 4.5 shows the gating kinetics of the channel. Kv2.1/Kv6.1 exhibits extremely slow monoexponential decay current with a voltage-independent time constant $\tau_{l_2} = 32$ s [11], which suggests that the regulatory subunit Kv6.1 virtually abrogates inactivation. The current is described by the following equation:

$$I_{\text{Kv6.1}} = \kappa_{\text{Kv6.1}} G_{\text{Kv6.1}} l_1 \; l_2 (V - E_{\text{K}}) \; , \tag{4.8}$$

where l_1 and l_2 represent the activation and inactivation gating variables, respectively. The corresponding steady-state activation and inactivation gating multipliers are l_{1_∞} and l_{2_∞}. $G_{\text{Kv6.1}}$ is the Kv2.1/Kv6.1 single channel conductance. The equations describing the gating kinetics are as follows:

$$l_{1_\infty} = \frac{1}{1 + \exp\left[\frac{-9.4 - V}{11.8}\right]} \; , \tag{4.9}$$

$$l_{2_\infty} = \frac{1}{1 + \exp\left[\frac{65.9 + V}{6.4}\right]} \; , \tag{4.10}$$

$$\tau_{l_1} = \frac{1}{\exp\left[\frac{-18.2 - V}{2}\right] + \exp\left[\frac{-107 + V}{30}\right]} \; . \tag{4.11}$$

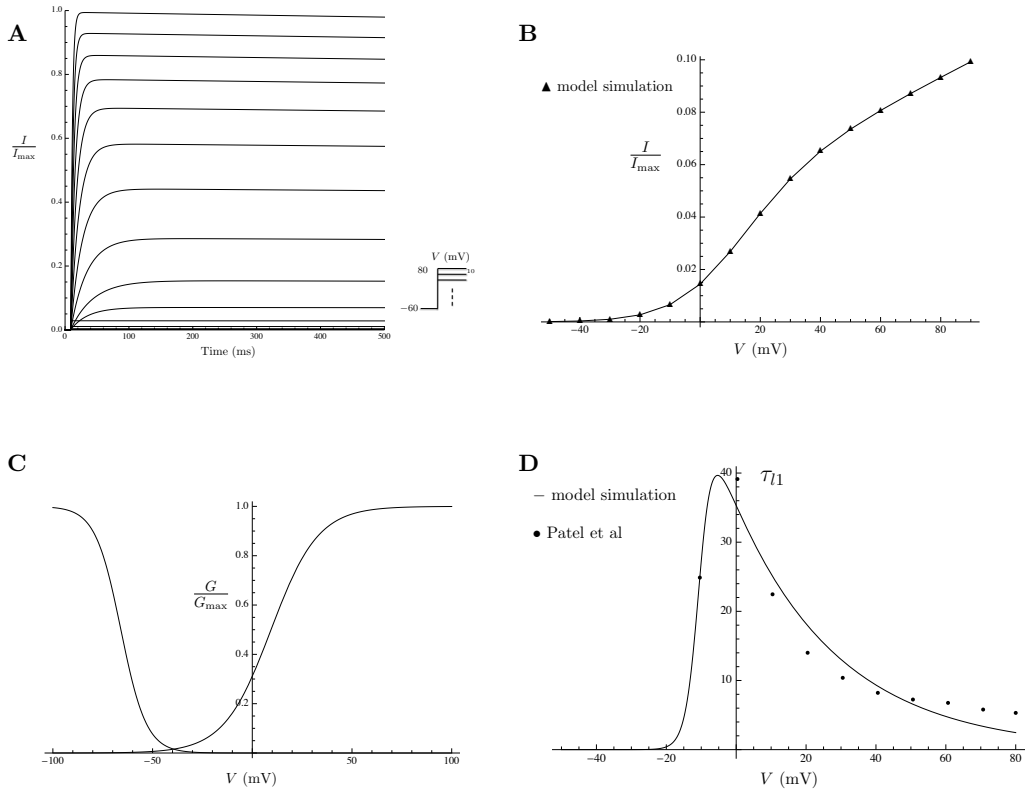

Figure 4.5: Properties of the $I_{\mathbf{Kv6.1}}$. (A) Normalised $I_{\mathrm{Kv6.1}}$ current trace generated by the model during simulated voltage-clamp experiments. Currents are recorded during 1 s voltage steps to potentials ranging from −50 to 80 mV from a holding potential of −60 mV. (B) Simulated (solid triangles) peak *I-V* curve obtained from the series of experiments shown in (A). Values are normalised to the peak current value. Steady state activation and inactivation curves from Kramer et al [11]. (D) Simulated activation time constant derived from experimental data (filled circles) from Patel et al [10].

Table 4.4: Notation for the Kv2.1/Kv6.1 potassium channel

Notation	Definition	Value and units
$G_{\text{Kv6.1}}$	Kv2.1/Kv6.1 conductance	12.5 pS
$\kappa_{\text{Kv6.1}}$	Kv2.1/Kv6.1 channel density	estimated
l_{1_∞}	steady state activation variable	
l_{2_∞}	steady state inactivation variable	
τ_{l_1}	activation time constant in ms	
τ_{l_2}	inactivation time constant	32 s
State Variables		
l_1	activation gating variable	
l_2	inactivation gating variable	

A-type, voltage-gated potassium channel Kv3.4

The current $I_{\text{Kv3.4}}$ is carried by the channel expressed by the *KCNC4* gene. This is an A-type fast inactivating potassium channel; it produces a transient outward current and operates in the subthreshold range of the AP. Current starts activating at high voltages, around -10 mV, rises fast, then quickly inactivates. This rapid inactivation is due to the specialised N-terminus that closes the channel from the intracellular side (discussed above). Rudy et al [12] demonstrated an A-current in *Xenopus* oocytes when co-expressed with human potassium shaker channel HKShIIIC ($\equiv$ Kv3.4). The activation and inactivation gating variables are a_1 and a_2 and the corresponding steady-state activation and inactivation variables $a_{1\infty}$ and $a_{2\infty}$ (described by equations (4.13) and (4.14), respectively). From Rudy et al [12], for activation, V_{half} is 19.1 mV and the slope is 11.3 mV, while for inactivation $V_{\text{half}} = -15$ mV and $k = -7.4$ mV. The function, described by equation (4.15), is chosen for the activation time constants τ_{a_1} to fit the equation $t_p = \tau_{a_1} \ln(1 + n\tau_{a_2}/\tau_{a_1})$ [120] to time-to-peak experimental data from Rudy et al [12], where n is the order of the activation kinetics (here $n = 1$). For inactivation, τ_{a_2} (equation (4.16)) is selected to fit experimental data by Rudy et al [12]. The current formulation and the equations describing the gating kinetics are as follows:

$$I_{\text{Kv3.4}} = \kappa_{\text{Kv3.4}}\, G_{\text{Kv3.4}}\, a_1\, a_2\, (V - E_{\text{K}})\,, \tag{4.12}$$

$$a_{1\infty} = \frac{1}{1 + \exp\left[\frac{19.1 - V}{11.3}\right]}\,, \tag{4.13}$$

$$a_{2\infty} = \frac{1}{1 + \exp\left[\frac{15 + V}{7.4}\right]}\,, \tag{4.14}$$

$$\tau_{a_1} = 40 - \frac{37.7}{1 + \exp\left[-V/28\right]}\,, \tag{4.15}$$

$$\tau_{a_2} = 12 + 165.6\, \exp\left[-V/11.2\right]\,. \tag{4.16}$$

Figure 4.6 shows the activation and inactivation kinetics and the definitions of the parameters and their values are stated in Table 4.5.

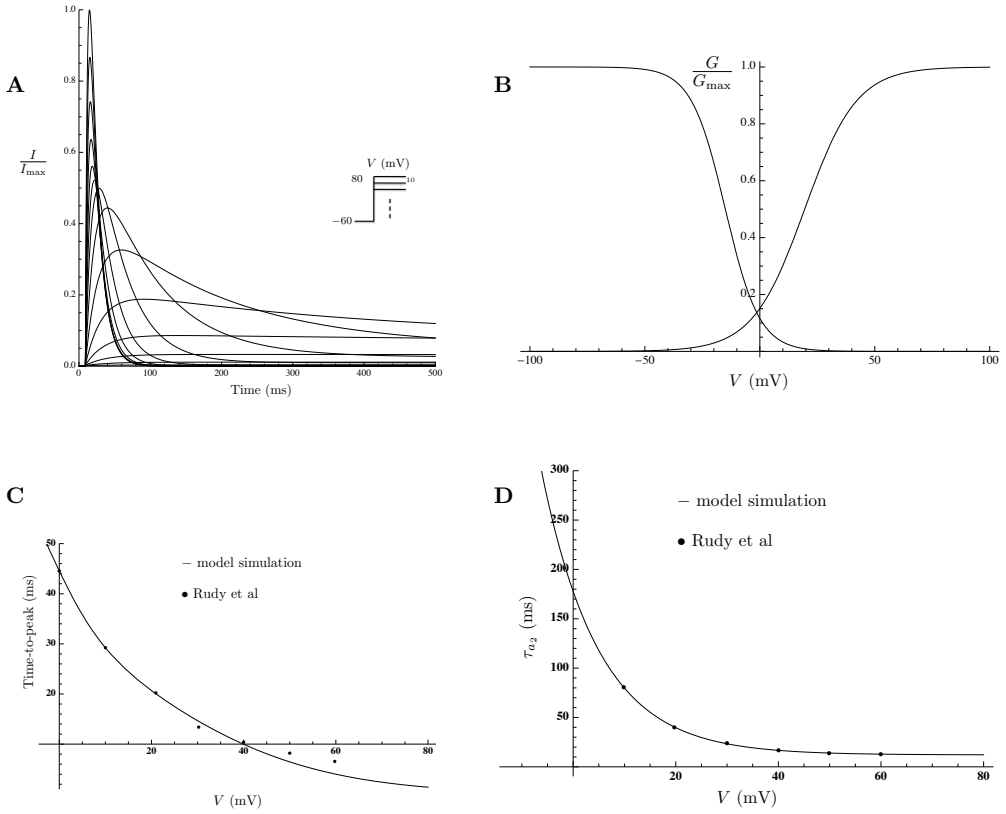

Figure 4.6: Properties of the $I_{\mathbf{Kv3.4}}$. (A) Normalised $I_{\mathrm{Kv3.4}}$ current trace generated by the model during simulated voltage-clamp experiments. Currents are recorded during 1 s voltage steps to potentials ranging from −50 to 80 mV from a holding potential of −60 mV. (B) Steady state activation and inactivation curves from Rudy et al [12] (C) Simulated time-to-peak derived from data (bullets) from Rudy et al [12]. (D) Simulated inactivation time constant derived from experimental data (bullets) from Rudy et al [12].

Table 4.5: Notation for the Kv3.4 potassium channel

Notation	Definition	Value
$G_{\text{Kv3.4}}$	Kv3.4 conductance	14 pS
$\kappa_{\text{Kv3.4}}$	Kv3.4 channel density	estimated
a_{1_∞}	steady state activation variable	
a_{2_∞}	steady state inactivation variable	
τ_{a_1}	activation time constant in	
τ_{a_2}	fast inactivation time constant in ms	
State Variables		
a_1	activation gating variable	
a_2	inactivation gating variable	

A-type, voltage-gated potassium channel Kv4.1

Another transient A-type potassium current is $I_{\mathrm{Kv4.1}}$. It is carried by the Kv4.1 channel, which is expressed in myometrial cells according to the mRNA data [8,90]. The gene expressing the channel is the *KCND1* gene. Jerng et al [13] modelled activation as fourth-order Boltzmann function. We derive the activation time constant τ_{b_1}, equation (4.20), from the time-to-peak data of Nakamura et al [14] in a manner similar to the derivation of τ_{a_1} (for the Kv3.4 channel) with $n = 4$. Inactivation follows a more complex time course that could be described by the sum of three exponential terms. The corresponding time constants $\tau_{\mathrm{fast}b_2}$, $\tau_{\mathrm{inter}b_2}$, and $\tau_{\mathrm{slow}b_2}$, representing fast, intermediate and slow kinetics, respectively, were obtained by fitting the sum of the three terms to the decay phase of the current [13]. We assume that the corresponding relative magnitudes to be time- and voltage-independent and equal to 18%, 42%, and 40% (they are slightly voltage-dependent according to Jerng et al [13]). The intermediate and slow components account for the recovery from inactivation, which determines the interspike interval during repetitive firing. We fit the inactivation exponential functions, shown in equations (4.21), (4.22), and (4.23), to data from Jerng et al [13]. The current is described as follows:

$$I_{\mathrm{Kv4.1}} = \kappa_{\mathrm{Kv4.1}}\, G_{\mathrm{Kv4.1}}\, {b_1}^4\, (0.18\, b_{2_{\mathrm{fast}}} + 0.42\, b_{2_{\mathrm{Inter}}} + 0.4\, b_{2_{\mathrm{Slow}}})\, (V - E_{\mathrm{K}})\ , \quad (4.17)$$

where b_1 and b_2 represent the activation and inactivation gating variables with corresponding steady-state activation and inactivation multipliers $b_{1\infty}$ and $b_{2\infty}$. For activation, $V_{\mathrm{half}} = -\ 49$ mV and $k = 22.3$ mV, whereas for inactivation $V_{\mathrm{half}} = -\ 69$ mV and $k = -\ 5$ mV. The properties of the Kv4.1 channel are summarised in Figure 4.7. The Kv4.1 kinetics is described by the following equations:

$$b_{1\infty} = \frac{1}{1 + \exp\left[\frac{-49-V}{22.3}\right]}\ , \quad (4.18)$$

$$b_{2\infty} = \frac{1}{1 + \exp\left[\frac{69+V}{5}\right]}\ , \quad (4.19)$$

$$\tau_{b_1} = 1.96 + \frac{5.5}{1 + \exp\left[V/12.5\right]}\ , \quad (4.20)$$

$$\tau_{b_{2_{\mathrm{fast}}}} = 16 + 11.4 \exp\left[-V/15.9\right]\ , \quad (4.21)$$

$$\tau_{b_{2_{\mathrm{inter}}}} = 73.6 + 18 \exp\left[-V/19\right]\ , \quad (4.22)$$

$$\tau_{b_{2_{\mathrm{slow}}}} = 252.2 + 0.74V\ . \quad (4.23)$$

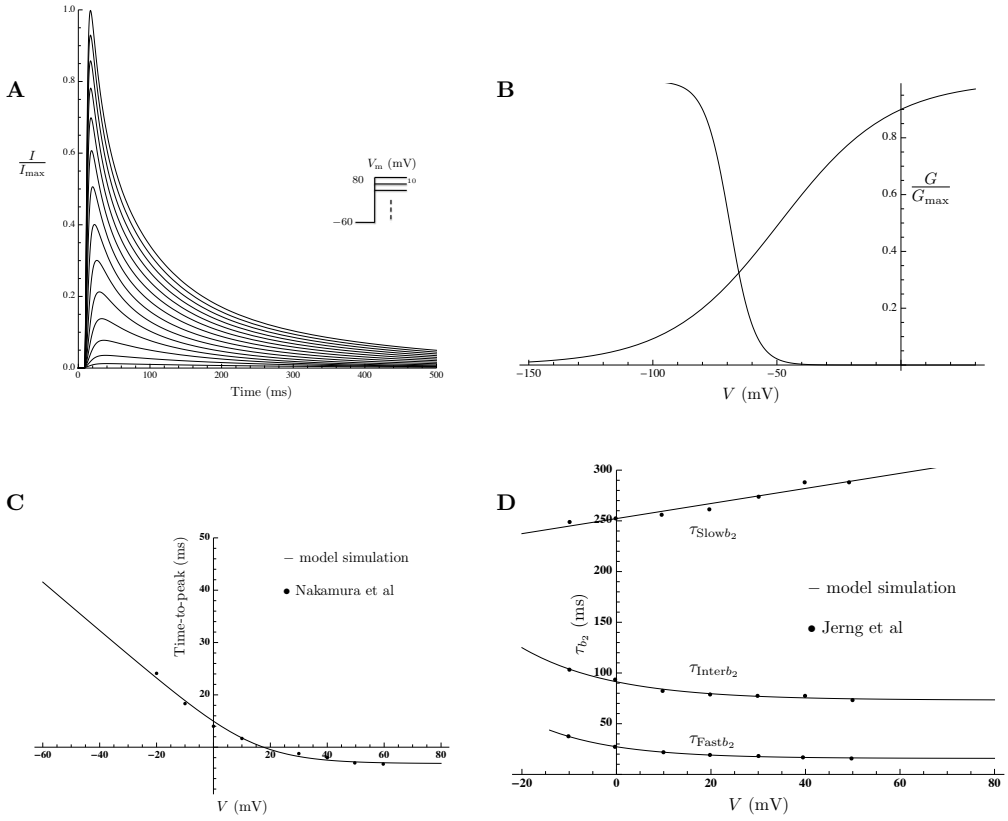

Figure 4.7: Properties of $I_{\mathbf{Kv4.1}}$. (A) Normalised $I_{\mathrm{Kv4.1}}$ current trace generated by the model during simulated voltage-clamp experiments. Currents are recorded during 1 s voltage steps to potentials ranging from −50 to 80 mV from a holding potential of −60 mV. (B) Steady state activation and inactivation curves from Jerng et al [13]. (C) Simulated time-to-peak derived from data (filled circles) from Nakamura et al [14]. (D) Simulated inactivation time constants derived from experimental data (filled circles) from Jerng et al [13].

Parameters and their values are stated in Table 4.6.

Table 4.6: Notation for the Kv4.1 potassium channel

Notation	Definition	Value and units
$G_{\text{Kv4.1}}$	Kv4.1 conductance	5 pS
$\kappa_{\text{Kv4.1}}$	Kv4.1 channel density	estimated
b_{1_∞}	steady state activation variable	
b_{2_∞}	steady state inactivation variable	
τ_{b_1}	activation time constant in ms	
$\tau_{b_{2_{\text{fast}}}}$	fast inactivation time constant in ms	
$\tau_{b_{2_{\text{inter}}}}$	intermediate inactivation time constant in ms	
$\tau_{b_{2_{\text{slow}}}}$	slow inactivation time constant in ms	
State Variables		
b_1	activation gating variable	
$b_{2_{\text{fast}}}$,$b_{2_{\text{inter}}}$,$b_{2_{\text{slow}}}$	inactivation gating variables	

A-type, voltage-gated potassium channel Kv4.2

The Kv4.2 channel conducts another transient outward potassium current. The gene encoding this channel is the *KCND2* gene. The gene encoding for the Kv4.2 was not found at transcript level when using mRNA-seq [8]. In contrast, using LCM in combination with qRT-PCR, Kv4.2 was expressed at relatively high density and changes significantly during gestation: ΔCT=19.57$\pm$0.1 (normalised to r18s mRNA) in samples taken from non-pregnant patients and ΔCT=21$\pm$0.13 in samples taken from pregnant patients [90]. Accordingly, we have modelled the Kv4.2 as follows. The activation variable could be described by a fourth-order Boltzmann function with $V_{\text{half}} = -38.2$ mV and k =20.6 mV, and similarly inactivation could be represented as a three-component inactivation gate with $V_{\text{half}} = -57.4$ mV and $k = -5$ mV [15], as with the Kv4.1 inactivation. However, we chose instead to model the Kv4.2 channel with the detailed Markov model, shown in Figure 4.9, from Bahring et al [15], because this allows for an accurate representation of different inactivation pathways, such as inactivation that originate from the open state or from any of the closed states. In the Markov model the channel conducts ions only when it occupies the open state and therefore the current is described as follows:

$$I_{\text{Kv4.2}} = \kappa_{\text{Kv4.2}}\, G_{\text{Kv4.2}}\, O^{[\text{Kv4.2}]}\, (V - E_{\text{K}})\,, \tag{4.24}$$

where $O^{[\text{Kv4.2}]}$ is the probability of the channel being in the open state. As shown in Figure 4.8, the transitions (in s^{-1}) along the activation pathway from the resting state to the final pre-open closed state are voltage-dependent and of the form:

$$\begin{aligned} \alpha^{[\text{Kv42}]} &= 133 \exp\left[\frac{VF}{RT}\right]\,, \\ \beta^{[\text{Kv42}]} &= 4 \exp\left[-1.54\frac{VF}{RT}\right]\,. \end{aligned} \tag{4.25}$$

The values of voltage-independent transition rates are shown in Table 4.7. We derive the differential equations describing the behaviour of the Kv4.2 channel according

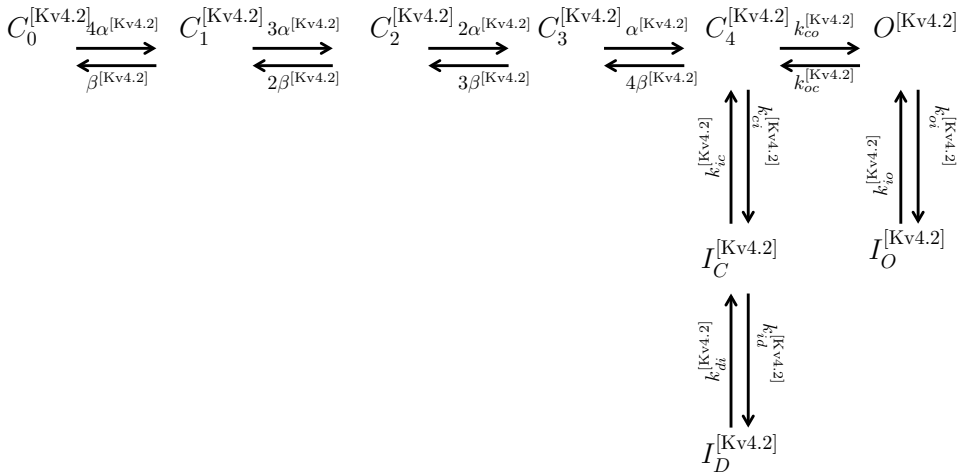

Figure 4.8: State transition diagram of the Markov model for the Kv4.2 channel. The simulation includes inactivation both from a closed state ($C_4^{[\mathrm{Kv4.2}]} \rightarrow I_C^{[\mathrm{Kv4.2}]}$) and from open state ($O^{[\mathrm{Kv4.2}]} \rightarrow I_O^{[\mathrm{Kv4.2}]}$). The closed-state also accesses a deeper inactivated state ($I_D^{[\mathrm{Kv4.2}]}$) [15]. The transition rates between the states are given in Table 4.7 and equations (4.25).

to the Markov model shown in Figure 4.8 as follows:

$$
\begin{aligned}
\frac{dC_0^{[\mathrm{kv4.2}]}}{dt} &= \beta^{[\mathrm{Kv4.2}]} C_1^{[\mathrm{Kv4.2}]} - 4\alpha^{[\mathrm{Kv4.2}]} C_0^{[\mathrm{Kv4.2}]} \,, \\
\frac{dC_1^{[\mathrm{Kv4.2}]}}{dt} &= 4\alpha^{[\mathrm{Kv4.2}]} C_0^{[\mathrm{Kv4.2}]} - \beta^{[\mathrm{Kv4.2}]} C_1^{[\mathrm{Kv4.2}]} + 2\beta^{[\mathrm{Kv4.2}]} C_2^{[\mathrm{Kv4.2}]} - 3\alpha^{[\mathrm{Kv4.2}]} C_1^{[\mathrm{Kv4.2}]} \,, \\
\frac{dC_2^{[\mathrm{Kv4.2}]}}{dt} &= 3\alpha^{[\mathrm{Kv4.2}]} C_1^{[\mathrm{Kv4.2}]} - 2\beta^{[\mathrm{Kv4.2}]} C_2^{[\mathrm{Kv4.2}]} + 3\beta^{[\mathrm{Kv4.2}]} C_3^{[\mathrm{Kv4.2}]} - 2\alpha^{[\mathrm{Kv4.2}]} C_2^{[\mathrm{Kv4.2}]} \,, \\
\frac{dC_3^{[\mathrm{Kv4.2}]}}{dt} &= 2\alpha^{[\mathrm{Kv4.2}]} C_2^{[\mathrm{Kv4.2}]} - 3\beta^{[\mathrm{Kv4.2}]} C_3^{[\mathrm{Kv4.2}]} + 4\beta^{[\mathrm{Kv4.2}]} C_4^{[\mathrm{Kv4.2}]} - \alpha^{[\mathrm{Kv4.2}]} C_3^{[\mathrm{Kv4.2}]} \,, \\
\frac{dC_4^{[\mathrm{Kv4.2}]}}{dt} &= \alpha^{[\mathrm{Kv4.2}]} C_3^{[\mathrm{Kv4.2}]} - 4\beta^{[\mathrm{Kv4.2}]} C_4^{[\mathrm{Kv4.2}]} \\
&\quad + k_{oc}^{[\mathrm{Kv4.2}]} O^{[\mathrm{Kv4.2}]} - k_{co}^{[\mathrm{Kv4.2}]} C_4^{[\mathrm{Kv4.2}]} + k_{ci}^{[\mathrm{Kv4.2}]} I_C^{[\mathrm{Kv4.2}]} - k_{ci}^{[\mathrm{Kv4.2}]} C_4^{[\mathrm{Kv4.2}]} \,, \\
\frac{dO^{[\mathrm{Kv4.2}]}}{dt} &= k_{co}^{[\mathrm{Kv4.2}]} C_4^{[\mathrm{Kv4.2}]} - k_{oc}^{[\mathrm{Kv4.2}]} O^{[\mathrm{Kv4.2}]} + k_{io}^{[\mathrm{Kv4.2}]} I_O^{[\mathrm{Kv4.2}]} - k_{oi}^{[\mathrm{Kv4.2}]} O^{[\mathrm{Kv4.2}]} \,, \\
\frac{dI_C^{[\mathrm{Kv4.2}]}}{dt} &= k_{ci}^{[\mathrm{Kv4.2}]} C_4^{[\mathrm{Kv4.2}]} - k_{ic}^{[\mathrm{Kv4.2}]} I_C^{[\mathrm{Kv4.2}]} + k_{di}^{[\mathrm{Kv4.2}]} I_D^{[\mathrm{Kv4.2}]} - k_{id}^{[\mathrm{Kv4.2}]} I_C^{[\mathrm{Kv4.2}]} \,, \\
\frac{dI_D^{[\mathrm{Kv4.2}]}}{dt} &= k_{id}^{[\mathrm{Kv4.2}]} I_C^{[\mathrm{Kv4.2}]} - k_{di}^{[\mathrm{Kv4.2}]} I_D^{[\mathrm{Kv4.2}]} \,, \\
\frac{dI_O^{[\mathrm{Kv4.2}]}}{dt} &= k_{oi}^{[\mathrm{Kv4.2}]} O^{[\mathrm{Kv4.2}]} - k_{io}^{[\mathrm{Kv4.2}]} I_O^{[\mathrm{Kv4.2}]} \,.
\end{aligned}
\tag{4.26}
$$

The simulated Kv4.2 current trace and peak I-V curve are shown in Figure 4.9; the parameters, their descriptions and values are stated in Table 4.7.

Table 4.7: Notation for the Kv4.2 potassium channel

Notation	Definition	Value
$G_{\text{Kv4.2}}$	Kv4.2 unitary conductance	5 pS
$\kappa_{\text{Kv4.2}}$	Kv4.2 channel density	–
$k_{co}^{[\text{Kv4.2}]}$	Rate constant for channel opening	400 s^{-1}
$k_{oc}^{[\text{Kv4.2}]}$	Rate constant for channel closing	1100 s^{-1}
$k_{oi}^{[\text{Kv4.2}]}$	Rate constant for open state inactivation	100 s^{-1}
$k_{io}^{[\text{Kv4.2}]}$	Rate constant for open state inactivation	10 s^{-1}
$k_{ci}^{[\text{Kv4.2}]}$	Rate constant for closed state inactivation	30 s^{-1}
$k_{ic}^{[\text{Kv4.2}]}$	Rate constant for closed state inactivation	5 s^{-1}
$k_{id}^{[\text{Kv4.2}]}$	Rate constant for trapping in the deep inactivation	8 s^{-1}
$k_{di}^{[\text{Kv4.2}]}$	Rate constant for trapping in the deep inactivation	0.5 s^{-1}
States Variables		
$C_0^{[\text{Kv4.2}]} - C_4^{[\text{Kv4.2}]}$	Closed states	
$O^{[\text{Kv4.2}]}$	Open state	
$I_C^{[\text{Kv4.2}]}$, $I_O^{[\text{Kv4.2}]}$, $I_D^{[\text{Kv4.2}]}$	Inactivation states	

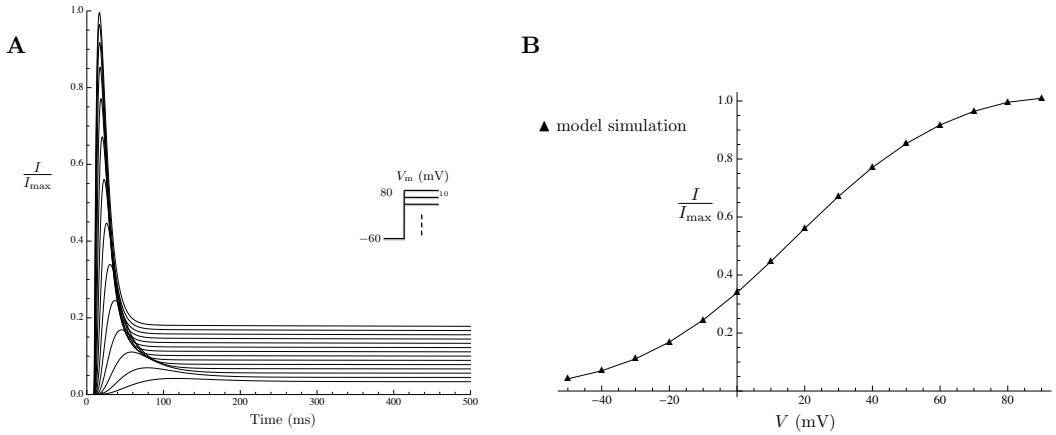

Figure 4.9: Properties of the $I_{\mathbf{Kv4.2}}$. (A) Normalised $I_{\mathrm{Kv4.2}}$ current trace generated by the model during simulated voltage-clamp experiments. Currents are recorded during 1 s voltage steps to potentials ranging from −50 to 80 mV from a holding potential of −60 mV. (B) Simulated (solid triangles) peak I-V curve obtained from the series of experiments shown in (A). Values are normalised to the peak current values.

A-type, voltage-gated potassium channel Kv4.3

Voltage-gated potassium current is carried by the channel encoded by the *KCND3* gene, or Kv4.3 channel. This channel is an A-type potassium channel exhibiting a transient outward current, fast activation, and inactivation. Similar to Kv4.2, Kv4.3 is expressed at high density at the transcriptional level [8, 90] and changes significantly during gestation: ΔCT=18.11$\pm$0.09 (normalised to r18s mRNA) in samples taken from non-pregnant patients and ΔCT=17.88$\pm$0.1 in samples taken from pregnant patients [90]. According to Patel et al [108], $V_{\text{half}} = -7.9$ mV and k =12.34 mV for activation and $V_{\text{half}} = -68.9$ mV and $k = -6.31$ mV for inactivation. Inactivation of the Kv4.3 is a complex process that can occur from both closed and open states [108, 121]. Beck et al [107] expressed Kv4.3 in *Xenopus* oocytes and modelled the changes in its kinetics using the allosteric model shown in Figure 4.10. The simulated Kv4.3 current trace and peak I-V relationships are shown in Figure 4.11. The current is described by:

$$I_{\text{Kv4.3}} = \kappa_{\text{Kv4.3}}\, G_{\text{Kv4.3}}\, O^{[\text{Kv4.3}]}\, (V - E_{\text{K}})\,, \tag{4.27}$$

where $O^{[\text{Kv4.3}]}$ is the probability of being in the open state of the Kv4.3 channel.

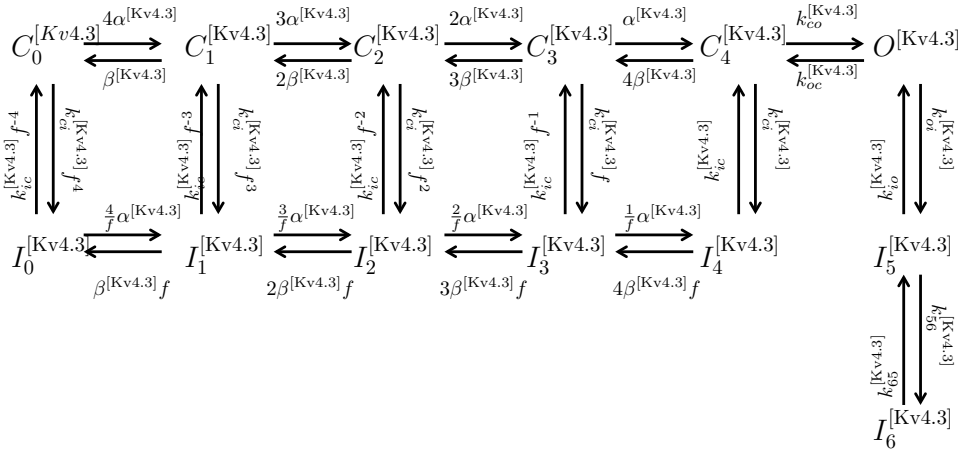

Figure 4.10: State transition diagram of the Markov model for the Kv4.3 channel. $C_0^{[\text{Kv4.3}]}$ – $C_4^{[\text{Kv4.3}]}$ are closed states; $O^{[\text{Kv4.3}]}$ is the open state and $I_0^{[\text{Kv4.3}]}$ – $I_6^{[\text{Kv4.3}]}$ are the inactivation states. $\alpha^{[\text{Kv4.3}]}$, $\beta^{[\text{Kv4.3}]}$, $k_{ci}^{[\text{Kv4.3}]}$, $k_{ic}^{[\text{Kv4.3}]}$, $k_{oc}^{[\text{Kv4.3}]}$, $k_{co}^{[\text{Kv4.3}]}$, $k_{56}^{[\text{Kv4.3}]}$ and $k_{65}^{[\text{Kv4.3}]}$ are the transition rates between the states as given in Table 4.8 and equations (4.28).

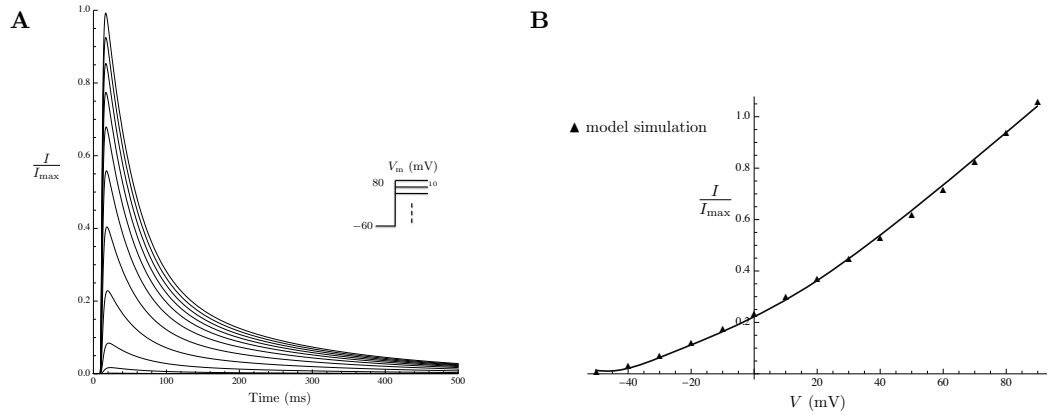

Figure 4.11: Properties of the $I_{\mathbf{Kv4.3}}$. (A) Normalised $I_{\mathrm{Kv4.3}}$ current trace generated by the model during simulated voltage-clamp experiments. Currents are recorded during 1 s voltage steps to potentials ranging from −50 to 80 mV from a holding potential of −60 mV. (B) Simulated (solid triangles) peak I-V curve obtained from the series of experiments shown in (A). Values are normalised to the peak current value.

The voltage-dependent rates (in s^{-1}) are as follows:

$$\begin{aligned}
\alpha^{[\mathrm{Kv4.3}]} &= 12\exp\left[0.77\frac{VF}{RT}\right] , \\
\beta^{[\mathrm{Kv4.3}]} &= 42\exp\left[-0.54\frac{VF}{RT}\right] , \\
k_{co}^{[\mathrm{Kv4.3}]} &= 100\exp\left[0.25\frac{VF}{RT}\right] , \\
k_{oc}^{[\mathrm{Kv4.3}]} &= 300\exp\left[-0.05\frac{VF}{RT}\right] .
\end{aligned} \tag{4.28}$$

The values of the voltage-independent rates are in Table 4.8. We describe the Kv4.3 kinetics by the following system of ODEs based on the model proposed by Beck et al [107]:

$$
\begin{aligned}
\frac{dC_0^{[\mathrm{Kv4.3}]}}{dt} &= 1-(O^{[\mathrm{Kv4.3}]}+\sum_{i=1}^{4}C_i^{[\mathrm{Kv4.3}]}+\sum_{i=0}^{6}I_i^{[\mathrm{Kv4.3}]}) \ , \\
\frac{dC_1^{[\mathrm{Kv4.3}]}}{dt} &= 4\alpha^{[\mathrm{Kv4.3}]}C_0^{[\mathrm{Kv4.3}]}-(\beta^{[\mathrm{Kv4.3}]}+3\alpha^{[\mathrm{Kv4.3}]}+k_{ci}^{[\mathrm{Kv4.3}]}f^3)C_1^{[\mathrm{Kv4.3}]} \\
&\quad +2\beta^{[\mathrm{Kv4.3}]}C_2^{[\mathrm{Kv4.3}]}+\frac{k_{ic}^{[\mathrm{Kv4.3}]}}{f^3}I_1^{[\mathrm{Kv4.3}]} \ , \\
\frac{dC_2^{[\mathrm{Kv4.3}]}}{dt} &= 3\alpha^{[\mathrm{Kv4.3}]}C_1^{[\mathrm{Kv4.3}]}-(2\beta^{[\mathrm{Kv4.3}]}+2\alpha^{[\mathrm{Kv4.3}]}+k_{ci}^{[\mathrm{Kv4.3}]}f^2)C_2^{[\mathrm{Kv4.3}]} \\
&\quad +3\beta^{[\mathrm{Kv4.3}]}C_3^{[\mathrm{Kv4.3}]}+\frac{k_{ic}^{[\mathrm{Kv4.3}]}}{f^2}I_2^{[\mathrm{Kv4.3}]} \ , \\
\frac{dC_3^{[\mathrm{Kv4.3}]}}{dt} &= 2\alpha^{[\mathrm{Kv4.3}]}C_2^{[\mathrm{Kv4.3}]}-(3\beta^{[\mathrm{Kv4.3}]}+\alpha^{[\mathrm{Kv4.3}]}+k_{ci}^{[\mathrm{Kv4.3}]}f)C_3^{[\mathrm{Kv4.3}]} \\
&\quad +4\beta^{[\mathrm{Kv4.3}]}C_4^{[\mathrm{Kv4.3}]}+\frac{k_{ic}^{[\mathrm{Kv4.3}]}}{f}I_3^{[\mathrm{Kv4.3}]} \ , \\
\frac{dC_4^{[\mathrm{Kv4.3}]}}{dt} &= \alpha^{[\mathrm{Kv4.3}]}C_3^{[\mathrm{Kv4.3}]}-(4\beta^{[\mathrm{Kv4.3}]}+k_o^{[\mathrm{Kv4.3}]}+k_{ci}^{[\mathrm{Kv4.3}]})C_4^{[\mathrm{Kv4.3}]} \\
&\quad +k_{-o}^{[\mathrm{Kv4.3}]}O_4^{[\mathrm{Kv4.3}]}+k_{ic}^{[\mathrm{Kv4.3}]}I_4^{[\mathrm{Kv4.3}]} \ , \\
\frac{dI_0^{[\mathrm{Kv4.3}]}}{dt} &= k_1^{[\mathrm{Kv4.3}]}f^4C_0^{[\mathrm{Kv4.3}]}-(\frac{k_{-1}^{[\mathrm{Kv4.3}]}}{f^4}+4\frac{\alpha^{[\mathrm{Kv4.3}]}}{f})I_0^{[\mathrm{Kv4.3}]}+\beta^{[\mathrm{Kv4.3}]}fI_1^{[\mathrm{Kv4.3}]} \ , \\
\frac{dI_1^{[\mathrm{Kv4.3}]}}{dt} &= 4\frac{\alpha^{[\mathrm{Kv4.3}]}}{f}I_0^{[\mathrm{Kv4.3}]}+k_1^{[\mathrm{Kv4.3}]}f^3C_1^{[\mathrm{Kv4.3}]}-(f\beta^{[\mathrm{Kv4.3}]}+\frac{k_{ic}^{[\mathrm{Kv4.3}]}}{f^3} \\
&\quad +3\frac{\alpha^{[\mathrm{Kv4.3}]}}{f})I_1^{[\mathrm{Kv4.3}]}+2\beta^{[\mathrm{Kv4.3}]}fI_2^{[\mathrm{Kv4.3}]} \ , \\
\frac{dI_2^{[\mathrm{Kv4.3}]}}{dt} &= 3\frac{\alpha^{[\mathrm{Kv4.3}]}}{f}I_1^{[\mathrm{Kv4.3}]}+k_1^{[\mathrm{Kv4.3}]}f^2C_2^{[\mathrm{Kv4.3}]}-(2f\beta^{[\mathrm{Kv4.3}]}+\frac{k_{ic}^{[\mathrm{Kv4.3}]}}{f^2} \\
&\quad +2\frac{\alpha^{[\mathrm{Kv4.3}]}}{f})I_2^{[\mathrm{Kv4.3}]}+3\beta^{[\mathrm{Kv4.3}]}fI_3^{[Kv43]} \ , \\
\frac{dI_3^{[\mathrm{Kv4.3}]}}{dt} &= 2\frac{\alpha^{[\mathrm{Kv4.3}]}}{f}I_2^{[\mathrm{Kv4.3}]}+k_1^{[\mathrm{Kv4.3}]}fC_3^{[\mathrm{Kv4.3}]}-(3f\beta^{[\mathrm{Kv4.3}]}+\frac{k_{ic}^{[\mathrm{Kv4.3}]}}{f} \\
&\quad +\frac{\alpha^{[\mathrm{Kv4.3}]}}{f})I_3^{[\mathrm{Kv4.3}]}+4\beta^{[\mathrm{Kv4.3}]}fI_4^{[Kv43]} \ , \\
\frac{dI_4^{[\mathrm{Kv4.3}]}}{dt} &= \frac{\alpha^{[\mathrm{Kv4.3}]}}{f}I_3^{[\mathrm{Kv4.3}]}+k_{ci}^{[\mathrm{Kv4.3}]}C_4^{[\mathrm{Kv4.3}]}-(4f\beta^{[\mathrm{Kv4.3}]}+k_{ic}^{[\mathrm{Kv4.3}]})I_4^{[\mathrm{Kv4.3}]} \ , \\
\frac{dI_5^{[\mathrm{Kv4.3}]}}{dt} &= -(k_{io}^{[\mathrm{Kv4.3}]}+k_{56}^{[\mathrm{Kv4.3}]})I_5^{[\mathrm{Kv4.3}]}+k_{io}^{[\mathrm{Kv4.3}]}O^{[\mathrm{Kv4.3}]} \\
&\quad +k_{65}^{[\mathrm{Kv4.3}]}I_6^{[\mathrm{Kv4.3}]} \ , \\
\frac{dI_6^{[\mathrm{Kv4.3}]}}{dt} &= k_{56}^{[\mathrm{Kv4.3}]}I_5^{[\mathrm{Kv4.3}]}-k_{65}^{[\mathrm{Kv4.3}]}I_6^{[\mathrm{Kv4.3}]} \ , \\
\frac{dO^{[\mathrm{Kv4.3}]}}{dt} &= k_{co}^{[\mathrm{Kv4.3}]}C_4^{[\mathrm{Kv4.3}]}-(k_{oc}^{[\mathrm{Kv4.3}]}+k_{oi}^{[\mathrm{Kv4.3}]})O^{[\mathrm{Kv4.3}]}+k_{io}^{[\mathrm{Kv4.3}]}I_5^{[\mathrm{Kv4.3}]} \ .
\end{aligned}
\tag{4.29}
$$

Table 4.8: Notation for the Kv4.3 Potassium Channel

Notation	Definition	Value
$G_{\text{Kv4.3}}$	Kv4.3 unitary conductance	5 pS
$\kappa_{\text{Kv4.3}}$	Kv4.3 channel density	–
$k_{io}^{[\text{Kv4.3}]}$	Rate constant for open state inactivation	8 s^{-1}
$k_{oi}^{[\text{Kv4.3}]}$	Rate constant for open state inactivation	60 s^{-1}
$k_{ci}^{[\text{Kv4.3}]}$	Rate constant for closed state inactivation	7 s^{-1}
$k_{ic}^{[\text{Kv4.3}]}$	Rate constant for closed state inactivation	0.08 s^{-1}
$k_{56}^{[\text{Kv4.3}]}$		5 s^{-1}
$k_{65}^{[\text{Kv4.3}]}$		4 s^{-1}
State variables		
$C_0^{[\text{Kv4.3}]} - C_4^{[\text{Kv4.3}]}$	Closed states	
$O^{[\text{Kv4.3}]}$	Open state	
$I_0^{[\text{Kv4.3}]} - I_6^{[\text{Kv4.3}]}$	Inactivation states	

Heteromeric potassium channel Kv4.2/Kv4.3

A current is carried by the heteromeric assembly of the Kv4.2 subunit with the Kv4.3 subunit. According to Guo et al [122], coexpression of Kv4.2 and Kv4.3 in HEK-293 cells produced transient outward potassium current with properties distinct from the expression of each of the homomeric expressed alone. The gating properties of the heteromeric Kv4.2/Kv4.3 channel are more similar to the properties of the native transient current than are the properties of the homomeric Kv4.2 or Kv4.3. Due to lack of experimental data, activation kinetics is assumed similar to the Kv4.3 kinetics of Patel et al [108] with $V_{\text{half}} = -7.9$ mV and k =12.34 mV (equation (4.31)). We derive the activation time constant τ_{h_1}, equation (4.33), from the Kv4.2 time-to-peak data of Nakamura et al [14] in a manner similar to the derivation of τ_{a_1} (for the Kv3.4 channel) with $n = 4$. Inactivation, on the other hand, was studied by Guo et al [122]: these authors found $V_{\text{half}} = -28.2$ mV and $k = -10.4$ mV, shown in equation (4.32), and an almost invariant (voltage-independent) time constant of 67 ms. The current is described as follows:

$$I_{\text{Kv4.2/Kv4.3}} = \kappa_{\text{Kv4.2/Kv4.3}}\, G_{\text{Kv4.2/Kv4.3}}\, h_1\, h_2\, (V - E_{\text{K}})\,, \tag{4.30}$$

where h_1 and h_2 represent the activation and inactivation gating variables of the Kv4.2/Kv4.3 channel, with corresponding steady-state activation and inactivation $h_{1\infty}$ and $h_{2\infty}$. The equations describing the kinetics are as follows:

$$h_{1\infty} = \frac{1}{1 + \exp\left[\frac{-7.9 - V}{12.34}\right]}\,, \tag{4.31}$$

$$h_{2\infty} = \frac{1}{1 + \exp\left[\frac{28.2 + V}{10.4}\right]}\,, \tag{4.32}$$

$$\tau_{h_1} = 1.12 + \frac{2.12}{1 + \exp\left[V/16.7\right]}\,. \tag{4.33}$$

The definitions of the parameters and their values are shown in Table 4.9.

Table 4.9: Notation for the Kv4.2/Kv4.3 potassium channel

Notation	Definition	Value
$G_{\text{Kv4.2/Kv4.3}}$	Kv4.2/Kv4.3 unitary conductance	10 pS
$\kappa_{\text{Kv4.2/Kv4.3}}$	Kv4.2/Kv4.3 channel density	–
h_{1_∞}	Steady state activation variable	
h_{2_∞}	Steady state inactivation variable	
τ_{h_1}	Activation time constant in ms	
τ_{h_2}	Fast inactivation time constant	67 ms
States Variables		
h_1	Activation gating variable	
h_2	Inactivation gating variable	

Potassium channel Kv4.3/KChIP2

Many auxiliary subunits have been shown to modulate Kv4 channels (especially Kv4.2 and Kv4.3). One family of regulatory subunits that appears to be of physiological significance is the KChIPs [107]. Members of the KChIP2 family, when heterologously coexpressed with Kv4 α-subunits, increase cell surface expression, slow down the inactivation kinetics, and accelerate recovery kinetics [108]. A regulatory characteristic of KChIPs on Kv4 channels is to increase cell surface expression as presented by an increase in peak macroscopic current amplitude with no effect on unitary channel conductance [107]. Patel et al [108] analysed the voltage-dependence of inactivation, recovery from activation, and deactivation kinetics of Kv4.3 expressed in the presence of KChIP2b and KChIP2d. Activation was modelled as a fourth-order Boltzmann function [108]. Inactivation followed a complex time course that is described by the sum of two exponential terms, that represent the fast and slow kinetics [108]. The corresponding time constants and relative magnitudes are voltage-dependent. The current for both the Kv4.3/KChIP2b and Kv4.3/KChIP2d channels is described as follows:

$$I_{\text{Kv4.3/KChIP2}} = \kappa_{\text{Kv4.3/KChIP2}}\, G_{\text{Kv4.3/KChIP2}}\, {k_1}^4\, (A_{\text{fast}}\, k_{2_{\text{fast}}} + A_{\text{slow}}\, k_{2_{\text{slow}}})\, (V - E_{\text{K}})\ , \tag{4.34}$$

where k_1 and k_2 represent the activation and inactivation gating kinetics with corresponding steady-state activation and inactivation multipliers $k_{1\infty}$ and $k_{2\infty}$.
For Kv4.3/ KChIP2b the steady state activation $V_{\text{half}} = -2.97$ mV and $k = 12.64$ mV, whereas for inactivation $V_{\text{half}} = -\ 57.4$ mV and $k = -\ 4.78$ mV [108]. As for Kv4.3/ KChIP2d activation, $V_{\text{half}} = -\ 2.3$ mV and $k = 12.49$ mV, while for inactivation $V_{\text{half}} = -\ 61.1$ mV and $k = -\ 5$ mV [108]. The parameters, their values, units and definitions are shown in Table 4.11. The channels' kinetics are shown in equations (4.35) to (4.50).
For Kv4.3/KChIP2b, the equations describing the channel kinetics are as follows:

$$k_{1_\infty} = \frac{1}{1 + \exp\left[\frac{-2.97 - V}{12.7}\right]}\ , \tag{4.35}$$

$$k_{2_\infty} = \frac{1}{1 + \exp\left[\frac{57.4 + V}{4.8}\right]}\ , \tag{4.36}$$

$$\alpha = 819 + \ \frac{-819}{1 + \exp\left[\frac{V - 14.6}{23.4}\right]} \quad \text{s}^{-1}\ , \tag{4.37}$$

$$\beta = \frac{185}{4(1 + \exp\left[\frac{V + 74}{13.2}\right]} \quad \text{s}^{-1}\ , \tag{4.38}$$

$$\tau_{k_1} = \frac{1000}{\alpha + 4\beta} \ , \tag{4.39}$$

$$\tau_{k_{2_{\text{fast}}}} = 54.5 + 58.8 \frac{\exp\left[-(30+V)\right]}{34.3} \ , \tag{4.40}$$

$$\tau_{k_{2_{\text{slow}}}} = 92 + 710.3 \frac{\exp\left[-(30+V)\right]}{28.3} \ , \tag{4.41}$$

$$\frac{A_{\text{fast}}}{A_{\text{fast}} + A_{\text{slow}}} = 0.63 + \frac{0.63}{1 + \exp\left[\frac{V-19.3}{8.5}\right]} \ . \tag{4.42}$$

For Kv4.3/KChIP2d, the equations describing the kinetics are:

$$k_{1_\infty} = \frac{1}{1 + \exp\left[\frac{-2.3-V}{12.49}\right]} \ , \tag{4.43}$$

$$k_{2_\infty} = \frac{1}{1 + \exp\left[\frac{61.1+V}{5}\right]} \ , \tag{4.44}$$

$$\alpha = 1044.6 + \ \frac{-1044.6}{1 + \exp\left[\frac{V-17.3}{24}\right]} \quad \text{s}^{-1} \ , \tag{4.45}$$

$$\beta = \frac{240.9}{4(1 + \exp\left[\frac{V+87.7}{16.3}\right])} \quad \text{s}^{-1} \ , \tag{4.46}$$

$$\tau_{k_1} = \frac{1000}{\alpha + 4\beta} \ , \tag{4.47}$$

$$\tau_{k_{2_{\text{fast}}}} = 54.6 + 40 \frac{\exp\left[-(30+V)\right]}{17.7} \ , \tag{4.48}$$

$$\tau_{k_{2_{\text{slow}}}} = 114.3 + 30.1 \ \frac{\exp\left[-(V-10)\right]}{5.9} \ , \tag{4.49}$$

$$\frac{A_{\text{fast}}}{A_{\text{fast}} + A_{\text{slow}}} = 0.8 + \frac{0.08}{1 + \exp\left[\frac{V-34}{4.3}\right]} \ . \tag{4.50}$$

Table 4.10: Notation for the Kv4.3/KChIP2 potassium channel

Notation	Definition	Value
$G_{\text{Kv4.3/KChIP2}}$	Kv4.3/KChIP2(b-d) unitary conductance	5 pS
$\kappa_{\text{Kv4.3/KChIP2}}$	Kv4.3/KChIP2(b-d) channel density	–
A_{fast},A_{slow}	Relative magnitude of the fast and slow inactivation kinetics	
b_{2_∞}	Steady state inactivation variable	
τ_{k_1}	Activation time constant in ms	
$\tau_{k_{2_{fast}}}$,$\tau_{k_{2_{slow}}}$	Fast and slow inactivation time constant in ms	
States Variables		
k_1	Activation gating variable	
$k_{2_{\text{fast}}}$,$k_{2_{\text{slow}}}$	Fast and slow inactivation gating variables	

Voltage-gated Kv4.3/KCNE3 and Kv4.3/KCNE3/KChIP2

The KCNE3 β-subunit has a strong inhibitory effect on current conducted by heterologously expressed Kv4.3 channels. The current amplitude is reduced; the channel activation, inactivation and recovery from inactivation slowed down [123]. KCNE3 also inhibits currents generated by Kv4.3 in complex with the accessory subunit KChIP2. We model two separate entities for the Kv4.3; one coexpressed with the KCNE3 subunit, and another coexpressed with both KCNE3 and KChIP2. Lundby et al [123] analysed the voltage-dependence of activation, inactivation, and recovery from inactivation for Kv4.3 coexpressed with KCNE3 in the presence and absence of KChIP2. We extract the data from Lundby et al [123]. For Kv4.3/ KCNE3 steady state activation V_{half} =6 mV and k = 17.5 mV, whereas for inactivation V_{half} = − 72 mV and k = − 11.1 mV. As for Kv4.3/ KCNE3/KChIP2 activation, V_{half} = − 5 mV and k = 17.5 mV, while for inactivation V_{half} = − 56 mV and k = − 11.1 mV. The corresponding time constants are assumed to be voltage-independent.
The current for both the Kv4.3/KCNE3 and Kv4.3/KCNE3/KChIP2d channels is described as follows:

$$I_{\text{Kv4.3/KCNE3}} = \kappa_{\text{Kv4.3/KCNE3}}\, G_{\text{Kv4.3/KCNE3}}\, m_1\, m_2\, m_3\, (V - E_{\text{K}})\,, \tag{4.51}$$

where m_1 and m_2 represent the activation, inactivation gates with corresponding steady-state activation and inactivation variables $m_{1\infty}$ and $m_{2\infty}$. We postulated an additional gate m_3 to account for the recovery from inactivation with corresponding steady-state variable $m_{2\infty}$ and time constant τ_{m_3}.

Kv4.3/KCNE3:

$$m_{1_\infty} = \frac{1}{1 + e^{(\frac{6-V}{17.5})}} \tag{4.52}$$

$$m_{2_\infty} = \frac{1}{1 + e^{(\frac{72+V}{11.1})}} \tag{4.53}$$

$$\begin{aligned} \tau_{m_1} &= 6.1 \text{ ms} \\ \tau_{m_2} &= 220 \text{ ms} \\ \tau_{m_3} &= 979 \text{ ms} \end{aligned} \tag{4.54}$$

Kv4.3/KCNE3/KChIP2:

$$m_{1_\infty} = \frac{1}{1 + e^{(\frac{5-V}{17.5})}} \tag{4.55}$$

$$m_{2_\infty} = \frac{1}{1 + e^{(\frac{56+V}{11.1})}} \tag{4.56}$$

$$\begin{aligned} \tau_{m_1} &= 13.7 \text{ ms} \\ \tau_{m_2} &= 251 \text{ ms} \\ \tau_{m_3} &= 118 \text{ ms} \end{aligned} \tag{4.57}$$

Table 4.11: Notation for the Kv4.3/KCNE3 and Kv4.3/KCNE3/KChIP2 Potassium Channel

Notation	Definition	Value
$G_{\text{Kv4.3/KCNE3}}$	Kv4.3/KCNE3 conductance	5 pS
$\kappa_{\text{Kv4.3/KCNE3}}$	Kv4.3/KCNE3 channel density	–
m_{1_∞}	Steady state activation variable	
m_{2_∞}	Steady state inactivation variable	
τ_{m_1}	Activation time constant in ms	
τ_{m_2}	Inactivation time constant in ms	
τ_{m_3}	Recovery from inactivation time constant in ms	
States Variables		
m_1	Activation gating variable	
m_2	Inactivation gating variable	
m_3	Recovery from inactivation gating variable	

Delayed rectifier (voltage-gated) potassium channel eag

The eag channel, also known as Kv10.1 or *ether-à-go-go*, is encoded by the *KCNH1* gene. It is a delayed rectifier voltage-gated potassium channel, which according to Ludwig et al [16] exhibits non-inactivating outward currents. Greenwood et al [124] demonstrated an important role for eag channels in suppressing uterine contractile activity in mice outside pregnancy, which aids the maintenance of the uterine quiescence. Application of dofetilide (eag-specific blocker) results in an increase of spontaneous contractility. On the other hand, upon applying PD118057 and NS1643 (eag activators), spontaneous contractility was inhibited [124]. The kinetics of eag strongly depends on the holding membrane potential; the activation kinetics is accelerated by depolarisation and slowed down by hyperpolarisation. The current has a threshold for activation between -40 mV to -30 mV. We extrapolate the data from the I-V curve by Ludwig et al [16] using the function $G(V) = I_{\text{eag}}/(V - E_{\text{K}})$ and normalised these data to the maximum value. The I-V and G-V curves are shown in Figure 4.12. The G-V curve is fitted to Boltzmann function with activation V_{half} of $+9.98$ mV and slope factor of 15.26 mV (equation (4.59)). The activation time constant τ_e is taken from experimental data by Tang et al [17] (equation (4.61)). This channel is sensitive to the extracellular Mg^{2+} $[Mg^{2+}]_e$ [17] and $[Ca^{2+}]_i$ [125]; $[Mg^{2+}]_e$ regulates transitions in the activation pathway of eag and controls the kinetics of the pore opening, whereas high $[Ca^{2+}]_i$ inhibits I_{eag} in the presence of Calmodulin. In the model we include e_{Ca}, equation (4.60), that gives the current the $[Ca^{2+}]_i$-dependent inhibition, while we assume the absence of $[Mg^{2+}]_e$. All parameters are shown in Table 4.12. The current is described as follows:

$$I_{\text{eag}} = \kappa_{\text{eag}}\, G_{\text{eag}}\, e_{\text{Ca}}\, e\, (V - E_{\text{K}})\,, \tag{4.58}$$

where e is the activation gating variable with steady state e_∞ and e_{Ca} is the $[Ca^{2+}]_i$-dependent inhibition. The equations describing the gating kinetics are as follows:

$$e_\infty = \frac{1}{1 + \exp[\frac{9.89 - V}{15.26}]}\,, \tag{4.59}$$

$$e_{\text{Ca}} = \frac{IC_{50\%}^{n_{[\text{eag}]}}}{IC_{50\%}^{n_{[\text{eag}]}} + [\text{Ca}]_i^{n_{[\text{eag}]}}}\,, \tag{4.60}$$

$$\tau_e = 10.6 \exp\left[V/38\right]\,. \tag{4.61}$$

Figure 4.12 displays the channel properties.

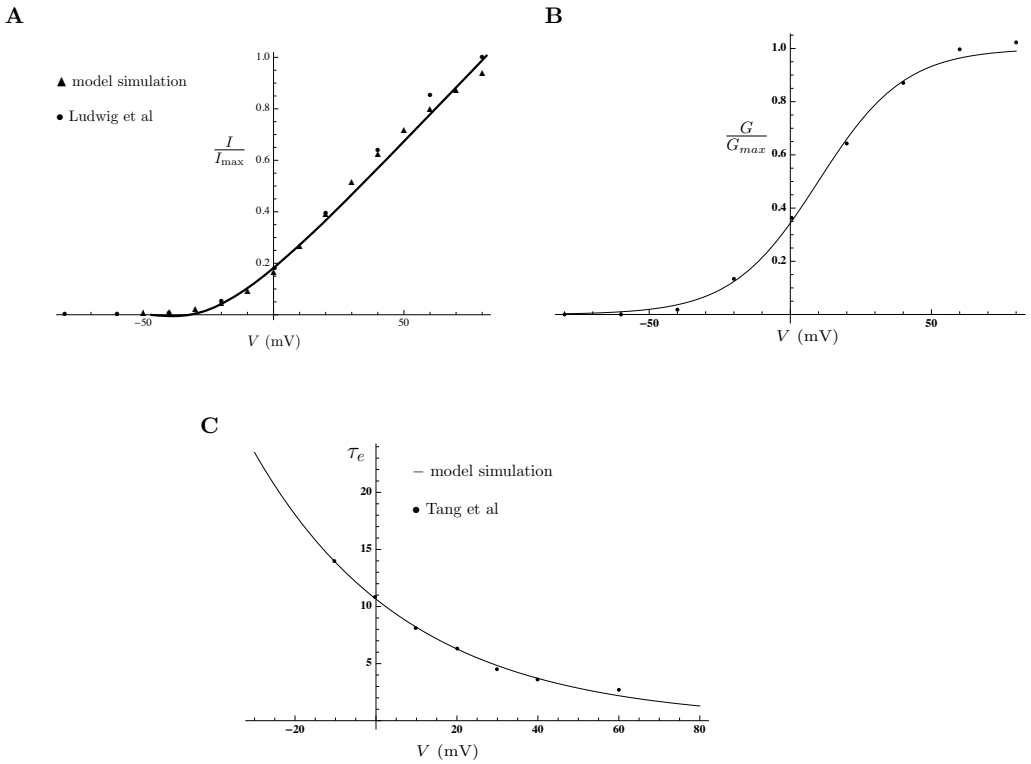

Figure 4.12: Properties of the $I_{\mathbf{eag}}$.
(A) Simulated (solid triangles) and experimental data from Ludwig et al [16] (bullets) peak I-V-curve obtained from a series of voltage clamp experiments. Values are normalised to the peak current values. (B) Steady state activation curve extrapolated from experimental data [16]. (C) Activation time constant from experimental data of Tang et al [17] obtained in the absence of Mg^{2+} from holding potential of −90 mV, 120 ms test pulses from −60 to +60 mV applied in 20 mV increments.

Table 4.12: Notation for the eag potassium channel

Notation	Definition	Value
G_{eag}	eag unitary conductance	4.9 pS
κ_{eag}	eag channel density	–
e_{Ca}	Ca-dependent inhibition factor	
e_{∞}	Steady state activation variable	
τ_e	Activation time constant in ms	
$IC_{50\%}$	Half-inhibition calcium concentration	106 nM
$n_{[\text{eag}]}$	Hill coefficient	4.2
States Variables		
e	Activation gating variable	

Voltage-gated potassium channel hERG

The hERG (the human *ether-à-go-go*-related Gene), or the *KCNH2* gene, encodes a protein known as Kv11.1 potassium ion channel. This channel is voltage-gated with inwardly rectification properties. According to Sanguinetti et al [126], the magnitude of its current increases up to -10 mV then progressively decreases with potentials ≥ 0 mV, which results in a negative slope of the I-V relationship. The peak outward current decreases with incremental depolarisation, which indicates that HERG rectifies. It is hypothesised that rectification is due to inactivation being much more rapid than activation [126]. Two competing processes: activation of the current and rapid inactivation that starts and completes before the current reaches a significant level, result in a reduction of the current magnitude compared to that predicted from steady-state activation variable and the driving force for the outward current [127]. Additionally, recovery from inactivation is much faster than deactivation [127]. We modeled the channel according to Wang et al [103], which expressed hERG in *Xenopus* oocytes and found that the current activation time course of the heterologously expressed hERG to be sigmoidal and that the dynamics requires a Markov model with at least three closed states (Figure 4.13). The intermediate closed state was voltage-insensitive. The properties of hERG resulting from the Markov model used are shown in Figure 4.14. The current is modeled as follows:

$$I_{\text{hERG}} = \kappa_{\text{hERG}}\, G_{\text{hERG}}\, O_{\text{hERG}}\, (V - E_{\text{K}})\,, \tag{4.62}$$

where O_{hERG} is the open channel probability.

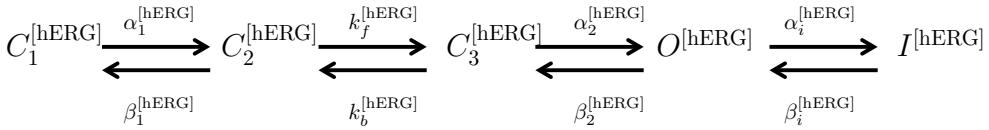

Figure 4.13: State transition diagram of the Markov model for the hERG channel.
$C_1^{[\text{hERG}]}$ – $C_3^{[\text{hERG}]}$ are closed states, $O^{[\text{hERG}]}$ is the open states and $I^{[\text{hERG}]}$ the inactivation state. The transition rates between the states are in ms.

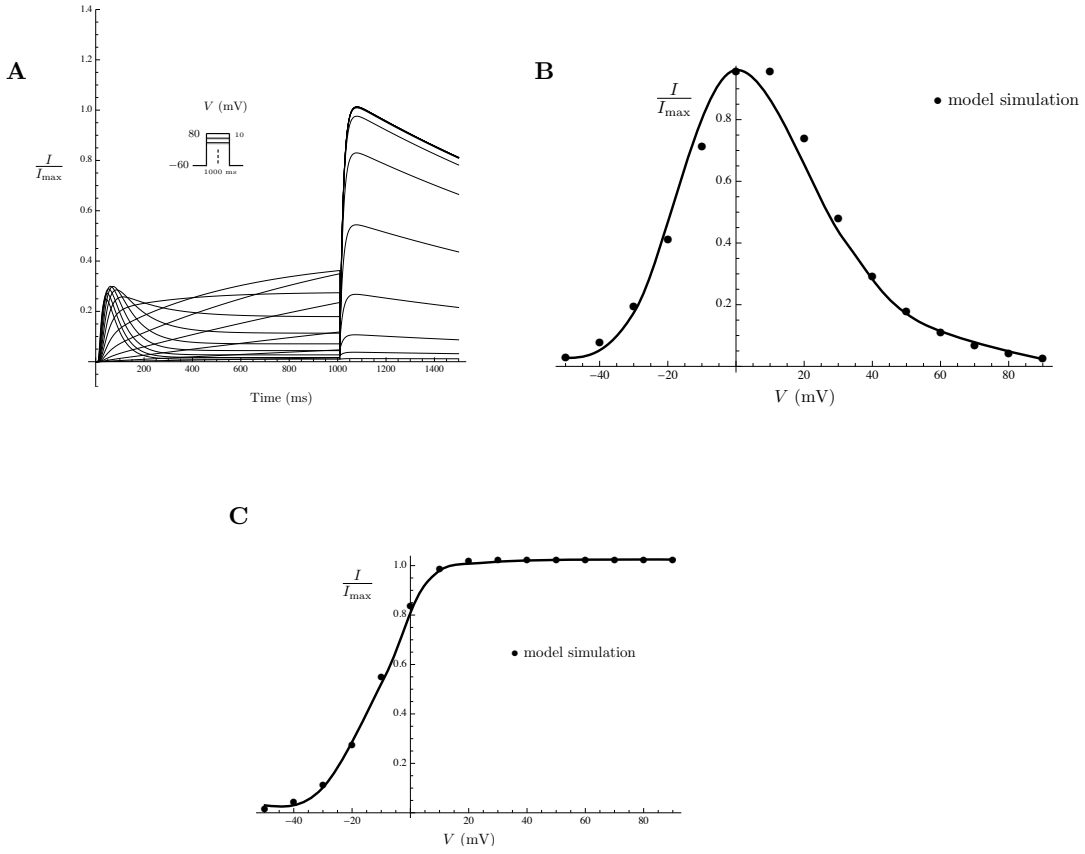

Figure 4.14: Properties of the $I_{\mathbf{hERG}}$.
(A) Simulated I_{hERG} current trace generated by the model during simulated voltage-clamp experiments. Currents are recorded during 1 s voltage steps to potentials ranging from -50 to 80 mV from a holding potential of -60 mV. Values are normalised to the peak current value. (B) Simulated I-V Curve obtained from the series of experiments shown in (A) at t =400ms. Values are normalised to the peak current value at the same time point. (C) Simulated peak tail I-V Curve obtained from the series of experiments shown in (A). Values are normalised to the peak tail current value.

The voltage-dependent transition rates in ms^{-1} are as follows:

$$\begin{aligned}
\alpha_1^{[\mathrm{hERG}]} &= 0.022348\exp[0.01176\ V]\ , \\
\beta_1^{[\mathrm{hERG}]} &= 0.047002\exp[-0.0631\ V]\ , \\
\alpha_2^{[\mathrm{hERG}]} &= 0.013733\exp[0.038198\ V]\ , \\
\beta_2^{[\mathrm{hERG}]} &= 0.0000689\exp[-0.04178\ V]\ , \\
\alpha_i^{[\mathrm{hERG}]} &= 0.090821\exp[0.023391\ V]\ , \\
\beta_i^{[\mathrm{hERG}]} &= 0.006497\exp[-0.03268\ V]\ .
\end{aligned} \tag{4.63}$$

The values of the voltage-insensitive rates are in Table 4.13. We describe the hERG kinetics using the following set of ODEs:

$$\begin{aligned}
\frac{dC_1^{[\mathrm{hERG}]}}{dt} &= -\alpha_1^{[\mathrm{hERG}]}C_1^{[\mathrm{hERG}]} + \beta_1^{[\mathrm{hERG}]}C_2^{[\mathrm{hERG}]}\ , \\
\frac{dC_2^{[\mathrm{hERG}]}}{dt} &= \alpha_1^{[\mathrm{hERG}]}C_1^{[\mathrm{hERG}]} - (\beta_1^{[\mathrm{hERG}]} + k_f^{[\mathrm{hERG}]})C_2^{[\mathrm{hERG}]} + k_b^{[\mathrm{hERG}]}C_3^{[\mathrm{hERG}]}\ , \\
\frac{dC_3^{[\mathrm{hERG}]}}{dt} &= k_f^{[\mathrm{hERG}]}C_2^{[\mathrm{hERG}]} - (\alpha_2^{[\mathrm{hERG}]} + k_b^{[\mathrm{hERG}]})C_3^{[\mathrm{hERG}]} + \beta_2^{[\mathrm{hERG}]}O^{[\mathrm{hERG}]}\ , \\
\frac{dO^{[\mathrm{hERG}]}}{dt} &= \alpha_2^{[\mathrm{hERG}]}C_3^{[\mathrm{hERG}]} - (\beta_2^{[\mathrm{hERG}]} + \alpha_i^{[\mathrm{hERG}]})O^{[\mathrm{hERG}]} + \beta_i^{[\mathrm{hERG}]}I^{[\mathrm{hERG}]}\ , \\
\frac{dI^{hERG}}{dt} &= \alpha_i^{[\mathrm{hERG}]}O^{[\mathrm{hERG}]} - \beta_i^{[\mathrm{hERG}]}I^{[\mathrm{hERG}]}\ .
\end{aligned} \tag{4.64}$$

Table 4.13: Notation for the hERG Potassium Channel

Notation	Definition	Value
G_{hERG}	hERG unitary conductance	2 pS
κ_{hERG}	hERG channel density	–
$\alpha_1^{[\text{hERG}]}$, $\alpha_2^{[\text{hERG}]}$	Forward voltage-dependent transition rate	
$\beta_1^{[\text{hERG}]}$, $\beta_2^{[\text{hERG}]}$	Backward voltage-dependent transition rate	
$k_f^{[\text{hERG}]}$	Voltage-insensitive forward rate constant	0.023761 ms^{-1}
$k_b^{[\text{hERG}]}$	Voltage-insensitive backward rate constant	0.036778 ms^{-1}
$\alpha_i^{[\text{hERG}]}$	Forward voltage-dependent inactivation rate	
$\beta_i^{[\text{hERG}]}$	Backward voltage-dependent inactivation rate	
State variables		
$C_0^{[\text{hERG}]}$ –$C_2^{[\text{hERG}]}$	Closed states	
$O^{[\text{hERG}]}$	Open state	
$I_0^{[\text{hERG}]}$	Inactivation state	

Delayed rectifier (voltage-gated) potassium channel Kv7.1

The channel Kv7.1 mediates a delayed rectifier potassium current and is encoded by the *KCNQ1* gene. When associated with the small subunit *KCNE1*, this channel behaves as a slow delayed rectifier voltage-gated potassium channel [128,129]. There was no evidence for the KCNE1 gene in the myometrium mRNA expression data; unlike the Kv7.1/ *KCNE1*, the homomeric Kv7.1 mediates a relatively fast outward current [128, 129]. The homomeric Kv7.1 channel was analysed by Pusch et al [109] using the *Xenopus* oocyte expression system. A delayed inactivation process that follows the channel activation is revealed by a transient increase in conductance after membrane repolarisation to negative values (manifested by an increase in the tail current), as shown in Figure 4.16. The inactivation of the Kv7.1 is incomplete even at positive voltages. Figure 4.16 shows the channel's properties, while the values and units of the parameters are stated in Table 4.14. An allosteric gating model has been suggested to account for the delayed, voltage-dependent onset and the incompleteness of inactivation [109]. The model shown in Figure 4.15 contains two open states and a voltage-independent inactivating step. The current through the homomeric Kv7.1 channel is described as follows:

$$I_{\text{Kv7.1}} = \kappa_{\text{Kv7.1}}\, G_{\text{Kv7.1}}\, P_o^{[\text{Kv7.1}]}\, (V - E_{\text{K}})\,, \tag{4.65}$$

where $G_{\text{Kv7.1}}$ is the single channel conductance (pS) and $P_o^{[\text{Kv7.1}]}$ is the probability of the Kv7.1 channel being in the open state.

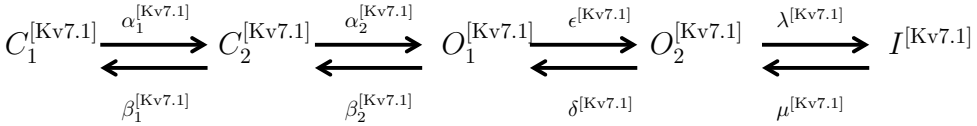

Figure 4.15: State transition diagram of the Markov model for the Kv7.1 channel.
$C_1^{[\text{Kv7.1}]} - C_2^{[\text{Kv7.1}]}$ are the closed states, $O_1^{[\text{Kv7.1}]}$-$O_2^{[\text{Kv7.1}]}$ are the open states and $I^{[\text{Kv7.1}]}$ the inactivation state. $\alpha_1^{[\text{Kv7.1}]}$, $\beta_1^{[\text{Kv7.1}]}$, $\alpha_2^{[\text{Kv7.1}]}$, $\beta_2^{[\text{Kv7.1}]}$, $\lambda^{[\text{Kv7.1}]}$, $\mu^{[\text{Kv7.1}]}$, $\delta^{[\text{Kv7.1}]}$, and $\epsilon^{[\text{Kv7.1}]}$ are the transition rates between the states as given in Table 4.14.

Kv7.1 is modulated in distinct ways by members of the *KCNE* family of accessory β-subunits. When co-expressed with *KCNE3* ($\equiv$ MiRP2), which exists at the mRNA expression level in MSMC [8, 90] with ΔCT of 21.6$\pm$0.22 in samples taken from non-pregnant patients and 21.5$\pm$0.03 in samples taken from pregnant patients [90], Kv7.1 loses its voltage-dependence gating properties and produces an instantaneous, nearly ohmic whole cell current [130]. In other words, the Kv7.1 current

becomes linearly dependent on voltage [130]. Accordingly we model the heteromeric Kv7.1/*KCNE3* as a potassium leak channel (as explained further in Section 4.6). On the other hand, *KCNE4* β-subunit which exists with great abundance at mRNA expression level in MSMC [8, 90], with ΔCT of 17.81$\pm$0.28 in samples taken from non-pregnant patients and 17.9$\pm$0.28 in samples taken from pregnant patients [90], has a dramatic inhibitory effect on the Kv7.1 when expressed in heterologous systems [131]. Morover, *KCNE4* can also inhibit Kv7.1 current even in the presence of other accessory subunits [132]. A recent publication [133] assessed the use of Kv7 channel activators as a potential myometrium relaxants in pregnant mice and humans. These authors found that Kv7 indeed suppressed myometrial contractions and that the *KCNQ* gene expression was sustained throughout gestation especially at term.

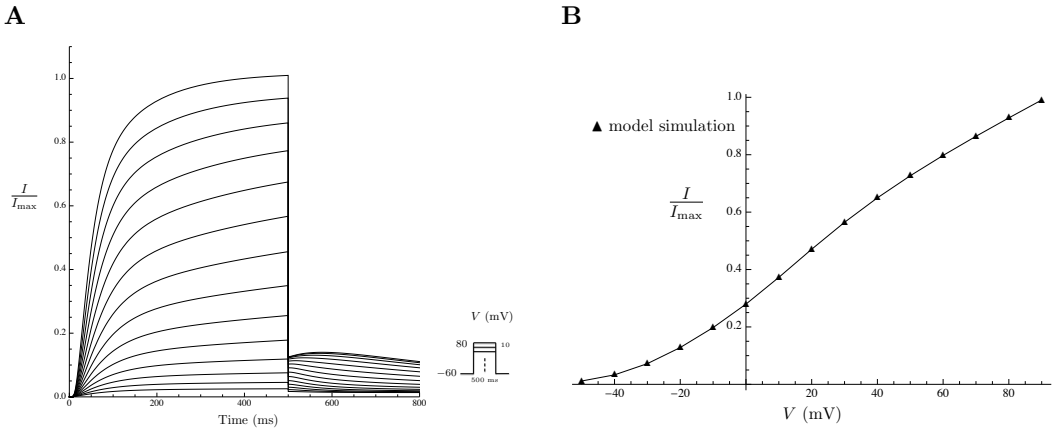

Figure 4.16: Properties of the $I_{Kv7.1}$. (A) Simulated voltage clamp traces of homomeric Kv7.1 channel from holding potential of -60 mV, the voltage was stepped to values up to $+80$ mV in 10 mV increments. (B) Simulated peak I-V curve obtained from the series of voltage clamp experiments.shown in (A). Values are normalized to the peak current values.

The voltage-dependent rates (s^{-1}), according to Pusch et al [109], for the allosteric

model in Figure 4.15 are as follows:

$$\begin{aligned}
\alpha_1^{[\mathrm{Kv7.1}]} &= 4.6 \exp\left[\frac{0.47\ VF}{RT}\right] , \\
\beta_1^{[\mathrm{Kv7.1}]} &= 33 \exp\left[\frac{-0.35\ VF}{RT}\right] , \\
\alpha_2^{[\mathrm{Kv7.1}]} &= 24 \exp\left[\frac{0.006\ VF}{RT}\right] , \\
\beta_2^{[\mathrm{Kv7.1}]} &= 19 \exp\left[\frac{-0.007\ VF}{RT}\right] , \\
\epsilon^{[\mathrm{Kv7.1}]} &= 4.6 \exp\left[\frac{0.8\ VF}{RT}\right] , \\
\delta^{[\mathrm{Kv7.1}]} &= 1.4 \exp\left[\frac{-0.7\ VF}{RT}\right] .
\end{aligned} \tag{4.66}$$

We derive the following system of four equations that corresponds to the Markov state model shown Figure 4.15:

$$\begin{aligned}
\frac{dC_1^{[\mathrm{Kv7.1}]}}{dt} &= -\alpha_1^{[\mathrm{Kv7.1}]} C_1^{[\mathrm{Kv7.1}]} + \beta_1^{[\mathrm{Kv7.1}]} C_2^{[\mathrm{Kv7.1}]} , \\
\frac{dC_2^{[\mathrm{Kv7.1}]}}{dt} &= \alpha_1^{[\mathrm{Kv7.1}]} C_1^{[\mathrm{Kv7.1}]} - (\beta_1^{\mathrm{Kv7.1}} + \alpha_2^{[\mathrm{Kv7.1}]}) C_2^{[\mathrm{Kv7.1}]} + \beta_2^{[\mathrm{Kv7.1}]} O_1^{[\mathrm{Kv7.1}]} , \\
\frac{dO_1^{[\mathrm{Kv7.1}]}}{dt} &= \alpha_2^{[\mathrm{Kv7.1}]} C_2^{[\mathrm{Kv7.1}]} - (\epsilon^{[\mathrm{Kv7.1}]} + \beta_2^{[\mathrm{Kv7.1}]}) O_1^{[\mathrm{Kv7.1}]} + \delta^{[\mathrm{Kv7.1}]} O_2^{[\mathrm{Kv7.1}]} , \\
\frac{dO_2^{[\mathrm{Kv7.1}]}}{dt} &= \epsilon^{[\mathrm{Kv7.1}]} O_1^{[\mathrm{Kv7.1}]} - (\delta^{\mathrm{Kv7.1}} + \lambda^{[\mathrm{Kv7.1}]}) O_2^{[\mathrm{Kv7.1}]} + \mu^{[\mathrm{Kv7.1}]} I^{[\mathrm{Kv7.1}]} , \\
\frac{dI^{[\mathrm{Kv7.1}]}}{dt} &= \lambda^{[\mathrm{Kv7.1}]} O_2^{[\mathrm{Kv7.1}]} - \mu^{[\mathrm{Kv7.1}]} I^{[\mathrm{Kv7.1}]} .
\end{aligned} \tag{4.67}$$

Table 4.14: Notation for Kv7.1 Potassium Channel

Notation	Definition	Value
$G_{\text{Kv7.1}}$	Kv7.1 unitary conductance	1.8 pS
$\kappa_{\text{Kv7.1}}$	Kv7.1 channel density	–
$\lambda^{[\text{Kv7.1}]}$	Rate constant for open state inactivation	142 s^{-1}
$\mu^{[\text{Kv7.1}]}$	Rate constant for open state inactivation	52 s^{-1}
$\alpha_1^{[\text{Kv7.1}]}$, $\alpha_2^{[\text{Kv7.1}]}$,$\epsilon^{[\text{Kv7.1}]}$	Forward voltage-dependent transition rates	
$\beta_1^{[\text{Kv7.1}]}$, $\beta_2^{[\text{Kv7.1}]}$,$\delta^{[\text{Kv7.1}]}$	Backward voltage-dependent transition rates	
State variables		
$C_1^{[\text{Kv7.1}]}$, $C_2^{[\text{Kv7.1}]}$	Closed states	
$O_1^{[\text{Kv7.1}]}$,$O_2^{[\text{Kv7.1}]}$	Open states	
$I^{[\text{Kv7.1}]}$	Inactivation state	

Delayed rectifier (voltage-gated) potassium channel Kv7.4

A voltage-gated potassium current is conducted by the Kv7.4 channel, which is encoded by the *KCNQ4* gene. This is another slow delayed rectifier voltage-gated potassium channel found at the transcription level in the MSMC [8,90]. The channel gives rise to a slowly activating, non-inactivating current [18]. Søgaard et al [134] studied the homomeric ionic current from the human Kv7.4 channels expressed in HEK-293 cells. For the Kv7.4 activation kinetics, the half-activation voltage was $V_{\text{half}} = -32$ mV and the slope factor was k =17.4 mV [134] (equation (4.69)). Schrøder et al [19] fitted the current to a double exponential function, with $\tau_{a_{\text{fast}}}$ and $\tau_{a_{\text{slow}}}$ (the former is shown in Figure 4.17 as a function of voltage (equation (4.70)), while the latter is almost voltage-independent with a value of 318 ms), which represent the time constants for the fast and slow components. The corresponding relative magnitudes did not change significantly with voltage, with the fast component accounting for about 35% [19]. We postulate an additional ultrafast activation gate d_2 to account for the extremely fast deactivation kinetics with deactivation time constant $\tau_{d_{\text{deac}}}$. The latter was fitted to a single exponential function to the deactivation tail current elicited at -120 mV following steps to potential ranging from -40 mV to 40 mV [19]. The model parameter values and units are shown in Table 4.15. The current is described by the following equation:

$$I_{\text{Kv7.4}} = \kappa_{\text{Kv7.4}}\, G_{\text{Kv7.4}}\, d_1\, d_2\, (V - E_{\text{K}})\,, \tag{4.68}$$

where d_1 and d_2 represent the activation and deactivation gates, both with corresponding steady-state variable d_∞.
The equations describing the Kv7.4 channel kinetics are as follows:

$$d_\infty = \frac{1}{1 + \exp\left[\frac{-32-V}{17.4}\right]}\,, \tag{4.69}$$

$$\tau_{d_{\text{fast}}} = \frac{1}{\exp\left[9(-65-V)\right] + \exp\left[0.03(-132.4+V)\right]}\,, \tag{4.70}$$

$$\tau_d = 0.35\ \tau_{d_{\text{fast}}} + 0.65\ \tau_{d_{\text{slow}}}\,, \tag{4.71}$$

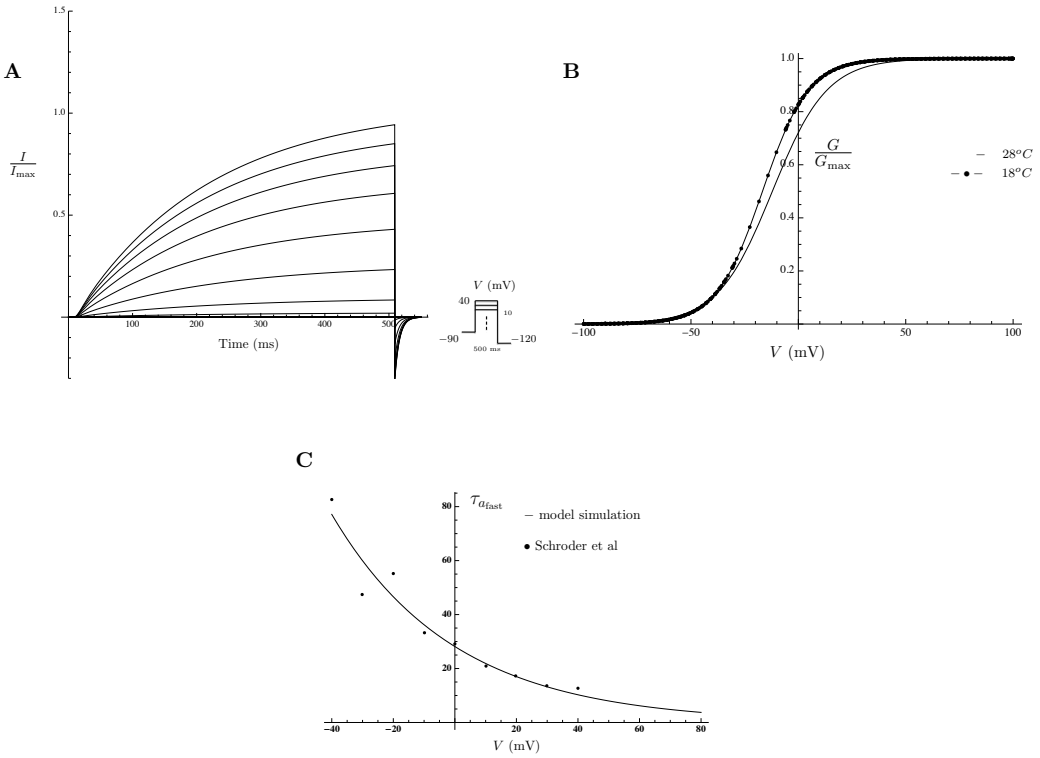

Figure 4.17: Properties of the $I_{\mathbf{Kv7.4}}$.
(A) Simulated voltage clamp traces of homomeric Kv7.1 channel at 28^oC from holding potential of -90 mV, the voltage was stepped to values up to $+40$ mV in 10 mV increments then stepped down to -120 mV. (B) Steady state activation curves from Miceli et al [18]. (C) Simulated activation fast time constant derived from experimental data (bullets) from Schrøder et al [19]

Table 4.15: Notation for the Kv7.4 Potassium Channel

Notation	Definition	Value
$G_{\text{Kv7.4}}$	Kv7.4 unitary conductance	2.1 pS
$\kappa_{\text{Kv7.4}}$	Kv7.4 channel density	
d_∞	Activation and deactivation steady state variable	
$\tau_{d_{\text{fast}}}$	Fast activation time constant in ms	ms
$\tau_{d_{\text{slow}}}$	Slow activation time constant	318 ms
τ_d	Activation time constant in ms	
$\tau_{d_{\text{deac}}}$	Deactivation time constant	7.5 ms
State variables		
d_1	Activation gating variable	
d_2	Deactivation gating variable	

4.1.2 Voltage- and calcium-gated potassium channels

The BK "big potassium" channels (also called Maxi-K or *slo1*) are regulated by variations in membrane potential as well as in $[Ca^{2+}]_i$. They are part of the calcium-gated potassium channels family (K_{Ca}). These channels are characterised by their large single channel conductance (in the range of 200-300 pS). The BK channel senses the elevation in membrane potential as well as $[Ca^{2+}]_i$ and opens accordingly. When it opens it repolarises the membrane potential, thus restoring the RMP; the channel acts as a break that regulates and guards the action of the calcium-driven processes from prolonged elevated $[Ca^{2+}]_i$ which in MSMC could lead to premature labour. When BK opens due to depolarisation and high $[Ca^{2+}]_i$, the voltage-dependent calcium channels (L-type and T-type) inactivate, preventing any further increase in $[Ca^{2+}]_i$. Consequently, throughout gestation, BK could provide an outward potassium current that counteracts any further increase in calcium influx. This prevents premature contractions and maintains cellular relaxation. During labour, BK loses its sensitivity to calcium either by the expression of another BK species that at term replaces the existing calcium-sensitive BK population or by undergoing certain modifications. In the latter case, the $[Ca^{2+}]_i$ necessary for contractions would be allowed to increase in the cell. BK has been reviewed extensively by Khan et al [135] and Magleby et al [136].

The BK channels are very diverse due to expression with various β-subunits and due to alternative splicing. Alternative splicing confers different properties on BK channels specially those related to calcium sensitivity, while association with different β-subunits changes inactivation and calcium-sensitivity. BK channels contain seven transmembrane segments with the N-terminus facing the extracellular side of the membrane. Similar to voltage-gated potassium channels, the S_4 segment acts as the voltage sensor. The COOH terminus is unusually long and has high affinity to calcium. The expression of the BK channel together with its β-subunits was significantly different between pregnant and non-pregnant uterus which could indicate a significant role during pregnancy [8, 90].

Calcium-dependent potassium channel BK_α

The current I_{BK_α} is carried by the channel BK_α, which is encoded by *KCNMA1* gene. This is the α-subunit of the large BK conductance. Cloning and heterologous expression studies revealed that this channel's α-subunit is a non-inactivating calcium-and voltage-sensitive channel. It displays a large single-channel conductance of around 260 pS [137–139]. At low $[Ca^{2+}]_i$, V_{half} for activation is around +125 mV,

this value decreases with the increase of $[Ca^{2+}]_i$ [98]. In other words, the $[Ca^{2+}]_i$ shifts the voltage-dependent parameters to more negative voltages, but the channel can still be fully activated by voltage alone [140]. BK_α is the highest expressed channel at mRNA [8, 90] level both in pregnant and non-pregnant uterus: ΔCT was 16.08±0.01 (normalised to r18s mRNA) in samples taken from non-pregnant patients and 14.92±0.27 in samples taken from pregnant patients [90]. An allosteric model, shown in Figure (4.18), was suggested by Horrigan et al [100]. The model contains five open (O) and five closed (C) states arranged in parallel. The kinetics and steady-state properties of BK are function of multiple components associated with the transitions between a closed to another closed state, an open to another open state, and a closed to an open state. The horizontal transitions represent movement of the channel's four voltage sensors, each of which can be either active or inactive, while the vertical transitions represent the conformational change by which the channel opens. This model has been shown to work well in the absence of $[Ca^{2+}]_i$ [100]. To consider the calcium sensitivity of BK_α, Bao et al [98] suggested two sets of four high-affinity calcium binding sites, which are structurally distinct but have similar binding properties. Each site is assumed to be independent from the other. Combined with the allosteric model of Horrigan, this information can produce a model that considers both calcium binding and voltage sensing and could describe the performance of the channel acceptably. The parameters are all taken from Bao et al [98] and are shown in Table 4.16. The channel gives rise to the following current:

$$I_{\mathrm{BK}_\alpha} = \kappa_{\mathrm{BK}_\alpha} P_{o\mathrm{BK}_\alpha} (V - E_{\mathrm{K}}) \,, \tag{4.72}$$

where $\kappa_{\mathrm{BK}_\alpha}$ is the channel density and $P_{o\mathrm{BK}_\alpha}$ is the open channel probability. The parameters, their definitions, units, and values are in Table 4.16.
The closed-to-open and open-to-closed voltage-dependent transition rates (s^{-1}) are as follows:

$$\begin{aligned} \delta_{xi} &= \delta_{o_i} \exp\left[\frac{z_\delta F V}{RT}\right] \,, \\ \gamma_{xi} &= \gamma_{o_i} \exp\left[\frac{z_\gamma F V}{RT}\right] \quad \text{where} \quad i = 0 \ldots 4 \,. \end{aligned} \tag{4.73}$$

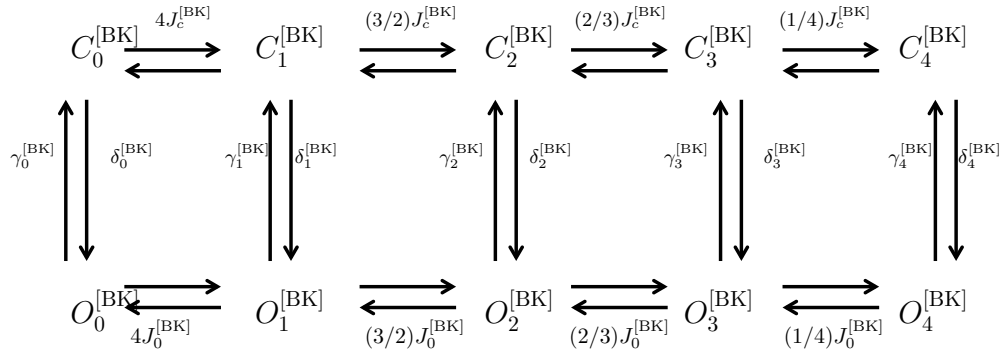

Figure 4.18: State transition diagram of the Markov model for the BK_α channel. $C_1^{[BK]}$ – $C_4^{[BK]}$ are the closed states and $O_1^{[BK]}$-$O_4^{[BK]}$ are the open states. Horizontal transitions represent voltage sensor movement while vertical transitions represent channel opening. Transition rates between the states are given in Table 4.16 and set of equations (4.73).

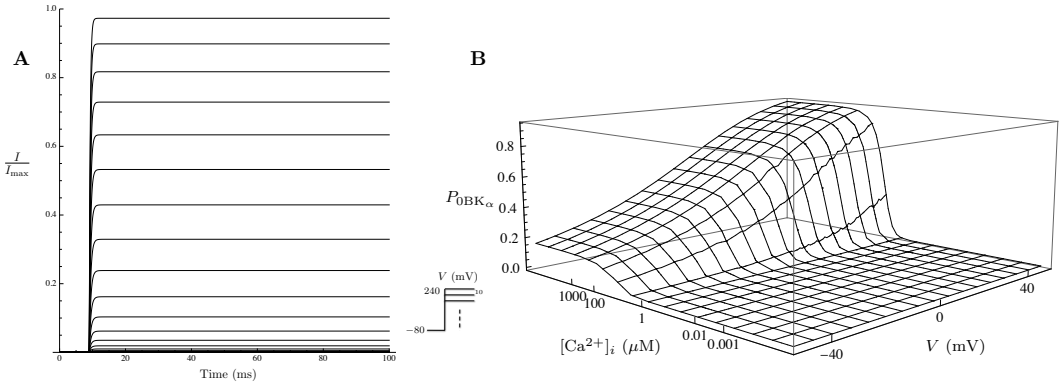

Figure 4.19: Properties of the I_{BK_α}.
(A) Simulated voltage clamp traces of α-subunit BK channel from holding potential of -80 mV, the voltage was stepped to values up to $+240$ mV in 10 mV increments. (B) Simulated open channel probability plotted against $[Ca^{2+}]_i$ and membrane potential.

Let

$$\begin{aligned} J_c &= \exp\left[\frac{z_J F(V - V_{hc})}{RT}\right] , \\ J_o &= \exp\left[\frac{z_J F(V - V_{ho})}{RT}\right] , \end{aligned} \tag{4.74}$$

the fractions of closed channels occupying the state that precedes each transition are as follows:

$$\begin{aligned} f_{co} &= \frac{1}{1 + 4J_c + 6{J_c}^2 + 4{J_c}^3 + {J_c}^4} , \\ f_{c1} &= \frac{4J_c}{1 + 4J_c + 6{J_c}^2 + 4{J_c}^3 + {J_c}^4} , \\ f_{c2} &= \frac{6{J_c}^2}{1 + 4J_c + 6{J_c}^2 + 4{J_c}^3 + {J_c}^4} , \\ f_{c3} &= \frac{4{J_c}^3}{1 + 4J_c + 6{J_c}^2 + 4{J_c}^3 + {J_c}^4} , \\ f_{c4} &= \frac{{J_c}^4}{1 + 4J_c + 6{J_c}^2 + 4{J_c}^3 + {J_c}^4} . \end{aligned} \tag{4.75}$$

and the fractions of open channels occupying the state that precedes each transition are:

$$\begin{aligned} f_{oo} &= \frac{1}{1 + 4J_o + 6{J_o}^2 + 4{J_o}^3 + {J_o}^4} , \\ f_{o1} &= \frac{4J_o}{1 + 4J_o + 6{J_o}^2 + 4{J_o}^3 + {J_o}^4} , \\ f_{o2} &= \frac{6{J_o}^2}{1 + 4J_o + 6{J_o}^2 + 4{J_o}^3 + {J_o}^4} , \\ f_{o3} &= \frac{4{J_o}^3}{1 + 4J_o + 6{J_o}^2 + 4{J_o}^3 + {J_o}^4} , \\ f_{o4} &= \frac{{J_o}^4}{1 + 4J_o + 6{J_o}^2 + 4{J_o}^3 + {J_o}^4} . \end{aligned} \tag{4.76}$$

The steady-state open probability and the corresponding activation time constant are:

$$P_{\mathrm{BK}_{\alpha/\alpha+\beta 1}{}_{ss}} = \frac{1}{1 + \left(\frac{1+\exp[z_J F(V-V_{hc})/RT]}{1+\exp[z_J F(V-V_{ho})/RT]}\right)^4 \left(\frac{1+\mathrm{Ca}_i/K_c}{1+\mathrm{Ca}_i/K_o}\right)^8 \frac{\exp[-z_L FV/RT]}{L}} \ , \tag{4.77}$$

$$\tau_{\mathrm{BK}_{\alpha/\alpha+\beta 1}} = \frac{1}{\gamma + \delta} \ , \tag{4.78}$$

where

$$\begin{aligned} \delta &= (\delta_{x1} * f_{co}) + (\delta_{x2} * f_{c1}) + (\delta_{x3} * f_{c2}) + (\delta_{x4} * f_{c3}) + (\delta_{x5} * f_{c4}) \ , \\ \gamma &= (\gamma_{x1} * f_{oo}) + (\gamma_{x2} * f_{o1}) + (\gamma_{x3} * f_{o2}) + (\gamma_{x4} * f_{o3}) + (\gamma_{x5} * f_{o4}) \ , \end{aligned} \tag{4.79}$$

and

$$\begin{aligned} L &= L_0 \ \exp\left[\frac{z_L FV}{RT}\right] \ , \\ D &= J_o/J_c \ . \end{aligned} \tag{4.80}$$

Bao et al [98] provides a detailed description of the above equations. The parameters, their definitions, and their values are stated in Table 4.16; a simulated current trace of the BK channel and the simulated open channel probability as function of $[\mathrm{Ca}^{2+}]_i$ and membrane potential are shown in Figure 4.19.

Table 4.16: Notation for the BK_α and the $BK_{\alpha+\beta1}$ channels

Parameter	Definition	Value
G_{BK}	BK unitary conductance (BK_α, $BK_{\alpha+\beta1}$)	289 pS
κ_{BK}	BK channel density (BK_α, $BK_{\alpha+\beta1}$)	–
P_{oBK}	BK open channel probability (BK_α, $BK_{\alpha+\beta1}$)	
L_0	(BK_α/$BK_{\alpha+\beta1}$)	2.2×10^{-6}/2.5×10^{-6}
z_J	Gating charge (BK_α/$BK_{\alpha+\beta1}$)	0.58e/0.57e
z_γ	” (BK_α/$BK_{\alpha+\beta_1}$)	0.1e/0.17e
z_δ	” $z_L - z_\gamma$	
z_L	Gating charge associated with closed-to-open conformational change (BK_α/$BK_{\alpha+\beta_1}$)	0.41e/0.46e
V_{ho}	Voltage sensor's half activation V when channel closed (BK_α/$BK_{\alpha+\beta_1}$)	27/−34 mV
V_{hc}	Voltage sensor's half activation V when channel is open (BK_α/$BK_{\alpha+\beta_1}$)	151/80 mV
D	Allosteric factor (BK_α/$BK_{\alpha+\beta_1}$)	16.8/12.8
δ_{0_1}	Rate constant for channel opening (BK_α/$BK_{\alpha+\beta_1}$)	0.016 / 0.003 s^{-1}
δ_{0_2}	”	$0.114/0.007s^{-1}$
δ_{0_3}	”	$1.98/0.198s^{-1}$
δ_{0_4}	”	$3.76/1.251s^{-1}$
δ_{0_5}	”	$57.12/4.934s^{-1}$
γ_{0_1}	Rate constant for channel closing (BK_α/$BK_{\alpha+\beta_1}$)	$7452.3/931.7s^{-1}$
γ_{0_2}	”	$4121.4/213.2s^{-1}$
γ_{0_3}	”	$5645.8/547.8s^{-1}$
γ_{0_4}	”	$851/333.5s^{-1}$
γ_{0_5}	”	$1025/126.7s^{-1}$
$P_{BK_{\alpha/\alpha+\beta1_{ss}}}$	Steady-state activation	
State variables		
$P_{oBK_{\alpha/\alpha+\beta1}}$	Open-state probability	

Calcium-dependent potassium channel BK$_{\alpha+\beta1}$

The current $I_{\mathrm{BK}_{\alpha+\beta1}}$ is elicited by the channel encoded by the α-subunit of the large BK conductance *KCNMA1* gene and the associated $\beta1$-subunit *KCNMB1*. The latter is highly expressed at mRNA level [8, 90] both in pregnant and non-pregnant uterus; ΔCT was 16.45±0.16 (normalised to r18s mRNA) in samples taken from non-pregnant patients and 15.32±0.28 in samples taken from pregnant patients [90]. The $\beta1$-subunit, when associated with the α-subunit, increases the calcium sensitivity, and decreases the voltage-dependence of the channel. Some studies [98, 141, 142] at the single channel level indicated that the $\beta1$-subunit shifts the calcium dose-response curve of the BK channel leftward. At +30 mV, the affinity was 9.2 and 2.6 μM for BK$_\alpha$ and BK$_{\alpha+\beta1}$ respectively. It has been suggested that about 80% of this shift is due to voltage sensing and about 20% due to calcium binding [98, 142]. In the absence of calcium, $\beta1$-subunit increases the open channel probability approximately 7 to 10-fold [98, 142]. The subunit has almost no effect on the equilibrium constants of the conformational change by which the BK channel opens and it does not affect the gating charge on the channel's voltage sensors; it only affects the voltage sensor activation when the channel is open or closed [98]. Voltage sensor activation occurs at more negative voltages; at 1 μM $[Ca^{2+}]_i$, activation V_{half} for BK$_{\alpha+\beta1}$ was 82.1 mV compared to 120.6 mV for BK$_\alpha$ [98]. Again, the BK$_{\alpha+\beta1}$ is modelled according to Horrigan allosteric model similar to BK$_\alpha$ (parameter values are stated in Table 4.16). The current through this channel is as follows:

$$I_{\mathrm{BK}_{\alpha+\beta1}} = \kappa_{\mathrm{BK}_{\alpha+\beta1}} P_{o\mathrm{BK}_{\alpha+\beta1}} (V - E_K) \,, \tag{4.81}$$

where $\kappa_{\mathrm{BK}_{\alpha+\beta_1}}$ is the channel density for BK$_{\alpha+\beta1}$ and $P_{o\mathrm{BK}_{\alpha+\beta_1}}$ is the open channel probability.

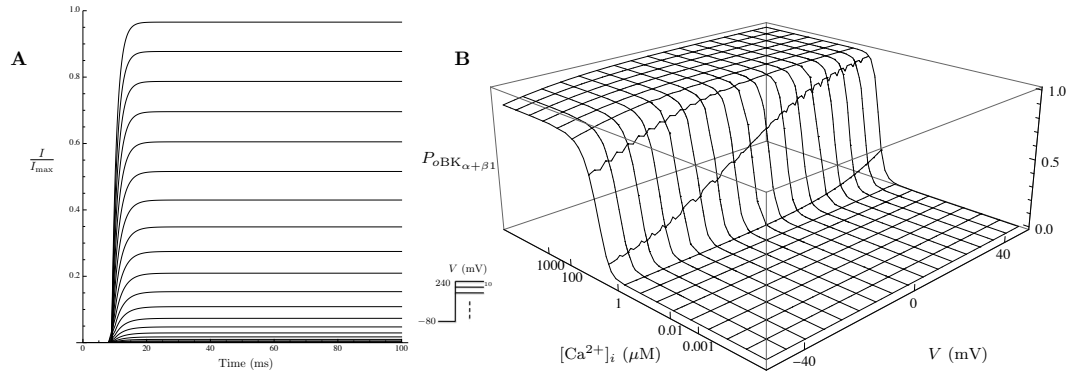

Figure 4.20: Properties of the $I_{\mathbf{BK}_{\alpha+\beta1}}$.
(A) Simulated voltage clamp traces of $\mathrm{BK}_{\alpha+\beta1}$ channel from holding potential of −80 mV, the voltage was stepped to values up to +240 mV in 10 mV increments in the absence of calcium. (B) Simulated open channel probability plotted against $[\mathrm{Ca}^{2+}]_i$ and membrane potential.

Calcium-dependent potassium channel BK$_{\alpha+\beta2}$

The BK$_{\alpha+\beta2}$ is a channel that results from the association of the BK$_\alpha$ with *KCNMB2*, known as the β2-subunit. When associated with the α-subunit, the β2-subunit inactivates the BK current during prolonged depolarising voltage steps, increases the calcium sensitivity, slows the channel's gating kinetics, and shifts the *I-V* relationship to more negative potentials [143, 144]. According to the transcription data, the ΔCT for the β2-subunit was 21.5$\pm$0.11 (normalised to r18s mRNA) in samples taken from non-pregnant patients and 25.6$\pm$0.32 in samples taken from pregnant patients [90]. For the BK$_{\alpha+\beta2}$ activation, V_{half} is calcium-dependent; the higher the $[Ca^{2+}]_i$, the bigger the shift toward more negative potential. At 2 nM, 1 μM, 4 μM and 10 μM $[Ca^{2+}]_i$, V_{half} was 147.4, 89.4, 20.7, and $-$11.9 mV, respectively [145]. For inactivation, as $[Ca^{2+}]_i$ is increased, V_{half} is shifted to more negative potentials ($V_{\text{half}} = -60.8$, -86.15, and -159.2 mV for 4, 10, and 60 μM of $[Ca^{2+}]_i$) [143]; the slope was almost invariant with value of -11.4 mV [143]. Sun et al [145] cloned the BK$_{\alpha+\beta2}$ of rat chromaffin cells in *Xenopus* oocytes and developed the allosteric model shown in Figure 4.21 to describe the kinetics of this channel. The scheme comprises a 15-state model for the BK$_{\alpha+\beta2}$ gating composed of four calcium binding steps with voltage-dependent closed to open conformational step. Inactivation process occurs from open states. Figure 4.22 shows simulated current trace and *I-V* curve for the BK$_{\alpha+\beta2}$, the parameters, their values and units are stated in Table 4.17. The current elicited from the above channel is:

$$I_{\text{BK}_{\alpha+\beta2}} = \kappa_{\text{BK}_{\alpha+\beta2}} P_{o\text{BK}_{\alpha+\beta2}} (V - E_{\text{K}}) \,, \tag{4.82}$$

where $\kappa_{\text{BK}_{\alpha+\beta2}}$ is the channel density and $P_{o\text{BK}_{\alpha+\beta2}}$ is the open channel probability.

The voltage-dependent transition rates for the BK$_{\alpha+\beta2}$ model in Figure 4.21 by Sun et al [145] are as follows:

$$\begin{aligned}
\alpha_i &= A_i \, \exp\left[z_{co}\frac{VF}{RT}\right] \,, \\
\beta_i &= B_i \, \exp\left[z_{oc}\frac{VF}{RT}\right] \,, \\
\delta_i &= C_i \, \exp\left[z_{oi}\frac{VF}{RT}\right] \,, \\
\gamma_i &= D_i \, \exp\left[z_{io}\frac{VF}{RT}\right] \qquad\qquad \text{where} \quad i = 0...5 \,.
\end{aligned} \tag{4.83}$$

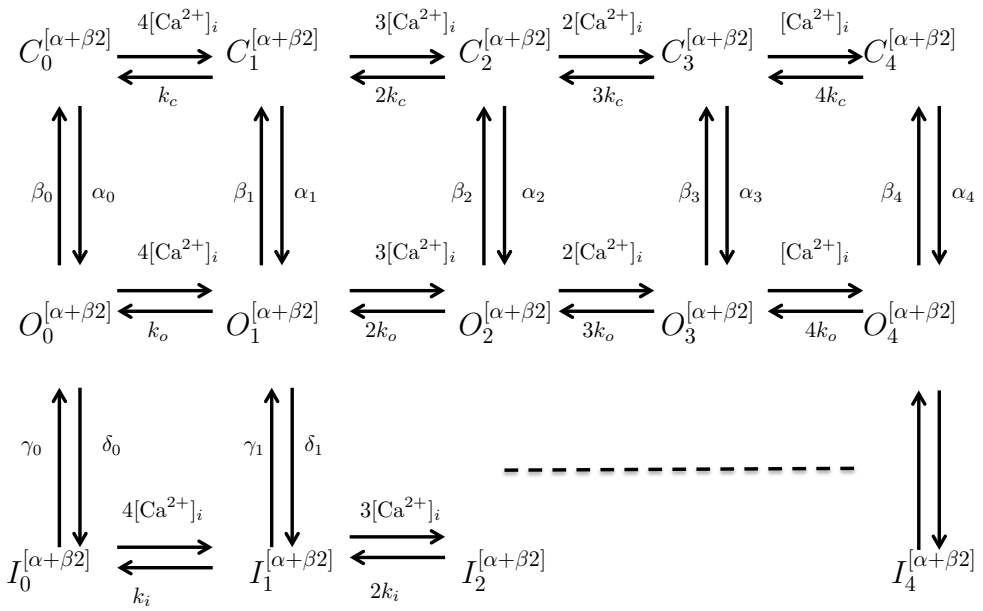

Figure 4.21: State transition diagram of the Markov model for the $\mathbf{BK}_{\alpha+\beta2}$ channel.
$C_0^{[\alpha+\beta2]}$ – $C_4^{[\alpha+\beta2]}$ are the closed states; $O_0^{[\alpha+\beta2]}$ – $O_4^{[\alpha+\beta2]}$ are the open states and $I_0^{[\alpha+\beta2]}$ – $I_4^{[\alpha+\beta2]}$ are the inactivation states. α_i, β_i, γ_i and δ_i (i=0....4) are the transition rates between the states as given in equations (4.83). For simplicity, only some of the states are shown. The other transitions are abbreviated by the dashed line.

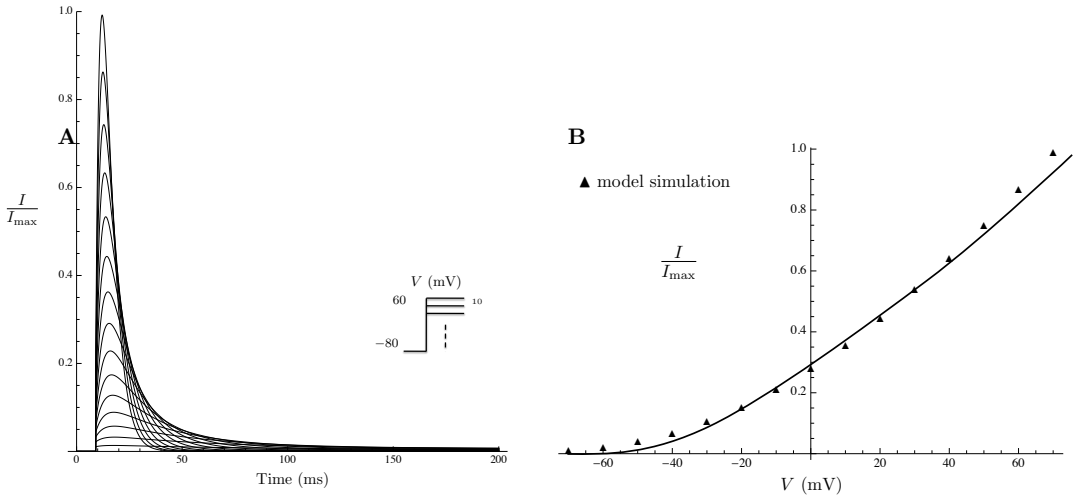

Figure 4.22: Properties of the $I_{\mathbf{BK}_{\alpha+\beta2}}$.
(A) Simulated voltage clamp traces of $BK_{\alpha+\beta2}$ channel from holding potential of −80 mV, the voltage was stepped to values up to +60 mV in 10 mV increments in 10 μM $[Ca^{2+}]_i$ (B) Simulated peak I-V curve obtained from the series of voltage clamp experiments shown in (A). Values are normalised to the peak current values.

We deduced the following system of ODEs that correspond to the Markov state model in Figure 4.21 [145]:

$$
\begin{aligned}
\frac{dC_0^{[\alpha+\beta 2]}}{dt} &= k_c\ C_1^{[\alpha+\beta 2]} - (4\ [\mathrm{Ca}]_i + \alpha_0)\ C_0^{[\alpha+\beta 2]} + \beta_0\ O_0^{[\alpha+\beta 2]} \\
\frac{dI_0^{[\alpha+\beta 2]}}{dt} &= k_i\ I_1^{[\alpha+\beta 2]} - (4\ [\mathrm{Ca}]_i + \gamma_0)\ I_0^{[\alpha+\beta 2]} + \delta_0\ O_0^{[\alpha+\beta 2]} \\
\frac{dO_0^{[\alpha+\beta 2]}}{dt} &= k_o\ O_1^{[\alpha+\beta 2]} - (4\ [\mathrm{Ca}]_i + \beta_0 + \delta_0)\ O_0^{[\alpha+\beta 2]} + \alpha_0\ C_0^{[\alpha+\beta 2]} + \gamma_0\ I_0^{[\alpha+\beta 2]} \\
\frac{dC_4^{[\alpha+\beta 2]}}{dt} &= [\mathrm{Ca}]_i\ C_3^{[\alpha+\beta 2]} - (4\ k_c + \alpha_4) C_4^{[\alpha+\beta 2]} + \beta_4\ O_4^{[\alpha+\beta 2]} \\
\frac{dO_4^{[\alpha+\beta 2]}}{dt} &= [\mathrm{Ca}]_i\ O_3^{[\alpha+\beta 2]} - (4\ k_o + \beta_4 + \delta_4) O_4^{[\alpha+\beta 2]} + \alpha_4\ C_4^{[\alpha+\beta 2]} + \gamma_4\ I_4^{[\alpha+\beta 2]} \\
\frac{dI_4^{[\alpha+\beta 2]}}{dt} &= [\mathrm{Ca}]_i\ I_3^{[\alpha+\beta 2]} - (4\ k_i + \gamma_4) I_4^{[\alpha+\beta 2]} + \delta_4\ O_4^{[\alpha+\beta 2]} \\
\frac{dC_n^{[\alpha+\beta 2]}}{dt} &= (5-n)[\mathrm{Ca}]_i\ C_{n-1}^{[\alpha+\beta 2]} + (n+1) k_c\ C_{n+1}^{[\alpha+\beta 2]} \\
&\quad -(n\ k_c + (5-n-1)[\mathrm{Ca}]_i - \alpha_n) C_n^{[\alpha+\beta 2]} + \beta_n\ O_n^{[\alpha+\beta 2]} \\
\frac{dO_n^{[\alpha+\beta 2]}}{dt} &= (5-n)[\mathrm{Ca}]_i\ O_{n-1}^{[\alpha+\beta 2]} + (n+1) k_o\ O_{n+1}^{[\alpha+\beta 2]} \\
&\quad -(n\ k_o + (5-n-1)[\mathrm{Ca}]_i - \beta_n + \delta_n) O_n^{[\alpha+\beta 2]} + \alpha_n\ C_n^{[\alpha+\beta 2]} + \gamma_n\ I_n^{[\alpha+\beta 2]} \\
\frac{dI_n^{[\alpha+\beta 2]}}{dt} &= (5-n)[\mathrm{Ca}]_i\ I_{n-1}^{[\alpha+\beta 2]} + (n+1) k_i\ I_{n+1}^{[\alpha+\beta 2]} - (n\ k_i + (5-n-1)[\mathrm{Ca}]_i \\
&\quad -\gamma_n) I_n^{[\alpha+\beta 2]} + \delta_n\ O_n^{[\alpha+\beta 2]} \qquad \text{where } n = 1, 2, 3
\end{aligned}
\tag{4.84}
$$

Table 4.17: Notation for the $BK_{\alpha+\beta2}$ channel

Parameter	Definition	Value
$G_{BK_{\alpha+\beta2}}$	$BK_{\alpha+\beta2}$ unitary conductance	289 pS
$\kappa_{BK_{\alpha+\beta2}}$	$BK_{\alpha+\beta2}$ Channel density	–
A_0	Closed to open transition rate at 0 mV	1 s^{-1}
A_1	”	2 s^{-1}
A_2	”	12 s^{-1}
A_3	”	120 s^{-1}
A_4	”	288 s^{-1}
B_0	Open to close transition rate at 0 mV	810 s^{-1}
B_1	”	135 s^{-1}
B_2	”	67 s^{-1}
B_3	”	56.25 s^{-1}
B_4	”	11.25 s^{-1}
C_0	Open to inactivated transition rate at 0 mV	105 s^{-1}
C_1	”	126 s^{-1}
C_2	”	147 s^{-1}
C_3	”	175 s^{-1}
C_4	”	210 s^{-1}
D_0	Inactivated to open transition rate at 0 mV	7 s^{-1}
D_1	”	3.36 s^{-1}
D_2	”	1.568 s^{-1}
D_3	”	0.7468 s^{-1}
D_4	”	0.3584 s^{-1}
z_{co}	Gating charge	0.513e
z_{oc}	”	0.5745 e
z_{oi}	”	0.1293 e
z_{io}	”	0.8617 e
k_c	Closed states dissociation constant	6.6
k_o	Open states dissociation constant	0.55
k_i	Inactvation states dissociation constant	0.22
State variables		
$P_{oBK_{\alpha+\beta2}}$	Open channel probability	

Calcium-dependent potassium channel BK$_{\alpha+\beta3}$

The expression of the BK$_\alpha$ subunit with the *KCNMB3* (β_3-subunit) results in a new entity, which we denote as BK$_{\alpha+\beta3}$. The current obtained from the expression of the BK$_{\alpha+\beta3}$ in *Xenopus* oocytes was an inactivating current that is both voltage- and calcium-dependent, with activation shifted to more negative potentials as $[Ca^{2+}]_i$ was increased [99]. At strong depolarisations and higher $[Ca^{2+}]_i$, the current exhibits a very rapid although incomplete inactivation [146] (Figure 4.24). Above +50 mV, current inactivates to a steady-state level that is 10–50% of the peak value, dependent on voltage, but largely independent on calcium [99]. BK$_{\alpha+\beta3}$ recovers rapidly from inactivation upon repolarisation [146]. Lingle et al [99] provided a detailed description of the kinetics of the BK$_{\alpha+\beta3}$ using a Markov model similar to the one used for the BK$_{\alpha+\beta2}$, as shown in Figure 4.23. The current mediated from the BK$_{\alpha+\beta3}$ channel is:

$$I_{\mathrm{BK}_{\alpha+\beta3}} = \kappa_{\mathrm{BK}_{\alpha+\beta3}} G_{\mathrm{BK}_{\alpha+\beta3}} P_{o\mathrm{BK}_{\alpha+\beta3}} (V - E_{\mathrm{K}}) \; ; \tag{4.85}$$

because the channel allows current in the inactivated state (incomplete inactivation) as well as the open state, the probability of being in the conducting state is:

$$P_{\mathrm{BK}_{\alpha+\beta3_o}} \quad = \quad \frac{(O_n^{[\alpha+\beta3]} + I_n^{[\alpha+\beta3]})}{(C_n^{[\alpha+\beta3]} + O_n^{[\alpha+\beta3]} + I_n^{[\alpha+\beta3]})} \; . \tag{4.86}$$

We describe the model in Figure 4.23 by the following set of differential equations:

$$
\begin{aligned}
\frac{dC_0^{[\alpha+\beta 3]}}{dt} &= k_c\ C_1^{[\alpha+\beta 3]} - (4\ [\mathrm{Ca}]_i + k_{f_0})\ C_0^{[\alpha+\beta 3]} + k_{r_0}\ O_0^{[\alpha+\beta 3]}\ , \\
\frac{dI_0^{[\alpha+\beta 3]}}{dt} &= k_i\ I_1^{[\alpha+\beta 3]} - (4\ [\mathrm{Ca}]_i + k_{b_0})\ I_0^{[\alpha+\beta 3]} + k_{b_0}\ O_0^{[\alpha+\beta 3]}\ , \\
\frac{dO_0^{[\alpha+\beta 3]}}{dt} &= k_o\ O_1^{[\alpha+\beta 3]} - (4\ [\mathrm{Ca}]_i + k_{r_0} + k_{b_0})\ O_0^{[\alpha+\beta 3]} + k_{f_0}\ C_0^{[\alpha+\beta 3]} + k_{u_0}\ I_0^{[\alpha+\beta 3]}\ , \\
\frac{dC_4^{[\alpha+\beta 3]}}{dt} &= [\mathrm{Ca}]_i\ C_3^{[\alpha+\beta 3]} - (4\ k_c + k_{f_4})C_4^{[\alpha+\beta 3]} + k_{r_4}\ O_4^{[\alpha+\beta 3]}\ , \\
\frac{dO_4^{[\alpha+\beta 3]}}{dt} &= [\mathrm{Ca}]_i\ O_3^{[\alpha+\beta 3]} - (4\ k_o + k_{r_4} + k_{b_4})O_4^{[\alpha+\beta 3]} + k_{f_4}\ C_4^{[\alpha+\beta 3]} + k_{u_4}\ I_4^{[\alpha+\beta 3]}\ , \\
\frac{dI_4^{[\alpha+\beta 3]}}{dt} &= [\mathrm{Ca}]_i\ I_3^{[\alpha+\beta 3]} - (4\ k_i + k_{u_4})I_4^{[\alpha+\beta 3]} + k_{b_4}\ O_4^{[\alpha+\beta 3]}\ , \\
\frac{dC_n^{[\alpha+\beta 3]}}{dt} &= (5-n)[\mathrm{Ca}]_i\ C_{n-1}^{[\alpha+\beta 3]} + (n+1)k_c\ C_{n+1}^{[\alpha+\beta 3]} - (n\ k_c + (5-n-1)[\mathrm{Ca}]_i \\
&\quad -k_{f_n})C_n^{[\alpha+\beta 3]} + k_{r_n}\ O_n^{[\alpha+\beta 3]}\ , \\
\frac{dO_n^{[\alpha+\beta 3]}}{dt} &= (5-n)[\mathrm{Ca}]_i\ O_{n-1}^{[\alpha+\beta 3]} + (n+1)k_o\ O_{n+1}^{[\alpha+\beta 3]} - (n\ k_o + (5-n-1)[\mathrm{Ca}]_i \\
&\quad -k_{r_n} + k_{b_n})O_n^{[\alpha+\beta 3]} + k_{f_n}\ C_n^{[\alpha+\beta 3]} + k_{u_n}\ I_n^{[\alpha+\beta 3]}\ , \\
\frac{dI_n^{[\alpha+\beta 3]}}{dt} &= (5-n)[\mathrm{Ca}]_i\ I_{n-1}^{[\alpha+\beta 3]} + (n+1)k_i\ I_{n+1}^{[\alpha+\beta 3]} - (n\ k_i + (5-n-1)[\mathrm{Ca}]_i \\
&\quad -k_{u_n})I_n^{[\alpha+\beta 3]} + k_{b_n}\ O_n^{[\alpha+\beta 3]} \qquad \text{where } n = 1, 2, 3\ ,
\end{aligned}
\tag{4.87}
$$

with

$$
\begin{aligned}
k_f &= k_{f_i}\ e^{(\frac{z_f VF}{RT})}\ , \\
k_r &= k_{r_i}\ e^{(\frac{z_r VF}{RT})}\ , \\
k_b &= k_{b_i}\ e^{(\frac{z_b VF}{RT})}\ , \\
k_u &= k_{u_i}\ e^{(\frac{z_u VF}{RT})} \qquad \text{where } i = 0, 1, 2, 3, 4\ .
\end{aligned}
\tag{4.88}
$$

The parameter values are taken from Lingle et al [99]; the values, definitions and units are in Table 4.18.

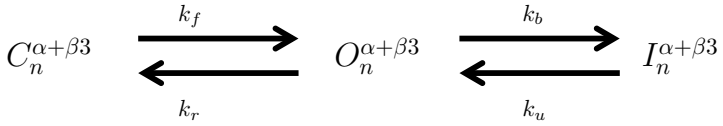

Figure 4.23: State transition diagram of the Markov model for the $BK_{\alpha+\beta3}$ channel.
$C_n^{[\alpha+\beta3]}$ is the closed state, $O_n^{[\alpha+\beta3]}$ is the open state, and $I_n^{[\alpha+\beta3]}$ is the inactivation state (n=15). k_f, k_r, k_b, and k_u are the transition rates between the states.

Table 4.18: Notation for the $BK_{\alpha+\beta3}$ channel

Parameter	Definition	Value
$G_{BK_{\alpha+\beta3}}$	$BK_{\alpha+\beta3}$ unitary conductance	289 pS
$\kappa_{BK_{\alpha+\beta3}}$	$BK_{\alpha+\beta3}$ channel density	–
k_{f_0}	Closed to open transition rate at 0 mV	1 s^{-1}
k_{f_1}	”	2 s^{-1}
k_{f_2}	”	6 s^{-1}
k_{f_3}	”	250 s^{-1}
k_{f_4}	”	500 s^{-1}
k_{r_0}	Open to close transition rate at 0 mV	4000 s^{-1}
k_{r_1}	”	1200 s^{-1}
k_{r_2}	”	800 s^{-1}
k_{r_3}	”	500 s^{-1}
k_{r_4}	”	100 s^{-1}
k_{b_n}	Open to inactivated transition rate at 0 mV	900 s^{-1}
k_{b_0}	”	900 s^{-1}
k_{b_4}	”	900 s^{-1}
k_{u_n}	Inactivated to open transition rate at 0 mV	750 s^{-1}
k_{u_0}	”	750 s^{-1}
k_{u_4}	”	750 s^{-1}
z_f	Gating charge	0.72e
z_r	”	0.67 e
z_b	”	0.072 e
z_u	”	0.361 e
k_c	Closed states dissociation constant	11.2
k_o	Open states dissociation constant	0.75
k_i	Inactivation states dissociation constant	0.72
State variables		
$P_{oBK_{\alpha+\beta3}}$	Open probability	

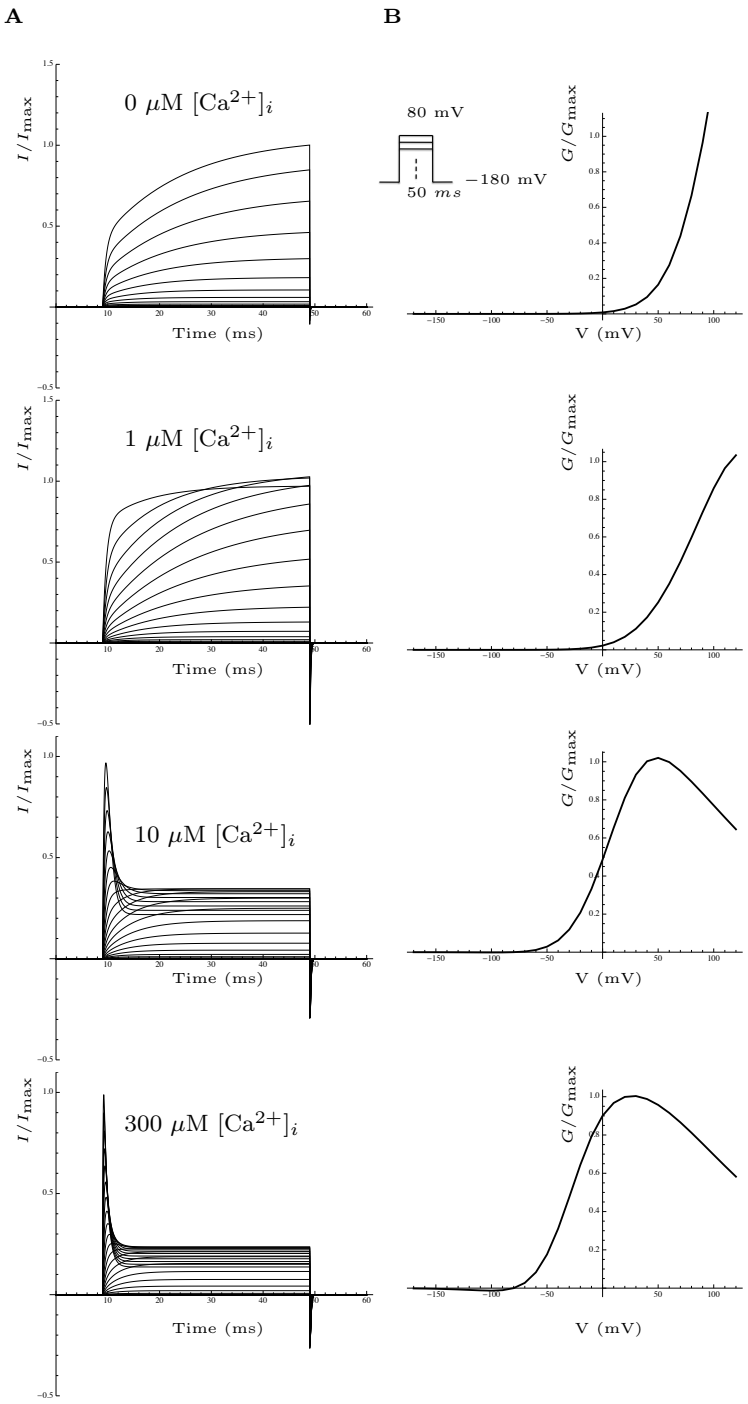

Figure 4.24: Properties of the $I_{\mathbf{BK}_{\alpha+\beta 3}}$.
(A) Simulated voltage clamp traces of $\mathrm{BK}_{\alpha+\beta 3}$ channel from holding potential of −180 mV, the voltage was stepped to values up to +80 mV in 10 mV increments for various μM $[\mathrm{Ca}^{2+}]_i$, then stepped back to −180 mV. (B) Simulated steady-state I-V curve obtained from the series of voltage clamp experiments shown in (A). Values are normalised to the peak current values.

Calcium-dependent potassium channel BK$_{\alpha+\beta4}$

Another potassium current is carried by the channel composed of the BK α-subunit, associated with the *KCNMB4* gene (or β4-subunit). The subunit was found at transcript level [8, 90]. The ΔCT for β4-subunit was 19.13±0.19 (normalised to r18s mRNA) in samples taken from non-pregnant patients and 21.15±0.04 in samples taken from pregnant patients [90]. The β4-subunit changes the biophysical characteristics of the α-subunit; it slows down the gating kinetics (the activation kinetics is reduced by almost 30 ms [147]), reduces the apparent voltage sensitivity of the channel activation, i.e. shifts the activation range to more depolarised voltages [147], and has complex effects on the apparent $[Ca^{2+}]_i$ sensitivity [101]. Unlike previous BK channels, expression with the β4-subunit decreases the calcium sensitivity in low $[Ca^{2+}]_i$, while increases the sensitivity in high $[Ca^{2+}]_i$. The most profound effect of β4-subunit is the decrease of the open channel probability of at least 11-fold (relative to α alone) in the absence of calcium binding and voltage sensor activation [148]. On the other hand, the subunit promotes the channel opening by increasing the voltage-dependence of the open probability at negative membrane potential. Similar to the other BK channels, we model the BK$_{\alpha+\beta4}$ using the allosteric model according to Horrigan et al [100] and we adopt the parameters from Wang et al [101]. The current through this channel is:

$$I_{\mathrm{BK}_{\alpha+\beta4}} = \kappa_{\mathrm{BK}_{\alpha+\beta4}} P_{o\mathrm{BK}_{\alpha+\beta4}} (V - E_{\mathrm{K}}), \tag{4.89}$$

where $\kappa_{\mathrm{BK}_{\alpha+\beta4}}$ is the channel density and $P_{o\mathrm{BK}_{\alpha+\beta4}}$ is the open channel probability.

We use the equations by Wang et al [101] to model the BK$_{\alpha+\beta4}$ channel as follows:

$$P_{o\mathrm{BK}_{\alpha+\beta4_{ss}}} = \frac{1}{1 + \frac{(1+J+K+JKE)^4}{L(1+KC+JKCDE)^4}}\ , \tag{4.90}$$

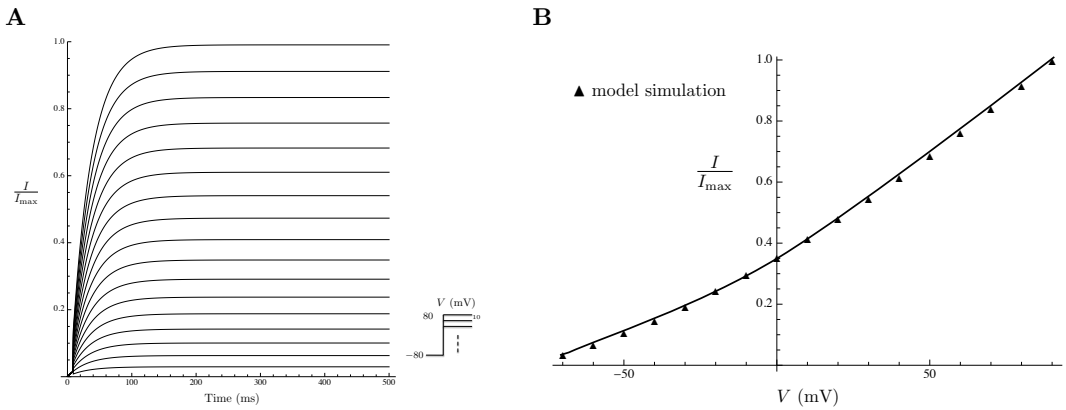

Figure 4.25: Properties of the $I_{\mathbf{BK}_{\alpha+\beta 4}}$. (A) Simulated voltage clamp traces of $\mathrm{BK}_{\alpha+\beta 4}$ channel from holding potential of −80 mV, the voltage was stepped to values up to +80 mV in 10 mV increments in 10 μM $[\mathrm{Ca}^{2+}]_i$. (B) Simulated peak I-V curve obtained from the series of voltage clamp experiments shown in (A). Values are normalised to the peak current values.

where

$$\begin{aligned} L &= L_0 e^{(\frac{-z_l FV}{RT})} , \\ J &= e^{(\frac{-z_j FV}{RT})} , \\ K &= \frac{[\mathrm{Ca}^{2+}]_i}{k_c} , \\ D &= e^{(\frac{-z_j F(V_{ho}-V_{hc})}{RT})} , \\ C &= \frac{k_c}{k_o} , \\ \tau_{\mathrm{BK}_{\alpha+\beta_4}} &= \tau_{\mathrm{BK}_\alpha} + 30 . \end{aligned} \tag{4.91}$$

The parameter values are taken from Wang et al [101]. The descriptions, values and units are stated in Table 4.19.

Table 4.19: Notation for the $BK_{\alpha+\beta4}$ channel

Parameter	Definition	Value
$G_{BK_{\alpha+\beta4}}$	$BK_{\alpha+\beta4}$ unitary conductance	289 pS
$\kappa_{BK_{\alpha+\beta4}}$	$BK_{\alpha+\beta4}$ channel density	–
L_0	The zero voltage value of L	$3.7*10^{-8}$
z_L	The partial charge of L	0.3 e
J_0	The zero voltage value of J	1
z_j	The partial charge of J	0.55 e
K_c	Calcium dissociation constant (closed channel and resting voltage sensors)	44 μM
C	Allosteric factor describing interaction between channel opening and calcium binding	23
K_o	Calcium dissociation constant (open channel, resting voltage sensors)	1.9 μM
D	Allosteric factor describing interaction between channel opening and voltage sensor activation	32
V_{ho}	Voltage sensor's half activation V when channel is open	25 mV
V_{hc}	Voltage sensor's half activation V when channel is closed	187 mV
E	Allosteric factor describing interaction between calcium binding and voltage sensor activation	3.7
$P_{BK_{\alpha+\beta4_{ss}}}$	Steady-state activation variable	
State variables		
$P_{oBK_{\alpha+\beta4}}$	Open-state probabiliity	

4.1.3 Calcium-gated potassium channels

Small and intermediate calcium-activated potassium channels (SK) constitute a subfamily of the calcium-activated potassium channels, along with the BKs. They are so called because of their small unitary conductance in the range of 2–10 pS. The $[Ca^{2+}]_i$ controls the SK channel gating mechanism. Calcium binds to protein Calmodulin (CaM), which binds to a CaM binding domain on the intracellular side of the SK channel. Four CaM-binding domains need to bind to CaM/calcium complex to change the SK conformation, which allows the channel to open.

Calcium-dependent potassium channel SK_1

A potassium current is elicited by the small-conductance calcium-activated potassium channel SK_1, encoded by the gene *KCNN1*. The channel is extremely sensitive to changes in $[Ca^{2+}]_i$. Low concentration of $[Ca^{2+}]_i$ (300–700 nM) activates the SK channel to 50%; this high degree of cooperativity is manifested in the calcium-dependence of the activation of the channel described by a Hill coefficient ranging from 3 to 5 [149]. The time constant for channel activation ranges from 5–15 ms; the single channel conductance is in the range between 2–10 pS. At mRNA level (according to RT-PCR in conjunction with LCM [90]), SK_1 is expressed with ΔCT of 21.66±0.11 (normalised to r18s mRNA) in samples taken from non-pregnant patients and 27.05±0.07 in samples taken form pregnant patients [90]. The level of expression of this channel is significantly different between pregnant to non-pregnant uterus. Köhler et al [20] cloned the human SK_1 (hSK_1) channel in *Xenopus* oocytes, resulting in a calcium-activated, linearly-dependent on voltage, potassium current with a half maximal effective calcium concentration $EC_{50\%} = 0.71\ \mu M$ and a Hill coefficient $n_h = 3.9$ [20]. The channel conductance is plotted as a function of $[Ca^{2+}]_i$ and is shown in Figure 4.26. The activation time constant, determined from a mono exponential fit, is assumed invariant, $\tau_{SK_1} = 5.8$ ms [22]. All parameters, their values, and their definitions are stated in Table 4.20. The current through SK_1 is:

$$I_{SK_1} = \kappa_{SK_1} G_{SK_1} P_{oSK_1} (V - E_K) \ , \tag{4.92}$$

where κ_{SK1} is the channel density, G_{SK1} the single channel conductance, and P_{oSK1} is the activation gate with gating kinetics $P_{SK1_{ss}}$ and τ_{SK_1}.
We describe the steady state open probability for SK1 by the Hill equation as follows:

$$P_{SK_{1ss}} = \frac{{[Ca^{2+}]_i}^4}{(0.71)^4 + {[Ca^{2+}]_i}^4} \ . \tag{4.93}$$

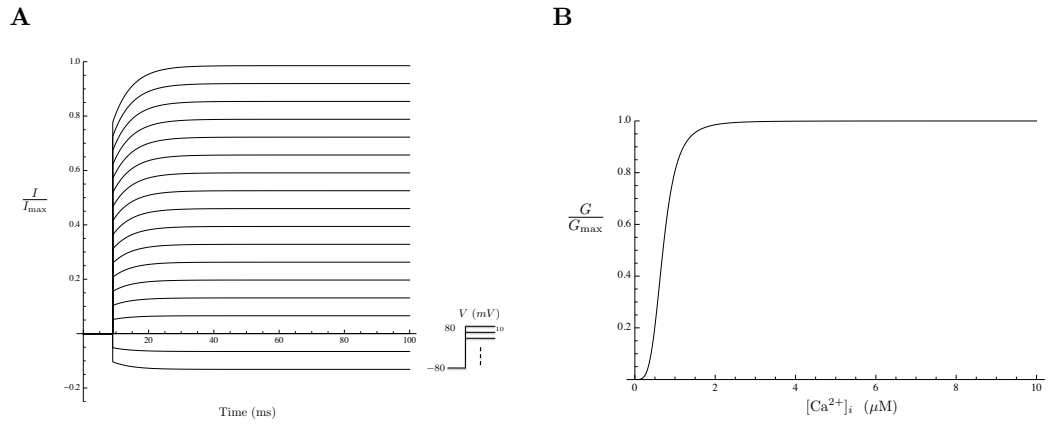

Figure 4.26: Properties of the $I_{\mathbf{SK1}}$.
(A) Simulated voltage clamp traces of SK1 channel from holding potential of −80 mV, the voltage was stepped to test potential between +80 mV and −100 mV in 10 mV increments in 5 μM $[Ca^{2+}]_i$ (B) Activation variable obtained from experimental data of Köhler et al [20] as function of $[Ca^{2+}]_i$.

Table 4.20: Notation for the SK_1 Potassium Channel

Notation	Definition	Value
G_{SK_1}	SK_1 unitary conductance	2 pS
κ_{SK_1}	SK_1 channel density	–
$P_{SK_{1ss}}$	Steady state activation variable	
τ_{SK_1}	Activation time constant	5.8ms
State variables		
P_{oSK_1}	Open channel probability	

Calcium-dependent potassium channel SK_2

A potassium current is carried by the SK_2 channel encoded by the gene *KCNN2*. The SK_2 is the second member of the small conductance calcium-activated and voltage-independent potassium channel family. When macroscopic currents were recorded from *Xenopus* oocytes expressing the rSK_2, the average open probability was 0.42 ±0.12 in 0.6 μM of $[Ca^{2+}]_i$ and 0.74 ±0.16 in 1 μM [20]. The open probability as a function of $[Ca^{2+}]_i$ fits to a Hill equation with $EC_{50\%} = 0.74$ μM and a Hill coefficient n_h =2.2 [20, 21] (Figure 4.27). The SK_2 is expressed at mRNA level [8, 90]. According to qRT-PCR screening to laser capture micro dissected myometrial smooth muscles, the ΔCT was 20.42±0.05 (normalised to r18s mRNA) in samples taken from non-pregnant patients and 20.58±0.17 in samples taken from pregnant patients [90]. Hirschberg et al [21] expressed this channel in *Xenopus*

oocytes and predicted the activation time constant of the SK_2 current from their experiment. Figure 4.27 shows a plot of the activation rate (τ^{-1}) versus $[Ca^{2+}]_i$. Over the range of 0.2 to 10 μM $[Ca^{2+}]_i$, the model predicted an approximately linear relationship between the activation rate of the macroscopic current and the $[Ca^{2+}]_i$. We extract the time constant from the activation rate data of Hirschberg et al [21] after fitting the activation rate to a linear function of $[Ca^{2+}]_i$. The current from the SK_2 is:

$$I_{SK_2} = \kappa_{SK_2} G_{SK_2} P_{oSK_2} (V - E_K) \ , \tag{4.94}$$

where P_{oSK_2} is the open channel probability with corresponding steady state $P_{SK_{2ss}}$ variable calculated with the following equation:

$$P_{SK_{2ss}} = P_{0,max} \frac{{[Ca^{2+}]_i}^{2.2}}{(0.74)^{2.2} + {[Ca^{2+}]_i}^{2.2}} \ , \tag{4.95}$$

and corresponding time constant extracted from the following equation:

$$\tau^{-1}_{SK_2} = -1.3 + 45.5[Ca^{2+}]_i \ . \tag{4.96}$$

The values of parameters and their units are shown in Table 4.21.

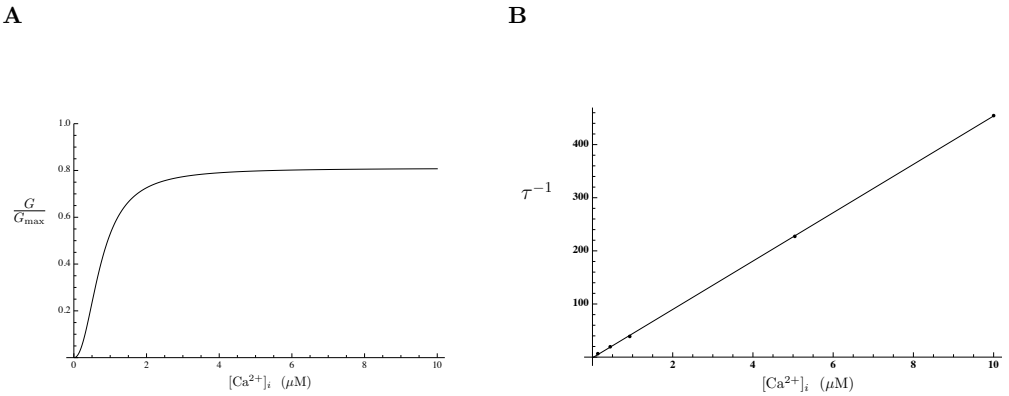

Figure 4.27: Properties of the I_{SK_2}.
(A) Activation variable as a function of $[Ca^{2+}]_i$ obtained from experimental data of Hirschbeg et al [21] as function of $[Ca^{2+}]_i$. (B) Activation time constant obtained from simulated current traces as function of $[Ca^{2+}]_i$

.

Table 4.21: Notation for the SK_2 Potassium Channel

Notation	Definition	Value
G_{SK_2}	SK_2 unitary conductance	2 pS
κ_{SK_2}	SK_2 Channel density	–
$P_{\mathrm{SK}_{2ss}}$	Steady state activation variable	
τ_{SK_2}	Activation time constant in ms	
State variables		
P_{SK_2}	Channel open probability	

***Calcium-dependent potassium channel SK*$_3$**

The third member of the calcium-activated potassium channel is the SK_3, which is encoded by the *KCNN3* gene. This channel is activated by $[Ca^{2+}]_i$ and similar to the rest of the SK family members, activation is voltage-independent. SK_3 is highly expressed at mRNA level with significant difference between pregnant and non-pregnant uterus. ΔCT is 16.55±0.24 (normalised to r18s mRNA) in samples taken from non-pregnant patients and 19.16±0.16 in samples taken from pregnant patients (unpublished data). According to Barfod et al [150], this channel experiences voltage-dependent inactivation at voltages more positive than -40mV. Due to lack of data about SK_3 voltage-dependent steady-state inactivation variable, we ignored the inactivation in our model. The calcium-dependent activation process is described with a Hill equation with $EC_{50\%} = 0.3$ μMole and a Hill coefficient $n_h = 5$ [22]. We assumed one invariant activation time constant $\tau_{\mathrm{SK}_3a} = 12.9$ ms. Brown et al [151] suggested that SK_3 plays a role in regulating uterine function by limiting the L-type calcium influx. This contributes to a negative feedback that regulates myometrial $[Ca^{2+}]_i$ and consequently help the relaxation of uterus, and interrupt phasic contractile events. SK_3 was found to be much less expressed during labour, allowing L-type calcium channel activity [151]. The current from the SK_3 is thus:

$$I_{\mathrm{SK}_3} = \kappa_{\mathrm{SK}_3} G_{\mathrm{SK}_3} P_{\mathrm{SK}_3} (V - E_{\mathrm{K}}) \,, \tag{4.97}$$

where κ_{SK_3} is the channel density, G_{SK_3} the single channel conductance, and P_{SK_3} is the activation gate with gating kinetics $P_{\mathrm{SK3}_{ss}}$ and $\tau_{\mathrm{SK3}a}$ calculated using the following equations:

$$\begin{aligned} P_{SK_{3ss}} &= \frac{{[Ca^{2+}]_i}^5}{(0.6)^5 + {[Ca^{2+}]_i}^5} \,, \\ \tau_{\mathrm{SK}_3a} &= 12.9 \text{ ms} \,. \end{aligned} \tag{4.98}$$

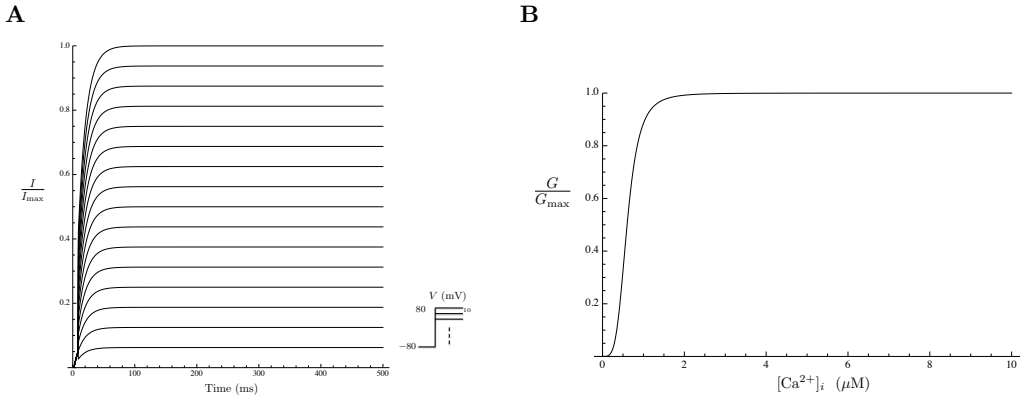

Figure 4.28: Properties of the $I_{\mathbf{SK_3}}$.
(A) Simulated voltage clamp traces of SK_3 channel from holding potential of −80 mV, the voltage was stepped to test potential up to +80 mV in 10 mV increments in 5 μM $[Ca^{2+}]_i$. (B) Activation variable obtained from experimental data of Xia et al [22] as function of $[Ca^{2+}]_i$.

Table 4.22: Notation for the SK_3 Potassium Channel

Notation	Definition	Value
G_{SK_3}	SK_3 unitary conductance	2 pS
κ_{SK_3}	SK_3 channel density	–
$P_{SK_{3ss}}$	Steady state activation variable	
τ_{SK_3}	Activation time constant	13 ms
State variables		
P_{SK_3}	Channel open probability	

Calcium-dependent potassium channel SK$_4$

The channel SK4 is also called the intermediate potassium channel IK1. This channel is activated via Calmodulin-dependent mechanism. It is considered to be a member of the SK family due to similar properties: the relatively low conductance of about 11 pS (higher than the other SKs) [102]; the weak dependence of their activity on membrane potential; and their calcium dependence. This channel has a significantly high affinity to calcium, according to Joiner et al [102], with $EC_{50\%} = 95$ nMole. The activation process is described by the Hill equation with Hill coefficient $n_H = 3.2$. We assume one invariant activation time constant similar to SK$_1$, $\tau_{\mathrm{SK}_4} = 5.8$ ms. The current from the SK$_4$ is:

$$I_{\mathrm{SK}_4} = \kappa_{\mathrm{SK}_4} G_{\mathrm{SK}_4} P_{o\mathrm{SK}_4} (V - E_{\mathrm{K}}) \ , \tag{4.99}$$

where κ_{SK_4} is the channel density, G_{SK_4} the single channel conductance, and $P_{o\mathrm{SK}_4}$ is the activation variable with gating kinetics $P_{\mathrm{SK}_{4ss}}$ and τ_{SK_4} shown in the following equations:

$$\begin{aligned} P_{\mathrm{SK}_{4ss}} &= \frac{[\mathrm{Ca}^{2+}]_i^{\,3.2}}{(0.095)^{3.2} + [\mathrm{Ca}^{2+}]_i^{\,3.2}} \ , \\ \tau_{\mathrm{SK}_4} &= 5.8 \text{ ms} \ . \end{aligned} \tag{4.100}$$

The parameters of SK$_4$, their definitions and values are shown in Table 4.25

Table 4.23: Notation for the SK4 Potassium Channel

Notation	Definition	Value
G_{SK_4}	SK$_4$ unitary conductance	11 pS
κ_{SK_4}	SK$_4$ Channel density	–
$P_{\mathrm{SK}_{4ss}}$	Steady state activation variable	
τ_{SK_4}	Activation time constant	5.8 ms
State variables		
P_{SK_4}	Open channel probability	

4.1.4 Inward rectifying potassium channel

Inward rectifying potassium channel (Kir), encoded by the *KCNJ* gene family, allows more K^+ into the cell than out of the cell; in other words, this family of channels allows larger flow of K^+ in the inward direction at membrane voltages negative to E_K than in the outward direction at voltages positive to E_K, even when the potassium concentrations on both sides of the membrane are made equal [152]. The outward rectification of the Kir channel is decreased due to the blocking of the channel pore by intracellular cations such as Mg^{2+} [153] and polyamines (e.g. spermine) [154, 155]. For more depolarised potentials the conductance decreases, while for more hyperpolarised potentials the conductance increases; the channels have high open channel probability at negative membrane potential, it is then blocked progressively as the membrane depolarises [156]. The inward current depends on external K^+ concentration; usually the current is taken to be roughly proportional to the square root of extracellular K^+ concentration [156]. There are seven subfamilies of the Kir channels (Kir1-Kir7) with nearly identical amino acid sequences across various species. The members of the subfamilies differ in their degree of rectification: some are strong rectifiers and some are weak. Kir channels are tetramers of four homomeric or heteromeric subunits each contains two transmembrane domains with a pore-forming region that allows the K^+ selectivity. The Kir channels are known to be an important regulator of cellular excitability; it helps establishing the RMP by conducting a depolarising potassium current when the potentials are negative to the RMP (hyperpolarized), this restores the cell back to its RMP.

Inward rectifier potassium channel Kir7.1

The channel Kir7.1 encoded by the *KCNJ13* gene is a member of the Kir family; it is $< 37\%$ identical to other Kir subunits [23]. Kir7.1 has a very low estimated single channel conductance ($\sim$50 fS) and no dependence of its inward rectification properties on the internal blocking particle Mg^{2+} [157]. All the unusual pore properties are explained by amino acids in the pore sequence that is different from the corresponding conserved residues in all other Kir channel proteins [23, 157]. Doring et al [23] injected human Kir7.1 into *Xenopus* oocytes. The generated Kir current showed a weakly dependence on $[K^+]_o$, which is another contrast to all other Kir channels. Consequently the dependence of the conductance of Kir7.1 on $[K^+]_o$ was modelled differently than the "roughly square root dependence" used for other Kir channels. We use the variable Y (equation (4.103)), which is function of the extracellular potassium concentration, to indicate a slight increase of current with various

$[K^+]_o$ (shown in Figure 4.29 in a double logarithmic plot). Channel activation kinetics, in response to hyperpolarising voltage pulses between − 60 mV and −150 mV, is rapid. The time constants of current activation at different membrane potentials was determined from single exponential fits to the time course of the current [23] (shown in Figure 4.29). We describe the voltage-dependence of the activation time constant with the equation (4.104). The G-V curve did not follow the typical Boltzmann function, we describe it by a single exponential fit to the data by Doring et al [23] (Figure 4.29). The current mediated by the above channel is:

$$I_{\text{Kir7.1}} = \kappa_{\text{Kir7.1}}\ G_{\text{Kir7.1}}\ P_{o\text{Kir7.1}}\ Y\ (V - E_{\text{K}})\ , \tag{4.101}$$

where $\kappa_{\text{Kir7.1}}$ is the channel density, $P_{o\text{Kir7.1}}$ the open channel probability, $G_{\text{Kir7.1}}$ is the single channel conductance, and Y is a term to account for the dependence of the conductance on $[K^+]_o$. The equations describing these variables are:

$$P_{\text{Kir7.1}_{ss}} = 0.083\ \exp\left[-0.018\ V\right]\ , \tag{4.102}$$

$$Y = 0.65\ [K^+]_o^{\,0.095}\ , \tag{4.103}$$

$$\tau_{\text{Kir7.1}} = 2 + 0.01\ V\ . \tag{4.104}$$

The parameters of Kir7.1, their values, units and definition are in Table 4.24

Table 4.24: Notation for the Kir7.1 Potassium Channel

Notation	Definition	Value
$G_{\text{Kir7.1}}$	Kir7.1unitary conductance	0.056 pS
$\kappa_{\text{Kir7.1}}$	Kir7.1 channel density	–
Y	The slope conductance dependence on $[K^+]_o$	
$P_{\text{Kir7.1}_{ss}}$	Steady state activation	
$\tau_{\text{Kir7.1}}$	Activation time constant in ms	
State variables		
$P_{\text{Kir7.1}}$	Channel open probability	

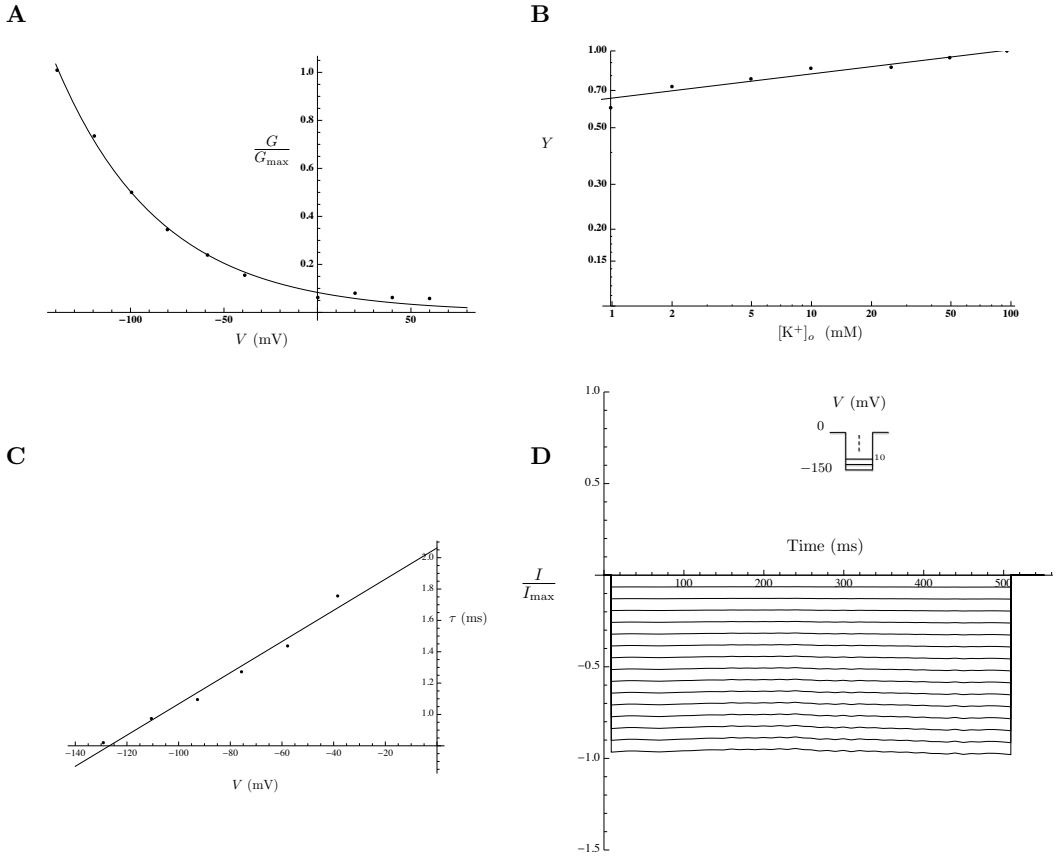

Figure 4.29: Properties of the $I_{\mathbf{Kir7.1}}$.
(A) Steady state activation curve from Doring et al [23] fit by a single exponential. (B) Double logarithmic plot for the Kir7.1 conductance as a function of $[K^+]_o$. (C) Simulated activation time constant derived from experimental data (filled circles) from Doring et al [23]. (D) Current trace generated by the model during simulated voltage-clamp experiments. Currents are recorded during 1 s voltage steps to potentials up to −150 mV from a holding potential of 0 mV. Values are normalised to the peak current values.

ATP-sensitive potassium channel K_{ATP}

Kir6.1 is a member of the Kir family. It is an inward-rectifier channel and a subunit of the ATP-sensitive potassium channel. The gene encoding the Kir6.1 is *KCNJ8*. The Kir6 channels associate with the sulfonylurea receptor (SUB) subunits to form the ATP-sensitive potassium channels. In common with other members of the Kir family, Kir6 subunits have two transmembrane domains that form the potassium selective pore; the SUR subunits have three additional transmembrane domains required for activation. The complex Kir6/SUR, associates with 1:1 stoichiometry to form a large tetrameric channel gated by ATP, also know as $\mathrm{K_{ATP}}$ [158]. It is suggested that the $\mathrm{K_{ATP}}$ channel in MSMC is the Kir6.1/SUR2B [159]. The Kir6.1 was found in the MSMC transcription data [90]; when expressed as a homomer, it acts as a weak inward rectifier. Studies have shown that Kir6.1/SUR2B is down regulated late in pregnancy, which may contribute to increased uterine excitability [159]. The open probability of $\mathrm{K_{ATP}}$ has a very little dependence on membrane potential and time; the I-V curve is linear with a slope of 32.9 pS [160]. The channel current is inhibited by intracellular ATP with IC_{50} = 0.6 mM and a Hill coefficient n =1.2 as shown in Figure 4.30 [161]. The current mediated by the $\mathrm{K_{ATP}}$ is modelled as follows:

$$I_{\mathrm{K_{ATP}}} = \kappa_{\mathrm{K_{ATP}}}\, G_{\mathrm{K_{ATP}}}\, P_{\mathrm{K_{ATP}}}\, (V - E_{\mathrm{K}})\,, \tag{4.105}$$

where $\kappa_{\mathrm{K_{ATP}}}$ is the channel density, $P_{\mathrm{K_{ATP}}}$ is the ATP-dependent open channel probability, and $G_{\mathrm{K_{ATP}}}$ is the single channel conductance. The dose-dependent inhibition of $\mathrm{K_{ATP}}$ current by ATP concentration [ATP] (or the open channel probability) is:

$$P_{\mathrm{K_{ATP}}} = \frac{1}{1 + ([\mathrm{ATP}]/IC_{50})^n}\,. \tag{4.106}$$

Table 4.25: Notation for the $\mathrm{K_{ATP}}$ Potassium Channel

Notation	Definition	Value
$G_{\mathrm{K_{ATP}}}$	$\mathrm{K_{ATP}}$ unitary conductance	32.9 pS
$\kappa_{\mathrm{K_{ATP}}}$	$\mathrm{K_{ATP}}$ Channel density	
$P_{\mathrm{K_{ATP}}}$	Open channel probability	
IC_{50}	Half-maximal inhibitory concentration	0.6 mM
n	Hill coefficient	1.2

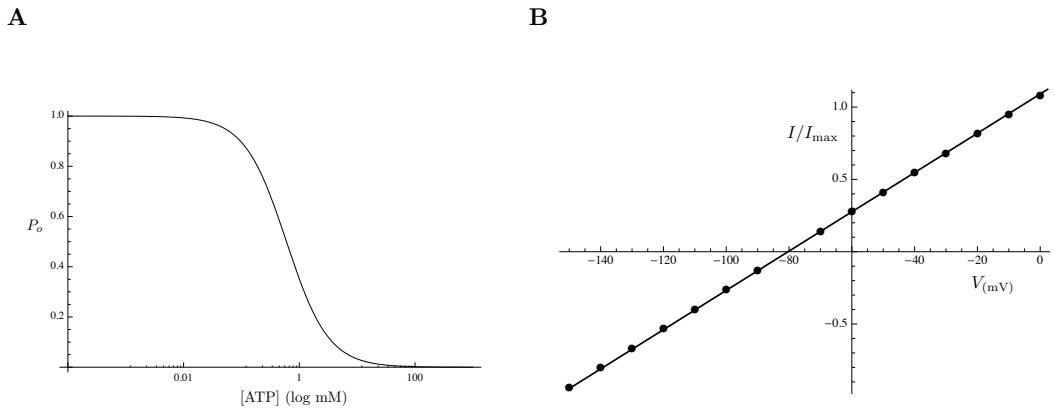

Figure 4.30: Properties of the $I_{\mathbf{K_{ATP}}}$.
(A) Dose-dependent inhibition of K_{ATP} current by ATP concentration. (B) Simulated peak I-V curve obtained from a series of voltage clamp experiments from holding potential of -80 mV and stepping the voltage to values up to $+80$ mV in 10 mV increments in 10 mM [ATP]. Values are normalised to the peak current values.

4.2 Voltage-gated calcium channels

Calcium channels are permeable to calcium ions; voltage-gated calcium channels (VGCC) are found in all excitable cells. Similar to the voltage-gated potassium channels, the VGCCs have a voltage-dependent gate that opens with different kinetics to an increase in membrane potential, then they inactivate during maintained depolarisation. The VGCCs conduct an inward calcium current that causes depolarisation of the membrane. In human MSMCs, the VGCCs account for the electrical excitability in muscle cells [67]. In rodents, they coexist with sodium channels for a partial contribution to the excitability.

VGCCs are essential to excitability. First, the opening of two types of VGCCs contributes to the firing of AP. The low-voltage activated calcium channel (LVA) may open around resting potential giving rise to a small depolarising current. this current opens the high-voltage activated calcium channel (HVA) that depolarises the membrane further and keeps the cell depolarised for some time. Second, calcium ions that flow into the cytoplasm of the muscle cell through the VGCCs act as an intracellular second messenger; the $[Ca^{2+}]_i$ increases transiently causing muscle contraction (as explained in Section 1.2.3). Third, the increase of $[Ca^{2+}]_i$ due to the opening of VGCCs has a direct effect on the gating of many ion channels: calcium, potassium, chloride, and non-specific ion channels. These channels have calcium-binding sites on their intracellular surfaces.

Voltage-gated calcium channel L-type

The L-type is encoded by the $Ca_v2.1$ gene, also known as *CACNA1C*. The gene is expressed at mRNA level [8, 90]. This is a member of the voltage-gated calcium channels family. According to Shmigol et al [36], the L-type is the major source of calcium entry into the MSMC. Upon membrane depolarisation, this HVA channel activates and opens with a sigmoidal time course allowing a calcium influx; then it inactivates. The current starts activating at around -50 mV then peaks at 0 mV [36]. The L-type channel is permeable to Ca^{2+}, K^+, and Na^+ ions but for simplicity, and because the dynamic changes in sodium and potassium concentrations are not accounted for in our model because they do not vary significantly, we assumed that it is only permeable to Ca^{2+}. The calcium reversal potential E_{Ca}, described by the Nernst equation, is allowed to vary according to changes in $[Ca^{2+}]_i$. Activation of the L-type channel is purely voltage-dependent while inactivation is thought to be a calcium-dependent process as well as voltage-dependent. Different values of the gating kinetics have been reported; this may be due to different $[Ca^{2+}]_o$, holding

potential or temperatures used in the experiments. In our model, the steady-state voltage-dependent activation d_∞ is derived from the I-V curve found by Blanks et al [24]. The experiments were performed on human myometrial samples from term, preterm, labour, and not in labour. Certain techniques [24] were used to separate the LVA and the HVA calcium currents. The activation curve was deduced and was described using Boltzmann equation with parameters $V_{\text{half}} = -18.9$ mV and $k = 8.8$ mV (equation (4.108)). These values closely match the values reported in Hu et al [162], when they expressed human $\alpha 1C$-subunit with $\beta 2a$- and $\alpha 2/\delta$-subunits in HEK 293 cells ($V_{\text{half}} = -17$ mV and $k = 7$ mV for smooth muscle cells). Voltage-dependent steady-state inactivation variable f_∞ was fit with a Boltzmann function, shown in equation (4.109), with $V_{\text{half}} = -53$ mV and $k = -9.9$ mV as reported in Shmigol et al [67]. We adopt the formula, for activation time constant, used in the Luo Rudy (LRd) model [104] (equation (4.110)). This time constant τ_d is of the same order of magnitude as the one used in the Tong model taken from the experimental data obtained by Jones et al [163] while studying the calcium activated chloride current in rat uterine myocytes. The inactivation time constant is described using the formula from LRd model [104] (equation (4.111)). The formula for the calcium-dependent steady-state inactivation variable, f_{Ca}, is adopted from the Ten Tusscher model [164] (equation (4.112)). The gating kinetics are shown in Figure 4.31. The current through the L-type channel is described as follows:

$$I_{\text{Ltype}} = \kappa_{\text{Ltype}}\, G_{\text{Ltype}}\, d\, f\, f_{\text{Ca}}(V - E_{\text{Ca}})\,, \tag{4.107}$$

where

$$d_\infty = \frac{1}{(1 + e^{\frac{-(V+18.9)}{8.8}})}\,, \tag{4.108}$$

$$f_\infty = \frac{1}{(1 + e^{\frac{(V+53)}{11}})}\,, \tag{4.109}$$

$$\tau_d = \frac{28.57(1 - e^{\frac{-(V+10)}{6.24}})}{(1 + e^{\frac{-(V+10)}{6.24}})(V + 10)}\,, \tag{4.110}$$

$$\tau_f = \frac{50}{1 + e^{\frac{-(V+10)^2}{881}}}\,, \tag{4.111}$$

$$f_{\text{Ca}} = \frac{1}{(1 + \frac{[\text{Ca}^{2+}]}{0.006})}\,. \tag{4.112}$$

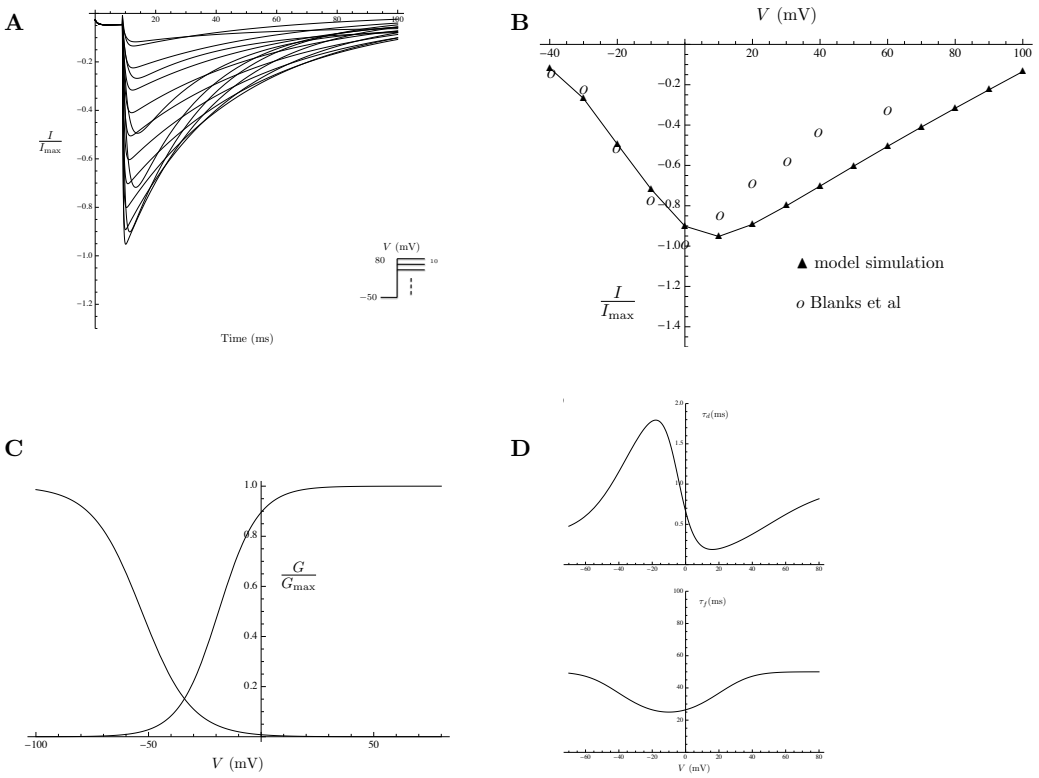

Figure 4.31: Properties of $I_{\text{L-type}}$.
(A) Normalised $I_{\text{L-type}}$ current trace generated by the model during simulated voltage-clamp experiments. Currents are recorded during 1s voltage steps to potentials ranging from -50 to 80 mV from a holding potential of -50 mV. (B) Simulated (solid triangles) peak I-V curve obtained from the series of experiments shown in (A). Values are normalised to the peak current values, data (empty circles) from Blanks et al [24]. (C) Steady state activation and inactivation curves. (D) Simulated activation and inactivation time constant.

Table 4.26: Notation for the L-type Calcium Channel

Notation	Definition	Value
$G_{\text{L-type}}$	L-type unitary conductance	25 pS
$\kappa_{\text{L-type}}$	L-type channel density	–
d_∞	Steady state activation variable	
f_∞	Steady state inactivation variable	
f_{Ca}	Calcium-dependent inactivation variable	
τ_d	Activation time constant in ms	
τ_f	Inactivation time constant in ms	
State variables		
d	Activation gating variable	
f	Inactivation gating variable	

Voltage-gated calcium channel T-type

The primary T-type subunit expressed in some MSMCs is the $Ca_v3.1$ (α1G-subunit) [24], which is encoded by *CACNA1G*. In contrast to the L-type channel, the T-type calcium current is transient and low voltage activated (LVA). It activates at potentials ranging from -50 mV to -30 mV, it begins to open after small depolarisations (10 mV) of plasma membrane [165] and displays fast inactivation. It has a relatively small conductance of 7.5 pS [105], and is detected in many excitable cells. This channel plays a role in the rise in $[Ca^{2+}]_i$ [24], but its main role remains unclear. Perez-Reyes et al [105] transfected HEK-293 cells with rat α1G, data were fitted to the Boltzmann equation to determine the parameters: $V_{\text{half}} = -28.6$ mV and slope is 8.9 mV for activation and $V_{\text{half}} = -72.4$ mV with slope $= -4.8$ mV for inactivation [105]. We calculate the time constants of activation and inactivation from exponential fits to the current traces obtained during test pulses by Perez-Reyes et al [105] (equations (4.116) and (4.117)). The properties of the T-type channel are shown in Figure 4.32. The current through the T-type channel is:

$$I_{\text{T-type}} = \kappa_{\text{T-type}}\, G_{\text{T-type}}\, a\, c\, (V - E_{\text{Ca}})\,, \tag{4.113}$$

where a and c are the activation and inactivation variables with corresponding steady states a_∞ and c_∞ given by the following equations:

$$a_\infty = \frac{1}{1 + e^{(\frac{-28.6-V}{8.9})}}\,, \tag{4.114}$$

$$c_\infty = \frac{1}{1 + e^{(\frac{72.4+V}{4.8})}}\,. \tag{4.115}$$

The activation and inactivation time constants are described as follows:

$$\tau_{\text{a}} = 1.7 + \frac{9.9}{1 + e^{(\frac{V+39}{7.6})}}\,, \tag{4.116}$$

$$\tau_{\text{c}} = 13.7 + \frac{5369.7}{1 + e^{(\frac{V+108.5}{11.24})}}\,. \tag{4.117}$$

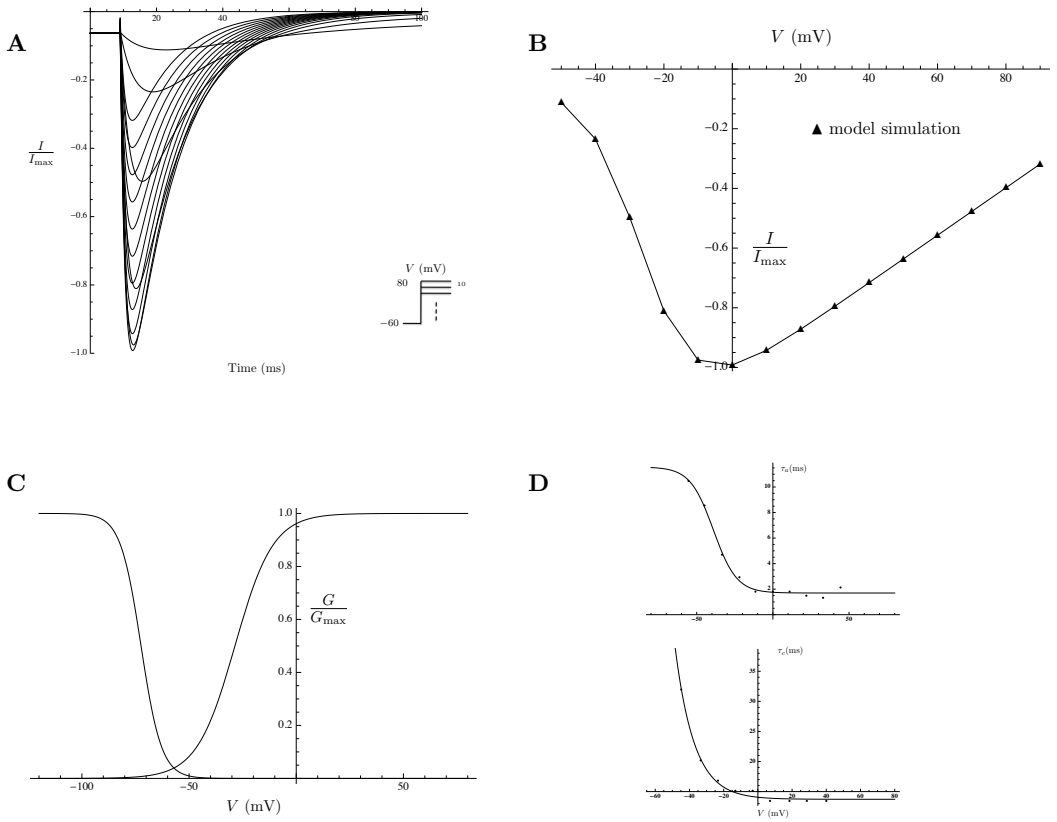

Figure 4.32: Properties of $I_{\text{T-type}}$.
(A) Normalised $I_{\text{T-type}}$ current trace generated by the model during simulated voltage-clamp experiments. Currents are recorded during 1s voltage steps to potentials ranging from -60 to 80 mV from a holding potential of -60 mV. (B) Simulated (filled circles) peak I-V curve obtained from the series of experiments shown in (A). Values are normalised to the peak current values. (C) Steady state activation and inactivation curves. (D) Simulated activation and inactivation time constant.

Table 4.27: Notation for the T-type Calcium Channel

Notation	Definition	Value
$G_{\text{T-type}}$	T-type unitary conductance	8 pS
$\kappa_{\text{T-type}}$	T-type channel density	–
a_∞	Steady state activation variable	
c_∞	Steady state inactivation variable	
τ_a	Activation time constant in ms	ms
τ_c	Inactivation time constant in ms	
State variables		
a	Activation gating variable	
c	Inactivation gating variable	

4.3 Calcium-dependent chloride channels

Calcium-dependent chloride channel CaCC

The calcium-activated chloride channel in MSMC is encoded by the gene *ANNO1*. The channel is voltage- and calcium-dependent; increasing $[Ca^{2+}]_i$ induces an increase in Cl^- current at all membrane potentials [106]. The steady-state *I-V* relationship showed outward rectification at low $[Ca^{2+}]_i$, then the *I-V* curve becomes linear as $[Ca^{2+}]_i$ increases because of a shift in the channel's activation towards more negative potentials. We adopt the model by Arreola et al [106]; the calcium-dependence of the steady-state channel activation at various membrane potentials was fitted using the Hill equation. The dissociation constant K_d and the Hill coefficient, were, in turn, both functions of the membrane potential [106]. Figure 4.33 shows the relative conductance obtained for voltage values of −66 mV and +74 mV for different $[Ca^{2+}]_i$, the K_d was 360 nM and 73 nM and the Hill coefficient was 1.2 and 2.3, respectively. Equations (4.119) and (4.120), representing the steady state activation and the corresponding time constant, together with the model parameters, K_1 and K_2 (equations (4.121)), are all taken from Arreola et al [106]. The chloride current is given by:

$$I_{\mathrm{CaCC}} = \kappa_{\mathrm{CaCC}}\, G_{\mathrm{CaCC}}\, cc\, (V - E_{\mathrm{Cl}})\,, \tag{4.118}$$

where

$$cc_\infty = \frac{1}{1 + K_2\, (\frac{K_1^2}{[\mathrm{Ca}^{2+}]^2} + \frac{K_1}{[\mathrm{Ca}^{2+}]} + 1)}\,, \tag{4.119}$$

$$\frac{1}{\tau_{cc}} = \frac{0.38}{\frac{K_1^2}{[\mathrm{Ca}^{2+}]^2} + \frac{K_1}{[\mathrm{Ca}^{2+}]} + 1} + 0.38\; K_2 \quad \mathrm{s}^{-1}\,, \tag{4.120}$$

with

$$\begin{aligned} K_1 &= 214\; e^{0.13\; FV/RT} \quad \mathrm{nM}\,, \\ K_2 &= 0.58\; e^{-0.24\; FV/RT} \quad \mathrm{nM}\,. \end{aligned} \tag{4.121}$$

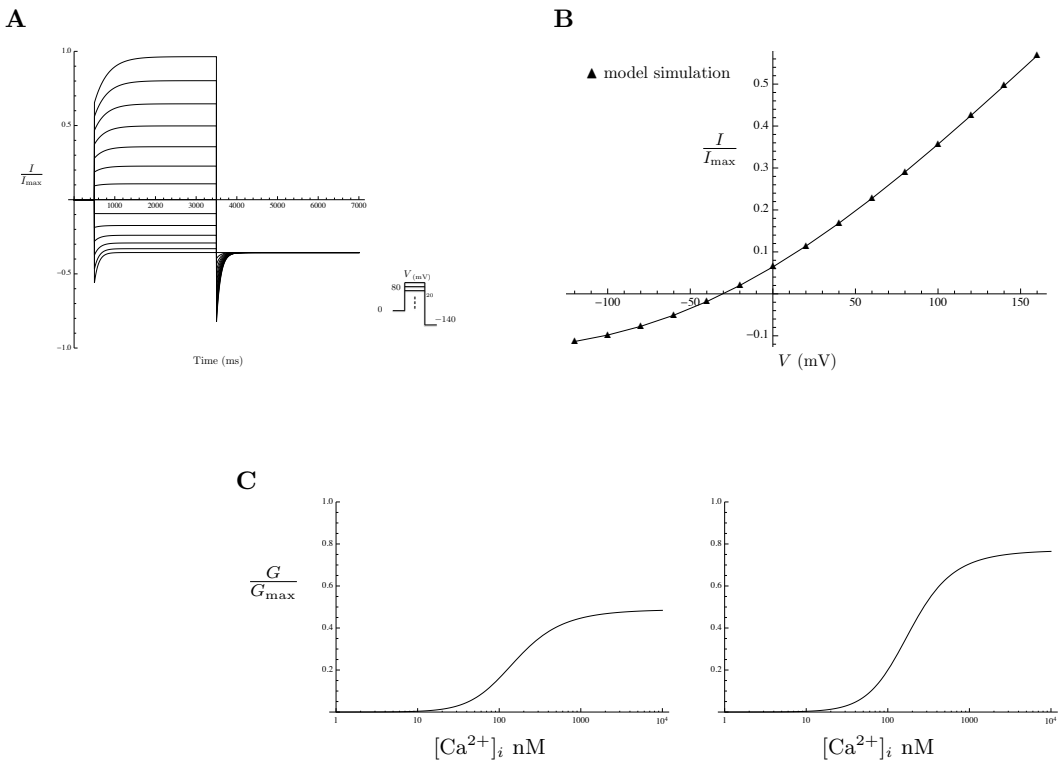

Figure 4.33: Properties of $I_{\mathbf{CaCC}}$.
(A) Normalised I_{CaCC} current trace generated by the model during simulated voltage-clamp experiments. Currents are recorded during 1s voltage steps to potentials ranging from -120 to 140 mV from a holding potential of 0 mV then followed by a repolarising pulse to -140 mV. (B) Simulated steady-state I-V curve obtained from the series of experiments shown in (A). Values are normalised to the peak current values. (C) $[\mathrm{Ca}^{2+}]_i$-dependence of CaCC channel activation. Conductance as a function of $[\mathrm{Ca}^{2+}]_i$ at -66 mV and $+74$ mV, respectively.

Table 4.28: Notation for the CaCC Chloride Channel

Notation	Definition	Value
G_{CaCC}	CaCC unitary conductance	7.5 pS
κ_{CaCC}	CaCC channel density	–
cc_∞	Steady state activation variable	
τ_{cc}	Activation time constan in ms	
State variables		
cc	Activation gating variable	

4.4 Ligand-gated channels

Purinergic membrane receptor P2RX4

The P2X4 receptor (P2RX4) is a member of ATP-gated cation receptor channel family. This family of ligand-gated ion channel receptors is composed of three subunits. Each subunit has two transmembrane domains [166]. Evidence of the existence of the P2RX4 channel in the MSMC and how we introduce it in the model is discussed in detail in Chapter 5. The channel is activated by extracellular ATP; continuous presence of ATP evoked a rapid inward current that desensitises. P2RX4 activates and deactivates rapidly and desensitises relatively slowly (within seconds of continuous agonist application). The rates of activation and desensitisation are dependent on $[\mathrm{ATP}]_o$ [167]. The activation and desensitisation time constants inversely correlate with $[\mathrm{ATP}]_o$. We describe the ATP-dependent steady-state of the activation variable by Hill equation chosen to fit experimental data by Toulme et al [25] (equation (4.125)), the fit give half maximal concentration EC_{50} of 32 μM for ATP and a Hill coefficient of 1.6 (shown in Figure 4.34). We extract the time constants of activation and desensitisation τ_{act}, τ_{des}, from the P2RX4 ATP-dependent current trace from Toulme et al [25] by fitting a single exponential to the data (equations (4.126) and (4.127)). The simulated current trace is shown in Figure 4.34. The P2RX4 is highly permeable to Ca^{2+} while equally permeable to Na^+ and K^+; it is however not permeable to Cl^- [168]. It is also permeable to other monovalent ions with a ratio of calcium to monovalent permeability $P_{\mathrm{Ca}}/P_{\mathrm{mono}}$ of 4.2. To calculate the reversal potential of the P2RX4, E_{P2RX4}, we use the modified GHK equation used for a mixtures of permeant ions of different valences [31, 56, 169]. The unitary conductance was about 36 pS [168]. The current mediated by the P2X4 receptor is described as follows:

$$I_{\mathrm{P2RX4}} = \kappa_{\mathrm{P2RX4}} G_{\mathrm{P2RX4}} P_{\mathrm{act}} P_{\mathrm{des}} (V - E_{\mathrm{P2RX4}}) \; . \tag{4.122}$$

where κ_{P2RX4} is the P2RX4 channel density , G_{P2RX4} is the unitary conductance, and P_{act} and P_{des} are the activation and desensitisation gating kinetics, respectively. The reversal potential for the modified GHK equation [56, 169] is:

$$E_{\mathrm{P2RX4}} = \frac{RT}{F} \ln \frac{[\mathrm{Na}^+]_o + \frac{P_{\mathrm{K}}}{P_{\mathrm{Na}}}[\mathrm{K}^+]_o + 4\frac{P'_{\mathrm{Ca}}}{P_{\mathrm{Na}}}[\mathrm{Ca}^{2+}]_o}{[\mathrm{Na}^+]_i + \frac{P_{\mathrm{K}}}{P_{\mathrm{Na}}}[\mathrm{K}^+]_i + 4\frac{P'_{\mathrm{Ca}}}{P_{\mathrm{Na}}}[\mathrm{Ca}^{2+}]_i e^{(\frac{FV}{RT})}} \; , \tag{4.123}$$

where

$$P'_{\mathrm{Ca}} = \frac{P_{\mathrm{Ca}}}{1 + e^{FV/RT}} \; . \tag{4.124}$$

The equations describing the P2RX4 ATP-dependent kinetics are:

$$P_{\mathrm{act}_{ss}} = \frac{[\mathrm{ATP}]_o^{1.6}}{32^{1.6} + [\mathrm{ATP}]_o^{1.6}} \ , \tag{4.125}$$

$$\tau_{\mathrm{des}} = 1000 + \frac{20000}{1 + e^{0.09(-47.32+[\mathrm{ATP}]_o)}} \ , \tag{4.126}$$

$$\tau_{\mathrm{deac}} = \frac{540}{(1 + e^{0.02(-10-[\mathrm{ATP}]_o)})(1 + e^{0.00065(-80+[\mathrm{ATP}]_o)})} \ . \tag{4.127}$$

The parameters used to model the P2X4 kinetics and their values are shown in Table 4.29

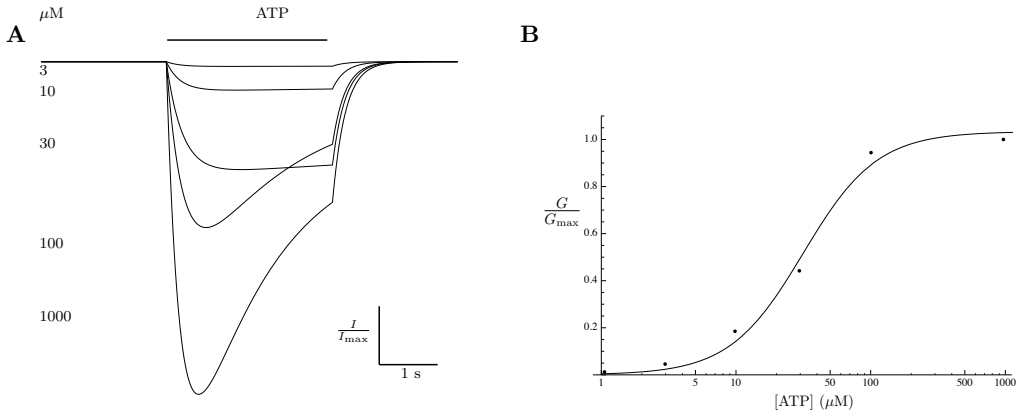

Figure 4.34: Properties of the I_{P2RX4}.
(A) Normalised I_{P2RX4} current trace generated by the model for various ATP concentrations at holding potential of -60 mV. (B) Simulated ATP-concentration effect curve (solid line) and experimental data by Toulme et al [25] (solid circles). Values are normalised to the peak current values.

Table 4.29: Notation for the P2RX4 receptor

Notation	Definition	Value
G_{P2RX4}	P2RX4 unitary conductance	36 pS
κ_{P2RX4}	P2RX4 channel density	
$P_{\mathrm{act}_{ss}}$	Steady state activation variable	
τ_{deac}	Activation and deactivation time constant	ms
τ_{des}	Desensitisation time constant	ms
State variables		
P_{act}	Activation gating variable	

Purinergic membrane receptor P2RX7

The P2X7 receptor (P2RX7) is expressed in myometrial cells according to mRNA expression data [8]. The channel is a member of the family of ATP-gated nonselective cation channels. Activation and deactivation of P2RX7 was reported to follow a complex pattern of gating [170–174]. To model the kinetics we adopt the Markov state gating model by Yan et al [174]. The model consists of 8 states described by the scheme in Figure 4.35. The equations are taken from Yan et al [174] and are shown below, together with the parameter values and definitions. The states of the receptor have various ATP bound: in C1 and C4 no ATP is bound, states C2 and C3 have one, Q1 and Q4 states have 2 and states Q2 and Q3 states have 3 bound ATP. The states C1, C2, C3 and C4 correspond to receptors possessing closed channel pores, whereas the states Q1, Q2, Q3 and Q4 have open pores. The model includes negative cooperativity of agonist (ATP) binding to unsensitised receptors caused by the occupancy of one or two binding sites, opening of the channel pore to a low conductance state (g_{12}) when two sites are bound, and sensitised with pore dilation to a high conductance (g_{34}) state when three sites are occupied [174]. The top states (C1,C2, Q1 and Q2) represent unsensitised receptors, while the other bottom states are assumed to be sensitised. For further details and description of the model consult Yan et al [174]. The whole-cell current is given by the equation:

$$I_{\mathrm{P2RX7}} = g_{12}(Q_1 + Q_2)(V_h - E_{P2RX7}) + g_{36}(Q_3 + Q_4)(V_h - E_{P2RX7}) \ ,$$

where g_{12} and g_{36} are the total conductances, E_{P2RX7} is the reversal potential (assumed to be equal to 0 mV [174]) and V_h is the holding potential.

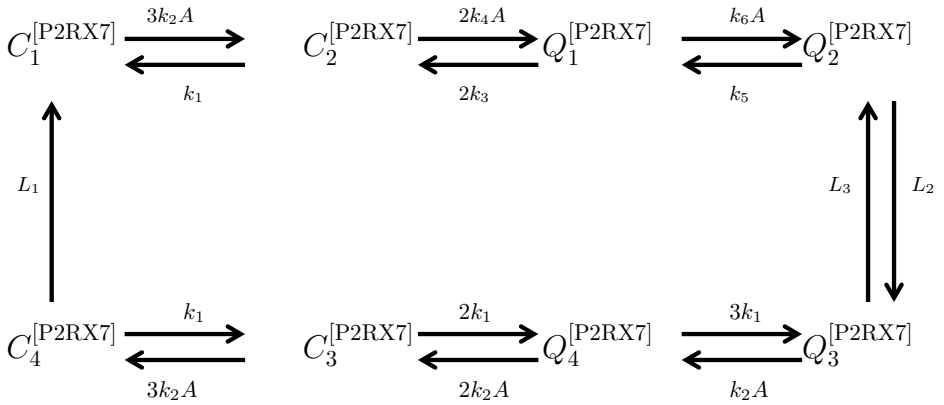

Figure 4.35: State transition diagram of the Markov model for the P2RX7 channel.
The states C_i^{P2RX7} are the closed channel pore and Q_i^{P2RX7} are the open channel pore, where $i = 1, 2, 3, 4$. Each state has three binding sites. The upper row corresponds to the unsensitised states, while the bottom row corresponds to the sensitised states. k_1, k_2, k_3, k_4, k_5, k_6, L_1, L_2 and L_3 are the transition rates between the different states and A is the agonist (ATP) concentration.

The equations describing the Markov model in Figure 4.35 are as follows [174]:

$$
\begin{aligned}
\frac{dC_1^{[P2RX7]}}{dt} &= k_1\ C_2^{[P2RX7]} - 3k_2A\ C_1^{[P2RX7]} + L_1\ C_4^{[P2RX7]}\ , \\
\frac{dC_2^{[P2RX7]}}{dt} &= 3k_2A\ C_1^{[P2RX7]} + 2\ k_3Q_1^{[P2XR7]} - (k_1 + 2k_4A)C_2^{[P2RX7]}\ , \\
\frac{dQ_1^{[P2RX7]}}{dt} &= 2k_4AC_2^{[P2RX7]} + 3k_5Q_2^{[P2RX7]} - (2k_3 + k_6A)\ Q_1^{[P2RX7]}, \\
\frac{dQ_2^{[P2RX7]}}{dt} &= k_6AQ_1^{[P2RX7]} - (3\ k_5 + L_3)Q_2^{[P2RX7]} + L_2\ Q_3^{[P2RX7]}\ , \\
\frac{dQ_3^{[P2XR7]}}{dt} &= k_2A\ Q_4^{[P2RX7]} + L_3Q_2^{[P2RX7]} - (3k_1 + L_2)\ Q_3^{[P2RX7]}\ , \\
\frac{dQ_4^{[P2RX7]}}{dt} &= 2k_2AC_3^{[P2RX7]} + 3k_1\ Q_3^{[P2RX7]} - (2k_1 + 2k_2A)Q_4^{[P2RX7]}\ , \\
\frac{dC_3^{[P2RX7]}}{dt} &= 3k_2AC_4^{[P2RX7]} + 2k_1\ Q_4^{[P2RX7]} - (k_1 + +2k_2A)C_3^{[P2RX7]}\ , \\
\frac{dC_4^{[P2RX7]}}{dt} &= k_1C_3^{[P2RX7]} - (L_1 + 2k_2A)C_4^{[P2RX7]}\ .
\end{aligned}
\tag{4.128}
$$

The parameter values and descriptions are in Table 4.30.

Table 4.30: Notation for P2RX7

Notation	Definition	Value
k_1	transition rate	0.3 s^{-1}
k_2	”	4000 $(M.s)^{-1}$
k_3	”	2.4 s^{-1}
k_4	”	50000 $(M.s)^{-1}$
k_5	”	1.58 s^{-1}
k_6	”	7000 $(M.s)^{-1}$
L_1	”	0.0001 s^{-1}
L_2	”	0.004 s^{-1}
L_3	”	0.5 s^{-1}
g_{12}	$(Q_1 + Q_2)$ conductance	15 pS
g_{34}	$(Q_3 + Q_4)$ conductance	45 pS
State variables		
C_i^{P2RX7}	closed states	
Q_i^{P2RX7}	closed states	

4.5 Gap junctions

The gap junctions form a passage between adjacent cells, providing a direct pathway for electrical and metabolic signalling [32–34]. The connexion proteins of the gap junctions form a gene family that comprises around 20 members; connexion-43 has been identified as the principal protein of human myometrial gap junctions [175,176]. The gap junctions between MSMC increase dramatically during the first stages of pregnancy (over 200-fold increase during the last 12 hours of pregnancy in the rat MSMC) [7,177]. Miyoshi et al [7] used the double-whole-cell voltage-clamp approach to freshly isolated pairs of cells from rat myometrium to study the underlying gap junctions. The macroscopic gap junction currents decayed slowly from an instantaneous, constant-conductance level to a steady-state level (function of transjunctional voltage V_j) described with equation (4.129). The cell pairs tested by Miyoshi et al [7] could be divided into two populations, based on two types of voltage-dependence. The voltage-dependent kinetics of both types, Type I and Type II, are shown in Figure 4.36. Type I closely resembles currents seen in other preparations, where connexion-43 predominates. On the other hand, Type II showed a marked voltage-dependence that is similar to the currents associated with connexion-45 [178]. In our model, we incorporate two different entities to account for both types of gap junction populations. The junctional conductances were 85 pS for Type I [7] and 30 pS for Type II [178]. The normalised conductances as a function of V_j at the steady state were fitted to the following equation:

$$G_j = \frac{G_{\max} - G_{\min_{n/p}}}{1 + \exp[-A(V_j - V_{h_{n/p}})]} + G_{\min_{n/p}} \,, \tag{4.129}$$

where G_j is the normalised value of junctional conductance, $G_{\max}$ is the maximum value of G_j and is set to be equal to 1. $G_{\min}$ is the minimum value of G_j, V_h is the half inactivation voltage and A is the slope factor (mV^{-1}). The values of the parameters for Type I and Type II are in Table 4.31. Because of the discontinuity of the function G_j (equation (4.129)) at V_j =0, we use Gaussian functions to describe G_j as follows:

$$G_j(\text{Type I}) = 0.35 + \frac{90}{\sqrt{2\pi\sigma^2}\ \exp\left[\frac{-V_j^2}{2\sigma^2}\right]} \,, \tag{4.130}$$

$$G_j(\text{Type II}) = 0.25 + \frac{55}{\sqrt{2\pi\sigma^2}\ \exp\left[\frac{-V_j^2}{2\sigma^2}\right]} \,, \tag{4.131}$$

where σ =55 for Type I and 30 for Type II. Both, the functions of the steady-state variables used by Miyoshi (equation (4.129)) and the corresponding Gaussian functions that we use in our model (equations (4.130) and (4.131)), are shown in Figure 4.36. The junctional current was instantaneously activated then inactivated in a voltage dependent manner to a steady-state level [7]. Inactivation was incomplete even by the largest test voltages. We extract the inactivation time constant as function of V_j from data by Miyoshi et al [7]. We, then, fit the time course of the decline by an exponential function. The decay time constant changed in a voltage-dependent manner as shown in Figure 4.36. We describe the time constants as a function of V_j by the following equations:

$$\tau_j(\text{Type I}) = 9 + \frac{40 \times 10^3}{1 + 0.0033\ V_j^2}\ , \tag{4.132}$$

$$\tau_j(\text{Type II}) = 120 + \frac{7.43 \times 10^3}{1 + 0.0026\ V_j^2}\ . \tag{4.133}$$

We consider the following model for the gap junctional current:

$$I_{\text{GJ}} = \kappa_{\text{GJ}}\ G_{\text{GJ}}\ P_{\text{GJ}}\ (V_j)\ , \tag{4.134}$$

where P_{GJ} is the inactivation variable with steady-state G_j and time constant τ_j. On the assumption that the cell under investigation is the driving cell (the pacemaking cell), then the following model for the driving force can be assumed:

$$V_j = V(t) - V(t + t_d)\ , \tag{4.135}$$

where t_d is an effective delay time (a constant parameter). This is reasonable when the waveform passing through the system is similar for the driving cells and the adjacent cells. That is, the wave passes through the adjacent cells virtually unaltered with a time delay t_d. The membrane potential in the cell under investigation (through which the wave passes earlier) would be $V(t)$, while the membrane potential in the cell through which the wave passes later would be $V(t + t_d)$.

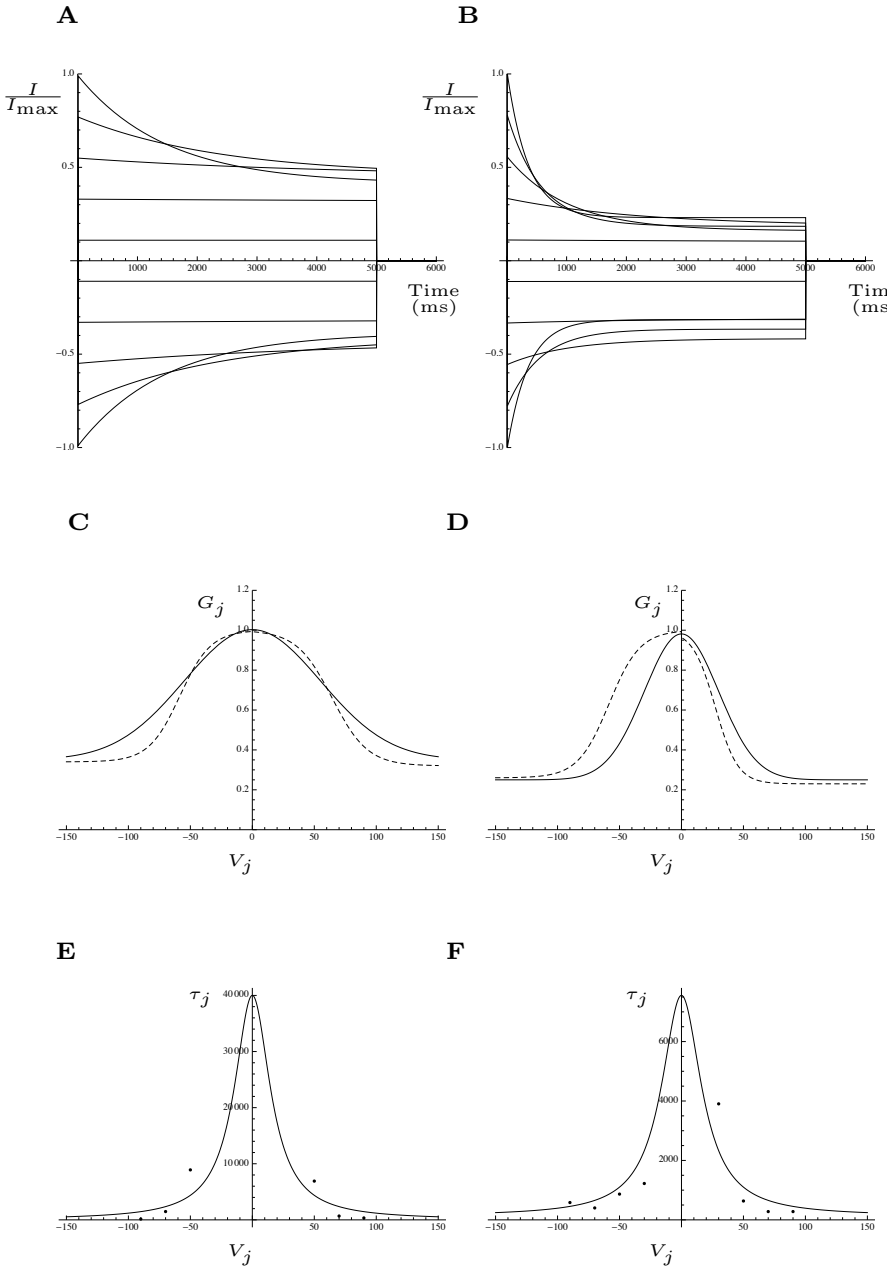

Figure 4.36: Properties of the gap junctions in MSMC.
Simulated currents for Type I and Type II are shown in *A*-*B*, respectively. The currents are elicited in response to 5 sec step pulses in the voltage range of ± 90 mV from holding potential of 0 mV. Steady-state conductance as function of V_j for Type I an Type II shown in *C*-*D*, respectively using quasi symmetrical Boltzmann functions (- - -) and the Guassian function (−). The time constant as function of V_j for Type I and Type II are shown in *E*-*F*, respectively. The function is fitted to the data representing the decay time constant for each voltage step.

Table 4.31: Notation for the Gap junction

Notation	Definition	Value
G_{GJ}	Gap junctional unitary conductance (Type I /Type II)	85/30 pS
κ_{GJ}	Gap junctional channel density	
G_j	Steady-state inactivation variable	
V_{h_n}	Half-inactivation voltage at which	
	G_j is reduced by 50% for negative V_j (Type I /Type II)	$-58.5/-24.4$ mV
V_{h_p}	Half-inactivation voltage at which	
	G_j is reduced by 50% for positive voltages (Type I /Type II)	64.4/27.3 mV
G_{min_n}	Minimum value of G_j for negative V_j (Type I /Type II)	0.34/0.26
G_{min_p}	Minimum value of G_j for positiveV_j (Type I /Type II)	0.32/0.23
G_{max}	Maximum value of G_j (Type I /Type II)	1
A_n	Slope factor for negative V_j (Type I /Type II)	$-0.07/-0.01$ mV^{-1}
A_p	Slope factor for positive V_j (Type I /Type II)	0.08/0.23 mV^{-1}
τ_{GJ}	Inactivation time constant in ms	
State variables		
P_{GJ}	Inactivation variable	

4.6 Background currents

Potassium background current

Many channels conduct K^+ background currents, which collectively are referred to as the leak current. The background K^+ current acts to maintain a negative resting potential and counterbalance depolarisation. From the mRNA transcript list, it is apparent that many background potassium channels are abundantly expressed in MSMC [8, 90].

The members of the two-pore domain (K2P) family of mammalian background potassium channels are regulated by voltage-independent factors, for instance pH, temperature, and membrane stretch. Each subunit of the K2P contains two K^+ channel pore loops, forming domains with four transmembrane segments (reviewed by Enyedi et al [179]). Three members of the K2P were expressed at the mRNA level in MSMC [8, 90]. The first member is the TWIK1, encoded by the *KCNK1* gene, also known as K2P1.1, was expressed both in the pregnant and non-pregnant human uterus at the mRNA level with ΔCT of 20.28$\pm$0.72 (normalized to r18s mRNA) in samples taken from non-pregnant patients and 20.12$\pm$0.29 in samples taken from pregnant patients [90]. The second member, the TASK1, encoded by the *KCNK3* gene, also known as K2P1.3, was expressed both in the pregnant and non-pregnant human uterus at the mRNA level with ΔCT of 21.49$\pm$0.17 (normalized to r18s mRNA) in samples taken from non-pregnant patients and 19.68$\pm$0.3 in samples taken from pregnant patients [90]. The third member is the TWIK2, encoded by the *KCNK6* gene, also known as K2P6.1, was expressed both in the pregnant and non-pregnant human uterus at the mRNA level with ΔCT of 18.13$\pm$0.45 (normalized to r18s mRNA) in samples taken from non-pregnant patients and 20.89$\pm$0.13 in samples taken from pregnant patients [90].

The Kv7.1/KCNE3 is another potassium channel that carries as background current. The Kv7.1, described earlier, when modulated by the KCNE3 subunit (also abundantly expressed at mRNA level [8,90]), loses its voltage-dependence gating and produces instantaneous, nearly ohmic current [130].

In our model, the total background current, that includes all the background channel mentioned, is modelled as follows:

$$I_{\mathrm{bgK}} = \kappa_{\mathrm{bgK}} G_{\mathrm{bgK}} (V - E_{\mathrm{K}}). \tag{4.136}$$

The parameters are defined in Table 4.33.

Chloride background current

A background chloride channel is added to the model to account for the non-specific chloride current. The current is described as follows:

$$I_{\mathrm{bgCl}} = \kappa_{\mathrm{bgCl}} G_{\mathrm{bgCl}} (V - E_{\mathrm{Cl}}) \ . \tag{4.137}$$

The parameters are defined in Table 4.33.

4.7 Pumps and Exchangers

Pumps and exchangers are active transporters, they require expenditure of energy to transport ions in and out of the cell. They maintain the ionic concentration gradients for the internal and external milieu. Some pumps are located on the plasma membrane, while others are located on the membrane of internal stores. In our model, we focus on the plasma membrane pumps, while the activity of the pumps located on the internal stores is incorporated in the simple calcium model explained in Section 4.8.

Plasma membrane Ca-ATPase

Relaxation is maintained largely by ATP-dependent extrusion of calcium from smooth muscle cells [180]; at rest, the $[Ca^{2+}]_i$ in MSMCs is kept low at 100-200 nM [36] compared to high extracellular concentration of about 1-2 mM. PMCA is a transport protein in the plasma membrane of the cell, which removes calcium ions from the intracellular milieu against their steep concentration gradient. This active transport requires expenditure of energy through hydrolysis of ATP. One calcium ion is removed for every hydrolysed molecule of ATP. Evidence of the expression of plasma membrane Ca-ATPase has been found in rat myometrium [180–182] and in human myometrium [183, 184]. The Ca-ATPase isolated from smooth muscle plasma membrane appears very similar to the calcium pump ATPase of the heart plasma membrane [185]. Therefore, we describe the PMCA activity with the model used for the cardiac myocytes by LRd by means of the Hill equation with saturation constant 0.0005 mM and a Hill coefficient of 1 [104]:

$$I_{\mathrm{PMCA}} = \kappa_{\mathrm{PMCA}} \frac{1.15}{1 + \frac{0.0005}{[Ca^{2+}]_i}} \ , \tag{4.138}$$

where I_{PMCA} is the current density in pA/pF.

Na^+/K^+-ATPase

The Na^+/K^+-ATPase pumps 3 Na^+ ions out of the cell and 2 K^+ ions into the cell. This maintains the RMP and the standing gradient of the sodium and potassium ions. The action of the pump requires energy expenditure by ATP hydrolysis, which supports a conformational change in the protein, forcing Na^+ out of the cell and K^+ into the cell. The Na^+/K^+-ATPase was found in rat [186] and in human myometrial smooth muscle cells [187]. In our model, we assume that the simulation does not appreciably affect the ionic environment of the cell and, therefore, the sodium and potassium ionic concentrations do not change dynamically in our simulations. The values of the intracellular and extracellular ionic concentrations are in Table 4.33. Due to lack of experimental data that describe the pump activity in myometrium, we adopted the cardiac myocytes model by LRd [104] for the Na^+/K^+-ATPase current:

$$I_{\mathrm{NaK}} = \kappa_{\mathrm{NaK}} I_{\mathrm{NaK_{max}}} f_{\mathrm{NaK}} I_{\mathrm{NaK,nai}} I_{\mathrm{NaK,ko}} \ , \tag{4.139}$$

where the dependence of the pump on $[Na^+]_i$ and $[K^+]_o$ is described using the Hill equation as follows:

$$\begin{aligned} I_{\mathrm{NaK,nai}} &= \frac{1}{1+(\frac{10}{[\mathrm{Na}^+]_i})^2} \ , \\ I_{\mathrm{NaK,ko}} &= \frac{1}{1+(\frac{1.5}{[\mathrm{K}^+]_o})} \ , \end{aligned} \tag{4.140}$$

while the effects of membrane potential and $[Na^+]_o$ are represented by the following functions:

$$\begin{aligned} f_{\mathrm{NaK}} &= \frac{1}{1+0.12\ e^{\frac{-0.1VF}{RT}}+0.037\ \sigma\ e^{\frac{VF}{RT}}} \ , \\ \sigma &= \frac{1}{7(e^{\frac{[\mathrm{Na}^+]_o}{67.3}}-1)} \ . \end{aligned} \tag{4.141}$$

The I_{NaK} is the current density in pA/pF. The remaining parameters with their values and definitions are in Table 4.33.

Na^+/Ca^+ exchanger

The NCX is a protein that spans the plasma membrane, like the Ca-ATase it removes calcium ions from the cell. Its activity helps maintaining the sodium and calcium concentration gradient across the cell membrane. The NCX mediates a calcium efflux at the expense of sodium influx (1 Ca^{2+}:3 Na^+); the exchanger has been identified and investigated biochemically in uterine cells [182, 188]. The NCX has low affinity, but high capacity for calcium ions. Therefore, its role is mainly in the regulation of higher, stimulatory $[Ca^{2+}]_i$ [189]; whereas the PMCA extrudes calcium at lower $[Ca^{2+}]_i$ thus provides a "fine tuning" of resting $[Ca^{2+}]_i$ [189]. Again, we adopted the model by LRd [104] (based on Varghese and Sell [190]); the NCX current is thus described as follows:

$$I_{\mathrm{NCX}} = \kappa_{\mathrm{NCX}}(0.00025e^{\frac{-0.65VF}{RT}} \frac{e^{\frac{VF}{RT}}[\mathrm{Na}^+]_i^3[\mathrm{Ca}^{2+}]_o - [\mathrm{Na}^+]_o^3[\mathrm{Ca}^{2+}]_i}{1 + 0.0001[\mathrm{Na}^+]_i^3[\mathrm{Ca}^{2+}]_o + [\mathrm{Na}^+]_o^3[\mathrm{Ca}^{2+}]_i}) \ , \tag{4.142}$$

where I_{NCX} is the current density in pA/pF. The remaining parameter values and definitions are in Table 4.33.

Because of the lack of data about the pumps' and exchangers' unitary conductance we adapt the macroscopic models from the literature where the currents are in pA/pF. In this case, κ_{PMCA}, κ_{NaK}, κ_{NCX} are dimensionless channel density factors that would be adjusted automatically within the SVD method.

4.8 Calcium dynamics

To represent the MSMC calcium dynamics, we developed a minimal model. Although the rise in $[Ca^{2+}]_i$ can be augmented by the release from the stores, calcium entry from the extracellular space is the major source of calcium-triggered contractions [29]. Therefore, the model only considers the increase of $[Ca^{2+}]_i$ due to the plasma membrane calcium channels (L-type and T-type), while ignoring the Ca^{2+} release from the internal stores. To determine the parameter values, the intracellular calcium concentration $[Ca^{2+}]_i$ has to be related to the signal that is experimentally observed, i.e. f/f_0 (further details of how f/f_0 signal was acquired are given in Chapter 2). Accordingly, $[Ca^{2+}]_i$ is related to the fluorescence intensity f by

$$[Ca^{2+}]_i = K_d \frac{(f - f_{\min})}{(f_{\max} - f)} \tag{4.143}$$

where K_d is the apparent calcium-binding affinity of the calcium indicator (Fluo-4), $f_{\min}$ and $f_{\max}$ are the minimum and maximum fluorescence intensities. We propose the following differential equation to account for the biophysical processes that affect cytosolic calcium dynamics:

$$\frac{d[Ca^{2+}]_i}{dt} = \gamma_L \; I_{\text{L-type}} + \gamma_T \; I_{\text{T-type}} - \lambda \; [Ca^{2+}]_i \tag{4.144}$$

where $I_{\text{L-type}}$ and $I_{\text{T-type}}$ are the voltage-activated calcium currents from the L-type and the T-type channels (resulting in calcium entry), respectively. The corresponding coefficients are γ_L and γ_T. The term $\lambda \; [Ca^{2+}]_i$ represents the recovery from excitation. The removal of calcium proceeds via calcium extrusion caused by the existing pumps or due to binding to the intracellular calcium buffers. We used the observed time series of the membrane potential (acquired as in Chapter 2 and shown in Figure 2.1) as a forcing function to drive the voltage-gated calcium channels. The simultaneous calcium fluorescence signal (acquired as in Chapter 2 and shown in Figure 2.1) was used to find the least squares fit of the calcium excitation model (Figure 4.37). The parameters of the model $K_d, f_{\max}, \gamma_L, \gamma_T, \lambda$, and the steady state $[Ca^{2+}]_i$ ($f_{\min} = 0$ for Fluo-4) were determined by means of least-squares estimation. The estimated parameter values are shown in Table 4.32. Although our model is a single-variable model and does not take into account calcium release from internal stores (via IP_3 receptors and RyR), it was able to reproduce experimental data with few free parameters.

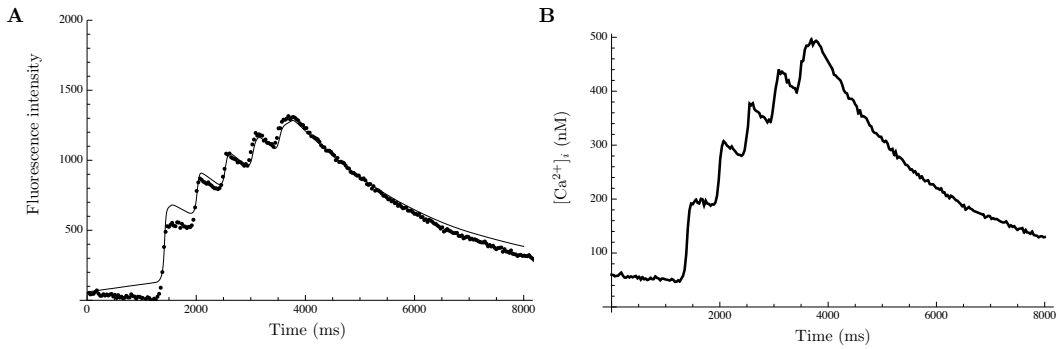

Figure 4.37: Calcium dynamics.
Left: calcium fluorescence signal (dots) together with the least-squares fit of the calcium excitation model (solid line). Parameter estimates are shown in Table 4.32. Right: estimated calcium concentration using the parameter estimates shown in Table 4.32

Table 4.32: Calcium dynamics parameter values

Parameter	Definition	Value
K_d	Apparent calcium-binding affinity of the calcium indicator (Fluo-4)	1050nM
$f_{\max}$	Maximum fluorescence intensity	4520
γ_L	L-type current coefficient	2251
γ_T	T-type current coefficient	1.38
λ	Coefficient for recovery from excitation	0.00063
$\mathrm{Ca}_{\mathrm{in}}$	Initial $[Ca^{2+}]_i$	60.7nM

Table 4.33: General model parameters

Parameter	Definition	Value
R	Gas constant	8.3143×10^{3}mV C $mol^{-1}K^{-1}$
T	Temperature	310 K
F	Faraday constant	96,4867 C mol^{-1}
C_m	Cell capacitance per unit surface area	2 μ F cm^{-2}
$[K]_o$	Extracellular K^+ concentration	5.4 mM
$[Na]_o$	Extracellular Na^+ concentration	140 mM
$[Ca]_o$	Extracellular Ca^{2+} concentration	2 mM
$[ATP]_o$	Extracellular ATP concentration	
G_{bgK}	K^+ background conductance	50 pS
G_{bgCl}	Cl^- background conductance	50 pS
G_{PMCA}	PMCA conductance for scaling purpose	1 pS
G_{NaK}	Na^+/K^+ conductance for scaling purpose	1 pS
G_{bgK}	NCX conductance for scaling purpose	1 pS
κ_{bgK}	K^+ background density	
κ_{bgCl}	Cl^- background density	
κ_{PMCA}	PMCA density	
κ_{NaK}	Na^+/K^+ density	
κ_{bgK}	NCX density	
$I_{\mathrm{NaK_{max}}}$		2.25

Chapter 5

Model results and applications

In this chapter, we survey the results of our method in detail, we discuss our model, we validate and test it. Finally, we propose some applications to our model.
We also apply the model to two hypotheses on the triggers of depolarisation in MSMC.

First we bring together all the methods and techniques we have set out in previous chapters. We constructed a mathematical model based on individual currents carried by the electrogenic transmembrane proteins in human MSMC. Our approach consisted of four basic steps: (i) characterise the *potential* repertoire of electrogenic proteins by means of expression studies; (ii) model each ion channel or transporter independently and determine its gating parameter values on the basis of biophysical data taken from the literature; (iii) characterise the space of possible solutions of conductomes consistent with experimentally observed calcium and membrane potential waveforms; (vi) select a putative conductome based on a suitable criterion, which we define below in more detail, to subsequently test various hypotheses in a "free-running" simulation.

We determined the complete repertoire of electrogenic proteins that are potentially expressed in MSMC, as indicated by mRNA expression data [8]. These proteins are in many cases subunits that contribute to functional channels. Moreover, since ion channels exist as various combinations of those subunits, the expression list generates a sizeable potential repertoire of conducting entities that may be present in the plasma membrane of the MSMC. A diagrammatic representation of all potential entities considered in the model is given in Figure 4.1A.

As explained in Chapter 4, we formulated a mathematical model for every oligomeric channel complex that (i) is consistent with the subunits in the mRNA expression list, and (ii) has been previously attested in the literature. For each

conductance, a mathematical model was adopted from the literature where available. Otherwise, a new set of equations was formulated on the basis of the available data. Accordingly, the biophysical and kinetic parameter values were in some cases adopted directly from the literature and in other cases obtained by means of least-squares fitting to the experimental data on heterologous expression systems as provided by the literature.

The current summation model accumulates the contributions from each of the conductances, as discussed in Chapter 3. Since the parameters of the gating kinetics of each species have been determined independently, the only remaining unknowns are the densities in the plasma membrane shown in Figure 4.1A. Native cell behaviour combining two simultaneously acquired data sets (voltage V and intracellular calcium $[Ca^{2+}]_i$ as a function of time; see Chapter 2 for detailed experimental procedures) was used to constrain the parameters. We apply the method described in Chapter 3 to estimate the channel densities of the conductances in the MSMC. Briefly, the observed voltage and Ca^{2+} time series, shown in Figures 5.1 and 4.37A, respectively, were used to drive the gating kinetics of each entity. The gating time series thus obtained were used to calculate the individual current densities. The observed membrane potential time series is linear in the channel densities, which implies that the space of all possible combinations of ion channel densities, that is consistent with the data, can be calculated from the kernel of a linear transformation. This kernel provides information about the functional redundancy in the system. Unless the kernel is zero-dimensional, no unique conductome can be inferred from the data and the parameter vector $\boldsymbol{\kappa}$ is unidentifiable. A vector in the null space can nonetheless be singled out by stipulating an additional criterion, such as the smallest ℓ_1-norm subject to non-negativity (smallest sum of non-negative channel densities), which can be interpreted as the most "parsimonious' way of realising the observed behaviour. Huys et al [191] proposed a similar approach but had not explicitly addressed the uncertainly problem. They acknowledged that the solution may not be unique and that no simple answer could be obtained, if the channels were more similar, or if their linear combination jointly well accounts for the data [191]. In fact, the method employed by Huys et al [191] can be characterised as quasi-macroscopic; their model comprised channels with perfectly distinguishable kinetics. The redundancy of the system corresponds to the biological fact that there are many different ways that a cell can produce the same observed behaviour. In mathematical terms, an estimate of the channel densities up to the indeterminacy of that kernel is obtained, and $\boldsymbol{\kappa}$ is given as the sum of a particular solution $\boldsymbol{\kappa}_p$ plus an arbitrary linear combination of the vectors that span null $\boldsymbol{W}$ (the matrix $\boldsymbol{W}$ is

defined in Chapter 3; a basis for null $\boldsymbol{W}$ is obtained numerically by means of the Singular Value Decomposition). One possible choice for $\boldsymbol{\kappa}_p$ is the pseudo-inverse $\boldsymbol{\kappa}^+$; this has the advantage that the discrepancy between the observed $V(t)$ and the time course of $V(t)$ as predicted by the model is minimised in the least-squares sense ($\boldsymbol{\kappa}^+$ has the smallest Euclidean norm out of all vectors that achieve this best fit). The affine space formed of $\boldsymbol{\kappa}^+$ plus a basis of null $\boldsymbol{W}$ is not guaranteed to intersect with the positive cone, which we must require since channel densities are bound to be non-negative. Therefore, our procedure was to find a vector $\boldsymbol{\kappa}_p$ in the positive cone that satisfies the non-negativity requirement, by means of non-linear least-squares fitting constrained to this cone. Within the space formed by this $\boldsymbol{\kappa}_p$ plus a linear combination of the basis of null $\boldsymbol{W}$, we then found the solution that was minimal in the ℓ_1-norm.

Table 5.1 and Figure 4.1B show a prediction of the channel densities of the conductance species, in number of channels/pF (a typical myometrium membrane cell capacitance is in the range of 100 to 150 pF), after constraining the parameters by the additional ℓ_1-norm criterion. Figure 5.1 exhibits the observed voltage trace together with the solution with the smallest Euclidean norm for the channel densities $\boldsymbol{\kappa}^+$ plus a basis of null $\boldsymbol{W}$, and the trace given by all the solutions that satisfy the non-negativity of the channel densities.

Table 5.1: Parameter estimation values (parsimonious solution)

Potential conductance species	number of channels/pF
Kv2.1	15.7
Kv9.3	6
Kv6.1	0.74
BK	0.064
BKβ1	0.3
BKβ3	0.037
BKβ4	0
SK_2	0
SK_3	0.776
SK_4	0.014
hERG	2.4
CaL (L-type)	10.5
CaT (T-type)	19.8
CaCC	0.45
Kv4.1	0
Kv4.3	0
Kv4.3+KCNE3	1.3
Kv4.3+KChIP2b	2.7
Kv4.3+KChIP2d	0.3
Kv4.3+KChIP2b+KCNE3	0
Kv3.4	5.2
Kv7.1	0
Kv7.4	0.844
Kir7.1	0
bgK, bgCl	0.5, 0.46
Gap1	0
Gap2	0
Potential conductance species	**channel density factor**
NCX	0.03
PMCA	3.9
NaK	1.1

5.1 The SVD method

The matrices resulting from the SVD method discussed in Chapter 3 provide an estimate of the channel densities of the conductances in the MSMC.

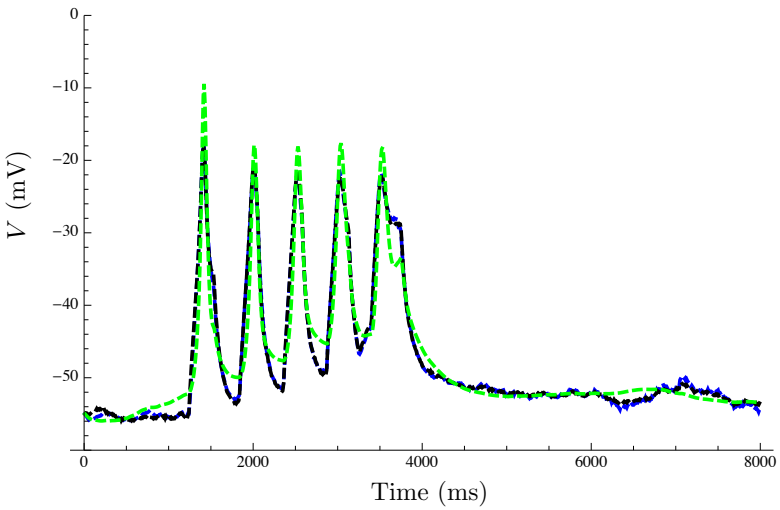

Figure 5.1: Observed voltage with the estimated fit.
Black: the observed voltage trace. Blue: fit with general least-squares estimate ($\widehat{\boldsymbol{\kappa}} = \boldsymbol{\kappa}^{+} + \sum_{j=1}^{n-r} \gamma_j \boldsymbol{v}_j^0$). Green: fit with the constrained least-squares estimate satisfying the non-negativity criterion ($\widehat{\boldsymbol{\kappa}} = \boldsymbol{\kappa}_p + \sum_{j=1}^{n-r} \gamma_j \boldsymbol{v}_j^0$) .

5.1.1 Imposing the forcing function

The channel densities are the sole unknown parameters, after estimating all kinetics of the various conductances from the literature. We used the native cell behaviour combining the simultaneously acquired data sets (V and $[\mathrm{Ca}^{2+}]_i$ as a function of time) to drive the gating kinetics of each entity in our model. The gating time series obtained are then used to calculate the individual currents (a selection of which is shown in Figure 5.2). Integrating the individual currents we obtain the virtual charges, which combine additively to give the membrane potential according to equation (3.14). From these virtual charges we construct the $m \times n$ matrix $\boldsymbol{W}$, as described in Chapter 3 where m is the number of data points and n is the number of entities.

5.1.2 Solution via SVD

To obtain the least-squares solution of equation (3.19), the matrix $\boldsymbol{W}$ is factorised, using SVD, into three matrices as exhibited in equation (3.2). The SVD produces two orthogonal matrices and one diagonal matrix. The first orthogonal matrix $\boldsymbol{U}$ is defined by the left singular vectors of the matrix $\boldsymbol{W}$ while the second orthogonal matrix $\boldsymbol{V}$ the right singular vectors. The rank of the matrix W, r, can be deduced from the number of non-zero singular values.

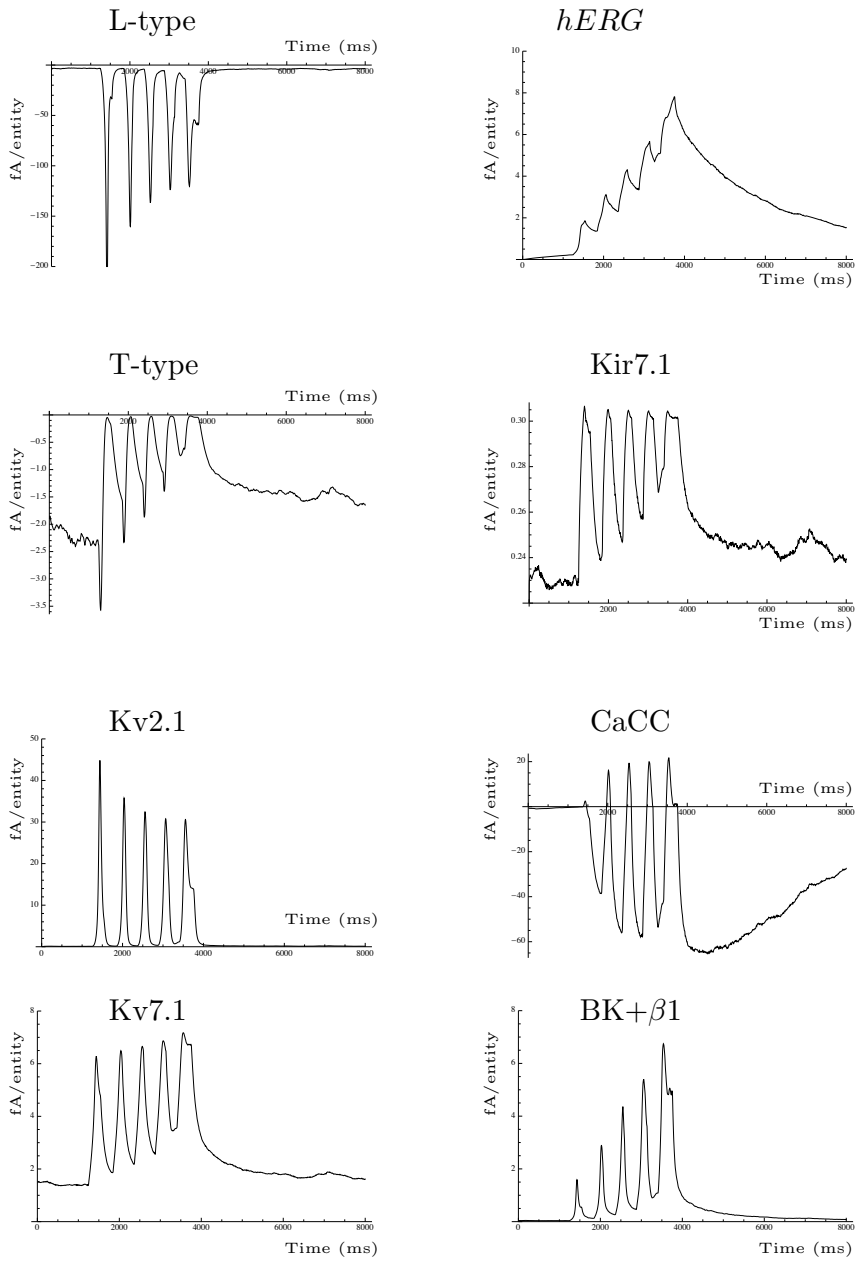

Figure 5.2: A selection of the major individual currents.
The individual currents result from the evaluation of the corresponding gating kinetics which are in turn driven by the observed functions shown in Figures 5.1 and 4.37. The abscissa is the time in ms and the ordinate is the individual current in fA per conductance species

The $\boldsymbol{U}$-matrix

The $\boldsymbol{U}$-matrix is an $m \times m$ matrix. The columns of the $\boldsymbol{U}$-matrix are called the left singular vectors. The $\boldsymbol{U}$-matrix effectively contains the vector space of voltage waveforms consistent with the individual currents arising from the gating kinetics driven by the observed voltage waveform, which is an element of that space. List plots of the columns of $\boldsymbol{U}$-matrix show the behavioural repertoire of the various components of the waveform (Figure 5.3).

The $\boldsymbol{S}$-matrix

The $\boldsymbol{S}$-matrix is an $m \times n$ diagonal matrix; the elements of $\boldsymbol{S}$-matrix are only nonzero on the diagonal, and are called the singular values. The diagonal elements are sorted in descending order, with the highest singular value (the dominant component) in the upper left index of the $\boldsymbol{S}$-matrix. The value of the diagonal element is indicative of its importance in explaining the data. The rank of the matrix W, r, can be inferred from the $\boldsymbol{S}$-matrix and is equal to the number of non-zero singular values.

$$\boldsymbol{S} = \begin{bmatrix} 703.2 & 0 & 0 & 0 & 0 & 0 & \dots & 0 \\ 0 & 44.34 & 0 & 0 & 0 & 0 & \dots & 0 \\ 0 & 0 & 38.21 & 0 & 0 & 0 & \dots & 0 \\ 0 & 0 & 0 & 6.99 & 0 & 0 & \dots & 0 \\ 0 & 0 & 0 & 0 & 3.1 & 0 & \dots & 0 \\ 0 & 0 & 0 & 0 & 0 & 1.44 & \dots & 0 \\ \vdots & & & \vdots & & & \ddots & \\ \vdots & & & \vdots & & & & \\ \vdots & & & \vdots & & & & \\ 0 & 0 & 0 & 0 & \dots & 0 & \dots & 0 \end{bmatrix} \tag{5.1}$$

The $\boldsymbol{V^T}$-matrix

The matrix $\boldsymbol{V^T}$ is an $n \times n$ matrix. The columns of $\boldsymbol{V}$ are the right singular vectors. This matrix shows the contributions of various conductances to the 'basis' waveforms in $\boldsymbol{U}$. For instance, the first row shows the contribution of different conductances to the dominant component of the signal (shown in red in Figure 5.3). Individual elements of $\boldsymbol{V^T}$ are displayed as circles in the heat map in Figure 5.3, and colour-coded using blue for negative values and green for positive values, with the intensity representing the magnitude. The first r columns of $\boldsymbol{V}$ form a basis of the subspace

that indicates how the densities in the parameter vector $\boldsymbol{\kappa}$ combine to generate the components of $\boldsymbol{U}$. The last $n - r$ rows of $\boldsymbol{V^T}$ form a basis for null $\boldsymbol{W}$.

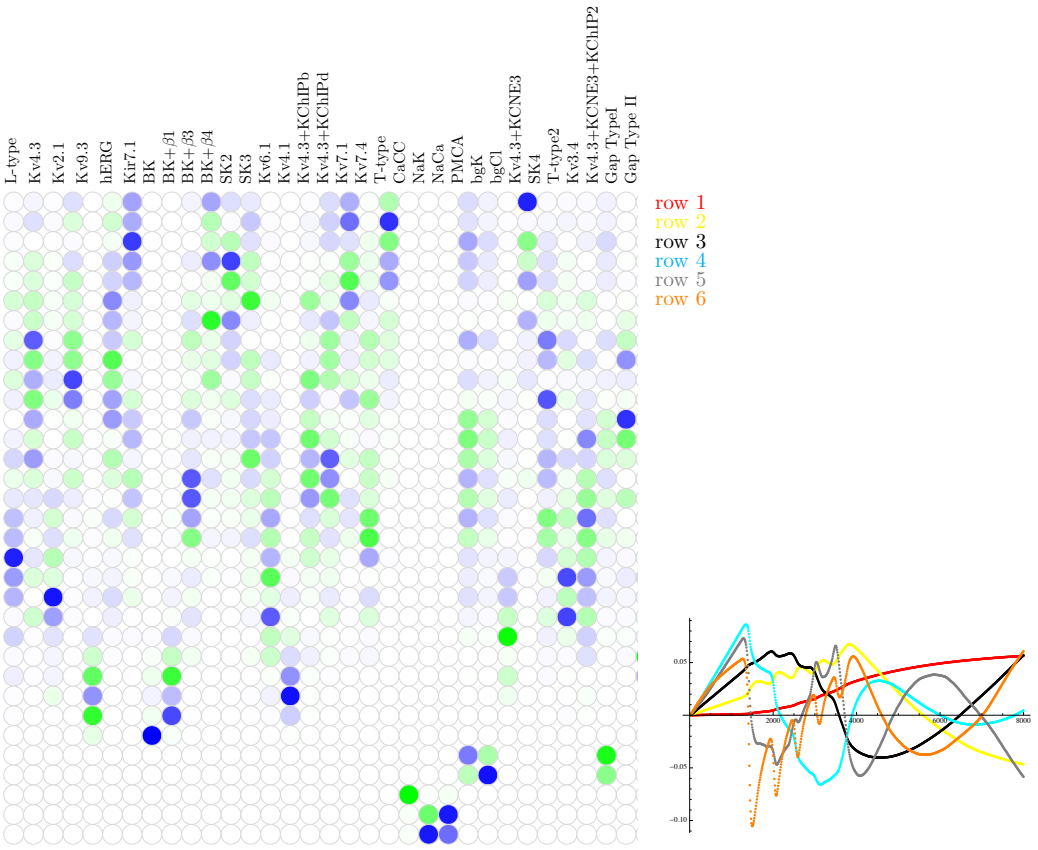

Figure 5.3: Representations of $\boldsymbol{V}^T$ and $\boldsymbol{U}$.
Left: heat map of the $\boldsymbol{V}^T$ where negative values (blue), and positive values (green) appear as various intensites (the rows of the heat map), the first r columns of $\boldsymbol{V}$. The various conductances are annotated. Right: plot of the first six columns of $\boldsymbol{U}$. Colour-codes indicate correlation between the rows of $\boldsymbol{V}^T$ and the list plots of the columns of $\boldsymbol{U}$.

5.2 Validation of the estimated conductome

Predictions were made on the basis of the conductome with the smallest ℓ_1-norm and were subsequently tested against experimental data. We obtained data from voltage-clamp experiments for isolated currents (performed by Dr. McCloskey): whole-cell currents were measured during 500 ms voltage steps from -150 mV to 80 mV in 10 mV increments from a holding potential of -60 mV. To isolate currents that are sensitive to inhibition by drug application, sets of currents were measured for control, drug inhibition current, and the drug-sensitive current obtained by subtracting the current recorded in the drug from the control current. Measurements of mean peak currents $\pm$SE were calculated from samples of n cells. Concurrently and independently, computer simulations were performed using the same voltage-clamp protocol, on the basis of the predicted parameter values, for various conductance ionic species. The simulated peak currents were measured at time t during 500 ms voltage steps from -150 mV to 80 mV in 10 mV increments from a holding potential of -60 mV.

ScTx, an inhibitor of Kv2.1 homomeric channels, the Kv2.1/Kv6.1, Kv2.1-/Kv9.3, and the A-type channels, was used to inhibit and consequently isolate the Kv2.1 currents. The late outward current is measured to separate Kv2.1 from A-type currents. The measured ScTx-sensitive late outward current (at $t = 450$ ms), resulting from voltage-clamp experiment at 40 mV after application of 100 nM ScTx, was 4.17$\pm$0.65 pA/pF (n=9). The total peak Kv2.1 currents (Kv2.1, Kv6.1, and Kv9.3) elicited by the simulation for the same voltage step (40 mV) was 3.77 pA/pF.

Dofetilide is a selective inhibitor of the hERG channels. The isolated dofetilide-sensitive peak current resulting from voltage-clamp experiments at 40 mV, after the application of 10 μM dofetilide, was 1.18$\pm$0.32 pA/pF (n=7) compared to 1.544 pA/pF for the simulated current elicited by hERG at the same voltage.

VU590 is a Kir7.1 and Kv2.1 channel blocker. The isolated peak Kir7.1 current was measured during the voltage-clamp experiment at -150 mV (to isolate the inwardly rectifying potassium current), after application of VU590 channel-blocker (10 μM). An external medium with elevated [K^+] solution was used in order to visualise the inward currents at -150 mV. The resulting current was 0.21$\pm$0.07 pA/pF (n=9) compared to 0 pA/pF for the current elicited by the simulated Kir7.1 at -150 mV.

Figure 5.4 shows the experimental current densities under the voltage-clamp conditions. The simulated values of peak currents at selected voltage steps agree, within the margins of experimental error, with the currents measured for Kv2.1

channels and hERG channel. For some channels such as Kir7.1, the simulated data differed from experimental values. The origin of this error can in all likelihood be attributed to the indeterminacy of the Kir7.1 current from the other background potassium currents within the model.

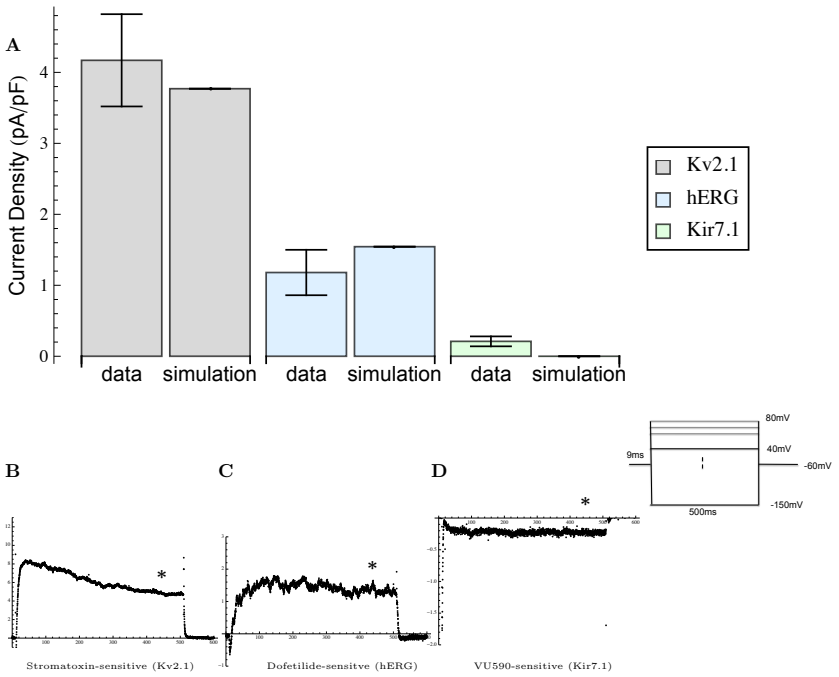

Figure 5.4: Validation of the model.
(A) Bar Chart comparing experimental and simulated Kv2.1, hERG, and Kir7.1 current densities. (B, C, D) ScTx-, Dofetilide-, and VU590-sensitive currents in D15 mice samples (mean±SD), under voltage-clamp conditions with 40 mV voltage step for ScTx- and Dofetilide-sensitive currents and −150 mV for VU590-sensitive current from holding potential of −60 mV. Simulated values of peak currents at selected voltage steps for Kv2.1 and hERG channels agreed with the experimental data within the margin of experimental error stated (see values in Section 5.2). This was not the case for Kir7.1.

5.3 Assessing the effect of varying individual channel densities

The model can be evaluated in "free-running" mode using the estimated parameter vector $\boldsymbol{\kappa}$ that contains the channel densities. A stimulus was applied to generate an AP (through ATP variation, explained below under **Hypothesis I**). We assessed the effect of increasing or decreasing various channel densities, as shown in Figure 5.5.

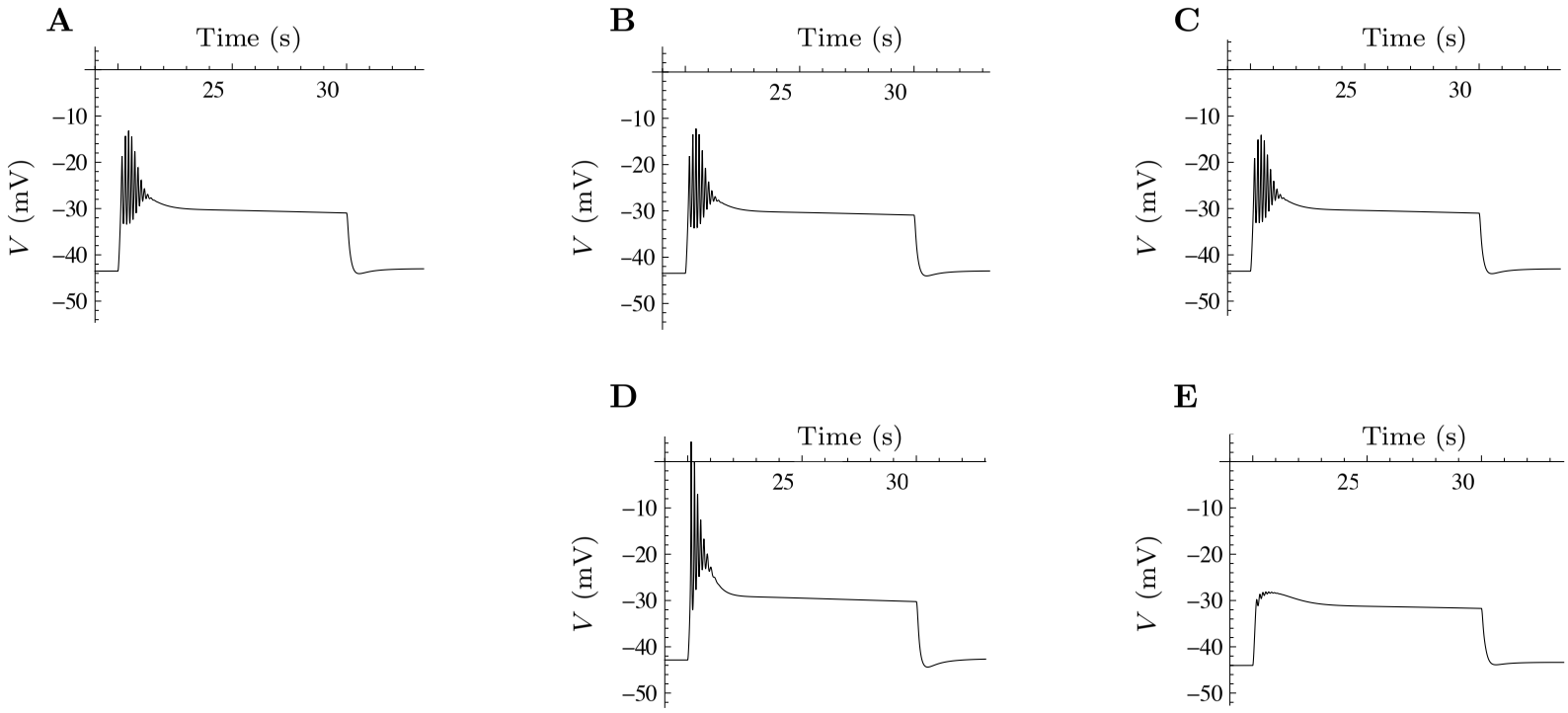

Figure 5.5: Free-running model simulations.
(A) AP triggered by a 10 sec extracellular ATP step function from 0 to 15 μM using the free-running model fitted with the parameters (constrained using the ℓ_1-norm). (B) Effect of reducing the channel densities of the BK and its isoforms to zero channels/pF. (C) Effect of doubling the channel densities of the BK and its isoforms. (D) Effect of reducing the channel density of the Kv2.1 channel to zero channels/pF. (E) Effect of doubling the channel density of the Kv2.1.

5.3.1 Effect of varying the Kv2.1 channel density

Using our free-running mode, we assessed the effect of varying the Kv2.1-containing channel densities (Kv2.1, Kv2.1/Kv9.3, and Kv2.1/Kv6.1 channels), from double the estimated channel densities to complete block of those channels, which had a substantial effect on the waveform as shown in Figure 5.6. When all Kv2.1-containing channels were blocked, we observed an increase in the initial AP spike amplitude, in the rate at which steady state is reached during the plateau phase of the AP, an increase in the spikes duration and amplitude, a more depolarised plateau phase, and a slight depolarisation of the RMP. To assess the effect of each of the Kv2.1-containing channels, we varied the channel density of each of them separately. Changing the density of the homomeric Kv2.1 channel had an effect on the first AP spike amplitude, on the rate at which the plateau phase was reached, on the plateau phase voltage, on the spikes amplitude, and on the spikes frequency of the AP. No effect on the RMP was observed. (Figure 5.8A). Blocking the heteromeric Kv2.1/Kv9.3 increased the initial AP spike amplitude, slightly depolarised the plateau phase of the AP, decreased the spikes frequency, and increased the spikes amplitude; but we observed no change in the rate at which steady state is reached. A slight depolarised RMP was observed when the Kv2.1/Kv9.3 channel was blocked (Figure 5.8B). This is in agreement with Patel et al [10]; they demonstrated that the Kv2.1/Kv9.3, unlike the Kv2.1, opens in the voltage range of the RMP of pulmonary artery myocytes [10]. This suggests that the Kv2.1/Kv9.3 channel complex may contribute to maintaining the RMP at the prevailing physiological level [10]. When the density of Kv2.1/Kv6.1 channel was varied, little variation in the AP spike frequency was observed, while there was no effect on any of the spikes amplitude, nor on the plateau phase potential, nor on the rate at which the plateau phase was reached (Figure 5.8C). Kv6.1 was most abundantly expressed at the mRNA level and its expression appears higher in the labouring samples [8]. This could suggest that a transition from homomeric Kv2.1 at mid-gestation to heteromeric Kv2.1/Kv6.1 at term would increase the contractile state of the human myometrium. At this stage of gestation, Kv6.1 regulates the activity of Kv2.1, rendering it less effective in suppressing contraction force and frequency, even at high density. As discussed in Chapter 4, Kv6.1 has been reported to shift the half inactivation voltage of Kv2.1 to more negative potentials, while it has no effect on the half activation voltage [11, 119]. As reported in those studies, Kv6.1 expression leads to Kv2.1 currents that activate over the same range but inactivate at much more negative potentials. The net result in the myometrium would be a narrowing of the potentials at which Kv2.1 would be available to influence and shape the AP.

This is in agreement with the results we report in Figure 5.8C, which shows that the effect of varying the density of Kv2.1/Kv6.1 is almost unnoticeable.

In order to determine what role Kv2.1 current might play in the whole tissue and test the predictions of the model, we undertook current clamp measurements of membrane potential from longitudinal layer of murine myometrium (experiments carried out by Dr. McCloskey). Typical examples of the activity observed in the myometrial muscle strips are shown in Figure 5.9A and Figure 5.9B, where we observe a spontaneous AP generated from RMP of approximately -45 mV and -50 mV under control conditions for both D15 and D18, respectively. The application of 100 nM ScTx, a selective inhibitor of the homomeric Kv2.1 as well as the heteromeric Kv2.1/Kv6.3 and Kv2.1/Kv9.1 [192], elicits a marked increase in AP spike amplitude in the D15 sample and in the D18 sample (albeit to a lesser extent). The summary (n =4 and n =6 for D15 and D18, respectively, *P$\leq$0.05) data for these experiments are presented in the graphs in Figure 5.9 C, D, E, and F, where mean AP spike amplitude was significantly increased from 42.87$\pm$5.07 mV to 53.25$\pm$3.78 mV in D15 and from 45.5$\pm$4.96 mV to 56.21$\pm$3.37 mV (p$\leq$0.05) in D18 tissue. Application of 100 nM ScTx also significantly increased AP frequency in D15 samples from a mean of 1.69$\pm$0.18 AP min^{-1} to 2.31$\pm$0.34 AP min^{-1} and 1.11$\pm$0.22 AP min^{-1} to 1.38$\pm$0.19 AP min^{-1}. All measurements are mean $\pm$SE. A modest yet consistent reduction in the duration of AP was apparent in APs recorded from D15 tissue. The experiments carried out in the current study was unable to show a significant change in RMP with ScTx application in either D15 or D18 cells (Figure 5.9F). The application of ScTx resulted in an increase in AP spike amplitude and in AP frequency. Also a reduction in the duration of AP was apparent in several recordings. A slight increase in the spike duration also was observed in the recordings. Figure 5.7 shows a zoom of these effects on the AP.

The predictions from both, the model simulations and the experimental recordings using ScTx, show that the Kv2.1 channels affect AP amplitude and frequency. However, when ScTx was used, under physiological conditions, there was no evidence that Kv2.1 channels play any role in setting the RMP. However, with the limited number of recordings made and the inherent variability from cell to cell recording RMP, we cannot rule out the possibility that such small (maximum predicted shift of around 4 mV) changes of RMP, as predicted by our model, would have been below the detection limit of the apparatus. We conclude that the Kv2.1 channels play a role in hyperpolarisation during the AP plateau. At potentials where there is good availability of the channel, it can serve as a hyperpolarising drive working to limit the depolarising drive of channels such as the VGCCs responsible for

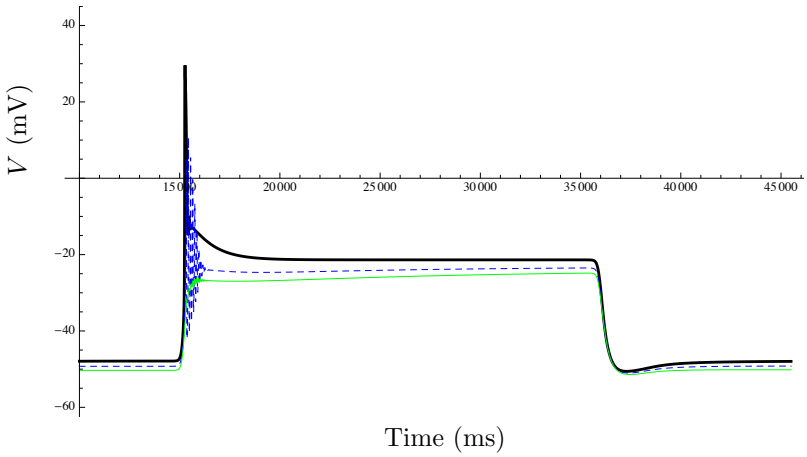

Figure 5.6: Free-running model simulations of the effect of varying all Kv2.1-containing channel densities.
Blue: AP triggered by a 10 sec extracellular ATP step function from 0 to 1 mM using the free-running model fitted with the parameters (constrained using the ℓ_1-norm). Black: effect of reducing the channel density of all Kv2.1-containing channels to zero channels/pF. Green: effect of doubling the channel density of all Kv2.1-containing channels

the AP spikes. Kv2.1 channels appear to play a role in modulating the excitability of the myometrium by acting to inhibit contraction frequency and amplitude while contributing very little to the RMP. Hristov et al [192] also found that ScTx (100nM) increased the spontaneous phasic contraction amplitude, muscle force, and muscle tone in guinea pig detrusor smooth muscle. The authors concluded that the Kv2.1-containing channels are important physiological regulators of excitability and contractility in smooth muscles.

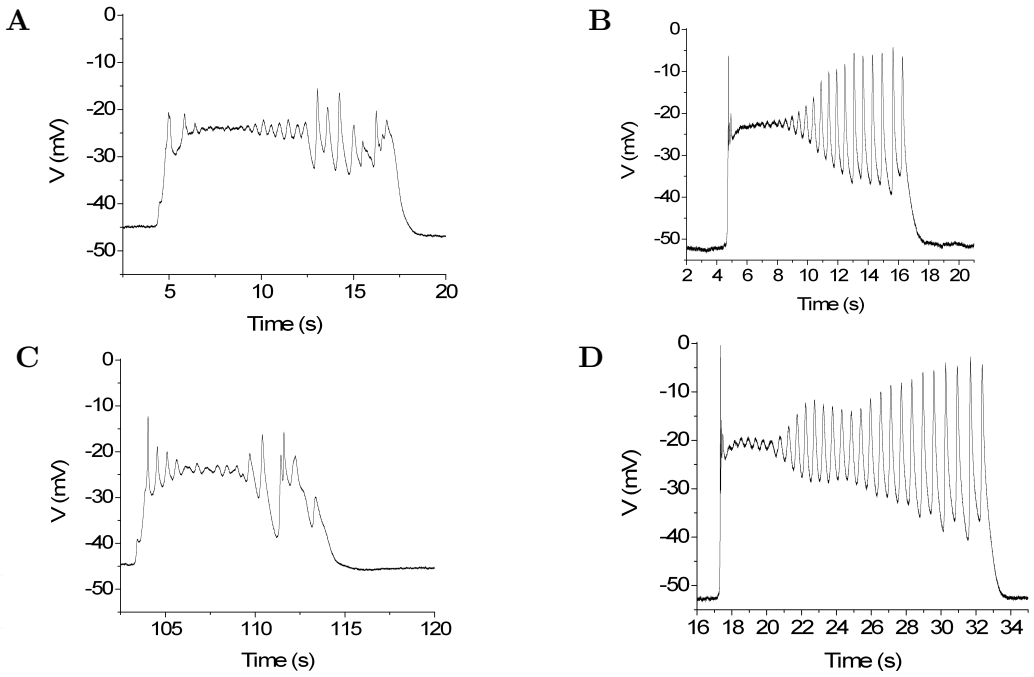

Figure 5.7: .ScTx modulates AP frequency, duration and spike amplitude. Spontaneous electrical activity recorded from the longitudinal layer of D15 and D18 myometrium (A and B). Activity consisted of slow depolarisation to threshold, followed by an AP composed of a plateau upon which a number of spikes were superimposed. (C,D) Mean AP spike amplitude significantly increased in D15 and D18 tissue. Application 100nM of ScTx also slightly increased spike duration in D15 and in D18 tissue. This figure is a zoom of Figure 5.9.

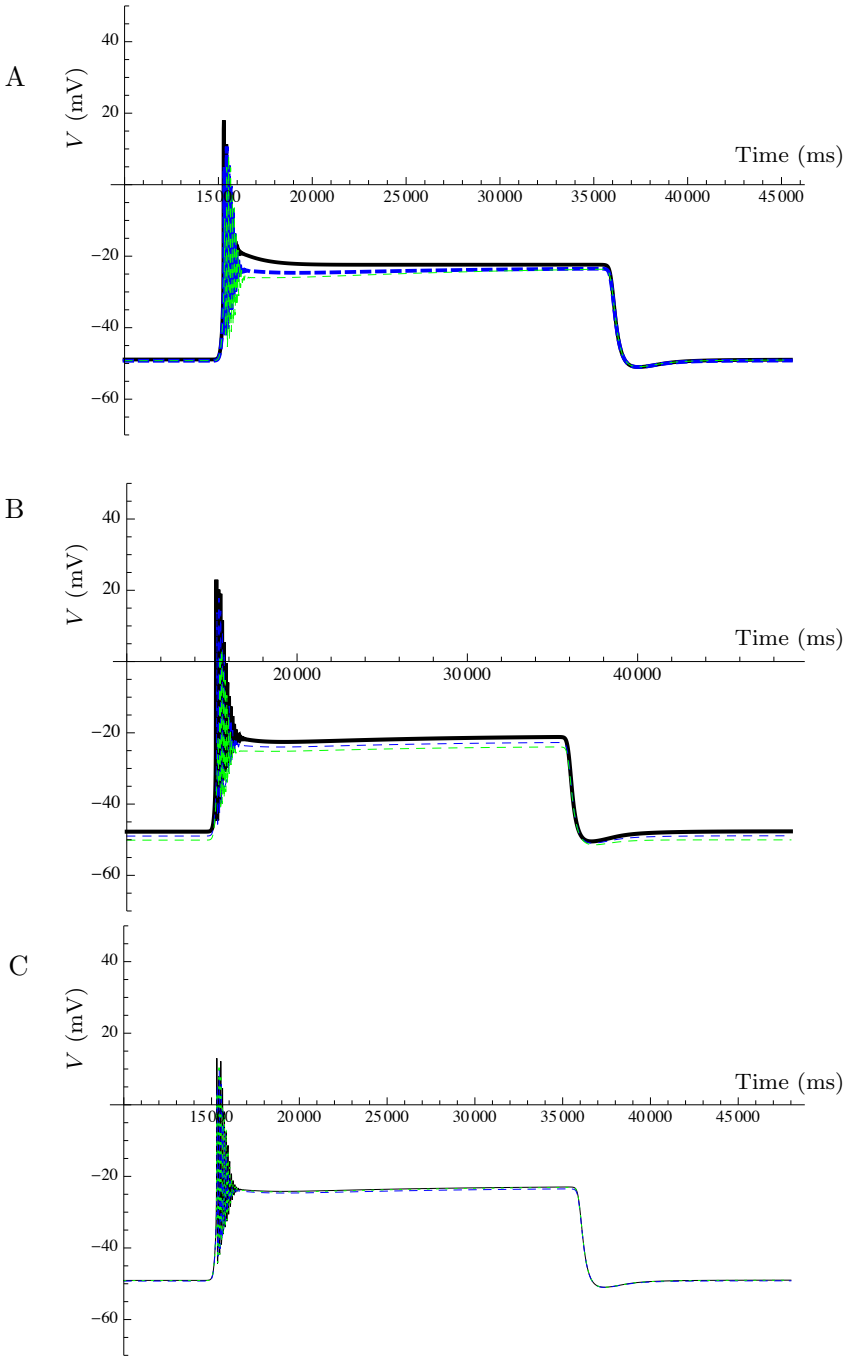

Figure 5.8: Free-running model simulations of the effect of varying Kv2.1-containing channel densities.
Blue: AP triggered by a 10 sec extracellular ATP step function from 0 to 1 mM using the free-running model fitted with the parameters (constrained using the ℓ_1-norm). Black: effect of reducing the channel density of the homomeric Kv2.1 channels (A), Kv2.1/Kv9.3 channels (B), and Kv2.1/Kv6.1 channels (C) to zero channels/pF. Green: effect of doubling the channel density of Kv2.1 channels (A), Kv2.1/Kv9.3 channels (B), and Kv2.1/Kv6.1 channels .

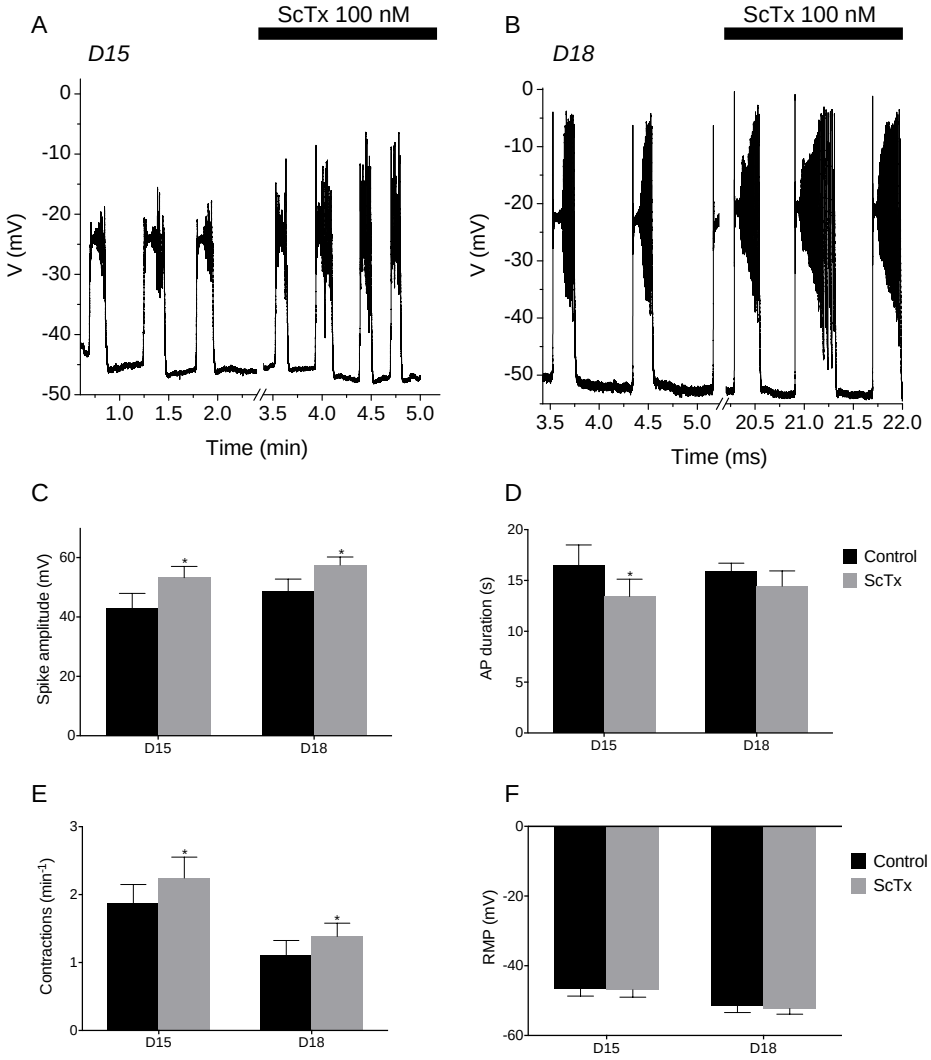

Figure 5.9: ScTx modulates AP frequency, duration and spike amplitude. Spontaneous electrical activity recorded from the longitudinal layer of D15 and D18 myometrium (A and B). Activity consisted of slow depolarisation to threshold, followed by an AP composed of a plateau upon which a number of spikes were superimposed. the bar represents the maximum effect in response to 100 nM ScTx. Summary bar charts for D15 (n=6) and D18 (n=6) cells show. (C) Mean AP spike amplitude significantly increased from 42.87±5.07 mV to 53.25±3.78 mV (P≤0.05) in D15 and from 45.5±4.96 mV to 56.21±3.37 mV in D18 tissue. (D) A significant decrease in mean AP duration from 16.77±2.14 s to 11.87±0.76 s (p≤0.05) in D15 tissue but no significant difference in D18. (E) Application 100nM of ScTx also significantly increased AP frequency in the D15 samples form a mean of 1.69±0.18 to 2.31±0.34 AP min^{-1} and from 1.11±0.22 to 1.38±0.19 AP min^{-1} in D18 tissue. (F) ScTx did not alter the RMP of either D15 or D18 (*P≤0.05; **P≤0.01).

5.3.2 Effect of varying the Kir7.1 channel density

The MSMC membrane potential is modulated in a gestation-dependent manner; in mid-gestation the membrane potential is hyperpolarised towards E_{K} [193]. This contributes to the uterus remaining quiescent during the development of the fetus. The membrane potential then depolarises gradually towards the end of gestation [187, 193]. The control of RMP and rises in intracellular calcium are essential for contraction in human MSMC [187]. Nevertheless, the precise mechanism is still unknown.

Inwardly rectifying potassium channels in many cell types hyperpolarise the RMP by remaining persistently open allowing a continuous inward potassium current [194]. They reduce the electrical activity of excitable cells. Kir7.1 (see Chapter 4 for description of its kinetics) is expressed at mRNA levels in MSMC [8]. It is found in many cell types but its physiological function is largely unknown [194].

McCloskey et al [90] identified Kir7.1 as being of crucial importance in maintaining a hyperpolarised membrane potential during uterine quiescence. They showed that Kir7.1 modulates the myometrial AP waveform, the RMP, and calcium entry (and hence force) during the AP. The relatively low conductance and the voltage and time-independence of the Kir7.1, as discussed in Chapter 4, together with the high expression of this channel [8] give rise to a stable hyperpolarised RMP. Thus, Kir7.1 maintains hyperpolarised membrane potential during gestation and when removed the potential becomes more depolarised; this could make the cell more excitable at term [90]. It is likely that Kir7.1 would contribute to setting the RMP in MSMC, and that it could shift the RMP to more hyperpolarised potential during quiescence.

To understand the function of Kir7.1 in the uterine activity, the model was used to investigate the potential impact of changes in Kir7.1 channel density on myometiral electrogenesis. We modelled the effect of increasing channel density on the myometrial AP waveform. In free-running simulations of membrane potential, we used a stimulating current (a 500 ms square pulse) to trigger the electrical activity of the cell. During the excitable phase of the AP, we increased the Kir7.1 channel density within a physiological range (from 0 to 1200 channels/pF). This hyperpolarised the RMP, decreased the calcium entry, and had significant effects on L-type, hERG, Kir7.1, SK4, BK, and other channels during the AP (Figure 5.10). Increasing Kir7.1 activity modulates calcium entry during the plateau phase of the complex AP, resulting in a decrease in contractile force and inefficient contractions. Decreasing Kir7.1 increases some potassium currents from other channels, such as hERG, Kv4.3, SK4, and BK. This increase can have the effect of reducing the depolarising

drive to ensure AP repolarisation [90].

On the other hand, increasing Kir7.1 density increased the T-type current as shown in Figure 5.10. The latter can be triggered by the hyperpolarisation of the membrane potential. T-type channels recover from inactivation in a process called "deinactivation" only after the hyperpolarisation of the membrane potential [195]. For neurones, low-threshold calcium spikes, elicited by the T-type channel, start to appear after membrane hyperpolarisation below -69 mV, with full amplitude spikes observed when the membrane was hyperpolarised to levels below -73 mV [195]. Upon return to RMP, the T-type channels open. They begin to activate at about -60 mV and typically produce a maximum current at around -30 mV as discussed in Chapter 4. The window current (a small range of voltages where the channel can open but do not inactivate completely [195]) obtained by superimposed steady state activation and inactivation variables of the T-type channel is enlarged by the hyperpolarised potential caused by the increase of Kir7.1 density.

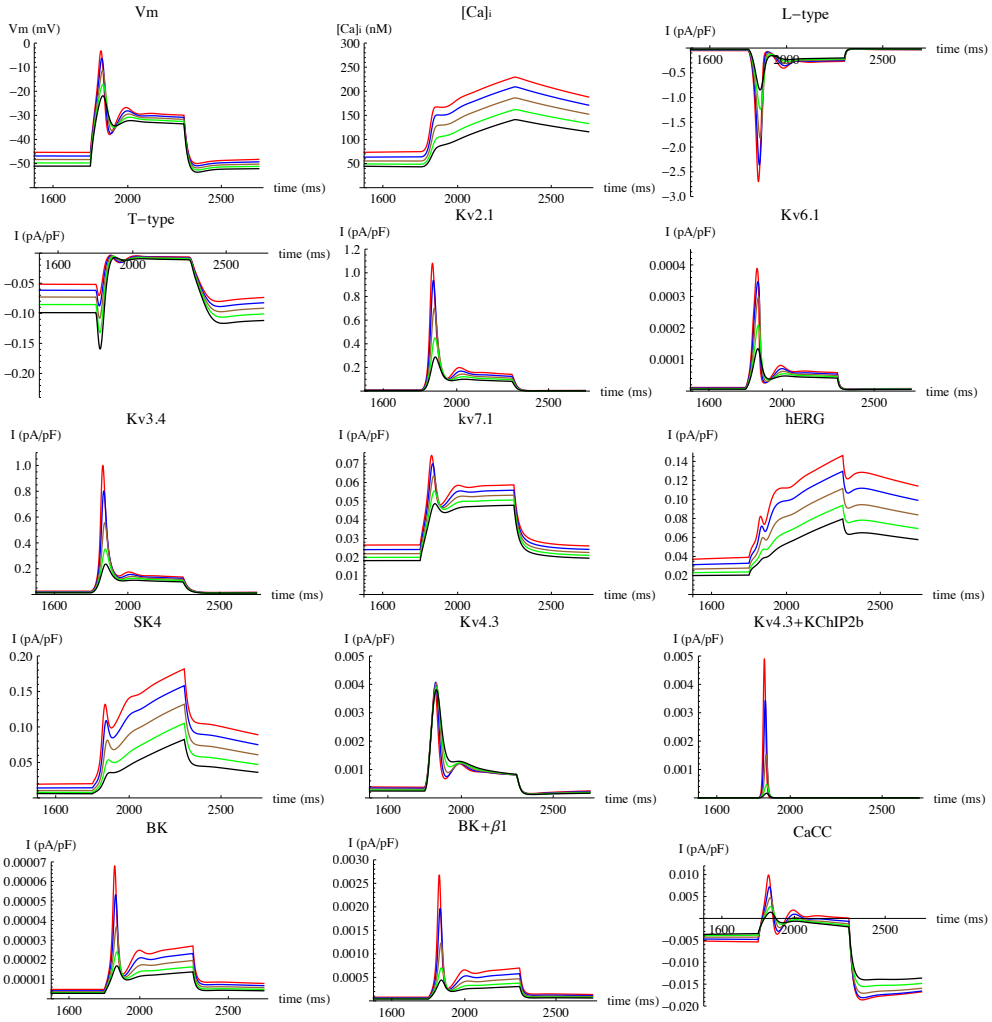

Figure 5.10: Effect of increasing Kir7.1 densities.
A free-running simulation of the effect of increasing Kir7.1 densities on the myometrial AP waveform. Time-dependent effect of increasing Kir7.1 densities (red=0 channels/pF, blue=300 channels/pF, brown=600 channels/pF, green=900 channels/pF, and black=1200 channels/pF) is depicted on V (mV), $[Ca^{2+}]_i$ (nM), and individual conductances (pA/pF) included in the simulation. Increasing density of Kir7.1 within physiologically realistic values, hyperpolarises RMP, whilst decreasing membrane excitability during depolarising excursions in V leading to decreasing calcium entry. Changing the channel density of Kir7.1 has a disproportionate effect on hERG, Kv7.1, SK4, and BK.

5.4 Representing the functional redundancy of the MSMC

The observed membrane potential time series is linear in the channel densities, which implies that the space of all possible combinations of ion channel densities that is consistent with the data can be calculated from the kernel of a linear transformation. This kernel provides information about the functional redundancy in the system. In order to visualise the redundancy, we formulated a basis of null $\boldsymbol{W}$ in echelon form, which is then presented in the form of heat maps such as those shown in Figures 5.11 and 5.13. For each row, a unit change in the density of the channel appearing in the leading (left-most) position can be functionally compensated by upward or downward shifts represented by the trailing elements (to the right). By "compensation" we mean the ability to exhibit the same electrophysiological behaviour despite altered channel densities. However, it is reasonable to expect that the compensatory shifts encoded by these "redundancy maps" are applicable for a more general range of behaviours, as we shall verify shortly.

Strictly speaking, this compensation is exact only for the voltage waveform that was used to determine the matrix $\boldsymbol{V}$. Moreover, the compensatory shifts are exact only for infinitesimal shifts in the leading channel density. For finite shifts in the leading variable, the corresponding shifts dictated by the trailing elements are only a first-order approximation, and there will be an operating range in which this is reasonably valid. This operating range is further constrained by physiologic feasibility. For instance, channel densities cannot be negative. Similarly, there will be a physiological upper bound to the current density that can be sustained, or to the quantities of channel proteins that can be synthesised and inserted into the cell membrane. Even the slightest shift in a "leading" channel density might require a massive shift in a compensating channel. To estimate such an upper bound for the channel densities, we used the procedure detailed Chapter 3.

5.4.1 BK

It was hypothesised that BK channels are modulated throughout gestation, thereby altering the excitability of the uterus and allowing the uterus to remain in a quiescent state during gestation. The uterus becomes more excitable toward the end of pregnancy and the role of BK decreases [135]. Several studies have also shown that the functional and molecular expression of BK channels diminishes in late pregnancy [196, 197]. However, this hypothesis was not confirmed by Aaronson et al [198], who investigated the role of voltage-gated and BK channels in regulating

basal contractility in MSMC by inhibiting these channels in non-pregnant rats, as well as during early, mid, and late pregnancy. None of the selective BK channel inhibitors significantly affected contractility in myometrial strips from either non-pregnant or pregnant animals. These results suggest that BK channels play little or no part in controlling contractions in rat MSMC.

To investigate the functional redundancy of the BK channels, we selected these channels as the leading variables for the echelon form, to give the redundancy map shown in Figure 5.11. This heat map indicates very small compensatory shifts, suggesting that the effect of BK can be compensated by extremely small variations in the other channels' densities, which is an indication that BK has only a minute effect on the waveform. Figure 5.12 shows the effect of increasing the BK channel density by 1 channel/pF on the membrane potential waveform. The shifts in the densities of the various channels, according to the values shown in the echelon form of Figure 5.11, compensate for the effect of shifting the BK channel density and virtually return the waveform back to its original form. Our functional redundancy analysis indicates that the effect of BK can be compensated by extremely small shifts in the channel densities of the other channels in the model. This suggests that BK exerts almost no effect on the voltage waveform that was observed in the present study.

Moreover, when we increased the channel densities of the BK channels in the free-running model (using the parameter fit according to the smallest ℓ_1-norm), we observed little effect on the waveform (Figure 5.5). Most of this small effect was compensated by the shifts in the channel densities that are shown in the echelon form (Figure 5.11). The effect of increasing the BK channel density and the effect of the compensation are shown in Figure 5.12. Our observation is in agreement with several studies that have indicated that BK channels play little or no part in controlling contractions [148, 197, 198].

5.4.2 hERG

ERG channel blockers were able to induce contractions in tissue strips that failed to develop spontaneous rhythmic activity [124]. Dofetilide (an ERG-specific blocker) induced contractions in quiescent tissues. This shows that blockade of ERG channels augments spontaneous uterine contractility *in vitro* [124]. On the other hand, ERG-activators inhibit spontaneous contractility [124].

We investigated the functional redundancy of the hERG channel. We moved the hERG channel in the leading position of the echelon form. As shown in the re-

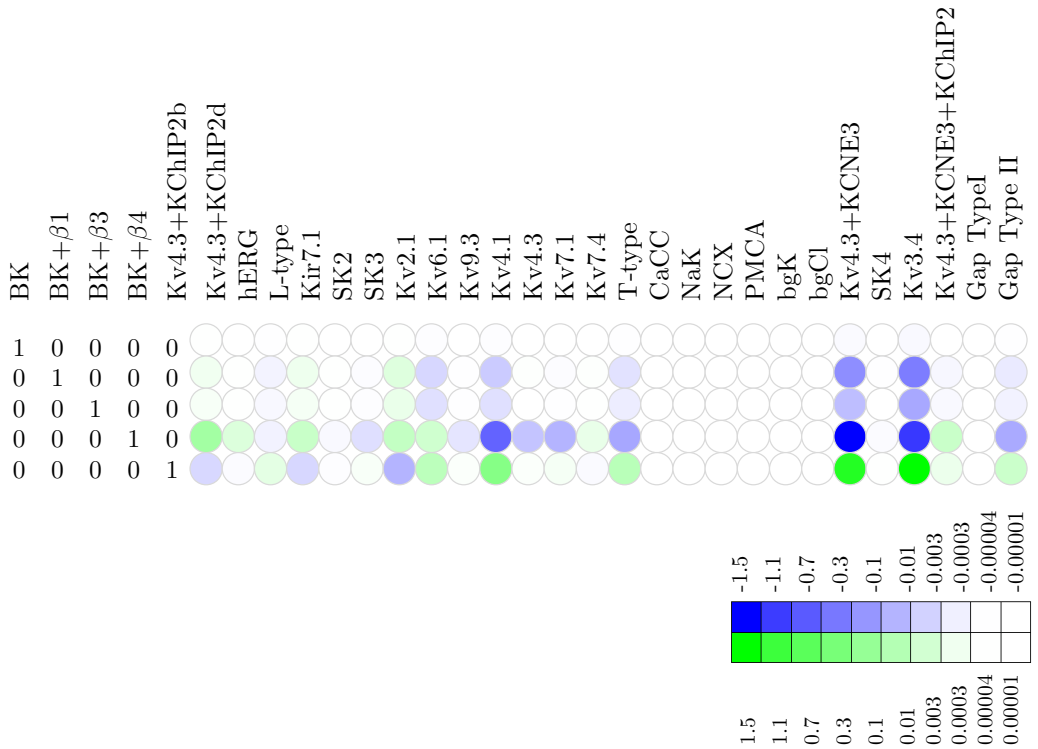

Figure 5.11: Echelon form of the null space with BK as a leading variable. The echelon form shows the redundancy inherent in the system organised in a way to have BK as a leading variable. A scale bar (shown on the right bottom corner) gives a quantitative approximation to the magnitude changes that correspond to the colour scheme used.

dundancy map in Figure 5.13, a minute decrease of 1 channel/pF in the hERG channel density would require 186000.43 channels/pF increase in BK, 9345.6 channels/pF decrease in $BK_{\alpha+\beta_3}$, and an increase of 138 channels/pF in the Kv4.3/KCNE3-/KChIP2. Such shifts are not physiologically plausible. The analysis indicates that small shifts in the hERG channel density could not be compensated by physiologically realistic shifts in the densities of the other channels, which means that the shifts prescribed by the redundancy map translate into very large compensatory shifts. In biological terms, this implies that hERG is *essential*, i.e., functionally non-redundant in the sense of being non-compensatable, relative to the observed voltage waveform. The channel is effectively "pinned"; a slight shift in its density cannot be compensated by a combination of shifts in other channels. This finding strongly suggests that hERG is a major suppressor of bursting activity in the MSMC.

5.4.3 SK

The genes encoding the family of SK channels share high overall structural homology, with little similarity to members of other potassium-channel subfamilies [22]. Therefore one would expect the members of the SK family to be interchangeable, i.e., functionally redundant (at least within the simulation). To investigate this hypothesis, we selected the SK_2 channel as one of the leading variables for the echelon form. We found that a unit shift in the latter can be compensated by an 0.49 negative shift in the SK_3 channel density, and 0.45 negative shift in the SK_4 channels density. Using the model in free-running form, we tested the effect of increasing the SK_2 channel density by 0.4 channels/pF on the membrane waveform. As shown in Figure 5.14, this shift could be compensated, as predicted, by decreasing the SK_3 channel density by 0.15 channels/pF and decreasing the SK_4 channel density by 0.14 channels/pF. These results suggest that SK_2, SK_3, and SK_4 are functionally fully interchangeable. The channels with the highest expression level in MSMC are SK_3 and SK_4 [8, 199].

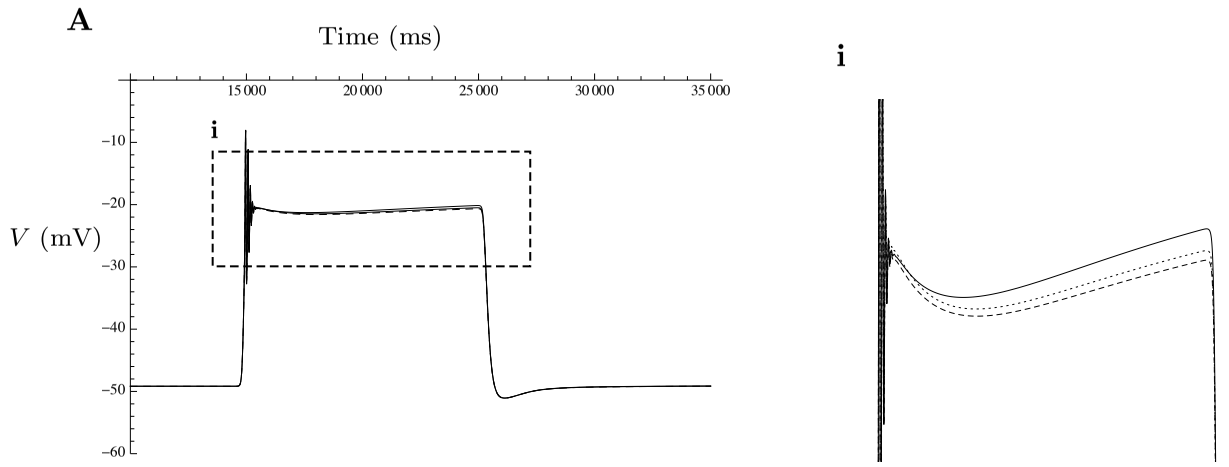

Figure 5.12: The effect of a shift in the BK channel density on AP.
The effect of varying the BK channels density (dashed line) on the AP triggered by a 10 sec extracellular ATP step function using the free-running model fitted with the parameters (constrained using the ℓ_1-norm) (solid line), together with the effect of the compensatory shifts shown in Figure 5.11 of the densities of the various channels (dotted line).

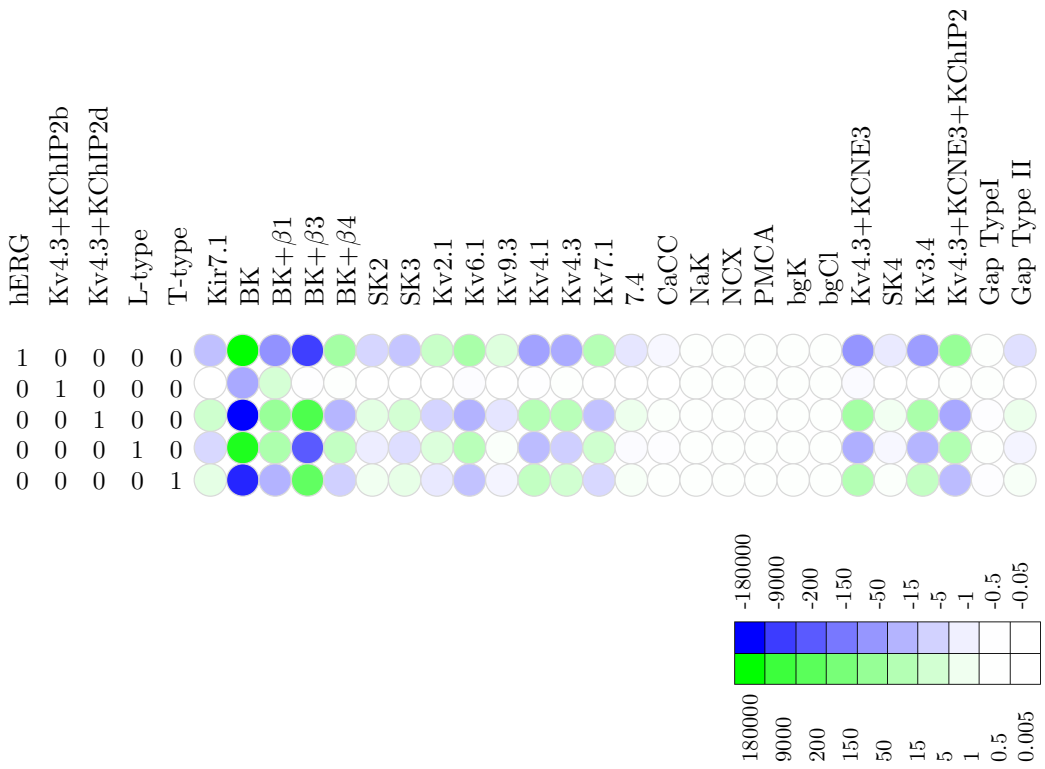

Figure 5.13: Echelon form of the null space with hERG as a leading variable. The echelon form shows the redundancy inherent in the system organised in a way to have hERG as a leading variable. A scale bar (shown on the right bottom corner) gives a quantitative approximation to the magnitude changes that correspond to the colour scheme used.

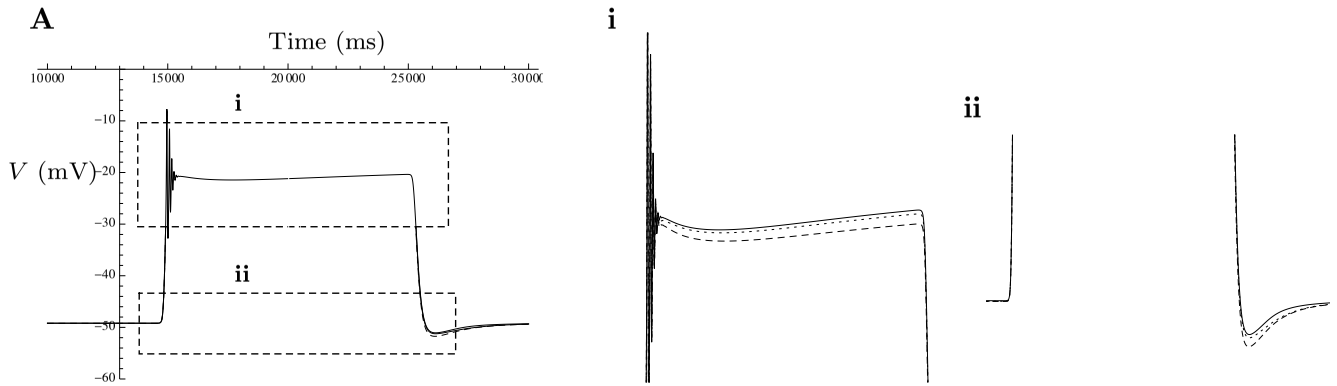

Figure 5.14: The effect of a shift in the SK_2 channel density on AP.
The effect of varying the SK_2 channels density (dashed line) on the AP triggered by a 10 sec extracellular ATP step function using the free-running model fitted with the parameters (constrained using the ℓ_1-norm) (solid line), together with the effect of the compensatory shifts from both SK_3 and SK_4 densities (dotted line).

5.5 Exploring possible periodic triggers for depolarisation

In the final section of this chapter, we demonstrate how the model can be used as a tool to explore various hypotheses. For instance, a fundamental but largely unanswered question in MSMC physiology is what triggers the initial depolarisation in a periodic fashion. Uterine contraction during labour is myogenic and characterised by its automaticity [29]. Although it is known that the contractions are generated by an increase in the concentration of intracellular calcium of MSMCs via L-type calcium channels, the regulation and spontaneity of uterine contractile waves are not fully understood [29]. We explored two mechanisms that could result in the initiation of the periodic spontaneous contractions. The first mechanism is through the activation of the purinergic membrane receptor (P2RX4), which is an ATP-gated ion channel. The second mechanism is through the periodic depletion of phosphatidylinositol-4,5 bisphosphate (PIP_2), which modulates the activation of a number of plasma membrane potassium ion channels. This activation, in turn, depolarises the cell and could cause contractions.

5.5.1 Hypothesis I: Availability of ATP

We investigated the role of ATP in the enhancement of MSMC activation and the initiation of spontaneous electrical activity. We hypothesise that the AP initial depolarisation is initiated by a periodic release of ATP via hemichannels [34, 152, 200–202]. Figure 5.15 shows a schematic diagram of our hypothesis.

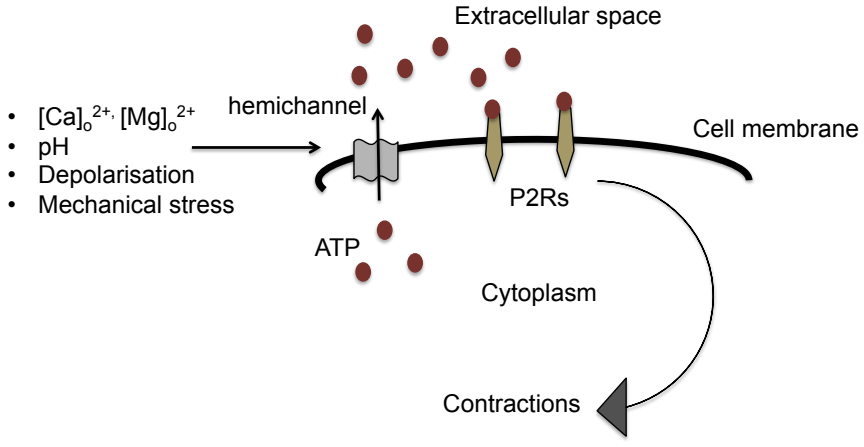

Figure 5.15: The hemichannel-P2RX pathway central to hypothesis I.

Several lines of evidence point to the existence of a purine-gated non-specific cationic conductance in MSMC [203–205]. The mRNA expression levels of P2RX4 and P2RX7 increase in rat myometrial samples as pregnancy progresses [203], suggesting that these receptors are associated with uterine contractions at term. The mRNA for these proteins is also increased upon stimulation with lipopolysaccharide (LPS), which is a known stimulant of preterm labour [203]. In freshly dissociated rat myometrial cells, a non-specific cationic conductance consistent with the biophysical properties of P2RX7 was measured upon stimulation with ATP [204, 205]. Human MSMC also express both isoforms; however, in contrast to the rat, P2RX4 is the dominant isoform [8].

In our human MSMC simulation, we modelled the current conducted by P2RX4, and added it to our model when evaluated in free-running mode. The time course of the extracellular ATP ($[\mathrm{ATP}]_o$) was represented by a step function. This was used as a forcing function to drive the ATP-gated kinetics of P2RX4. The latter is activated by $[\mathrm{ATP}]_o$, while continuous presence of ATP evokes a rapid inward current that desensitises [167]. P2RX4 activates and deactivates rapidly and desensitises relatively slowly, within seconds of continuous agonist application [167]. The rates of activation and desensitisation are dependent on $[\mathrm{ATP}]_o$ [167]. The activation and desensitisation time constants are inversely correlated with $[\mathrm{ATP}]_o$ [167]. To model P2RX4, we described ATP-dependent steady-state of the activation variable by fitting the experimental data of Toulme et al [25] to the Hill equation. We obtained an EC_{50} of 32 μM and a Hill coefficient of 1.6 (Figure 4.34B). The time constants of activation and desensitisation τ_{act} and τ_{des}, respectively, were both extracted from the P2RX4 ATP-dependent current trace from Toulme et al [25] by fitting a single exponential to the data. The simulated current trace is shown in Figure 4.34A. The P2RX4 is highly permeable to Ca^{2+}, while equally permeable to Na^{+} and K^{+}; it is, however, not permeable to Cl^{-} [168]. It is also permeable to other monovalent ions with a ratio of calcium to monovalent permeability $P_{\mathrm{Ca}}/P_{\mathrm{mono}}$ of 4.2. To calculate the reversal potential of the P2RX4, E_{P2RX4}, we used the modified GHK equation for a mixtures of permeant ions of different valences [31,56,169]. The unitary conductance is $\sim$36 pS [168]. The current mediated by P2RX4 is described by the following equation:

$$I_{\mathrm{P2RX4}} = \kappa_{\mathrm{P2RX4}} G_{\mathrm{P2RX4}} P_{\mathrm{act}} P_{\mathrm{des}} (V - E_{\mathrm{P2RX4}}) \,, \tag{5.2}$$

where κ_{P2RX4} is the P2RX4 channel density (varied in the free-running model to stimulate an AP), G_{P2RX4} is the unitary conductance, and P_{act} and P_{des} are the

activation and desensitisation gating kinetics, respectively. Further details can be found in Chapter 4. In free-running mode, using the conductome consistent with the smallest ℓ_1-norm, a 10 sec step function of $[\text{ATP}]_o$ (from 0 to 1 mM with $\kappa_{\text{P2RX4}} =$ 90 channels/pF) was used to drive the ATP-gated kinetics of the P2RX4 receptors. Figure 5.5 shows the triggered AP.

To assess how P2RX4 might initiate spontaneous contractions, isometric tension from small (approximately 5×10 mm) muscle strips of the human myometrium was recorded, examining the effects of 30 μM 5-BDBD (P2RX4 antagonist) on the activity (see Chapter 2 for details). Figure 5.16 shows a representative trace of the mechanical activity observed in term human myometrium where application of 30 μM 5-BDBD reduces contraction frequency to zero. Summary data presented in Figure 5.18 show that contraction frequency is significantly reduced from 0.2±0.09 to 0.01±0.01 contractions per minute (n=11, p≤0.001).

P2RX7 was another candidate gene associated with the initiation of spontaneous contractions. It is, however, much less expressed in human MSMCs [8]. A model was constructed to account for the P2RX7, as described in Chapter 4, and similar procedures (as P2RX4) were applied to include it in the free-running model. We were not able to trigger an AP with similar properties to the MSMC APs recorded in literature.

To assess how P2RX7 might initiate spontaneous contractions, we recorded isometric tension from small (approximately 5×10 mm) muscle strips of the human myometrium, examining the effects of 1 μM A438079 (P2RX7 antagonist) on the activity (see Chapter 2 for details). Figure 5.17 shows a representative trace of the mechanical activity observed in term human myometrium where application of A438079 had no effect on contraction frequency. Contraction frequency is significantly lower using BDBD compared to A438079 (Figure 5.19).

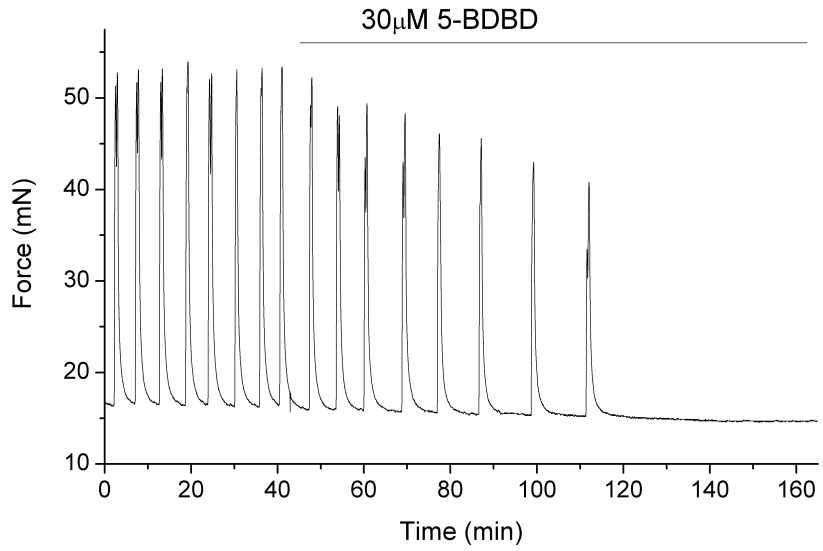

Figure 5.16: A representative trace of the mechanical activity observed in term human myometrium before and after BDBD (P2RX4 antagonist) application.

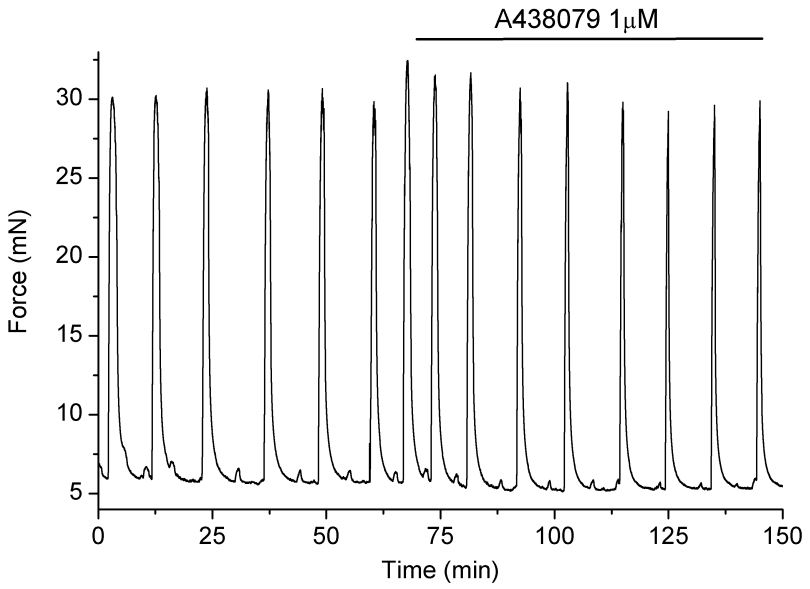

Figure 5.17: A representative trace of the mechanical activity observed in term human myometrium before and after A438079 (P2RX7 antagonist) application.

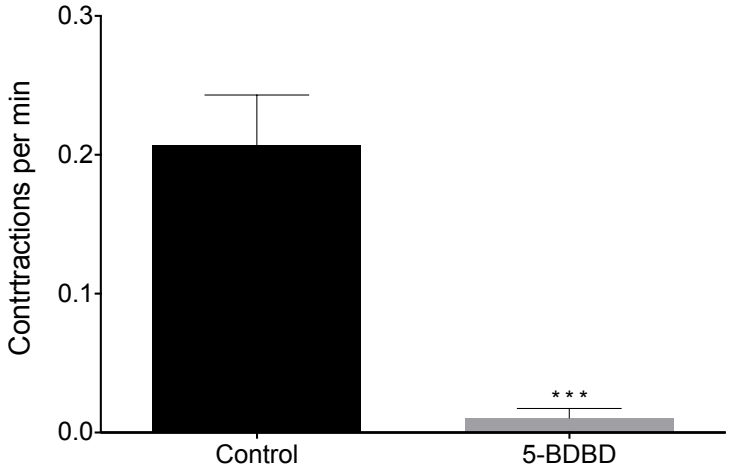

Figure 5.18: Contraction frequency reduction as a result of the P2RX4 antagonist (BDBD) application.

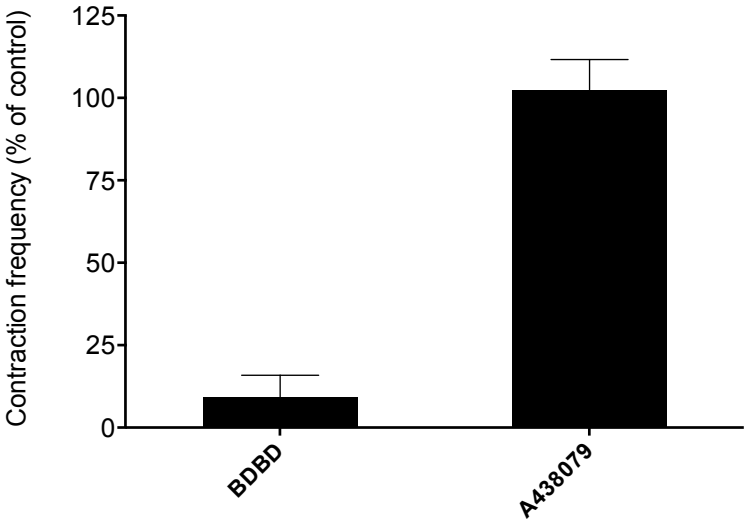

Figure 5.19: Contraction frequency reduction as a result of P2RX4 antagonist (BDBD) and P2RX7 antagonist (A438) application.

5.5.2 Hypothesis II: Periodic depletion of PIP_2

An alternative hypothesis to explain periodic depolarisation in the MSMC is that depletion of PIP_2 affects several plasma membrane potassium-conducting ion channels. The second-messenger precursor PIP_2 is located in the inner leaflet of the cell plasma membrane where it serves a number of physiological functions, including several signalling pathways, one of which produces the second messengers diacylglycerol and inositol 1,4,5 triphosphate [31]. Numerous plasma membrane ion channels require PIP_2 to function and can be inhibited by those signalling pathways that deplete PIP_2 [206]. Notably, PIP_2 regulates several myometrial potassium channels, such as Kir7.1, Kv7.1, Kv7.4, and hERG; PIP_2 could be a means by which the cell coordinates the intracellular processes with the events at the level of the plasma membrane. Changes in the kinetics of these channels could depolarise the cell and induce the electrical activity.

In view of a lack of dose-response data on PIP_2, we assumed a "two-level" mechanism: a release of PIP_2 followed by a temporary depletion and then a subsequent replenishment of PIP_2. We examined the effect of PIP_2 concentration on the kinetics of each of the ion channels affected. Two models, with different kinetics, were constructed for each of those channels, with and without PIP_2 application. We investigated the effect of PIP_2 on each of the susceptible channels.

Effect of PIP_2 on hERG

PIP_2 modulates hERG by increasing the hERG maximal current, concomitantly slowing deactivation and changing activation and inactivation gating [207]. The channel PIP_2-sensitivity is high to moderate in the range of physiological concentrations. At low PIP_2 levels, a fraction of hERG current persists (low sensitivity) [207]. In giant patch experiments, PIP_2 could strongly increase hERG current by increasing its maximal amplitude by up to three times, deactivation is accelerated during run-down (loss of the channel's activity) and slowed by PIP_2 application [207]. A Markov model (Figure 5.20), adopted from previously described hERG models (see Chapter 4), was used to simulate the effect of PIP_2 on hERG [207]. Inactivation was modelled as a late transition that is activation-dependent. All transition rates were voltage-dependent. The transition rates before the application of PIP_2 are as

follows:

$$
\begin{aligned}
\alpha_1^{[\mathrm{hERG}]} &= 0.783\exp[4.09\times10^{-4}\ V]\ , \\
\beta_1^{[\mathrm{hERG}]} &= 8.58\times10^{-3}\exp[-9.24\times10^{-3}\ V]\ , \\
\alpha_2^{[\mathrm{hERG}]} &= 8.89\times10^{-3}\exp[2.96\times10^{-2}\ V]\ , \\
\beta_2^{[\mathrm{hERG}]} &= 1.25\times10^{-4}\exp[-4.98\times10^{-2}\ V]\ , \\
\alpha_3^{[\mathrm{hERG}]} &= 3.27\times10^{-2}\exp[1.09\times10^{-2}\ V]\ , \\
\beta_3^{[\mathrm{hERG}]} &= 1.75\times10^{-2}\exp[-6.32\times10^{-3}\ V]\ , \\
\alpha_i^{[\mathrm{hERG}]} &= 3.19\times10^{-3}\exp[-3.15\times10^{-2}\ V]\ , \\
\beta_i^{[\mathrm{hERG}]} &= 9.05\times10^{-2}\exp[1.85\times10^{-2}\ V]\ , \\
\alpha_{ic}^{[\mathrm{hERG}]} &= 7.22\times10^{-2}\exp[2.27\times10^{-2}\ V]\ , \\
\beta_{ic}^{[\mathrm{hERG}]} &= (\beta_3^{[\mathrm{hERG}]}\alpha_i^{[\mathrm{hERG}]}\alpha_{ic}^{[\mathrm{hERG}]})/(\alpha_1^{[\mathrm{hERG}]}\beta_1^{[\mathrm{hERG}]})\ ,
\end{aligned}
\tag{5.3}
$$

while the transition rates after the application of PIP_2 are as follows:

$$
\begin{aligned}
\alpha_1^{[\mathrm{hERG}]} &= 1.083\exp[3.14\times10^{-4}\ V]\ , \\
\beta_1^{[\mathrm{hERG}]} &= 2.45\times10^{-3}\exp[-10.2\times10^{-3}\ V]\ , \\
\alpha_2^{[\mathrm{hERG}]} &= 7.76\times10^{-3}\exp[3.49\times10^{-2}\ V]\ , \\
\beta_2^{[\mathrm{hERG}]} &= 2.31\times10^{-4}\exp[-4.84\times10^{-2}\ V]\ , \\
\alpha_3^{[\mathrm{hERG}]} &= 7.63\times10^{-2}\exp[0.513\times10^{-3}\ V]\ , \\
\beta_3^{[\mathrm{hERG}]} &= 1.41\times10^{-2}\exp[-3.84\times10^{-3}\ V]\ , \\
\alpha_i^{[\mathrm{hERG}]} &= 5.68\times10^{-2}\exp[-2.7\times10^{-2}\ V]\ , \\
\beta_i^{[\mathrm{hERG}]} &= 8.66\times10^{-2}\exp[2.58\times10^{-2}\ V]\ , \\
\alpha_{ic}^{[\mathrm{hERG}]} &= 5.37\times10^{-2}\exp[2.32\times10^{-2}\ V]\ , \\
\beta_{ic}^{[\mathrm{hERG}]} &= (\beta_3^{[\mathrm{hERG}]}\alpha_i^{[\mathrm{hERG}]}\alpha_{ic}^{[\mathrm{hERG}]})/(\alpha_1^{[\mathrm{hERG}]}\beta_1^{[\mathrm{hERG}]})\ .
\end{aligned}
\tag{5.4}
$$

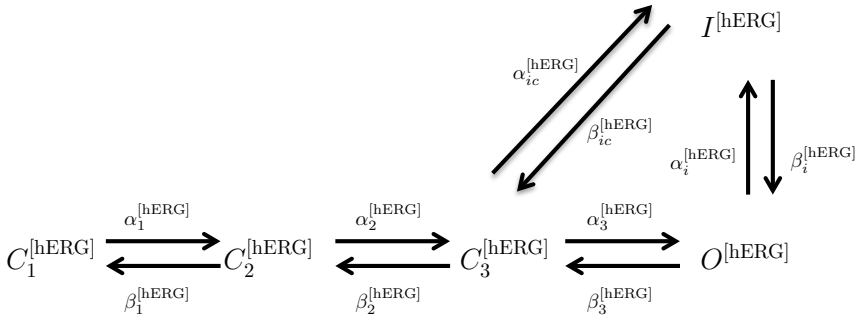

Figure 5.20: State transition diagram of the Markov model for the hERG channel used to model the effect of PIP_2 on the channel.
$C_1^{[\mathrm{hERG}]} - C_3^{[\mathrm{hERG}]}$ are closed states, $O^{[\mathrm{hERG}]}$ is the open states and $I^{[\mathrm{hERG}]}$ the inactivation state. The transition rates between the states for the hERG channel and the hERG channel after PIP_2 are in ms.

The equations describing the Markov kinetic model in Figure 5.20 are as follows:

$$
\begin{aligned}
\frac{dC_1^{[\mathrm{hERG}]}}{dt} &= -\alpha_1^{[\mathrm{hERG}]}C_1^{[\mathrm{hERG}]} + \beta_1^{[\mathrm{hERG}]}C_2^{[\mathrm{hERG}]} \ , \\
\frac{dC_2^{[\mathrm{hERG}]}}{dt} &= \alpha_1^{[\mathrm{hERG}]}C_1^{[\mathrm{hERG}]} - (\beta_1^{[\mathrm{hERG}]} + \alpha_2^{[\mathrm{hERG}]})C_2^{[\mathrm{hERG}]} + \beta_2^{[\mathrm{hERG}]}C_3^{[\mathrm{hERG}]} \ , \\
\frac{dC_3^{[\mathrm{hERG}]}}{dt} &= \alpha_2^{[\mathrm{hERG}]}C_2^{[\mathrm{hERG}]} - (\alpha_3^{[\mathrm{hERG}]} + \beta_2^{[\mathrm{hERG}]} + \\
&\quad \alpha_{ic}^{[\mathrm{hERG}]})C_3^{[\mathrm{hERG}]} + \beta_3^{[\mathrm{hERG}]}O^{[\mathrm{hERG}]} + \beta_{ic}^{[\mathrm{hERG}]}I^{[\mathrm{hERG}]} \ , \\
\frac{dO^{[\mathrm{hERG}]}}{dt} &= \alpha_3^{[\mathrm{hERG}]}C_3^{[\mathrm{hERG}]} - (\beta_3^{[\mathrm{hERG}]} + \alpha_i^{[\mathrm{hERG}]})O^{[\mathrm{hERG}]} + \beta_i^{[\mathrm{hERG}]}I^{[\mathrm{hERG}]} \ , \\
\frac{dI^{hERG}}{dt} &= \alpha_i^{[\mathrm{hERG}]}O^{[\mathrm{hERG}]} - (\beta_i^{[\mathrm{hERG}]} + \beta_{ic}^{[\mathrm{hERG}]})I^{[\mathrm{hERG}]} + \alpha_{ic}^{[\mathrm{hERG}]}C_3^{[\mathrm{hERG}]} \ .
\end{aligned}
$$

Effect of PIP_2 on Kir7.1

Members of Kir channel family were among the first channels demonstrated to be gated by PIP_2 [206]. In general, Kir channels run-down if PIP_2 is depleted and reactivate if PIP_2 is applied. Pattnaik et al [26] recorded whole-cell currents in solitary bovine RPE cells and isolated the Kir7.1 current as the Cs^+-sensitive component. From this study, we extracted the G-V curve from the Cs^+-sensitive I-V curve in a cell dialysed with solution containing 50 μM PIP_2 (Figure 5.21). The voltage-dependent conductance was described by a single exponential fit. The voltage-dependent conductance in the absence of PIP_2 is:

$$P_{\mathrm{Kir7.1}_{ss}} = 0.083\ e^{-0.018\ V} \tag{5.5}$$

and with PIP_2 at high levels:

$$P_{\mathrm{Kir7.1}_{ss}} = 0.17\ e^{-0.01144\ V}\ . \tag{5.6}$$

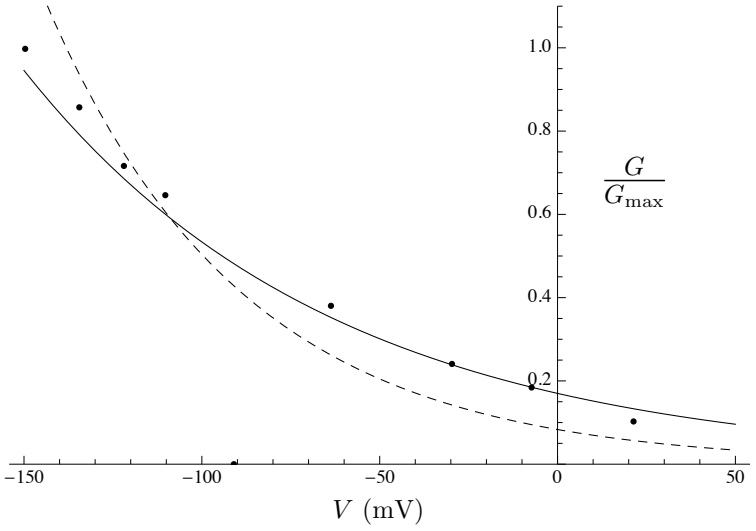

Figure 5.21: PIP_2 effect on G-V curve.
Simulated effect of PIP_2 (solid line) with data extracted from experiments by Pattnaik et al [26] (solid circles). The G-V curve in the absence of PIP_2 (dashed) is also shown for comparison.

Effect of PIP_2 on Kv7.1 and Kv7.4

PIP_2 controls the activity of the KCNQ1/KCNE1 potassium channel complex; the current is suppressed by depletion of PIP_2 [208]. However, there do not appear to be experimental data in the literature to support any effect of PIP_2 on the homomerics forms of Kv7.1 and Kv7.4.

In the free-running model, using the conductome consistent with the smallest ℓ_1-norm, we switched between the two levels from with to without PIP_2, for 30 sec. Following this change in PIP_2 concentration, a change in the kinetics of the above ion channels was induced as described. Under the investigated conditions, switching between the two states did not trigger an AP.

Chapter 6

Discussion

In this chapter, we discuss our approach, the methods used, some applications of our model, the advantages and the limitations of our approach. A large part of this chapter will be published in a forthcoming paper.

6.1 General discussion

Techniques such as qRT-PCR in conjunction with LCM [209] and mRNA-sequencing (mRNA-seq) have enabled significant advances in gene expression analysis of single cells and in tissues. Application of these techniques provided a complete repertoire of the mRNA population in the MSMC [8, 90], which we used to construct a list of possible electrogenic entities by combining all possible combinations of ion channel subunits that are potentially expressed in the MSMC. Since many channels exist as various combinations of subunits, we obtain a repertoire of 31 entities that may be present in the plasma membrane of the MSMC. A mathematical model for every individual potential oligomeric channel complex was formulated from the biophysical data, in the main part on the basis of heterologous expression systems in the literature.

We used native cell type behaviour (voltage and calcium time series, as detailed in Chapter 2; experiments conducted by Dr McCloskey) to drive the individual conductance currents. The only remaining unknowns are the densities in the plasma membrane of the various species, since all the gating kinetics were predetermined or deduced from the literature. The observed membrane potential time series is linear in these densities, which allows us to calculate the space of all possible solutions of ion channel densities that is consistent with the observed data, from the kernel of a linear transformation. The kernel describes the redundancy in the sys-

tem. To determine the parameters we considered the most parsimonious solution with the smallest ℓ_1-norm (minimising the sum of the channel densities) subject to non-negativity. Other solutions, using alternative criteria, could be considered, such as the solution of the parameters in close agreement with the mRNA expression data for the conductances. However, this awaits a more reliable accurate quantitative determination of mRNA levels. Predictions made using our model, with the conductome consistent with the smallest ℓ_1-norm, were tested against experimental data. The data employed were taken from voltage-clamp experiments for isolated currents that were sensitive to inhibition by drug application. The simulated values of peak currents at certain voltage steps closely matched those observed experimentally. With channels such as Kir7.1, the simulated data failed to predict the measured data accurately, which could be due to various factors. First, on the basis of the observed voltage time series, the Kir7.1 current and the background potassium current are indistinguishable (i.e., Kir7.1 behaves in the same manner as background potassium current). Whereas our approach allows us to capture and explore the currents conducted by the channels that exert a significant effect on the observed behaviour, we are not able to discriminate accurately between channels that have similar biophysical properties throughout the observed waveform (such as in the case of Kir7.1). In fact, to observe Kir7.1 currents, an elevated external $[K^+]_o$ is applied, which results in a higher reversal potential and hence increased peak current [90]. By contrast, the particular time series to which our model was fitted was obtained under physiological $[K^+]_o$, which may also explain why we were unable to distinguish this channel from the background.

Complex biophysical models often have to be hand-tuned in order to match measured physiological behaviours, which raises questions of identifiability and interpretability. The advantage of our approach is that the indeterminacy inherent in the available data is objectively represented, e.g. in the form of the 'echelon' heat maps as discussed in Chapter 5. The key insight of the method is that the total transmembrane current is linear in the current shapes of the various channels, both of which are readily computed once the voltage trace is known. Huys et al [191] proposed an approach that is quite similar to ours. They observed that the optimisation problem possesses a unique solution provided that the channel kinetics are associated with "sufficiently different" current shapes, which concurs with our analysis. This means that for both our model and according to Huys et al [191], if the investigated channels have similar kinetics, more data are needed to distinguish between the channels. Also, if the linear combination of some channels together well account for the data, more data will not discriminate between those channels

and there will be an uncertainty with respect to the different combinations of the channels. Only the sum of those conductances is relevant.

Previous models of the myometrium, discussed in more detail in Chapter 1, were developed at the tissue and the organ levels [80–82]. Bursztyn et al [41] presented an excitation-contraction model of the uterine muscle cells, representing the cellular mechanisms of calcium control. Another model was presented by Rihana et al [78]. The model used the Hodgkin-Huxely formulation, using macroscopic currents based on voltage-clamp experiments from literature. The model was able to reproduce a single AP or a train of peaks of APs, using a stimulating current pulse, with a 10-dimensional state space. Tong et al [79] formulated a mathematical model of MSMC electrical activity that included fourteen macroscopic ionic currents. APs were induced in the whole cell model by applying an external stimulus current. These models use macroscopic currents, which combine several conductances into one single entity in the model. In contrast, we constructed our model based on individual potential oligomeric channel complex.

6.2 Varying the various channel densities

The method proposed in the present thesis combines an SVD approach to data analysis with a completely parameterised description at the individual current level. Several applications have been considered. The first is assessing the effect of varying the channel density of the different entities on the AP waveform in the "free-running" mode where the model is allowed to run with the densities set to minimum ℓ_1-norm solution. A stimulus, corresponding to changes in the level of extracellular ATP, is applied to generate an AP.

6.3 The functional redundancy

A second application is a visualisation of the functional redundancy of the system. In essence, this shows which combinations of channels can be substituted for one another in regards to the observed behaviour that was fed into the algorithm. In other words, the functional redundancy kernel is strictly relative to the voltage waveform. This is a severe limitation in the present study, where only data on a short burst containing a small number of action potentials has been used. However, it is not a serious limitation of the general approach. In principle, it is possible to obtain a much longer time-series, or to concatenate a series of related experiments, in which a much wider range of behaviours is invoked from the cell under study. The

additional computational cost is negligible, but the redundancy kernel obtained will be much more representative of the full range of the cell's functional capabilities.

6.4 Explaining channel properties

Several properties of some of the most important potassium channels viz. BK, Kv2.1, SK_2, Kir7.1, and hERG, can be explained on the basis of the redundancy analysis, augmented with free-running simulation.

6.4.1 BK

The role of BK channel in the contractility in MSMC is still unresolved. Formerly, it was suggested that BK channels alter the excitability of the uterus by allowing it to remain quiescent for the duration of the pregnancy. The role of the BK then decreases as the uterus becomes more excitable towards the end of the pregnancy [135]. These studies show that in human labour myometrial tissue, the calcium activated BK is either missing or considerably functionally modified [135, 196]. Conversely, Aaronson et al [198] argue that BK channels play little or no part in controlling basal rhythmicity in rat myometrium.

Using our functional redundancy analysis, we investigated the effect of BK. The effect of BK could be easily compensated by extremely small shifts in the channel densities of the other expressed channels. This indicates that BK exerts almost no effect on the observed voltage waveform. We also investigated the BK using the free-running mode. We increased the channel densities of the BK channels as shown in Figure 5.12; we observed only a minute effect on the waveform. Most of this effect was compensated by the shifts in the channel densities prescribed by the redundancy map (Figure 5.11). Our observation is in agreement with several studies that have indicated that BK channels have a minute effect in controlling contractions [148, 197, 198].

6.4.2 hERG

Loss of ERG channels and their functional impact in late pregnancy supports a hypothesis that these channels play an important role in maintaining uterine quiescence [124]. Contractions are induced in quiescent tissues treated with ERG channel blockers, while ERG-activators inhibits spontaneous contractility [124].

Our functional redundancy analysis indicates that small shifts in the hERG channel density could not be compensated by physiologically realistic shifts in the

densities of the other channels (Figure 5.13); physiologically realistic values of the channel densities were bounded as detailed in Chapter 3. This finding strongly suggested that hERG is a major suppressor of bursting activity in the MSMC.

6.4.3 Kv2.1

Next we explored how Kv2.1 might have a role in the regulation of spontaneous contractions. The effects of ScTx on the activity of MSMC were examined experimentally (experiments performed by Dr McCloskey) and then compared to the results from our model. The application of ScTx resulted in an increase in AP spike amplitude and in AP frequency. Also a reduction in the duration of AP was apparent in some of the recordings. We assessed the effect of varying the Kv2.1 densities from a high density to zero density of the Kv2.1 channels (Kv2.1, Kv2.1/Kv9.3 and Kv2.1/Kv6.1) by means of simulation run in the free running mode. Blocking the Kv2.1 channels in the simulation resulted in an increase in the initial AP spike amplitude, an increase in the rate at which steady state is reached during the plateau phase of the AP, and a slightly depolarised RMP (Figure 5.5). The prediction from our model and ScTx effect show that the Kv2.1 channels affect AP amplitude and frequency. No evidence was found that Kv2.1 plays a role in setting the RMP using current clamp recordings under physiological conditions. However, in view of the limited number of recordings made and the inherent variability from cell to cell recording RMP, we cannot rule out the possibility that such small changes of RMP (maximum predicted shift of around 4 mV), as predicted by our model, would have been below the detection limit of our apparatus. The Kv2.1 channel is, however, well placed to play a role in depolarisation during the AP plateau, at potentials where there should be good availability of the channel, allowing it to serve as a hyperpolarising drive working to limit the depolarising drive of channels such as the VGCCs responsible for the AP spikes. We concluded that the Kv2.1 channels appear to play a role in modulating the excitability of the myometrium by acting to inhibit contraction frequency and amplitude, while having a negligible impact on the RMP.

6.4.4 Kir7.1

Kir7.1 has been identified as having a crucial role in maintaining a hyperpolarised membrane potential during uterine quiescence as well as modulating the myometrial AP waveform [90]. We used our free-running model to investigate the potential importance of the Kir7.1 channel. We varied the Kir7.1 density within a physiological

range. The RMP was hyperpolarised and the calcium entry was decreased when we increase the channel density. The variation had significant effects on other channels as shown in Figure 5.10. Thus, given the expression profile of the Kir7.1 coupled to its biophysics, it was hypothesised that Kir7.1 is a key regulator of myometrial membrane potential during gestation.

6.4.5 SK

Finally, we investigated the SK channels. Physiological similarities between the members of the SK subfamily are well established. Based on these similarities, one would expect the SKs to be readily interchangeable and to be able to functionally compensate for each other). From the redundancy map, we have shown that a unit shift in the SK_2 channel density can be compensated by a combination of shifts in the SK_3 and SK_4 densities. This was confirmed by means of the free-running simulation as in Figure 5.14.

6.5 Possible triggers of spontaneous contractions

In a final application, we considered two mechanisms that could trigger spontaneous contractions. The first is through an increase in extracellular ATP concentration. The hypothesis is that spontaneous electrical activity is initiated by a periodic release of ATP via hemichannels present on the MSMC plasma membrane [152, 201, 202]. Extracellular ATP can activate P2RX4 and P2RX7 receptors expressed in the myometrium and have been reported to enhance uterine contractility [203] (a full description of the receptors' kinetics can be found in Chapters 4 and 5). Several lines of evidence support our hypothesis. The expression levels of P2RX4 receptors increase during late gestation at the time of delivery [8]. In rat MSCMs, the mRNA expression levels of P2RX4 and P2RX7 increase significantly throughout gestation [7, 203]. This suggests a significant role of these purinergic receptors in the uterine contractions. Moreover, a known stimulant of preterm labour, LPS [210–212], causes elevated mRNA levels of P2X purinergic receptors [162, 213]. The predominant isoform in rats is most likely the P2RX7 [204, 205], while in humans, P2RX4 is higher at mRNA levels [8]. A diagram representing this hypothesis is shown in Figure 5.15.

To test the hypothesis experimentally (experiments performed by Dr McCloskey), we used isometric tension recorded from strips of human myometrium before and after application of BDBD and A438079 (specific inhibitors of P2RX4 and P2RX7 [214, 215], respectively) on the activity; see Chapter 2 (Figure 5.16).

The contraction frequency was significantly reduced after BDBD application, while no change in the frequency was observed after A43079 application.

We incorporated P2RX4 and P2RX7 currents (see Chapters 4 and 5) in the model, while in free-running mode fitted with the parameter values obtained as described earlier. P2RX4 is activated and deactivates rapidly then desensitises relatively slowly during continuous presence of ATP (a full discussion of P2RX4 kinetics and its ATP-dependence can be found in Chapter 4). As regards P2RX7, it follows a complex pattern of gating; we used a Markov state model to describe its kinetics. The P2RX7 is a trimeric channel with three binding sites for ATP [174]. The occupancy of these sites affects the gating of the receptor. The P2RX7 model is discussed in detail in Chapter 4. An elevation of extracellular ATP, from 0 to 1 mM during a 10 second time window, was used to drive P2RX4 kinetics in the free-running mode. This concentration is reasonable; if the steady-state extracellular ATP concentration is substantially below the intracellular steady-state cytosolic concentration of ATP, the gradient for ATP efflux will be considerable. A typical intracellular ATP concentration is 3 to 10 mM [216, 217]. Naturally, if a pathway is activated for ATP release, ATP would exit the cell down a very favourable chemical concentration gradient [217].

Using the ATP step function to drive the P2RX4 and under the described conditions and parameter estimates, we were able to trigger a burst and plateau type AP with similar properties to the ones recorded previously from MSMCs [3,187,218]. However, we were not able to trigger adequate APs when we used ATP step function, within physiological ranges, to drive the P2RX7 kinetics.

The second mechanism acts through depletion of PIP_2. A temporary depletion of PIP_2 could occur in several signalling pathways such as signalling by PLC [206]. In particular it is known that the reduction of PIP_2 affects the kinetics of several myometrial potassium channels, namely Kir7.1, Kv7s and hERG [206,219]. The changes in their kinetics can depolarise then repolarise the membrane potential. Due to the lack of experimental data on the dose-response characteristics as function of the PIP_2 concentration, we assumed two levels of PIP_2 concentration; this describes a liberation of PIP_2 followed by a temporary depletion, after which PIP_2 levels return to normal. Two models with different kinetics, one with and one without PIP_2, were formulated for each of the PIP_2-sensitive channels. Under the conditions used and the parameter estimates, this mechanism was unable to initiate any electrical activity. The reason behind this could be that the effect of the PIP_2 is not well accounted for in the model; the physiological roles that PIP_2 plays in many of the conductances remain unknown, such as the effect on Kv7 channels [206], BK

calcium-activated channels, and Na/Ca exchangers [219]. Whereas most, if not all, inward rectifier potassium channels are strongly PIP_2-dependent, the situation with Kv channels is very different. Many gaps exist in the knowledge about the role of PIP_2 for those individual channels and transporters. PIP_2 effects on Kv channels can be large, small, variable or absent, and PIP_2 can evidently modify primarily activation/deactivation parameters, inactivation or channel availability in different cases [219]. While the effect on the channels, accounted for in the model, was not enough to trigger any spontaneous contraction, several other effects could be incorporated. This would be prompted with further advances in the understanding of how PIP_2 metabolism controls ion channels in cells.

Both hypotheses await further experimental results. The model analysis would become more robust if extracellular ATP concentration was to be measured during an AP, since this would allow us to formulate the current time-series more accurately. Moreover the analysis would be further bolstered by PIP_2 dose-response data, since this would allow an accurate modelling of the PIP_2-sensitive channels' kinetics as a function of PIP_2.

6.6 Different AP shapes generated by the model

Myometrial APs have complex waveforms, which may be classified as either plateau-type or burst-type [220] as discussed in Chapter 1. Both types of AP occur spontaneously and propagate between myocytes via gap junctions. The typical pattern of electrical activity in human myometrium is a single prominent spike potential occurring prior to each contraction wave followed by a partial early repolarisation then a long plateau phase [218]. The duration of plateau potentials is typically greater than 15 s. The plateau potential is usually between -20 and -30 mV [3]. The RMP is between -45 mV and -56 mV [3, 36]. The pattern of electrical activity in MSMCs changes throughout pregnancy from small irregular spikes to regular sustained activity sometimes accompanied by a plateau phase [91]. Occasional bursts of spikes occurs [218]. The changes in the densities and properties of calcium and potassium currents during gestation reshape the AP waveforms. Voltage-gated potassium channels are activated at different stages of the AP. Figure 6.1 shows currents, as simulated by the model, that contribute to the AP. Several conductances maintain or modulate the RMP. The inward rectifier potassium channel, Kir7.1, carries substantial current near RMP and also carries some current at depolarised potentials as discussed in Chapter 5. Additionally, some delayed rectifier potassium channels, such as Kv2.1-containing channels discussed in detail in Chapter 5, have a

small effect on the RMP (Figure 6.1). At rest, the NCX acts in the reverse mode by allowing one calcium ion into the cell and removing three sodium ions from the cell, this results in a small net outward current (Figure 6.1). The first upstroke spike is due to the inward calcium current through the L-type channel (discussed in Chapter 4). On the other hand, the plateau phase is due to a combined effect of sustained inward calcium current and a decrease in the voltage-sensitive potassium outward current. The L-type channel must have an effect in the formation of the plateau potential with its high threshold potential and slow inactivation (as discussed in Chapter 4). The individual channel currents in Figure 6.1, indicate a sustained L-type current during the plateau phase. Because of the large increase in slow inward calcium current through L-type and the transient nature of some of the potassium channels such as the Kv4.3-containing channels, the repolarisation phase is delayed and a plateau phase in the AP occurs. In cardiac, during the plateau phase, the NCX acts in the reverse mode; calcium enters in exchange for sodium [221]. NCX generates an outward current for a brief time. However, the current does not remain outward for long, because the AP triggers calcium release from the SR. This results in a transient rises in intracellular calcium that shifts the reversal potential of NCX and results in an inward current [222]. The NCX current shape shown in Figure 6.1 resembles that of the cardiac [223]; during plateau phase, NCX generates a brief outward current and acts in the reverse mode. The exchanger then reverses direction and generates an inward current (forward mode), extruding calcium in exchange of sodium influx, as a result of the influx of calcium through the L-type calcium channel [224]. This is in agreement with studies that have shown that the NCX, together with PMCA, play an important role in the decay of depolarisation-induced calcium transients in MSMC [188, 225]. The simulated NCX current produced by our model illustrates this effect in Figure 6.1. The plateau phase prolongs the AP duration making the myometrium AP one of the longest APs found in nature.

In free-running mode, the model was able to reproduce various AP shapes, as reported in the literature [3,187,218], when the channel densities of some entities were modified. A large variety of AP shapes can be reproduced as shown in Figure 6.2: plateau type, bursting then plateau type, and bursting type. The model can reproduce the APs by changing the channel densities of the L-type channel and the P2RX4 receptor density within physiological ranges (Figure 6.2). A plateau-type AP can be reproduced using the parameter values we determined (Figure 6.2A). Increasing the L-type channel density resulted in an increase in the cell bursting together with an increase in the amplitude of the AP. In fact, the amplitude of the bursting AP produced by our model after increasing the L-type density was higher

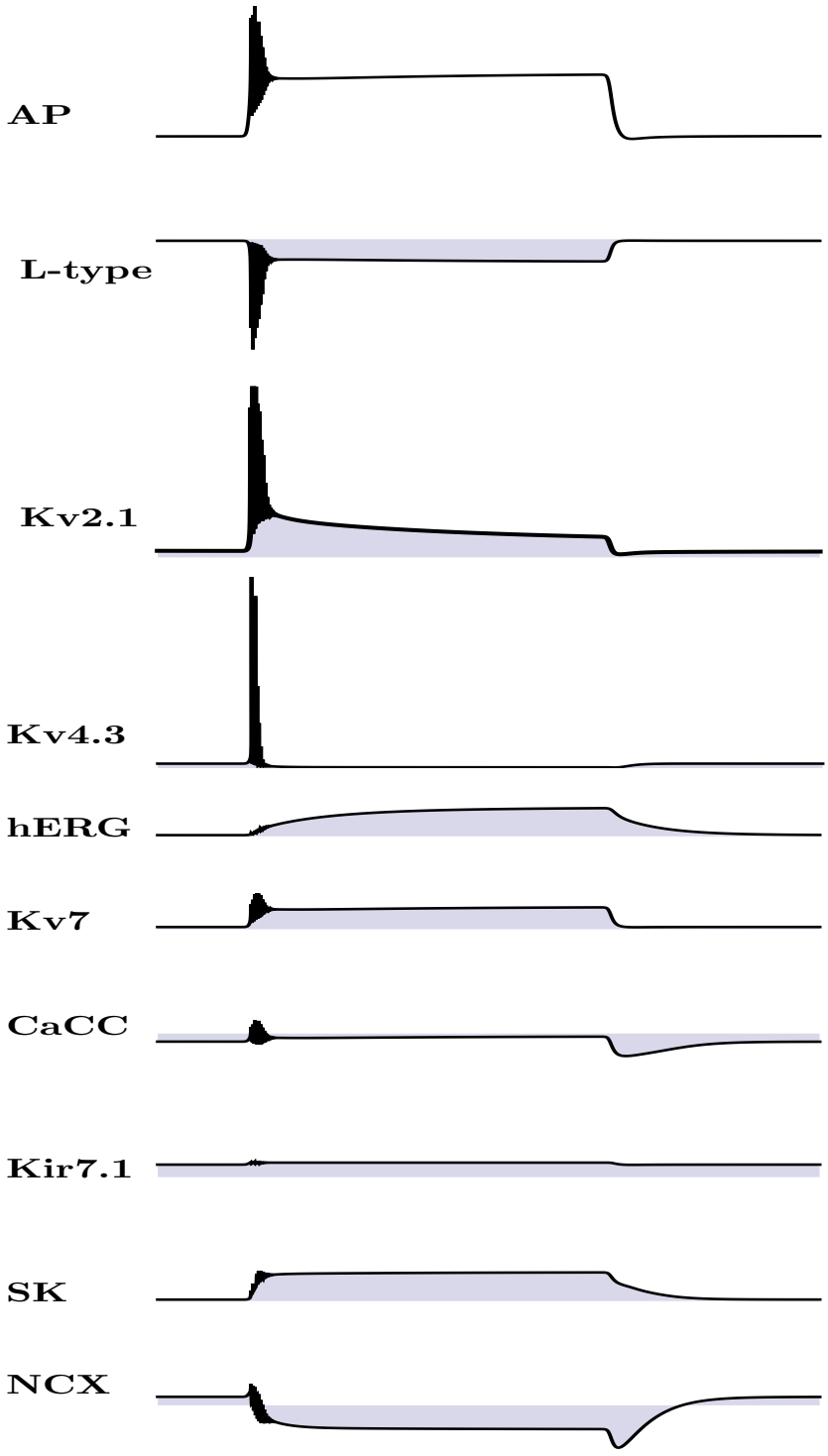

Figure 6.1: Simulated currents and channels that contribute to the MSMC AP. The top trace illustrates a representative MSMC AP. Successive traces represent various currents that are activated during the AP. Downward deflections represent inward currents, while upward deflections represent outward currents. The currents are not to scale and are intended for demonstrating the shapes only.

than the recorded AP amplitudes [3, 187, 218] (Figure 6.2 B and D). Parkington et al [187] showed that all spontaneous increase in intracellular calcium, APs, and contractions were abolished by nifedipine, a voltage-gated calcium channels inhibitor. This is in agreement with our results, indicating a prominent role of the L-type calcium channel in the bursting activity. Increasing the density of some potassium channels, namely the entities containing the Kv4.3 channels (transient outward current, discussed in Chapter 4), resulted in a reduction in the AP upstroke and amplitude (Figure 6.2 F). The evoked AP matches the previously recorded APs [3, 218]. This is justified because the transient outward potassium channels activate and inactivate rapidly and could underlie the early phase of the AP repolarisation. The Kv4.3 current shown in Figure 6.1 is in agreement with this observation; the current activates transiently causing rapid repolarisation within the early phase of the AP then rapidly inactivates. Activity of Kv4.3 channels regulates the shape of the cardiac AP and myometrium contractility [226]. Song et al [226] shows that Kv4.3 transcript expression is reduced at the end of pregnancy and that the predominant Kv4 gene underlying myometrium transient outward potassium currents is Kv4.3. On the other hand, when we increase Kv2.1 channels densities in our simulation, the AP spike amplitude was reduced and bursting was abolished (frequency was significantly reduced). The waveform turns back into the plateau-type AP. Increasing the L-type density to three times the estimated value resulted in a train of spikes even with zero ATP concentration, as shown in Figure 6.2G. Tezuka et al [227] demonstrate by RT-PCR that the expression of voltage-activated calcium channel subunits in rat myometrium increases during both term and preterm labour. This increase may assist uterine contractility during labour by increasing calcium entry. A zoom of the bursting AP elicited by our model is shown in Figure 6.3. The duration of each spike is around 160 ms; this duration is in agreement with the recorded APs shown in Figure 5.9 with spike duration of approximately 200-400 ms.

6.7 Advantages of our approach

Understanding the activity of the transmembrane proteins such as ion channels is the essence of cellular electrical activity. The development of a detailed model of ionic permeation through the plasma membrane channels could facilitate lab experiments by first running faster and cheaper computer experiments. Thus a reliable computational model would have an enormous impact on the pharmaceutical community and on the design of new drugs. In the present thesis we have shown that

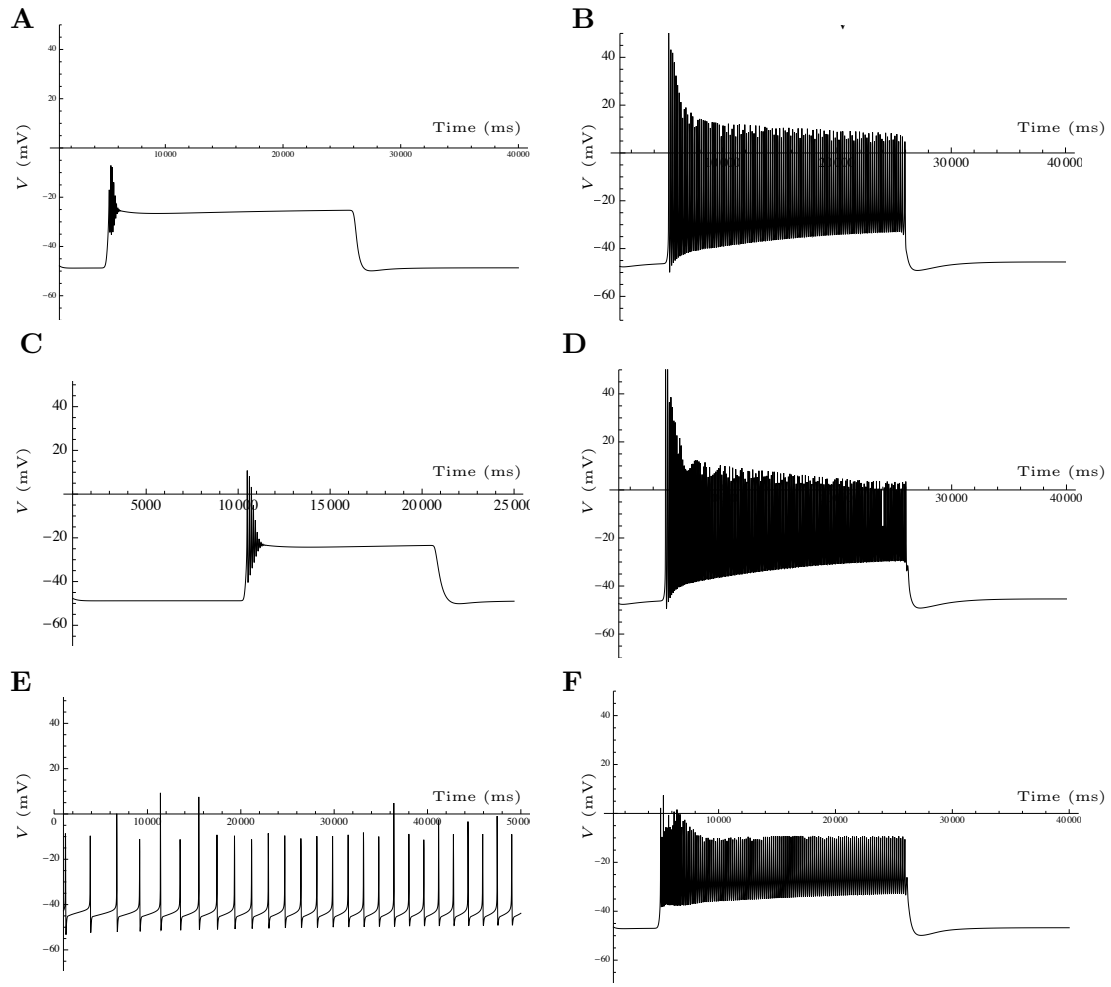

Figure 6.2: Simulated AP shapes
The MSMC model exhibit different types of AP: mixed plateau and bursting type (A,C), bursting (B,D,F), and a train of spikes (E).

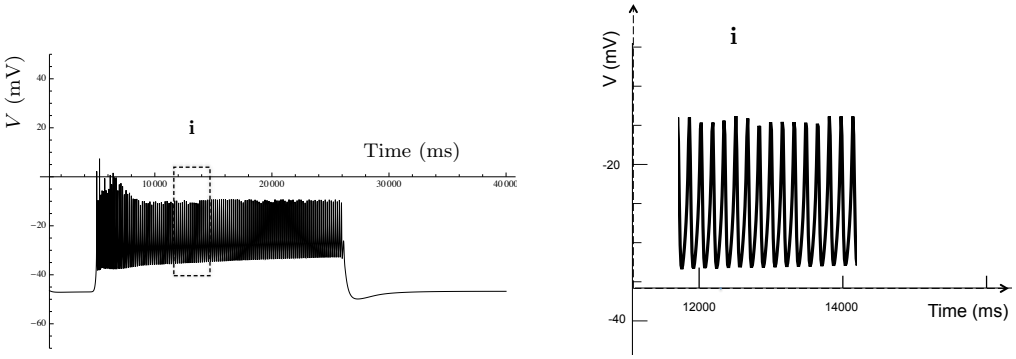

Figure 6.3: Simulated bursting type AP

native cell type behaviour in conjunction with advanced gene expression analysis can be used to construct a whole cell model with a high degree of accuracy. We produce a data-efficient method to describe the electrical activity of excitable cells. Moreover we have made use of the most recent advances in transcriptomics together with a wealth of biophysical data in the literature, and native cell behaviour, to construct the model.

Several simple and complex biophysical models were developed to describe different cell types in different species [78, 79, 104, 164]. Those models are restricted to "macroscopic currents", which combine several oligomeric complexes into single entities in the model. Such models suffer from the disadvantage of not being sufficiently detailed for pharmacological purposes, and rely on the accurate assessment of currents within native cells that is often technically difficult to achieve. It was thus desirable to determine the conductome at the level of individual molecular species. In our model, using mRNA expression data that provided us with a complete repertoire of the mRNA population in the cell, we introduced, as individual entities, all possible oligomeric complexes that may be present in the plasma membrane of our cell of interest. This renders our model as complete as possible subject to availability of data in the literature.

The kinetics of individual entities in our model relies on heterologous expression systems. The latter are characterised by high expression levels that can be measured with a high degree of accuracy. Whereas if the measurements were done in native cells, it is challenging to measure the required current in the presence of other currents. Although, in reality, heterologous systems cannot completely imitate the status of a channel in native cells, using electrophysiology to investigate the ion channels is extremely challenging. Most cells simultaneously express a significant number of diverse channels, where it is extremely difficult to distinguish the currents mediated by the channel of interest.

We represent the indeterminacy inherent in our model in the form of echelon heat maps discussed in Chapter 5. Several models depend on evaluating their biophysical parameters by fitting the models to the available data [79, 164]. The modifications of parameter values are made to represent particular dynamics. However, it might be the case that different combinations of model parameters can explain the observations equally well. In this case the model parameters are not identifiable, where the experimental data have not provided sufficient constraining power to enable unique estimation of their true value. Studying the functional redundancy, which strictly relative to the observed voltage waveform that drives the kinetics in the model, allowed us to explain properties of several channels that are

expressed in our model, viz. BK, hERG, and SK channels.

We analyse the method relative to a specific behaviour with the available electrophysiological data, kinetic data from literature, and transcriptomics. The quality and redundancy of the parameter estimates depend on the quality of the model input: the time series (electrophysiological data) and the components kinetics from the literature. A longer time series or a sequence of related experiments producing time series, specifically ones in which a wider range of behaviours of the true system are evoked, will contain more information. This can be expected to resolve the system with less redundancy, up to the true functional redundancy in the system. As regards to the quality of the components kinetics, the model can be updated with new data and readily extended to include more channels and more updates on kinetics material.

Our cell of interest is the MSMC, which undergoes major modifications during the course of pregnancy as discussed in Chapter 1. In fact, electrical excitability of MSMC during delivery is relatively high compared with various other smooth muscles, while they remain quiescent throughout most of gestation. Our model can be used to represent and describe different stages of pregnancy, if electrophysiological data are available. At any given moment in time, membrane potential depends upon the coordinated activity of different ion channels, pumps, and exchangers that can either act to depolarise or hyperpolarise the membrane. The densities of those proteins change throughout pregnancy. To date, several types of conductances have been identified to be regulated during gestation; they include the voltage-activated L-type calcium channel, the calcium-activated BK channel, the voltage-gated Kv7s potassium channels, the ERG channels, and the gap junctions. The expression of L-type at the mRNA and protein levels changed significantly during gestation [228]. Furthermore, protein expression levels of the BK α-subunit during labour are significantly reduced compared with the protein levels at the end of pregnancy without labour [197]. The BK α-subunit expression levels at end of pregnancy are significantly increased relative to the non-pregnant state [197]. Additionally, gap junctions are only present during or immediately prior to delivery, while absent during gestation [229]. In pregnant mice, the expression of Kv7 genes drops dramatically at early stages of gestation and recovers to robust levels by late stages [133]. Transcripts for KCNE4 (which inhibits the Kv7.1 currents) increased in mouse myometrium throughout pregnancy [124]. If electrophysiological behaviours for different pregnancy stages were available, our model can generate different parameter values for every pregnancy stage. These estimated parameter values can be compared and vital ion channels identified for a better understanding of the mechanisms that determine

normal and pathological uterine contractility.

6.8 Limitations of our method, and future work

An important caveat is that we considered data obtained from different cell types. Although it is reasonable to assume that the basic biophysics of a given ion channel expressed in various cell types of different species is similar, there may nonetheless be a variation between species and tissue types due to interactions with intra- and extracellular agents that are partially unknown and have not been accounted for here. Ideally, the data for each conductance would have been obtained in the cell type of interest.

Another caveat is that the kernel expressing the functional redundancy is, necessarily relative to the waveform that is fed into the calculations. If the observed time series used to force the gating kinetics were to cover a wider range of possible physical behaviours of the MSMC, we would expect the dimension of the kernel to be diminished or even vanish.

In order to investigate the role of P2RX4 on spontaneous contraction in more detail, we require an extracellular ATP time series that is simultaneous with the observed voltage and calcium time series. This would enable us to use the extracellular ATP time series as a forcing function to drive the ATP-gated currents more accurately. In the present analysis, a step increase in ATP for the duration of the AP was assumed for the sake of simplicity. Additionally, to investigate the role of PIP_2 depletion in the initiation of spontaneous electrical activity in MSMC, more detailed dose-response data on PIP_2 would be required. A time course of the depletion of PIP_2 (simultaneous with the AP) with a specific time constant could consequently be considered. This would affect the way the ion channels are modulated by PIP_2.

In the same context, the down-step of the extracellular ATP square pulse induces the repolarisation. We hypothesised that closure of hemichannels or removal of ATP from the extracellular space underlie the termination of the AP. Research has been performed to elucidate the molecular mechanism involved in the control of opening and closing of the hemichannels, and while the exact mechanism remains to be resolved, the most studied are the changes in membrane potential, phosphorylation, pH, intracellular calcium concentration, extracellular divalent cations, and mechanical stimulus [34,200,202,230]. Hemichannels open in response to membrane depolarisation, mechanical stress, extracellular calcium loss, and high pH [231]. Due to the large size of the aqueous pore, hemichannel opening in the plasma membrane

have to be highly regulated [232]. First, current mediated by hemichannels are greatly reduced at negative membrane potentials or when extracellular calcium is larger than 1 mM. ATP release is shown to be sensitive to low extracellular calcium concentrations [202, 231]. Also, the hemichannels could be blocked by extracellular divalent cations such as Ca^{2+} and Mg^{2+} [232]. On the other hand, the magnitude of intracellular calcium stimulus is critical in triggerering hemichannel opening: both small and large stimuli are ineffective and only intracellular calcium changes in the range of above 200 nM and below 1000 nM can elicit a response [230]. The opening of hemichannels can also be induced by mechanical stimulation [201,202,231]. After cessation of the mechanical stimulus, the extracellular ATP level returns to its baseline [202]. Further studies are required to explore other effects of this hemichannel-mediated ATP release and depletion on MSMC function. Removal of ATP from the extracellular space could also be mediated by enzymes such as ectonucleotidases [233]. Metabolic processes can be linked to contraction duration via the opening and closing of the plasma membrane hemichannels that cause the release and the depletion of ATP in the extracellular space. In our model we started and terminated the ATP stimulus, which in turn activated and then inactivated the P2RX4. It is reasonable to assume that the gating of the hemichannels could be the physiological explanation behind the termination of the AP. This is justified because, in all muscle cells, the rate and duration of contraction is related to the underlying metabolic status [234–236]. A problem arises when we attempt to predict the right duration of an AP and which conductance entities could affect this duration. Modelling the kinetics of the hemichannels can assist in improving our understanding of the uterine spontaneous contractions and its relation to the metabolic status of the tissue.

Finally, for MSMC calcium dynamics, we developed the minimal model explained in Section 4.8. A simplification that we have made, one that is often made in even the most complex models, is that the concentration of calcium is the same throughout the cell. This eliminates spatial structuring and leaves only dependence on time. In doing so, we ignore important spatial patterns, such as calcium waves spreading through the MSMC and local calcium signals. Global calcium response, due to the arrival of AP which activates the contractile machinery, is usually measured using the conventional calcium measuring techniques. However, it is the local calcium signal affecting each entity that has the most substantial effect. The calcium signals occurring as calcium is released from the SR can be characterised by their spatially local and transient nature. These release events occur spontaneously and are modified by stimulation. The local calcium signals are called calcium puffs

and sparks, depending upon whether they arise from the activation of IP_3 receptors or RyRs, respectively [237]. For instance, calcium- and voltage-activated potassium channels, such as BK and its isoforms associated with accessory beta subunits, have a high affinity to calcium (see Chapter 4). The coupling of calcium sparks to transient outward currents has been demonstrated in several smooth muscles, and the average time course of both events is similar [237]. It has been estimated that a single calcium spark activates 13 BK channels [238]. As discussed by Fay et al [238], given what is known about the calcium required to activate BK channels (i.e., several micro molar level), it is likely that the calcium spark amplitude is larger than that revealed by global calcium imaging. High resolution imaging methods using fluo-3 and a high speed widefield imaging system was conducted [239]. The conclusion reached was that BK channels are located close to RyRs and experience calcium concentrations of 20–150 μM. Global calcium rises of lower amplitude would not be capable of activating the BK channels. The BK channels provide a negative feedback mechanism which opposes any local calcium increase. The locality of these channels could affect how much calcium has an impact on them. The magnitude of the potassium current through this channel, hence, increases significantly from the estimated value. This channel has a very large unitary conductance, consequently any minor change in the local calcium concentration will result in a huge influx of potassium ions, which could lead to muscle relaxation. Under normal circumstances, the BK channel does not have a significant effect, as predicted by our model (although very highly expressed in mRNA level), because BK is mostly calcium-gated and largely voltage-independent in physiological ranges (the kinetics is discussed in detail in Chapter 4). However, BK could be critically important if it experienced a high calcium concentration. While global calcium is not high enough to activate BK channel, spacial changes in calcium can locally reach extreme levels. Calcium concentration influence BK channels in the range between 0.1 μM to 100 μM [240]. It is possible that during gestation, when calcium exceeds a certain level that could have a damaging effect on the MSMCs, BK channels would open and act as an 'emergency brake' to prevent further depolarisation and hence reduce the activity of the L-type calcium channels [135].

6.9 Conclusion

Computational models can be important research tools that complement experimental work, not only by gleaning more information from the available data, but also by suggesting what might be the most informative experiment to perform next.

In this thesis, we have developed a method to characterise the expression profile of electrogenic transmembrane proteins (the conductome) and hence the electrical activity of excitable cells. The strength of the method is that it specifies precisely the space of conductomes that is consistent with the available data, which can help guide further experimentation and also provides a clue to the functional redundancy that is inherent in the biological system itself. Our approach readily lends itself to modular expansion: more channels and pumps can be added, as well as, where available, time series of relevant gating signals such as extracellular messengers such as ATP and intracellular messengers such as PIP_2.

Bibliography

[1] R. Keynes, D. Aidley, and C. Huary, *Nerve and Muscle*. Cambridge University Press, 4th ed., 2001.

[2] M. Trauner and P. Jansen, *Molecular Pathologenesis of Cholestasis*. N Engl J Med, 1998.

[3] K. Nakao, Y. Inoue, K. Okabe, T. Kawarabayashi, and K. Kitamura, "Oxytocin enhances action potentials in pregnant human myometrium - a study with microelectrodes," *American Journal of Obstetrics and Gynecology*, vol. 177(1), pp. 222–228, 1997.

[4] R. Garfield and W. Maner, "Physiology and electrical activity of uterine contractions," *Semi Cell Dev Biol*, vol. 18(3), pp. 289–295, 2007.

[5] T. F. Weiss, *Cellular Biophysiscs, Volume 2: Electrical Properties*. MIT Press, 1996.

[6] S. Doi, J. Inoue, Z. Pan, and K. Tsumoto, *Computational Electrophysiology*. Springer, 2010.

[7] H. Miyoshi, B. Mary, and B. Lynette, "Voltage-clamp studies of gap junctions between uterine muscle cells during term and preterm labor," *Biophys J*, vol. 71, pp. 1324–1334, 1996.

[8] Y. Chan, H. van den Berg, J. Moore, S. Quenby, and A. Blanks, "Assessment of myometrial transcriptome changes associated with spontaneous human labour by high-throughput RNA-seq," *Exp Physiol*, vol. 99(3), pp. 510–524, 2014.

[9] G. C. Frech, A. M. J. Vandongen, G. Schuster, A. M. Brown, and R. H. Joho, "A novel potassium channel with delayed rectifier properties isolated from rat-brain by expression cloning," *Nature*, vol. 340, pp. 642–645, 1989.

[10] A. J. Patel, M. Lazdunski, and E. Honore, "Kv2.1/Kv9.3, A novel ATP-dependent delayed-rectifier K^+ channel in oxygen-sensitive pulmonary artery myocytes," *EMBO J*, vol. 16, pp. 6615–6625, 1997.

[11] J. W. Kramer, M. A. Post, A. M. Brown, and G. E. Kirsch, "Modulation of potassium channel gating by coexpression of Kv2.1 with regulatory Kv5.1 or Kv6.1 alpha-subunits," *Am J Physiol Cell Physiol*, vol. 274, p. C1501, 1998.

[12] B. Rudy, K. Sen, E. Vega-Saenz De Miera, D. Lau, T. Ried, and D. C. Ward, "Cloning of a human cDNA expressing a high voltage-activating, TEA-sensitive, type-A K^+ channel which maps to chromosome-1 band-p21," *J Neurosci Res*, vol. 29, pp. 401–412, 1991.

[13] H. H. Jerng and M. Covarrubias, "K^+ channel inactivation mediated by the concerted action of the cytoplasmic N- and C-terminal domains," *Biophys J*, vol. 72, pp. 163–174, 1997.

[14] T. Y. Nakamura, D. J. Pountney, S. Nandi, M. Artman, B. Rudy, and W. A. Coetzee, "Different effects of the Ca^{2+}-binding protein, KChIP1, on two Kv4 subfamily members, Kv4.1 and Kv4.2," *J Mol Cell Cardiol*, vol. 33, p. A83, 2001.

[15] R. Bahring, L. M. Boland, A. Varghese, M. Gebauer, and O. Pongs, "Kinetic analysis of open- and closed-state inactivation transitions in human Kv4.2 A-type potassium channels," *J Physiol*, vol. 535, pp. 65–81, 2001.

[16] J. Ludwig, H. Terlau, F. Wunder, A. Bruggemann, L. A. Pardo, A. Marquardt, W. Stuhmer, and O. Pongs, "Functional expression of a rat homolog of the voltage-gated ether a go-go potassium channel reveals differences in selectivity and activation kinetics between the Drosophila channel and its mammalian counterpart," *EMBO J*, vol. 13, pp. 4451–4458, 1994.

[17] C. Y. Tang, F. Bezanilla, and D. M. Papazian, "Extracellular Mg^{2+} modulates slow gating transitions and the opening of Drosophila ether-a-go-go potassium channels," *J Gen Physiol*, vol. 115, pp. 319–337, 2000.

[18] F. Miceli, M. R. Cilio, M. Taglialatela, and F. Bezanilla, "Gating currents from neuronal Kv7.4 channels general features and correlation with the ionic conductance," *Channels*, vol. 3, pp. 274–283, 2009.

[19] R. L. Schrøder, T. Jespersen, P. Christophersen, D. Strøbæk, B. S. Jensen, and S. P. Olesen, "KCNQ4 channel activation by BMS-204352 and retigabine," *Neuropharmacol*, vol. 40, pp. 888–898, 2001.

[20] M. Köhler, B. Hirschberg, C. T. Bond, J. M. Kinzie, N. V. Marrion, J. Maylie, and J. P. Adelman, "Small-conductance, calcium-activated potassium channels from mammalian brain," *Science*, vol. 273, pp. 1709–1714, 1996.

[21] B. Hirschberg, J. Maylie, J. P. Adelman, and N. V. Marrion, "Gating of recombinant small-conductance Ca^{2+}-activated K^+ channels by calcium," *J Gen Physiol*, vol. 111, pp. 565–581, 1998.

[22] X. M. Xia, B. Fakler, A. Rivard, G. Wayman, T. Johnson-Pais, J. E. Keen, T. Ishii, B. Hirschberg, C. T. Bond, S. Lutsenko, J. Maylie, and J. P. Adelman, "Mechanism of calcium gating in small-conductance calcium-activated potassium channels," *Nature*, vol. 395, pp. 503–507, 1998.

[23] F. Doring, C. Derst, E. Wischmeyer, C. Karschin, R. Schneggenburger, J. Daut, and A. Karschin, "The epithelial inward rectifier channel Kir7.1 displays unusual K^+ permeation properties," *J Neurosci*, vol. 18, pp. 8625–8636, 1998.

[24] A. M. Blanks, Z. H. Zhao, A. Shmygol, G. Bru-Mercier, S. Astle, and S. Thornton, "Characterization of the molecular and electrophysiological properties of the T-type calcium channel in human myometrium," *J Physiol*, vol. 581, pp. 915–926, 2007.

[25] E. Toulme, A. Garcia, D. Samways, and T. Egan, "P2X4 receptors in activated C8-B4 cells of cerebellar microglial origin," *J Gen Physiol*, vol. 135, pp. 333–353, 2010.

[26] B. Pattnaik and B. Hughes, "Regulation of Kir channels in bovine retinal pigment epithelial cells by phosphatidylinositol 4,5-bisphosphate," *Am J Physiol Cell Physiol*, vol. 297, pp. C1001–C1011, 2009.

[27] M. Baggish, R. Valle, and H. Guedj, *Hysteroscopy: Visual Perspective of Uterine Anatomy, Physiology and Pathology*. Lippincott Williams & Wilkins, 3rd ed., 2007.

[28] T. Chard and J. Grudzinskas, *The uterus*. Cambridge University Press, 1st ed., 1995.

[29] S. Wray, "Uterine contraction and physiological-mechanisms of modulation," *Am J Physiol*, vol. 264, pp. C1–C18, 1993.

[30] J. Keener and J. Sneyd, *Mathematical physiology*. Springer-Verlag, New York, 1993.

[31] B. Hille, *Ion Channels of Excitable Membrane*. Sinauer Associates, Inc, 3rd ed., 2001.

[32] M. Bennett, "Connexins in disease," *Nature*, vol. 368, pp. 18–19, 1994.

[33] C. Elfgang, H. Eckert, A. Lichtenberg-Frate, O. Butterweck, and R. Klein, "Specific permeability and selective formation of gap junction channels in connexin-trasfected HeLa cells," *J Cell Biol*, vol. 129, pp. 805–817, 1995.

[34] D. Goodenough, D. Godiger, and D. Paul, "Connexins, connexons, and intercellular communication," *Annu Rev Biochem*, vol. 65, pp. 475–502, 1996.

[35] D. Paul, "Molecular cloning of cDNA for rat liver gap junction protein," *J Cell Biol*, vol. 103, pp. 123–134, 1986.

[36] A. V. Shmigol, D. A. Eisner, and S. Wray, "Properties of voltage-activated Ca_i^{2+} transients in single smooth muscle cells isolated from pregnant rat uterus," *J Physiol*, vol. 511, pp. 803–811, 1998.

[37] T. Kawarabayashi and H. Sugimori, "Effect of osytocin and prostaglandin $f_{2\alpha}$ on pregnant human myometrium recorded by the single sucrose-gap method: comparison of an in vitro experiment and an in vivo trial," *Asia Oceania J Obstet Gynecol*, vol. 11, pp. 247–253, 1985.

[38] T. Kawarabayashi, T. Kishikawa, and H. Sugimori, "Effect of osytocin on spontaneous electrical and mechanical activities in pregnant human myometrium," *Am J Obstet Gynecol*, vol. 155, pp. 671–676, 1986.

[39] A. Nakajima, "Action potential of human myometrial fibers," *Am J Obstet Gynecol*, vol. 111, pp. 266–269, 1971.

[40] A. Shmygol, A. M. Blanks, G. Bru-Mercier, J. E. Gullam, and S. Thornton, "Control of uterine Ca^{2+} by membrane voltage toward understanding the excitation-contraction coupling in human myometrium," *Reproductive Biomechanics*, vol. 1101, pp. 97–109, 2007.

[41] O. Bursztyn, L.and Eytan, A. Jaffa, and D. Elad, "Mathematical model of excitation-contraction in a uterine smooth muscle cell," *Am J Physiol Cell Physiol*, vol. 292, pp. C1816–C1829, 2007.

[42] S. Wray, K. Jones, S. Kupittayanant, Y. Li, and A. Matthew, "Calcium signalling and uterine contractility," *J Soc Gynecol Investig*, vol. 10, pp. 252–264, 2003.

[43] S. Wray, "Insights into the uterus," *Exp Physiol*, vol. 92, pp. 621–631, 2007.

[44] R. Young and R. Hession, "Three-dimensional structure of the smooth muscle in the term-pregnant human uterus," *Obstet Gynecol*, vol. 93, pp. 94–99, 1999.

[45] C. Steer, "The electrical activity of the human uterus in normal and abnormal labour," *Am J Obstet Gynecol*, vol. 68, pp. 867–890, 1954.

[46] R. Garfield, K. Chwalisz, L. Shi, G. Olson, and G. Saade, "Instrumentation for the diagnosis of term and preterm labour-Review," *J Perinat Med*, vol. 26(6), pp. 413–436, 1998.

[47] R. Garfield, G. Saade, C. Buhimschi, and I. Buhimschi, "Control and assessment of uterus and cervix during pregnancy and labour," *Hum Reprod Update*, vol. 4(5), pp. 673–695, 1998.

[48] M. Lucovnik, R. Kuon, L. Chambliss, W. Maner, S. Shi, L. Shi, J. Balcucci, and R. Garfield, "Use of uterine electromyography to diagnose term and preterm labor," *Acta Obstet Gynecol Scand*, vol. 90(2), pp. 150–157, 2011.

[49] W. Maner, R. Garfield, H. Maul, G. Olson, and G. Saade, "Predicting term and preterm delivery with transabdominal uterine electromyography," *Obstet Gynecol*, vol. 101(6), pp. 1254–1260, 2003.

[50] H. Eswaran, H. Preissl, J. Wilson, P. Murphy, and C. Lowery, "First magnetomyographic recordings of the uterine activity with spatial temporal resolution using a 151 channel sensor array," *Am J Obstet Gynecol*, vol. 187(1), pp. 145–151, 2002.

[51] H. Eswaran, H. Preissl, J. Wilson, P. Murphy, and C. Lowery, "Prediction of labor at term and preterm pregnancies using non-invasive magnetomyographic recordings of uterine contractions," *Am J Obstet Gynecol*, vol. 190(6), pp. 1598–1602, 2004.

[52] D. Goldman, "Potential, impedance, and rectification in membranes," *J Gen Physiol*, vol. 27, no. 1, pp. 37–60, 1943.

[53] P. Fatt and B. Ginsborg, "The ionic requirements for the production of action potentials in crustacean muscle fibres," *J Physiol*, vol. 142, pp. 516–543, 1958.

[54] L. Jan and Y. Jan, "L-glutamate as an excitatory transmitter at the Drosophila larval neuromuscular junction," *J Physiol*, vol. 262, pp. 215–236, 1976.

[55] C. Lewis, "Ion-concentration dependence of the reversal potential and the single channel conductance of ion channels at the frog neuromuscular junction," *J Physiol*, vol. 286, pp. 417–445, 1979.

[56] S. Spangler, "Expansion of the constant field equation to include both divalent and monovalent ions," *Ala J Med Sci*, vol. 9, pp. 218–223, 1972.

[57] K. Cole, "Dynamic electrical characteristics of the squid axon membrane," *Arch Sci Physiol*, vol. 3, pp. 253–258, 1949.

[58] A. L. Hodgkin and A. F. Huxley, "Currents carried by sodium and potassium ions through the membrane of the giant axon of loligo," *J Physiol*, vol. 116, pp. 449–472, 1952.

[59] A. L. Hodgkin and A. F. Huxley, "Propagation of electrical signals along giant nerve fibres," *Proc Biol Sci*, vol. 140, pp. 177–183, 1952.

[60] A. L. Hodgkin and A. F. Huxley, "The components of membrane conductance in the giant axon of loligo," *J Physiol*, vol. 116, pp. 473–496, 1952.

[61] A. L. Hodgkin and A. F. Huxley, "A quantitative description of membrane current and its application to conduction and excitation in nerve," *Bull of Math Biol*, vol. 52, pp. 25–71, 1990.

[62] K. Cole and H. Curtis, "Electric impedance of the squid giant axon during activity," *J Gen Physiol*, vol. 22, pp. 649–670, 1940.

[63] A. Hodgkin, "Evidence for electrical transmission in nerve. part i," *J Physiol*, vol. 90, pp. 183–210, 1937.

[64] H. Curtis and K. Cole, "Membrane action potentials from the squid giant axon," *J Cell Comp Physiol*, vol. 15, pp. 147–157, 1940.

[65] A. Hodgkin and B. Katz, "The effect of sodium ions on the electrical activity of the giant axon of the squid," *J Physiol*, vol. 108, pp. 37–77, 1949.

[66] W. J. Stewart, *Introduction to the Numerical Solution of Markov Chains*. Pinceton University Press, 1994.

[67] A. Shmigol, D. Eisner, and B. Wray, "Simultaneous measurements of changes in sarcoplasmic reticulum and cytosolic Ca^{2+} in rat uterine smooth muscle cells," *J Physiol*, vol. 531, pp. 707–713, 2001.

[68] S. Szal, J. Repke, E. Seely, S. Graves, C. Parker, and K. Morgan, "$[Ca^{2+}]_i$ signalling in pregnant human myometrium," *Am J Physiol*, vol. 267, pp. E77–87, 1994.

[69] M. Taggart, T. Burdyga, T. Heaton, and S. Wray, "Stimulus-dependent modulation of smooth muscle intracellular calcium and force by altered intracellular pH," *Pflügers Archiv*, vol. 432, pp. 803–811, 1996.

[70] S. Orrenius, B. Zhivotovsky, and N. Pierluigi, "Regulation of cell death, the calcium apoptosis link," *Nat Rev Mol Cell Biol*, vol. 4, pp. 552–565, 2003.

[71] A. Benavides, D. Pastor, N. Fradejas, D. Tornero, and S. Calvo, "Differential regulation of calcium channel coding genes by prolonged depolarization," *Neurochem Int*, vol. 50 (2), pp. 395–403, 2007.

[72] A. Goldbeter, G. Dupont, and M. J. Berridge, "Minimal model for signal-induced Ca^{2+} oscillations and for their frequency encoding through protein phosphorylation," *PNAS*, vol. 87, pp. 1461–1465, 1990.

[73] G. De Young and J. Keizer, "A single pool IP_3-receptor based model for agonist-simulated Ca^{2+} oscillations," *Proc of the Natl Acad Sci, USA*, vol. 89, pp. 9895–9899, 1992.

[74] A. Atri, J. Amundson, D. Claphan, and J. Sneyd, "A single-pool model for intracellular calcium oscillations and waves in the Xenopus laevis oocyte," *Biophys J*, vol. 65, pp. 1727–1739, 1993.

[75] D. Friel, "Ca^{2+} oscillations in sympathetic neurones: an experimental test of theoretical model," *Biophys J*, vol. 68, pp. 1752–1766, 1995.

[76] A. Fabiato, "Two kinds of calcium-induced release of calcium from the sarcoplasmic reticulum of skinned cardia cells," *Plenum Press*, 1992.

[77] A. Wong, A. Fabiato, and J. Bassingthwaigthe, "Model of calcium-induced calcium-release mechanism in cardiac cells," *Bull of Math Biol*, vol. 54, pp. 95–116, 1992.

[78] S. Rihana, "Mathematical modelling of electrical activity of uterine muscle cells," *Med Biol Eng Comput*, vol. 47, pp. 667–675, 2009.

[79] W. Tong, C. Y. Choi, S. Karche, A. V. Holden, H. Zhang, and M. J. Taggart, "A computational model of the ionic currents, Ca^{2+} dynamics and action potentials underlying contraction of isolated uterine smooth muscle," *PLoS ONE*, vol. 6(4), p. e18685, 2011.

[80] H. Andersen and M. Barclay, "A computer model of uterine contractions based on discrete contractile elements," *Obstet Gynecol*, vol. 86, pp. 108–111, 1995.

[81] C. Vauge and T. Mignot, "A mathematical model of the spontaneous contractions of the isolated uterine smooth muscle from patients receiving progestin treatment," *Acta Biotheor*, vol. 51, pp. 19–34, 2003.

[82] R. Young, "A computer model of uterine contractions based on action potential propagation and intercellular calcium waves," *Obstet Gynecol*, vol. 89, pp. 604–608, 1997.

[83] C. Hai and R. Murphy, "Cross-bridge phosphorylation and regulation of latch state in smooth muscle," *Am J Physiol Cell Physiol*, vol. 254, pp. C99–C106, 1988.

[84] T. Osa, "An interaction between the electrical activities of longitudinal and circular smooth muscles of pregnant mouse uterus," *Jpn J Physiol*, vol. 24, pp. 189–203, 1974.

[85] Y. Inoue, K. Nakao, and K. Okabe, "Some electrical properties of human pregnant myometrium," *Am J Obstet Gynecol*, vol. 162, pp. 1090–1098, 1990.

[86] C. Bond, R. Sprengel, W. Bissonnette, J.M.and Kaufmann, D. Pribnow, and T. Neelands, "Respiration and parturition affected by conditional overexpression of the calcium-activated potassium channel subunit, SK3," *Science*, vol. 289, pp. 1942–1946, 2000.

[87] B. Modzelewska, T. Kleszczewski, and A. Kostrzewska, "The effect of a selective inhibition of potassium channels on the relaxation induced by nitric oxide in the human pregnant myometrium," *Cell Mol Biol Lett*, vol. 8, pp. 69–75, 2003.

[88] B. Modzelewska, A. Kostrzewska, M. Sipowicz, T. Kleszczewski, and S. Batra, "Apamin inhibits NO- induced relaxation of the spontaneous contractile activity of the myometrium from non-pregnant women," *Reprod Biol Endocrinol*, vol. 1, p. 8, 2003.

[89] A. Brown, T. Cornwell, I. Korniyenko, V. Solodushko, C. Bond, and J. Adelman, "Myometrial expression of small conductance Ca^{2+}-activated K^+ channels depresses phasic uterine contraction," *Am J Physiol Cell Physiol*, vol. 292, pp. C832–40, 2007.

[90] C. McCloskey, C. Rada, E. Bailey, S. McCavera, H. van den Berg, J. Atia, D. Rand, A. Shmygol, Y. Chan, S. Quenby, J. Brosens, M. Vatish, J. Zhang, J. Denton, M. Taggart, C. Kettleborough, D. Tickle, J. Jerman, P. Wright, T. Dale, S. Kanumilli, D. Trezise, S. Thornton, P. Brown, R. Catalano, N. Lin, S. England, and A. Blanks, "The inwardly rectifying K^+ channel KIR7.1 controls uterine excitability throughout pregnancy," *EMBO Mol Med*, vol. 6(9), pp. 1161–1174, 2014.

[91] B. Sanborn, "Relationship of ion channel activity to control of myometrial calcium," *J Soc Gynecol Investig*, vol. 1, pp. 4–11, 2000.

[92] H. Aguilar and B. Mitchell, "Physiology pathways and molecular mechanisms regulating uttering contractility," *Hum Reprod Update*, vol. 16, pp. 725–744, 2010.

[93] K. Okabe, Y. Inoue, and H. Soeda, "Estradiol inhibits Ca^{2+} and K^+ channels in smooth muscle cells from pregnant rat myometrium," *Eur J Pharmacol*, vol. 376, pp. 101–108, 1999.

[94] T. Yamamoto, "Effects of estrogens on Ca channels in myometrial cells isolated from pregnant rats," *Am J Physiol*, vol. 268, pp. C64–9, 1995.

[95] R. Tribe, "Regulation of human myometrial contractility during pregnancy and labour: are calcium homeostatic pathways important," *Exp Physiol*, vol. 86(2), pp. 247–254, 2001.

[96] A. Shmygol and A. Blanks, "Control of Uterine Ca^{2+} by membrane potential. Toward understanding the excitation-contraction coupling in human myometrium," *Ann N Y Acad Sci*, vol. 1101, pp. 97–109, 2007.

[97] K. G. Klemic, C. C. Shieh, G. E. Kirsch, and S. W. Jones, "Inactivation of Kv2.1 potassium channels," *Biophys J*, vol. 74, pp. 1779–1789, 1998.

[98] L. Bao and D. H. Cox, "Gating and ionic currents reveal how the BK_{Ca} channel's Ca^{2+}sensitivity is enhanced by its beta 1 subunit," *J Gen Physiol*, vol. 126, pp. 393–412, 2005.

[99] C. J. Lingle, X. H. Zeng, J. P. Ding, and X. M. Xia, "Inactivation of BK channels mediated by the NH2 terminus of the beta 3b auxiliary subunit involves a two-step mechanism: Possible separation of binding and blockade," *J Gen Physiol*, vol. 117, pp. 583–605, 2001.

[100] F. T. Horrigan and R. W. Aldrich, "Coupling between voltage sensor activation, Ca^{2+} binding and channel opening in large conductance (BK) potassium channels," *J Gen Physiol*, vol. 120, pp. 267–305, 2002.

[101] B. Wang, B. S. Rothberg, and R. Brenner, "Mechanism of beta 4 subunit modulation of BK channels," *J Gen Physiol*, vol. 127, pp. 449–465, 2006.

[102] W. J. Joiner, L. Y. Wang, M. D. Tang, and L. K. Kaczmarek, "hSK4, a member of a novel subfamily of calcium-activated potassium channels," *Proc Natl Acad Sci USA*, vol. 94, pp. 11013–11018, 1997.

[103] S. M. Wang, S. G. Liu, M. J. Morales, H. C. Strauss, and R. L. Rasmusson, "A quantitative analysis of the activation and inactivation kinetics of hERG expressed in *Xenopus* oocytes," *J Physiol*, vol. 502, pp. 45–60, 1997.

[104] L. Livshitz and Y. Rudy, "Uniqueness and stability of action potential models during rest, pacing, and conduction using problem-solving environment," *Biophys J*, vol. 97, pp. 1265–1276, 2009.

[105] E. Perez-Reyes, L. L. Cribbs, A. Daud, A. E. Lacerda, J. Barclay, M. P. Williamson, M. Fox, M. Rees, and J. H. Lee, "Molecular characterization of a neuronal low-voltage-activated T-type calcium channel," *Nature*, vol. 391, pp. 896–900, 1998.

[106] J. Arreola, J. E. Melvin, and T. Begenisich, "Activation of calcium-dependent chloride channels in rat parotid acinar cells," *J Gen Physiol*, vol. 108, pp. 35–47, 1996.

[107] E. J. Beck, M. Bowlby, W. F. An, K. J. Rhodes, and M. Covarrubias, "Remodelling inactivation gating of Kv4 channels by KChIP1, a small-molecular-weight calcium-binding protein," *J Physiol*, vol. 538, pp. 691–706, 2002.

[108] S. P. Patel, R. Parai, and D. L. Campbell, "Regulation of Kv4.3 voltage-dependent gating kinetics by KChIP2 isoforms," *J Physiol*, vol. 557, pp. 19–41, 2004.

[109] M. Pusch, R. Magrassi, B. Wollnik, and F. Conti, "Activation and inactivation of homomeric KvLQT1 potassium channels," *Biophys J*, vol. 75, pp. 785–792, 1998.

[110] G. M. Faber, J. Silva, L. Livshitz, and Y. Rudy, "Kinetic properties of the cardiac L-type Ca^{2+} channel and its role in myocyte electrophysiology: A theoretical investigation," *Biophys J*, vol. 92, pp. 1522–1543, 2007.

[111] T. Hoshi, W. Zagotta, and R. . Aldrich, "Biophysical and molecular mechanisms of Shaker potassium channel inactivation," *Science*, vol. 250, pp. 533–538, 1990.

[112] T. Hoshi, W. Zagotta, and R. Aldrich, "Two types of inactivation in Shaker K^+ channels: effects of alterations in the carboxy-terminal region," *Neuron*, vol. 7, pp. 547–556, 1991.

[113] G. Bett, I. Dinga-Madou, Q. Zhou, V. Bondarenko, and R. Rasmusson, "A model of the interaction between N-type and C-type inactivation in Kv1.4 channels," *Biophys J*, vol. 100, no. 1, pp. 11–21, 2011.

[114] G. A. Knock, S. V. Smirnov, and P. I. Aaronson, "Voltage-gated K^+ currents in freshly isolated myocytes of the pregnant human myometrium," *J Physiol*, vol. 518, pp. 769–781, 1999.

[115] K. G. Klemic, C. C. Shieh, G. E. Kirsch, and S. W. Jones, "Gating kinetics of the rat Kv2.1 potassium channel expressed in Xenopus oocytes," *Biophys J*, vol. 72, p. MPOS8, 1997. Part 2.

[116] R. W. Aldrich, "Inactivation of voltage-gated delayed potassium current in molluscan neurons - a kinetic model," *Biophys J*, vol. 36, pp. 519–532, 1981.

[117] B. Kyle, E. Bradley, S. Ohya, G. P. Sergeant, N. G. McHale, K. D. Thornbury, and M. A. Hollywood, "Contribution of Kv2.1 channels to the delayed rectifier current in freshly dispersed smooth muscle cells from rabbit urethra," *Am J Physiol Cell Physiol*, vol. 301, no. 5, pp. C1186–C1200, 2011.

[118] D. Kerschensteiner, F. Monje, and M. Stocker, "Structural determinants of the regulation of the voltage-gated potassium channel Kv2.1 by the modulatory alpha-subunit Kv9.3," *J Biol Chem*, vol. 278, pp. 18154–18161, 2003.

[119] M. A. Post, G. E. Kirsch, and A. M. Brown, "Kv2.1 and electrically silent Kv6.1 potassium channel subunits combine and express a novel current," *FEBS Lett*, vol. 399, pp. 177–182, 1996.

[120] C. Bonifazzi, O. Belluzzi, and O. Sacchi, "Kinetic analysis of incomplete current tracings according to the Hodgkin-Huxley model," *J Theor Biol*, vol. 130, pp. 183–190, 1988.

[121] S. M. Wang, V. E. Bondarenko, Y. J. Qu, G. C. L. Bett, M. J. Morales, R. L. Rasmusson, and H. C. Strauss, "Time- and voltage-dependent components of Kv4.3 inactivation," *Biophys J*, vol. 89, pp. 3026–3041, 2005.

[122] W. N. Guo, H. L. Li, F. Aimond, D. C. Johns, K. J. Rhodes, J. S. Trimmer, and J. M. Nerbonne, "Role of heteromultimers in the generation of myocardial transient outward K^+ currents," *Cir Res*, vol. 90, pp. 586–593, 2002.

[123] A. Lundby and S. Olesen, "KCNE3 is an inhibitory subunit of the Kv4.3 potassium channel," *Biochem Biophys Res Commun*, vol. 346, pp. 958–967, 2006.

[124] I. A. Greenwood, S. Y. Yeung, R. M. Tribe, and S. Ohya, "Loss of functional K^+ channels encoded by *ether-à-go-go*-related genes in mouse myometrium prior to labour onset," *J Physiol*, vol. 587, pp. 2313–2326, 2009.

[125] R. Schonherr, K. Lober, and S. H. Heinemann, "Inhibition of human *ether-à-go-go* potassium channels by Ca^{2+}/calmodulin," *EMBO J*, vol. 19, pp. 3263–3271, 2000.

[126] M. C. Sanguinetti, C. G. Jiang, M. E. Curran, and M. T. Keating, "A mechanistic link between an inherited and an acquired cardiac-arrhythmia - hERG encodes the I_{KR} potassium channel," *Cell*, vol. 81, pp. 299–307, 1995.

[127] M. C. Sanguinetti and M. Tristani-Firouzi, "hERG potassium channels and cardiac arrhythmia," *Nature*, vol. 440, pp. 463–469, 2006.

[128] J. Barhanin, F. Lesage, E. Guillemare, M. Fink, M. Lazdunski, and G. Romey, "KvLQT1 and IsK (minK) proteins associate to form the I_{Ks} cardiac potassium current," *Nature*, vol. 384, pp. 78–80, 1996.

[129] M. C. Sanguinetti, M. E. Curran, A. Zou, J. Shen, P. S. Spector, D. L. Atkinson, and M. T. Keating, "Coassembly of KvLQT1 and minK (IsK) proteins to form cardiac I_{KS} potassium channel," *Nature*, vol. 384, pp. 80–83, 1996.

[130] B. C. Schrœder, S. Waldegger, S. Fehr, M. Bleich, R. Warth, R. Greger, and T. J. Jentsch, "A constitutively open potassium channel formed by KCNQ1 and KCNE3," *Nature*, vol. 403, pp. 196–199, 2000.

[131] M. Grunnet, T. Jespersen, H. B. Rasmussen, T. Ljungstrom, N. K. Jorgensen, S. P. Olesen, and D. A. Klaerke, "KCNE4 is an inhibitory subunit to the KCNQ1 channel," *J Physiol*, vol. 542, pp. 119–130, 2002.

[132] L. J. Manderfield, M. A. Daniels, C. G. Vanoye, and A. L. George, "KCNE4 domains required for inhibition of KCNQ1," *J Physiol*, vol. 587, pp. 303–314, 2009.

[133] L. McCallum, S. Pierce, S. England, I. Greenwood, and R. Tribe, "The contribution of Kv7 channels to pregnant mouse and human myometrial contractility," *J Cell Mol Med*, vol. 15(3), pp. 577–586, 2010.

[134] R. Søgaard, T. Ljungstrøm, K. Pedersen, S. Olesen, and B. Jensen, "KCNQ4 channels expressed in mammalian cells: functional characteristics and pharmacology," *Am J Physiol Cell Physiol*, vol. 280, pp. C859–C866, 2001.

[135] R. N. Khan, B. Matharoo-Ball, S. Arulkumaran, and M. L. J. Ashford, "Potassium channels in the human myometrium," *Exp Physiol*, vol. 86, pp. 255–264, 2001.

[136] K. L. Magleby, "Kinetic gating mechanisms for BK channels: When complexity leads to simplicity," *J Gen Physiol*, vol. 118, pp. 583–587, 2001.

[137] N. S. Atkinson, G. A. Robertson, and B. Ganetzky, "A component of calcium-activated potassium channels encoded encoded by the *Drosophila*-Slo locus," *Sci*, vol. 253, pp. 551–555, 1991.

[138] A. Butler, S. Tsunoda, D. P. McCobb, A. Wei, and L. Salkoff, "mSlo, a complex mouse gene encoding mouse gene encoding Maxi calcium-activated potassium channels," *Science*, vol. 261, pp. 221–224, 1993.

[139] L. Pallanck and B. Ganetzky, "Cloning and characterization of human and mouse homologs of the drosophila calcium-activated potassium channel gene, slowpoke," *Hum Mol Genet*, vol. 3, pp. 1239–1243, 1994.

[140] D. H. Cox and R. W. Aldrich, "Role of the beta1 subunit in large-conductance Ca^{2+}-activated K^+ channel gating energetics - mechanisms of enhanced Ca^{2+} sensitivity," *J Gen Physiol*, vol. 116, pp. 411–432, 2000.

[141] C. M. Nimigean and K. L. Magleby, "β-subunits increase the calcium sensitivity of mSlo by stabilizing bursting kinetics," *Biophys J*, vol. 76, p. A328, 1999. Part 2.

[142] C. M. Nimigean and K. L. Magleby, "Functional coupling of the β1 subunit to the large conductance Ca^{2+}-activated K^+ channel in the absence of Ca^{2+} increased Ca^{2+} sensitivity from a Ca^{2+}-independent mechanism," *J Gen Physiol*, vol. 115, no. 6, pp. 719–734, 2000.

[143] J. P. Ding and C. J. Lingle, "Steady-state and closed-state inactivation properties of inactivating BK channels," *Biophys J*, vol. 82, pp. 2448–2465, 2002.

[144] M. Wallner, P. Meera, and L. Toro, "Molecular basis of fast inactivation in voltage and Ca^{2+}-activated K^+ channels: A transmembrane beta-subunit homolog," *Proc Natl Acad Sci U S A*, vol. 96, pp. 4137–4142, 1999.

[145] L. Sun, Y. Xiong, X. Zeng, Y. Wu, N. Pan, C. J. Lingle, A. Qu, and J. Ding, "differential regulation of action potentials by inactivating and noninactivating BK Channels in Rat Adrenal chromaffin Cells," *Biophys J*, vol. 97, pp. 1832–1842, 2009.

[146] X. M. Xia, J. P. Ding, and C. J. Lingle, "Molecular basis for the inactivation of Ca^{2+}- and voltage-dependent BK channels in adrenal chromaffin cells and rat insulinoma tumor cells," *J Neurosci*, vol. 19, pp. 5255–5264, 1999.

[147] T. M. Weiger, M. H. Holmqvist, I. B. Levitan, F. T. Clark, S. Sprague, W. J. Huang, P. Ge, C. C. Wang, D. Lawson, M. E. Jurman, M. A. Glucksmann, I. Silos-Santiago, P. S. DiStefano, and R. Curtis, "A novel nervous system beta subunit that downregulates human large conductance calcium-dependent potassium channels," *J Neurosci*, vol. 20, pp. 3563–3570, 2000.

[148] L. J. Wang and E. A. Sobie, "Mathematical model of the neonatal mouse ventricular action potential," *Am J Physiol Heart Circ Physiol*, vol. 294, pp. H2565–H2575, 2008.

[149] M. Stocker and D. Kerschensteiner, "Cloning and tissue distribution of two new potassium channel alpha-subunits from rat brain," *Biochem Biophys Res Commun*, vol. 248, pp. 927–934, 1998.

[150] E. T. Barfod, A. L. Moore, and S. D. Lidofsky, "Cloning and functional expression of a liver isoform of the small conductance Ca^{2+}-activated K^+ channel SK3," *Am J Physiol Cell Physiol*, vol. 280, pp. C836–C842, 2001.

[151] A. Brown, J. Adelman, C. Bond, I. Korniyenko, and M. Taylor, "Modulation of uterine contractility by small-conductance Ca^{2+}-activated K^+ SK3 channels," *FASEB J*, vol. 20, p. A1242, 2006.

[152] Z. Lu, "Mechanism of rectification in inward-rectifier K^+ channels," *Ann Rev of Physiol*, vol. 66, pp. 103–129, 2004.

[153] H. Matsuda, A. Saigusa, and H. Irisawa, "Ohmic conductance through the inwardly rectifying K channel and blocking by internal Mg^{2+}," *Nature*, vol. 325, pp. 156–159, 1987.

[154] E. Ficker, M. Tablialatela, A. Brown, S. Graves, C. Parker, and K. Morgan, "Spermine and spermidine as gating molecules for inward rectifier K^+ channels," *Science*, vol. 266, pp. 1068–1072, 1994.

[155] A. Lopatin, E. Makhina, and C. Nichols, "Potassium channel block by cytoplasmic polymaines as the mechanism of intrinsic rectification," *Nature*, vol. 372, pp. 366–369, 1994.

[156] S. Hagiwara and K. Takahashi, "The anomalous rectification and cation selectivity of the membrane of a starfish egg cell," *J Membrane Biol*, vol. 18, pp. 61–80, 1974.

[157] G. Krapivinsky, I. Medina, L. Eng, L. Krapivinsky, Y. H. Yang, and D. E. Clapham, "A novel inward rectifier K^+ channel with unique pore properties," *Neuron*, vol. 20, pp. 995–1005, 1998.

[158] K. Clement, J. P.and IV, G. Kunjilwar, M. Gonzalez, and U. Schwan-Stecher, "Association and stoichiometry of K_{ATP} channel subunits," *Neuron*, vol. 18, pp. 827–838, 1997.

[159] M. Curley and M. Cairns, "Expression of mRNA transcripts for ATP-sensitive potassium channels in human myometrium," *Mol Hum Reprod*, vol. 8, pp. 941–945, 2002.

[160] M. Yamada, S. Isomoto, S. Matsumoto, C. Kondo, T. Shindo, Y. Horio, and Y. Kurachi, "Sulphonylurea receptor 2B and Kir6.1 form a sulphonylurea-sensitive but ATP-insensitive K^+ channel," *J Physiol*, vol. 499, pp. 715–720, 1997.

[161] X. R. Wang, J. P. Wu, L. Li, F. X. Chen, R. P. Wang, and C. Jiang, "Hypercapnic acidosis activates KATP channels in vascular smooth muscles," *Cir Res*, vol. 92, pp. 1225–1232, 2003.

[162] H. Hu and E. Marban, "Isoform-specific inhibition of L-type calcium channels by dihydropyridines is independent of isoform-specific gating properties," *Molecular Pharmacology*, vol. 53, pp. 902–907, 1998.

[163] K. Jones, A. Shmygol, S. Kupittayanant, and S. Wray, "Electrophysiological characterization and functional importance of calcium-activated chloride channel in rat uterine myocytes," *Pflügers Arch*, vol. 448, pp. 36–43, 2004.

[164] K. ten Tusscher, D. Noble, P. J. Noble, and A. V. Panfilov, "A model for human ventricular tissue," *Am J Physiol Heart Circ Physiol*, vol. 286, pp. H1573–H1589, 2004.

[165] J. H. Lee, A. N. Daud, L. L. Cribbs, A. E. Lacerda, A. Pereverzev, U. Klockner, T. Schneider, and E. Perez-Reyes, "Cloning and expression of a novel member of the low voltage-activated T-type calcium channel family," *J Neurosci*, vol. 19, pp. 1912–1921, 1999.

[166] B. Fredholm and C. Kennedy, "Purinoceptors: are there families of P2X and P2Y purinoceptors?," *Pharmacol Ther*, vol. 64, pp. 445–475, 1994.

[167] S. Stojikovic, Y. Zonghe, T. Obsil, and H. Zemkova, "Structural insights into the function of P2X4: and ATP-gated ratio channel of neuroendocrine cells," *Cell Mol Neurobiol*, vol. 30, pp. 1251–1258, 2010.

[168] F. Soto, M. Garcia-Guzman, J. Gomez-Hernandez, M. Hollmann, and C. Karschin, "P2X4: An ATP-activated ionotropic receptor cloned from rat brain," *Neurobiology*, vol. 93, pp. 3684–3688, 1996.

[169] C. Lewis, "Ion-concentration dependence of the reversal potential and the single channel conductance of ion channels at the frog neuromuscular junction," *J Physiol*, vol. 286, pp. 417–445, 1979.

[170] P. Pelegrin and A. Surprenant, "Pannexin-1 mediates large pore formation and interleukin-1beta release by the ATP-gated P2X7," *EMBO J*, vol. 25, pp. 5071–5082, 2006.

[171] I. Chessel, C. Grahames, A. Michel, and P. Humphrey, "Dynamics of P2X7 receptor pore dilation: pharmacological and functional consequences," *Drug Dev Res*, vol. 53, pp. 60–64, 2001.

[172] M. Klapperstück, C. Büttner, G. Schmalzing, and F. Markwardt, "Functional evidence of distinct ATP activation sites at the human $P2X_7$ receptor," *J Physiol*, vol. 534, pp. 25–35, 2001.

[173] M. Smart, B. Bu, R. Panchal, J. Wiley, B. Cromer, D. Williams, and S. Petrou, "P2X7 receptor cell surface expression and cytolytic pore formation are regulated by a distal C-terminal region," *J Biol Chem*, vol. 278, pp. 8853–8860, 2003.

[174] Z. Yan, A. Khadra, S. Li, M. Tomic, A. Sherman, and S. Stojilkovic, "Experimental characterisation and mathematical modelling of P2X7 receptor channel gating," *J Neurosci*, vol. 30(42), pp. 14213–14224, 2010.

[175] L. Chow and S. Lye, "Expression of the gap junction connexin-43 is increased in the human myometrium toward term and with onset of labor," *Am J Obstet Gynecol*, vol. 170, pp. 788–795, 1994.

[176] T. Tabb, G. Thilander, and A. Grover, "An immunohistochemical and immunocytologic study of increase in myometrial gap junctions (and connexin43) in rats and human during pregnancy," *Am J Obstet Gynecol*, vol. 167, pp. 559–567, 1992.

[177] R. Garfield, S. Sims, M. Kannan, and E. Daniel, "Possible role of gap junctions in activation of myometrium during parturition," *Am J Physiol*, vol. 235, pp. C168–C179, 1978.

[178] J. Saffitz, B. Davis, and U. Darrow, "The molecular basis of anisotropy: role of gap junctions," *Electrophysiol*, vol. 6, pp. 498–510, 1995.

[179] P. Enyedi and G. Czirjak, "Molecular background of leak K^+ currents: two-pore domain potassium channels," *Physiol Rev*, vol. 90, pp. 559–605, 2010.

[180] R. Janis, D. Crankshaw, and E. Daniel, "Control of intracellular Ca^{2+} activity in rat myometrium," *Am J Physiol*, vol. 232, pp. C50–C58, 1977.

[181] P. Enyedi and G. Czirjak, "Molecular background of leak K^+ currents: Two-pore domain potassium channels," *Physiol Rev*, vol. 90, pp. 559–605, 2010.

[182] A. Grover, C. Kwan, and E. Daniels, "Ca^{2+}-dependence of calcium uptake by rat myometrium plasma membrane," *Am J Physiol*, vol. 242, pp. C278–C282, 1982.

[183] F. Carrera, T. Proverbio, and R. Marin, "Ca-ATPase of human myometrium plasma membranes," *Physiol Res*, vol. 49, pp. 331–338, 2000.

[184] D. Guerini, "The significance of the isoforms of plasma membrane calcium ATPase," *Cell Tissue Res*, vol. 292, pp. 191–197, 1998.

[185] L. Popescu and P. Ignat, " Calmodulin-dependent Ca^{2+}-pump ATPase of human smooth muscle sarcolemma," *Cell Calcium*, vol. 4, pp. 219–235, 1983.

[186] F. Taylor and D. Paton, "Characteristics of electrogenic sodium pumping in rat myometrium," *J Gen Physiol*, vol. 56, pp. 360–375, 1970.

[187] H. Parkington and M. Tonta, "Contractile activity, membrane potential, and cytoplasmic calcium in human uterine smooth muscle in the their trimester of pregnancy and during labor," *Am J Obstet Gynecol*, vol. 181, pp. 1445–1451, 1999.

[188] A. Shmigol, D. Eisner, and S. Wray, "Carboxyeosin decreases the rate of decay of the $[Ca^{2+}]_i$ transient in uterine smooth muscle cells isolated from pregnant rats," *Pflügers Arch*, vol. 437, pp. 158–160, 1998.

[189] A. Matthew, A. Shmygol, and S. Wray, "Ca^{2+} entry, efflux and release in smooth muscle," *Biol Res*, vol. 37, pp. 617–624, 2004.

[190] A. Varghese and G. Sell, "A conservation principle and its effect on the formulation of Na-Ca exchanger current in cardiac cells," *J Theoret Biol*, vol. 189, pp. 33–40, 1997.

[191] Q. Huys, M. Ahrens, and L. Paninski, "Efficient estimation of detailed single-neuron models," *J Neurophysiol*, vol. 96, pp. 872–890, 2006.

[192] K. Hristov, M. Chen, R. Soder, S. Parajuli, Q. Cheng, W. Kellett, and G. Petkov, "Kv2.1 and electrically silent kv channel subunits control excitability and contractility of guinea pig detrusor smooth muscle," *Am J Physiol cell Physiol*, vol. 302, pp. C360–C372, 2012.

[193] R. Casteels and M. Kuriyama, "Membrane potential and ionic content in pregnant and non-pregnant rat myomtrium," *J Physiol*, vol. 177, pp. 262–287, 1965.

[194] H. Hibino, A. Inanobe, K. Furutani, S. Murakami, I. Findlay, and Y. Kurachi, "Inwardly rectifying potassium channels: their structure, function and physiological roles," *Physiol Rev*, vol. 90, pp. 291–366, 2009.

[195] E. Perez-Reyes, "Molecular physiology of low-voltage activated T-type calcium channels," *Physiol Rev*, vol. 83, pp. 117–161, 2003.

[196] S. Wang, M. Yoshino, J. Sui, M. Wakui, P. Kao, and Kao.C.Y, "Potassium current in freshly dissociated uterine myocytes from nonpregnant and late-pregnant rats," *J Gen Physiol*, vol. 112, pp. 737–756, 1998.

[197] B. Matharoo-Ball, M. Ashford, S. Arulkumaran, and R. Khan, "Down-regulation of the alpha- and beta- subunits of the calcium-activated potassium channel in human myometrium with parturition," *Biol Reprod*, vol. 68, pp. 2135–2141, 2003.

[198] P. Aaronson, U. Sarwar, S. Gin, U. Rockenbauch, M. Connolly, and Tillet.A, "A role for voltage-gated, but not Ca^{2+}-activated, K^+ channels in regulating spontaneous contractile activity in myometrium from virgin and pregnant rats," *Br J Pharmacol*, vol. 147, pp. 815–824, 2006.

[199] S. L. Pierce, V. Kresowik, K. Lamping, and S. England, "Overexpression of SK3 channels dampens uterine contractility to prevent preterm labor in mice," *Biol Reprod*, vol. 78, pp. 1058–1063, 2008.

[200] M. Retamal, "Connexin and pannexin hemichannels are regulated by redox potential," *FPHYS*, vol. 5, 2014.

[201] P. Gomes, S. Srinivas, W. Van Driessche, J. Vereecke, and B. Himpens, "ATP release through connexion hemichannels in corneal endothelial cells," *Invest Ophthalmol Vis Sci*, vol. 46, no. 4, pp. 1208–1218, 2005.

[202] H. Zhao, Y. Ning, and C. Fleming, "Gap junctional hemichannel-mediated ATP release an hearing controls in the inner ear," *PNAS*, vol. 102, no. 51, pp. 18724–18729, 2005.

[203] S. Urabe, H. Miyoshi, H. Fujiwara, K. Yamaoka, and Y. Kudo, "Enhanced expression of P2X4 and P2X7 purinergic receptors in the myometrium of pregnant rats in preterm delivery models," *Reprod Sci*, vol. 16, pp. 1186–1192, 2009.

[204] H. Miyoshi, K. Yamaoka, S. Urabe, and Y. Kudo, "Functional expression of purinergic P2X7 receptors in pregnant rat myometrium," *Am J Physiol*, vol. 298(4), pp. R1117–R1124, 2010.

[205] H. Miyoshi, K. Yamaoka, S. Urabe, and Y. Kudo, "ATP-induced currents carried through P2X7 receptor in rat myometrial cells," *Reprod Sci*, vol. 19(12), pp. 1285–1291, 2012.

[206] B. Hille, "PIP_2 is a necessary cofactor for ion channel function: How and Why," *Annu Rev Biophys*, vol. 37, pp. 175–195, 2008.

[207] N. Rodriguez and M. Amarouch, "Phosphatidylinositol-4,5-Bisphosphate (PIP_2) stabilizes the open pore conformation of the Kv11.1 (hERG) channel," *Biophys J*, vol. 99, pp. 1110–1118, 2010.

[208] K. Loussouarn, K. Park, C. Bellocq, I. Baro, F. Charpentier, and D. Escande, "Phosphatidylinositol-4,5-bisphosphate, PIP_2, controls KCNQ1/KCNE1 voltage-gated potassium channels: a functional homology between voltage-gated and inward rectifier K^+ channels," *EMBO J*, vol. 22, no. 20, pp. 5412–5421, 2003.

[209] M. Emmert-Buck, R. Bonner, P. Smith, R. Chuaqui, Z. Zhuang, and Goldstein.S.R, "Laser capture microdissection," *Sci*, vol. 274, pp. 998–1001, 1996.

[210] S. Murphy, L. Fast, N. Hanna, and S. Sharma, "Uterine NK cells mediate inflammation-induced fetal demise in IL-10-null mice," *J Immunol*, vol. 175, pp. 4084–4090, 2005.

[211] S. Murphy, N. Hanna, L. Fast, S. Shaw, and G. Berg, "Evidence for participation of uterine NK cells in the mechanisms responsible for spontaneous preterm labor and delivery," *Am J Obstet Gynecol*, vol. 200, pp. 308e1–308e9, 2009.

[212] Y. Lin, Z. Liu, J. Di, and Y. Zeng, "Premature delivery induced by LPS in syngenetically impregnated BALB/c and NOD/SCID mice," *Ch J Cel Mol Immunol*, vol. 23(1), pp. 32–35, 2007.

[213] G. Dubyak, E. Clifford, B. Humphreys, S. Kertesy, and K. Martin, "Expression of multiple atp receptor subtypes during the differentiation and inflammatory activation of myeloid leukocytes," *Drug Dev Res*, vol. 39, pp. 269–278, 1996.

[214] B. Balázs, T. Dankó, G. Kovács, L. Köles, M. Hediger, and A. Zsembery, "Investigation of the inhibitory effects of the benzodiazepine derivative, 5-BDBD on P2X4 purinergic receptors by two complementary methods," *Cell Physiol Biochem*, vol. 32(1), pp. 11–24, 2013.

[215] R. Hodges, J. Vrouvlianis, M. Shatos, and D. Dartt, "Characterization of $P2X_7$ purinergic receptors and their function in rat lacrimal gland," *Invest Ophthalmol Vis Sci*, vol. 50(12), pp. 5681–5689, 2009.

[216] I. Beis and E. Newsholme, "The contents of adenine nucleotides, phosphagens and some glycolytic intermediates in resting muscles from vertebrates and invertebrates," *Biochem J*, vol. 152(1), pp. 23–32, 1975.

[217] E. Schwiebert and A. Zsembery, "Extracellular atp as a signalling molecule for epithelial cells," *BBA Biomembranes*, vol. 1615(1-2), pp. 7–23, 2003.

[218] M. Wikland and B. Lindblom, "Relationship between electrical and mechanical activity of the isolated term-pregnant human myometrium," *Europ J Obstet Gynec Biol*, vol. 20, pp. 337–346, 1985.

[219] D. Hilgemann, "Fitting K_v potassium channels into the PIP_2 puzzle: Hille group connects dots between illustrious HH groups," *J Gen Physol*, vol. 140(3), pp. 245–248, 2012.

[220] G. Bru-Mercier, J. Gullan, S. Thornton, A. Blanks, and A. Shmygol, "Characterization of the tissue-level Ca^{2+} signals in spontaneously contracting human myometrium," *J Cell Mol Med*, vol. 16, pp. 2990–3000, 2012.

[221] D. Sato, S. Despa, and D. Bers, "Can the sodium-calcium exchanger initiate or suppress calcium sparks in cardiac myocytes," *Biophys J*, vol. 102, pp. L31–L33, 2012.

[222] N. Janvier and M. Boyett, "The role of Na-Ca exchange current in the cardiac action potential," *Cardiovasc Res*, vol. 32, pp. 69–84, 1996.

[223] D. J. Snyders, "Structure and function of cardiac potassium channels," *Cardiovasc Res*, vol. 42, pp. 377–390, 1999.

[224] M. Berridge, "Smooth muscle cell calcium activation mechanisms," *J Physiol*, vol. 586(21), pp. 5047–5061, 2008.

[225] A. Shmigol, D. Eisner, and W. Susan, "The role of the sarcoplasmic reticulum as a Ca^{2+} sink in rat uterine smooth muscle cells," *J Physiol*, vol. 520(1), pp. 153–163, 1999.

[226] M. Song, G. Helguera, M. Eghabali, N. Zhu, M. Zarei, R. Olcese, L. Toro, and E. Stefani, "Remodeling of Kv4.3 potassium channel gene expression under the control of sex hormones," *J Biol Chem*, vol. 276, pp. 31883–31890, 2001.

[227] N. Tezuka, M. Ali, K. Chawalisz, and R. Garfiled, "Changes in transcripts encoding calcium channel subunits of rat myometrium during pregnancy," *Am J Physiol*, vol. 269, pp. C1008–17, 1995.

[228] J. Mershon, G. Mikala, and A. Schwartz, "Changes in the expression of the L-type voltage-dependent calcium channel during pregnancy and parturition in the rat," *Biol Reprod*, vol. 51, pp. 993–999, 1994.

[229] R. Garfield, S. Sims, and E. Daniel, "Gap junctions: their presence and necessity in myometrium during parturition," *Science*, vol. 198 (4320), pp. 958–960, 1977.

[230] E. De Vuyst, E. Decrock, L. Cabooster, G. Dubyak, C. Naus, W. Evans, and L. Leybaert, "Intracellular calcium changes trigger connexin 32 hemichannel opening," *EMBO*, vol. 25(1), pp. 34–44, 2005.

[231] K. Shintani-Ishida, K. Uemura, and K. Yoshida, "Hemichannels in cardiomyocytes open transiently during ischemia and contribute to repercussion injury following brief ischemia," *Am J Physil*, vol. 293, pp. H1714–H1720, 2007.

[232] V. Verselis and M. Srinivas, "Divalent cations regulate connexion hemichannels by modulating intrinsic voltage-dependent gating," *J Gen Physiol*, vol. 132(3), pp. 315–327, 2008.

[233] J. Gordon, "Extracellular atp: effects, sources and fate," *Biochem J*, vol. 233, pp. 309–319, 1986.

[234] M. Hogan, E. Ingham, and S. Kurdak, "Contraction duration affects metabolic energy cost and fatigue in skeletal muscle," *Am J Physiol*, vol. 274, pp. E397–402, 1998.

[235] S. Kolwicz, S. Purohit, and R. Tian, "Cardiac metabolism and its interactions with contraction, growth, and survival of cardiomyocytes," *Circ Res*, vol. 113(5), pp. 603–616, 2013.

[236] M. Barany, *Biochemistry of Smooth Muscle Contraction.* Academic Press, 1996.

[237] E. A. Dennis and R. A. Bradshaw, *Intracellular signalling in development and disease: cell signalling collection.* Academic Press, 2011.

[238] F. Fay, "Calcium sparks in vascular smooth muscle: relaxation regulators," *Science*, vol. 270, pp. 588–589, 1995.

[239] R. ZhuGe, R. Tuft, K. Fogarty, K. Bellve, F. Fay, and J. Walsh, "The influence of sarcoplasmic reticulum Ca^{2+} concentration on Ca^{2+} sparks and spontaneous

transient outward currents in single smooth muscle cells," *J Gen Physiol*, vol. 113, pp. 215–228, 1999.

[240] R. Latorre and S. Brauchi, "Large conductance Ca^{2+}-activated K^+ (BK) channel: activation by Ca^{2+} and voltage," *Biol Res*, vol. 39(3), pp. 385–401, 2006.